Selective vulnerability of the primary motor cortex in amyotrophic lateral sclerosis

Matthew Nolan

St. Hugh's College, University of Oxford

Academic Unit of Neuropathology, Nuffield Department of Clinical Neurosciences

A thesis submitted in part fulfilment of the requirements for the Degree of Doctor of Philosophy from the University of Oxford.

Trinity term, 2019.

Word count: 34,059

"Clear your mind must be, if you are to

discover the real villains behind this plot."

Jedi Master Yoda

Selective vulnerability of the primary motor cortex in amyotrophic lateral sclerosis

Matthew Nolan, St. Hugh's College

Submitted for the Degree of Doctor of Philosophy, Trinity term, 2019.

Abstract

The 'selective vulnerability' of cells and systems to disease pathomechanisms is a defining feature of amyotrophic lateral sclerosis (ALS), where the relative clinical and pathological involvement of cortical motor neurons varies between patients. Mislocalisation and aggregation of hyperphosphorylated TDP-43 (pTDP-43) is the major neuropathological finding in the majority of ALS cases (ALS-TDP), however the relationship between TDP-43 aggregation and neurodegeneration remains unclear. Here, we sought to reconcile the selective vulnerability of specific cell types within the human primary motor cortex to the pathological hallmarks of ALS, and define commonalities and differences of neurodegenerative phenotypes across the genetic spectrum of the disease. We analysed human post-mortem tissue from a large cohort of genetically defined ALS/FTD (n = 78), and mean age-matched control cases (n = 15) using a combination of quantitative immunohistochemical techniques and multi-level generalized linear modelling. The utility of novel methods such as CLARITY, imaging mass cytometry, combined RNA-ISH/IHC and multiplexed immunofluorescence is also explored. Additionally, two monogenic forms of the disease which exhibit striking UMN/LMN predominance, ALS-*FUS* and ALS-*OPTN*, are discussed and compared in the context of a novel BAC transgenic mouse and a unique human index case.

We show that there is considerable variance in neuropathology within the ALS primary motor cortex both within and across the genetic spectrum of disease, including in pTDP-43 aggregation, microglial activation, and inhibitory interneuron number. We also assess the extent of this pathology across the corticospinal neuraxis, and begin to examine the interactive relationship of pathologies using multiplexed immunofluorescence. Using RNA-ISH, we also show that while *FUS* is significantly more highly expressed in the primary motor cortex, *TARDBP* demonstrates a higher retention of transcripts localised to the nucleus. We also begin to assess the expression of transcription factors associated with projection neuron diversity including *CTIP2*, *SATB2* and *TBR1* in the primary motor cortex. Broadly, this thesis refines the concept of selective vulnerability within the ALS motor cortex across genetic subtypes, whilst highlighting the distinction between cellular vulnerability to proteinopathy and vulnerability to degeneration itself. These findings have implications for our understanding of disease pathogenesis and the development of genotype-specific therapies.

Acknowledgements

I wish to extend my considerable gratitude to the following people for their help completing the work involved in the generation of this thesis.

Firstly, to my supervisor, Dr. Olaf Ansorge, Academic Unit of Neuropathology, Oxford, whose patience during the whole process was truly a virtue, and whose knowledge and guidance I will always be grateful for. I am extremely fortunate to have such a mentor. My thanks also go to Prof. Kevin Talbot and Prof. Martin Turner, NDCN, University of Oxford for their advice and encouragement at all stages of this work and in referring many of the patients to the Oxford Brain Bank whose tissue was used in this study. Thanks also to Dr. Daniel Lunn, Department of Statistics, University of Oxford, whose assistance in the analysis of my results was invaluable. Thanks also to Dr. Menuka Pallebage Gamarallage for her helpful advice and guidance in the lab and in coffee breaks.

Outside of Oxford, my thanks go to Dr. Dan Meyer, GE Global Research, who agreed to collaborate with us in using the MxIF platform. The 'wet lab' MxIF work described in this thesis was performed at GE Global Research, Niskayuna, USA. The digital images produced through this collaboration were then processed and analysed by the author at the University of Oxford. All other work, including the production of all data, analysis and figure creation was conducted by the author at the University of Oxford.

I would also like to thank our funders, the Motor Neurone Disease Association, as well as all the donors and their families, without whom our work would not be possible. The tissue used in this study was sourced from the Oxford Brain Bank, MRC London Neurodegenerative Diseases Brain Bank and the Sheffield Brain Tissue Bank.

Finally, this work is dedicated to my grandparents - whose belief in me was unswerving, even as my own frequently faltered. I hope you'd have been proud.

Contents

List of Figures

List of tables

Abbreviations

AD – Alzheimer's disease

ADMA - Asymmetrically dimethylated arginine

AH – Anterior horn

ALS – Amyotrophic lateral sclerosis

ANOVA – Analysis of variance

BAC – Bacterial artificial chromosome

BIBD - Basophilic inclusion body disease

CA – Corpora amylacea

CBD – Corticobasal degeneration

CBP – Calcium binding protein

CI – Confidence interval

CNS – Central nervous system

CPN – Callosal projection neuron

CSMN – Corticospinal motor neuron

CSPG - Chondroitin sulphate proteoglycan

CST – Corticospinal tract

CThPN – Corticothalamic projection neuron

CyTOF – Cytometry time-of-flight

DAB - 3,3'-Diaminobenzidine

DAPI - 4′,6-diamidino-2-phenylindole

DNA – Deoxyribonucleic acid

DPR – Dipeptide repeat protein

EMG – Electromyography

FDA – Food and Drug Administration

FFPE – Formalin fixed, paraffin embedded

FTD – Frontotemporal dementia

FTLD – Frontotemporal lobar degeneration

FUS – Fused-in sarcoma

GABA – Gamma aminobutyric acid

GFAP – Glial fibrillary acid protein

GLI – Grey level index

GLM – Generalised linear modelling

GM – Grey matter

H&E – Haematoxylin and eosin

HnRNP1 – Human ribonucleoprotein 1

HRP – Horseradish peroxidase

HSP – Hereditary spastic paraplegia

IHC – Immunohistochemistry

IMC – Imaging mass cytometry

IMS – Industrial methylated spirit

ISH – In-situ hybridization

LMN – Lower motor neuron

LSC – Lumbar spinal cord

MCx – Motor cortex

MMA - Monomethylated arginine

MND – Motor neuron disease

MSA – Multiple systems atrophy

MxIF – Multiplexed immunofluorescence

NBF – Neutral buffered formalin

NCI – Neuronal cytoplasmic inclusion

NES – Nuclear export signal

NIFID - Neuronal intermediate filament inclusion disease

NLS – Nuclear localization signal

NMJ – Neuromuscular junction

OD – Optical density

OPC – Oligodendrocyte precursor cells

OPTN – Optineurin

PBS – Phosphate buffered saline

PD – Parkinson's disease

PET – Positron emission tomography

PFA - Paraformaldehyde

PLS – Primary lateral sclerosis

PMA – Progressive muscular atrophy

PMC – Primary motor cortex

PMD – Post-mortem delay

PMI – Post-mortem interval

PNFA – Progressive non-fluent aphasia

RAN- Repeat associated, non-ATG mediated

RIN – RNA integrity

RNA – Ribonucleic acid

ROI – Region of interest

RT-qPCR – Reverse transcription quantitative polymerase chain reaction

SCPN – Subcerebral projection neuron

SD – Semantic dementia

SDS – Sodium dodecyl sulfate

SMA – Spinal muscular atrophy

SNP – Single nucleotide polymorphism

SOD1 – Superoxide dismutase 1

TDP-43 – Transactive response DNA-binding protein 43kDa

UMA - Unmethylated arginine

UMN – Upper motor neuron

WB – Western blot

WES – Whole-exome sequencing

WGS – Whole-genome sequencing

WM – White matter

WT – Wild type

Publications

At the time of submission, sections of this thesis have been published or are under consideration for peer review as follows:

Published:
Nolan, M., Talbot, K. and Ansorge, O. (2016) Pathogenesis of FUS-associated ALS and FTD: insights from rodent models. *Acta Neuropathologica Communications*, **4**: 99.

In preparation/submitted:
Nolan, M., Barbagallo, P., Talbot, K., Turner, M., Keogh, M., Chinnery, P. and Ansorge, O. Novel homozygous R217X *OPTN* mutation causes knock-out of functional C-terminal domains and upper motor neuron predominant amyotrophic lateral sclerosis.

Nolan, M., Scott, C., Hof, P. and Ansorge, O. Betz cells of the primary motor cortex.

Nolan, M., Scott, C., Pallebage-Gamarallage, M., Lunn, D., Carpenter, K., McDonough, L., Meyer, D., Kaanumalle, S., Santamaria-Pang, A., Turner, M., Talbot, K. and Ansorge, O. Selective vulnerability of the primary motor cortex in amyotrophic lateral sclerosis.

Chapter one

Introduction

1. Introduction

This thesis is concerned with assessing the extent and nature of neuropathological substrates in the ALS primary motor cortex, both within molecularly defined cell-types and across the genetic spectrum of the disease. The clinical, genetic and pathological background of the disease will be discussed, followed by an introduction of novel histological techniques that may be applicable to the investigation of post-mortem human tissue. An assessment of motor cortex neuropathology in a large cohort of post-mortem ALS cases using immunohistochemistry and fully quantitative digital image analysis is conducted, and the utility of RNA-ISH explored. Finally, the neuropathology of a novel transgenic ALS-*FUS* mouse model utilising the human LMN predominant P525L mutation will be assessed and contrasted with the striking UMN predominant pathology seen in an index case of homozygous recessive ALS-*OPTN*.

1.1 Amyotrophic lateral sclerosis

1.1.1 History

ALS is a progressive neurodegenerative disease, commonly (but somewhat imprecisely) referred to as motor neurone disease (MND) within the United Kingdom. ALS as a clinical phenomenon was first described by the pre-eminent neurologist Jean-Martin Charcot in his seminal paper of 1869 [3], who using histological methods now considered primitive, was still able to shrewdly note the susceptibility of particular anatomical regions and cell types to the disease. Since Charcot's original description, substantive progress has been

made in elucidating the genetics, neuropathology and molecular mechanisms underlying ALS pathogenesis.

1.1.2 Epidemiology

ALS is a comparatively rare disease, with an average incidence globally of around 2 cases/100,000 people [4], but is also the most common manifestation of the motor neurone disease class. Death occurs on average 2-3 years after symptom onset [5-7], although a small percentage of patients survive for 10 years or more [6]. Around 90% of cases are 'sporadic', meaning there is no clear Mendelian component. The remaining 10% of cases have been referred to historically as 'familial', in that they are inherited through mutations to one or more ALS genes, of which over thirty have been described at the time of writing (ALS ALSoD database: http://alsod.iop.kcl.ac.uk/). However, usage of the term 'familial' can perhaps be both misleading and inaccurate for two reasons. Firstly, the concept of family history is vague, especially in the context of mutations within several genes which are able to cause the expression of multiple clinically distinct phenotypes, meaning specific disease-mutation segregation within a given lineage can be difficult to ascertain. Secondly, a small percentage of sporadic cases actually turn out to be caused by high penetrance mutations that have arisen either in a pure *de novo* fashion or inherited recessively through both parents being carriers. As to the best of our knowledge identical *de novo* mutations in the same gene cause the same disease as those that have been dominantly inherited, the term familial is considered something of a misnomer and will be avoided for the purpose of this thesis.

While many studies have now reconciled an increased occurrence of the disease with various environmental influences [8-10], particularly in geographical areas with high

incidence rates [11-13], the significance of these influences is debated. Some environmental studies suffer from small population sizes or lack of rigour, and the influence of these environmental factors is therefore considered inconclusive.

1.1.3 Clinical manifestations

While a clinically heterogeneous disease, the most common clinical presentation (and diagnostic requirement) of classical ALS is a combination of both upper and lower motor neuron signs [14]. Upper motor neuron signs include increased muscle tone and spasticity, increased reflexes including Babinski's sign, and pyramidal weakness. Lower motor neuron signs include decreased muscle tone and associated muscular atrophy, and muscle fasciculations [15]. Diagnosis of ALS is primarily made on the basis of clinical assessment in the context of patient history and examination, plus monitoring of progression, with the minimum requirement as defined by the El Escorial criteria being "progressive upper and lower motor neuron deficits in at least one limb or region of the human body", or "lower motor neuron deficits as defined by clinical examination (one region) and/or by EMG in two body regions" [16]. While neurophysiology can be useful in some cases, neuroimaging is essentially used to rule out mimic disorders [17, 18]. The majority of cases are limb onset, with smaller numbers of patients exhibiting bulbar or respiratory onset forms [14]. Death normally occurs as a result of the progressive paralysis of the diaphragm and subsequent respiratory arrest or pneumonia secondary to recurrent aspiration.

1.1.4 Neuroanatomically restricted phenotypes

In addition to ‘classical’ ALS that exhibits broad equivalency between upper and lower motor neuron signs, there are also a number of rarer restricted phenotypes that present with a predominance of upper/lower motor neuron features, which are sometimes associated with an improved prognosis and less aggressive disease course. These include:

- Progressive Bulbar Palsy: affecting only the corticobulbar pathways and the cranial nerves IX, X, XI and XII [16, 19]
- Flail arm/leg syndrome: exhibiting an asymmetry of onset of arms or legs [16, 20]
- Progressive muscular atrophy (PMA)[21]: Exhibiting predominantly lower motor neuron signs in the absence of upper motor neuron features. However of note is that at autopsy, up to 50% of patients assessed as PMA actually also show degeneration of neurons in the pyramidal tract [22]
- Primary lateral sclerosis [23]: Exhibiting predominantly upper motor neuron signs in the absence of lower motor neuron features.

The variability of motor neurone disease presentation highlights the importance of not only defined diagnostic criteria for ALS, but also consistent criteria for the monitoring of progression. Such criteria are essential for the appropriate design of therapeutic trials involving patients who naturally exhibit varying rates of progression and disease severity.

1.1.5 Treatment

Treatment for ALS is mainly supportive. There is no disease-modifying treatment available, and over 50 major phase II/III clinical trials involving ALS patients having failed. Riluzole, a putative anti-glutamatergic that is thought to act through the prevention of excitoxicity and is widely prescribed, produces only a modest increase in survival time of three months in clinical trials [24]. Recently, a drug originally developed for the treatment of ischaemic stroke, Edaravone, was granted approval by the FDA for the treatment of ALS in the United States. However, in Phase III clinical trials Edaravone showed no effect on ALSFRS scores, and a significance level was only reached in a small cohort of patients with narrowly defined presentation in post-hoc analysis [25]. Additionally, Edaravone requires repeat IV infusions, its effect on survival is unknown, and a course of treatment costs $145,000. Further clinical trials of Edaravone are suggested [26].

1.2 The relationship between ALS and Frontotemporal dementia

FTD and its pathological presentation - Frontotemporal Lobar Degeneration (FTLD) – is the second most common form of young-onset dementia after Alzheimer's disease [27]. FTLD is characterised by widespread degeneration of neurons in the frontal and temporal lobes, presenting clinically as significant behavioural or language abnormalities [28], with relative sparing of memory until late disease stages. FTD is clinically categorised as one of three subtypes: behavioural variant FTD (bvFTD), semantic dementia (SD) or progressive non-fluent aphasia (PNFA) [29, 30]. As for ALS, no disease modifying therapy is available. Symptomatic treatment includes selective serotonin re-uptake

inhibitors (SSRI's) to control compulsive behaviour [31] and general supportive care [28]. Diagnosis for both ALS and FTD is made primarily on clinical grounds in the context of an appropriate history and examination. Neurophysiological testing is useful in ALS, but other investigations such as imaging are essentially used to rule out mimic disorders [17, 18, 32]. While detectable cognitive dysfunction may be present in up to 50% of ALS cases [33, 34], around 15% of patients meet formal clinical criteria for both ALS and FTD (ALS-FTD) [33, 35, 36], the combination of which being associated with a worse prognosis and reduction in survival time of around one year [36].

Despite significant clinical heterogeneity, the overlap in genetics and pathology between ALS and FTD have led them to be widely considered as being part of a clinico-pathological disease continuum, with pure ALS and pure FTD representing spectral extremes [37]. Cases with mutations in more than one ALS/FTD gene are being increasingly reported [38-40], suggesting that 'oligogenic' factors may be one element in a 'multiple-hit' model of disease [41].

1.3 Genetics

The majority of ALS cases (~90%) display no clear genetic causation, while the remaining ~10% of cases are caused by one or more mutations of varying penetrance (see Table 1 for examples). It follows that the more highly penetrant mutations are found, the less likely more are to be discovered in the future. A few isolated examples notwithstanding, it is now entirely possible that the era of finding definitively causative mutations in ALS is over. This naturally means that mutations that are discovered now require a higher evidence of pathogenicity than those discovered previously, which tend to be more obviously penetrant. Additionally, the picture building in ALS genetics is one of the

disease being accounted for mainly by rarer, lower penetrance variants, which can only be elucidated through the sequencing of thousands of genomes on a worldwide scale. Initiatives such as Project MinE (https://www.projectmine.com/) have been established to assail this, but suffer from being conducted using peripheral blood, which is not affected by the disease. Notably, mutations to some genes seem to predispose patients towards the development of either upper or lower motor neuron predominant ALS [42-45]. A majority of dominantly-caused genetic ALS is caused by mutations to four genes – *C9ORF72*, *SOD1*, *FUS* and *TARDBP* (Table 1).

Gene	Location	Function/processes	Reference
C9ORF72	9p21.2	Toxic RNA/dipeptide repeat aggregation/haploinsufficiency	[46]
SOD1	21q22.11	Toxic aggregation, free radical scavenger enzyme	[47]
FUS	16p11.2	DNA/RNA metabolism	[48]
TARDBP	1p36.22	DNA/RNA metabolism	[49]
OPTN	10p13	Autophagy	[50]
CHMP2B	3p12.1	Autophagy, lysosomal pathway	[51]
HNRNPA1	12q13.1	RNA metabolism	[52]

Table 1: Some of the genes that are implicated in ALS and that are included in this study.

1.3.1 *C9ORF72*

In 2011, two independent groups reported that a hexanucleotide (G_4C_2) expansion within a non-coding region of the chromosome 9, open reading frame 2 (*C9ORF72)* gene was responsible for 40% of genetically caused ALS cases [46, 53], making it the most common genetic cause of the disease, accounting for around 35% genetically-dominant ALS cases [54] and around 25% FTD cases [55]. While the normal expression of *C9ORF72* is relatively low in the CNS, it is highly conserved across several regions [56]. However the normal physiological function of *C9ORF72* is unclear. A recent computational study predicted that C9ORF72 possesses putative DENN domains [57], which act as generalized regulators of Rab GTPases. This was later followed by mechanistic studies supporting the role of *C9ORF72* in the regulation of endosomal trafficking through association with such enzymes [58, 59]. While a normal repeat range might be considered to be <30, the precise number of repeats required to elicit disease is unclear. Pathogenic repeat sizes in the hundreds or thousands are commonly reported [60]. However, repeat sizes also vary significantly both within and across tissue types, including the brain [61].

Phenotypically, at least two studies have identified a relationship between age of C9-ALS disease onset and repeat length [61, 62], postulated to be caused by an increase in methylation of 5' CpG islands [62], however this is apparently not recapitulated in FTD [61]. Intermediate repeat sizes have also been associated with an increased risk of neuropsychiatric symptoms in non-ALS/FTD phenotypes [63]. The variance of repeat length across the sporadic ALS brain and whether this influences phenotype is unknown. However, unlike in other expansion disorders (e.g *HTT* in Huntington's disease), there appears to be no element of genetic anticipation in *C9ORF72* ALS/FTD.

The way in which the expansion induces pathogenicity is debated, but three primary mechanisms have achieved prominence. Firstly, a reduced expression of both *C9ORF72* RNA and protein is found in the frontal cortex, cerebellum and blood of C9-ALS patients [64, 65], implicating haploinsufficiency of the gene as a pathogenic mechanism. This is supported by motor phenotypes in both zebrafish [66] and *C.elegans* knock-out models [67], as well as a recent study detailing the toxic effect of haploinsufficiency caused by the expansion in patient-derived motor neurons [68]. However, several independently-generated *C9ORF72* knock-out mice do not develop a motor phenotype or neurodegeneration [69-71], although interestingly do display various immunological deficits. The contribution of haploinsufficiency as a mechanism of C9-ALS is therefore somewhat inconclusive.

Secondly, mRNA containing the expansion is liable to undergo unconventional repeat-associated, non-ATG mediated (RAN) translation, resulting in the formation of five distinct dipeptide repeat (DPR) species. The toxicity of these DPR's has been demonstrated in several cell-model [72-74] and *Drosophila* [75] models. In humans however, the toxicity conferred by DPR formation is less clear. The highest DPR burden in human C9-ALS is within the cerebellum and hippocampus [76, 77], areas which are largely unaffected by neurodegeneration in ALS, while DPR's are sparse within the spinal cord [78], the site of primary ALS pathology. Only the presence of Poly-GP correlates with clinically affected areas and co-localizes with pTDP-43 [77]. Additionally, two *C9ORF72* BAC-transgenic mice developed both DPR and RNA foci pathology but not neurodegeneration or the phenotypic features suggestive of ALS/FTD [79, 80]. However, one C9 mouse model utilising the full-length *C9ORF72* gene displayed both DPR pathology and neurodegeneration [81]. Case reports of extensive DPR pathology in unaffected patients both with and without the expansion provides further evidence of their

potentially limited influence in humans [82, 83], and suggest that their effect is possibly well tolerated. This is a significant cause of debate within the *C9ORF72* field at present, where what we can detect in the lab (nucleocytoplasmic defects caused by DPR's etc) is seemingly at odds with the realities of human biology.

Finally, foci containing RNA transcribed in both the sense and antisense directions have been identified in patient brain tissue, peripheral blood and in transgenic cell lines [84, 85]. Unlike DPR's which seem to only occur within neurons, RNA foci containing the expansion have been identified in both neurons and glial cells [86]. Such foci contribute to toxicity by sequestering RNA-binding proteins and their subsequent effect on pre-mRNA splicing [85, 87]. A recent study using human brain tissue found that the biggest target of C9-RNA is the RNA binding protein hnRNP H, which regulates the alternative splicing of multiple target exons. In C9 brains many of these target exons were aberrantly included/excluded, and the presence of insoluble hnRNP H correlated with the level of splicing dysregulation in that region [88]. Sense RNA foci (containing GGGGCC) are most numerous in the cerebellar granule neurons, while antisense foci (containing CCCCGG) are more numerous in Purkinje cells and motor neurons [89]. Notably, only the presence of anti-sense foci have been correlated with increased levels of mislocalized TDP-43 [90].

1.3.2 *FUS*

Note: Some sections related to FUS in this thesis have been published. See publications, page xv.

FUS encodes a 526 amino acid, 15-exon RNA binding protein of the FET family, containing several distinct functional domains including a RNA-recognition motif and a

highly-conserved C-terminal nuclear localization signal (NLS) [91], where many of the identified mutations occur (Fig 1). The precise normal physiological function of *FUS* is unclear. However, known roles include transcriptional control [92], RNA processing through splicing regulation of pre-mRNA's [93], and DNA repair [94] [95]. While there is still some debate on the nature of FUS toxicity, the range of functions involving *FUS* highlight its potential susceptibility to dysfunction and the consequences for the maintenance of cellular RNA homeostasis. Evidence to support both gain and loss-of-function mechanisms now exists, and it appears likely that both mechanisms are implicated, depending on the particular mutation and its functional connotations.

Under normal physiological conditions FUS is predominantly localized in the nucleus in neurons, but is exclusively nuclear-based in glia [96]. However as an RNA-binding protein, it possesses the ability to move between both through its role in nucleocytoplasmic transport [97]. The characteristic presence of FUS-immunoreactive inclusions in the cytoplasm of ALS-*FUS* (Fig 2) and FTLD-FUS (Table 2) has led to the suggestion that mislocalization of FUS to the cytoplasm contributes to neurodegeneration in these cases, by a gain-of-toxicity mechanism. This concept is closely tied to the formation of stress granules, which notably contain mutant FUS but not endogenous wild-type FUS [98]. The role of mutant FUS in stress-assembly dynamics is now well documented [98-100] and illustrates an obvious differential between normal and disease physiology. For example, one study has demonstrated how oxidative stress recruits mutant FUS into stress granules where it can sequester wild-type FUS to disrupt RNA processing and potentially initiate cell death [101]. Knock-down zebrafish models, however, display a subtle motor phenotype and hyper extended axonal branching that cannot be rescued with mutant FUS, suggesting loss-of-function [102]. A combination of both mechanisms remains possible.

Disease		Neuropathology	Genetics	Epidemiology	Clinical features
ALS-*FUS*		- Degeneration of both upper and lower motor neurons - Significant neuronal loss within anterior horn of spinal cord - Moderate neuronal loss of Betz cells within layer IV of motor cortex and motor nuclei of brainstem - Dystrophic neurites, astrogliosis, microglial activation - TDP43-negative, FUS-positive neuronal and glial cytoplasmic inclusions	*FUS* – over 50 mutations described, particularly missense variations within C-terminal Nuclear Localization Signal	*FUS* mutations account for ~4% fALS and ~1% sALS	- Progressive muscular atrophy - Dysphagia - Dysarthria - Respiratory failure - Spasticity - Death normally within 2-3 years from symptom onset
FTLD-FUS	Atypical FTLD with Ub (aFTLD-U)	- Widespread degeneration of frontal cortex and ventral temporal lobe - Tau/TDP43-negative, FUS-positive neuronal or glial inclusions predominantly within hippocampus, amygdala, frontotemporal cortex and striatum	Rare evidence of FUS mutations in clinical FTD but without neuropathological verification	~10% FTLD cases display FUS pathology	- Normally behavioural variant FTD - Changes in personality and emotion - Irrationality, compulsiveness, confusion, repetition, inappropriate behaviour - Psychiatric symptoms, depression and anxiety common - Memory, motor function and perception are relatively preserved until late disease stages
	NIFID	- Neuronal cytoplasmic inclusions containing abnormal intermediate filament accumulation in addition to FUS pathology			
	BIBD	- Significant FUS-pathology plus subcortical basophilic inclusions on H&E staining			

Table 2: Phenotype-pathology correlations of FUS-linked human ALS/FTD. ALS, Amyotrophic Lateral Sclerosis; FTLD, Frontotemporal Lobar Degeneration; FTD, Frontotemporal Dementia; NIFID, Neuronal Intermediate Filament Inclusion Disease; BIBD, Basophilic Inclusion Body Disease; *FUS*, Fused-in-sarcoma; H&E, Haematoxylin and eosin.

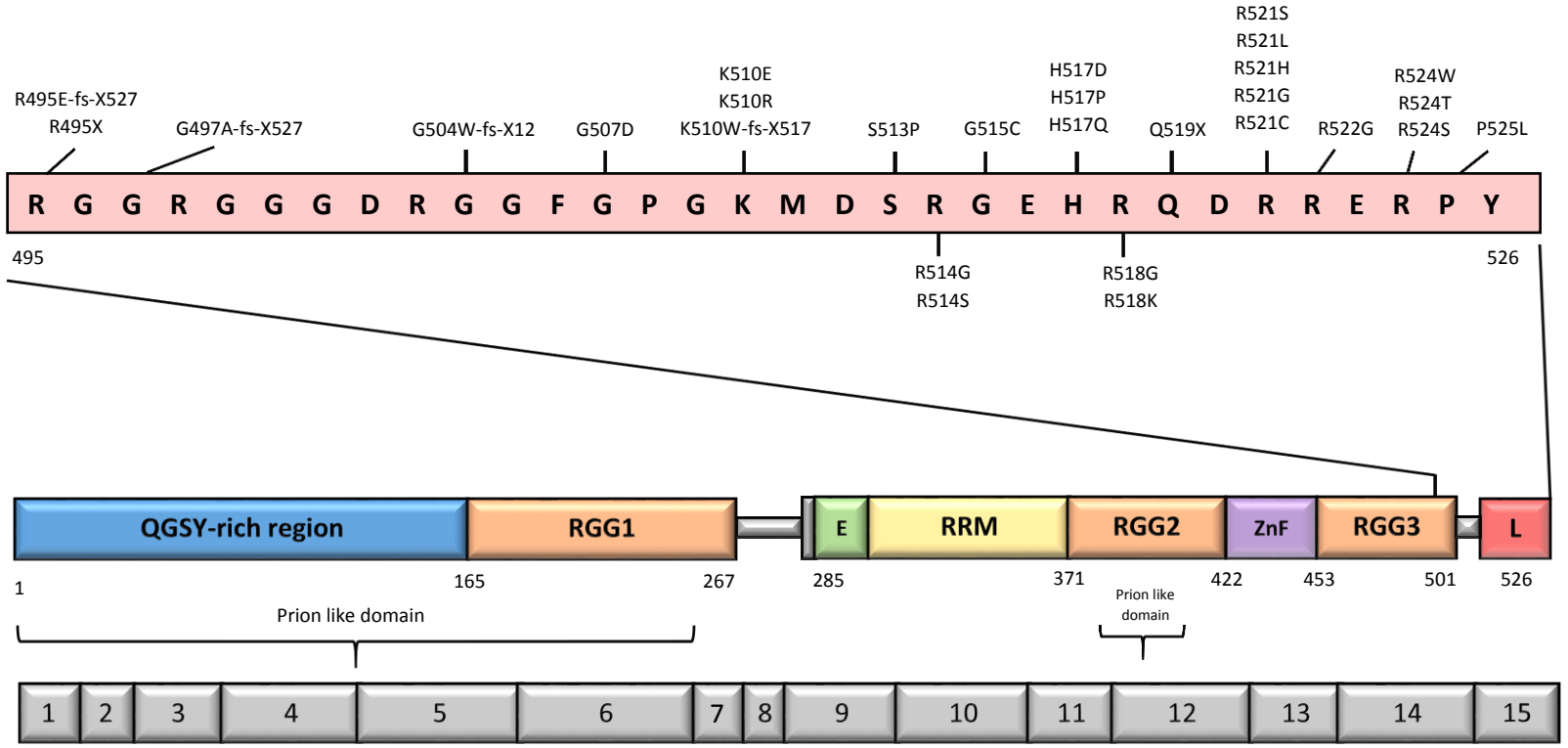

Figure 1: Structure and functional domains of FUS. FUS is a member of the FET family of proteins, and contains several functional domains including a QGSY-rich region, multiple RNA binding regions, a C-terminal Zinc-finger motif and two low complexity or putative 'prion-like' domains. The majority of mutations in ALS-FUS are located within the C-terminal nuclear localization signal domain in exon 15. Arginine methylation of the RGG3 region is emerging as an important post-translational modification in the context of nuclear import.

1.3.3 ALS-*FUS*

Over 50 mutations in the *FUS* gene have now been reported in ALS – most of which are missense – with a minority being in-frame deletions [91]. Many, including the most common *FUS* mutation in humans, R521C, occur within the highly conserved C-terminal nuclear localization signal [103]. Nearly all display an autosomal dominant pattern of inheritance, albeit with varying degrees of penetrance. Notably, some mutations such as P525L are associated with a more severe disease progression [104] and juvenile onset [105, 106], with apparently sporadic occurrence, presumably because the condition is frequently lethal before it can be transmitted [107].

The neuropathology of ALS-*FUS* may be related to its specific genetic cause and subsequent disease course [108]. Predominantly a LMN disease with a younger average age of onset and an aggressive course, patients typically display severe neuronal loss in the spinal cord anterior horn with only low or moderate neuronal loss of Betz cells within layer V of the motor cortex [54]. Neuronal and glial cytoplasmic inclusions (NCI) containing ubiquitinated FUS in the motor cortex, basal ganglia and spinal cord, as well as dystrophic neurites [109] are seen (Table 2). TDP-43 pathology is entirely absent. Certain variants including P525L seemingly predispose the formation of basophilic inclusions (BI) [108], which can be readily viewed using haematoxylin and eosin (H&E) (Figure 2A). Clinical presentation is consistent with classical ALS, although three groups have reported similar clinical features in patients with the p.R521C variant, suggesting correlation between individual mutations and specific clinical abnormalities [103, 110, 111].

1.3.4 FTLD-FUS

FUS mutations have only rarely been reported in FTD, and mostly co-exist with ALS, making their significance in its pathogenesis unclear [91, 112-114]. One study identified a unique variant within exon 4 (P106L) in a patient with pure bvFTD [115] (which could not be confirmed as co-segregating because of lack of DNA from other family members), and another reported a novel mis-sense variation (M254V) with predicted pathogenicity in an FTD patient without ALS [116], but neither case has been confirmed post-mortem. Indeed, there have been no reported cases of pure, clinical FTD that were both genetically and neuropathologically confirmed as *FUS*-related. Additionally, the largest genome-wide association study (GWAS) of clinical FTD to date involving exome sequencing of 3526 FTD patients and 9402 healthy controls found only weak association with variants at the *FUS* locus, with none being at a genome-wide significance level [27]. Genome-wide association studies, however, are only powered to detect an association between common variants and a disease. The picture emerging from ALS genetics, though as yet unconfirmed in FTD, is a genetic contribution mostly accounted for by rare variants.

Despite the absence of confirmed genetic cases, inclusions immunoreactive for FUS are present in a small proportion FTLD cases (FTLD-FUS) and can be neuropathologically sub-categorised as atypical FTLD-U, neuronal intermediate filament inclusion disease (NIFID), or basophilic inclusion body disease (BIBD) [117, 118](Table 2). All are defined by the presence of FUS-positive, tau/TDP-43 negative inclusions of varying formation, often co-localized with the other two FET proteins EWS and TAF15, alongside prominent degeneration of the frontal and temporal lobes. Atypical FTLD-U cases display uniform, round neuronal cytoplasmic inclusions (NCI) throughout the brain, but mainly within frontal and temporal neocortex, hippocampus and striatum [119]. NIFID is characterized

by NCI's that are immunoreactive for all class IV neurofilament chains - the form of which vary according to neuronal type and region [119] - with additional cytoplasmic granules of FUS aggregation [120]. BIBD cases show large, round basophilic neuronal inclusions on H&E staining that also show strong immunoreactivity for FUS, predominantly within subcortical regions [121]. Interestingly, basophilic inclusions have been noted in ALS-*FUS* without FTLD [104, 105, 122]. The considerable variation in neuropathology between patients with FTLD does not correlate clearly with differences in clinical features, compounding the difficulty in making assertions regarding neuropathological aetiology. However, there is some evidence that aFTLD-U cases show stereotypic clinical characteristics [112].

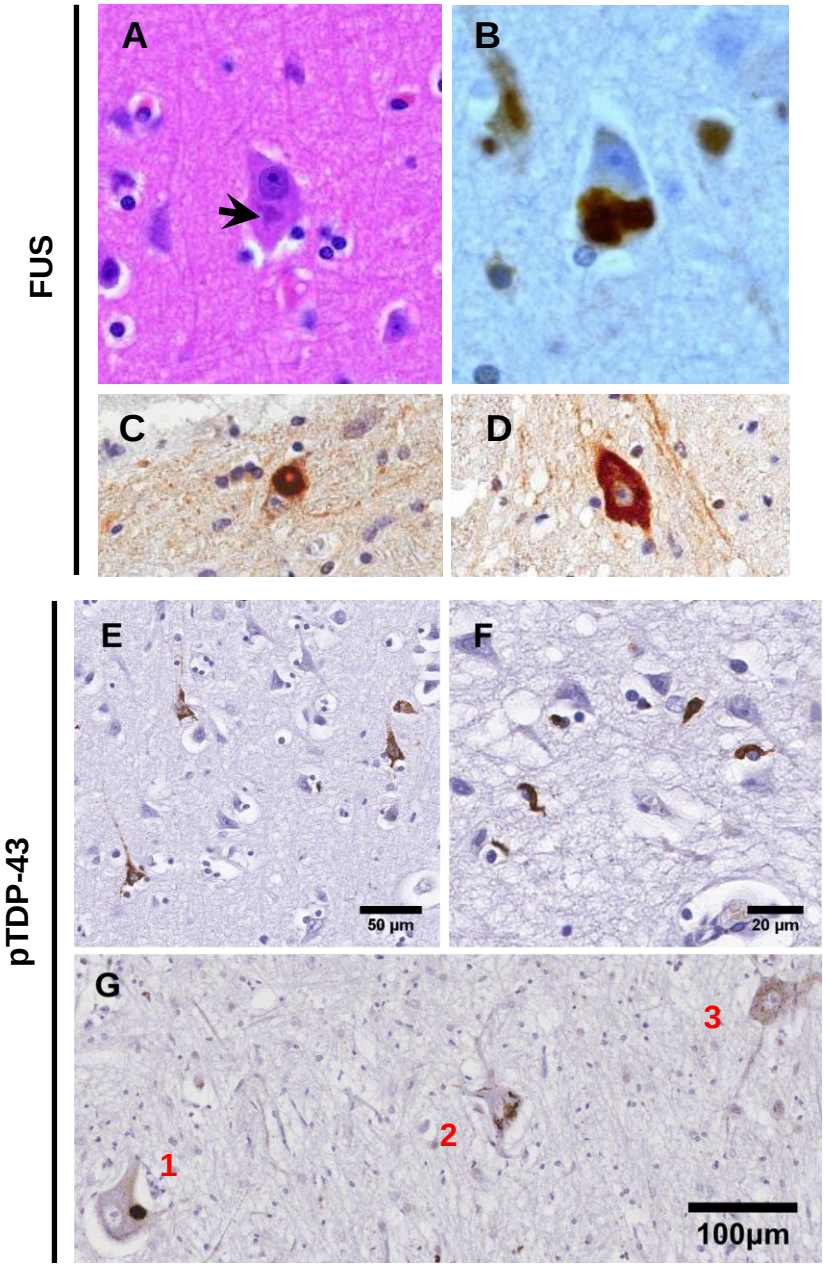

Figure 2: The heterogenous appearance of FUS and pTDP-43 pathology in ALS. Inclusions associated with the FUS P525L mutation, which exhibits clinically as a juvenile onset and aggressive disease course (A,B). Basophilic neuronal inclusions are present in ALS-*FUS* (arrowed) and can be viewed using H&E stain, X63 Obj (A). Discrete neuronal inclusion immunoreactive for FUS associated with the P525L mutation, X63 Obj (B). ALS-FUS inclusions in the anterior horn of spinal cord, both X40 Obj (C,D). Well defined, compact inclusions (C) or intense diffuse cytoplasmic staining (D) are commonly seen, often with clear nuclear clearance. pTDP-43 pathology exists within neurons where it can be seen within both the cell soma and apical dendrites (E). It is also prominent in glial cells, where it can take the format of so called 'cat-eye' shaped inclusions (F). Pathology is often more varied within the large anterior horn neurons of the spinal cord (G) where it can exist as discrete inclusions [1] skein like inclusions [2] or cellular punctate [3].

1.3.5 Evidence for distinct pathogenesis of ALS-*FUS* and FTLD-FUS

Despite structural and functional similarities between FUS and TDP-43, they are differentially post-translationally modified (Table 3). TDP-43, for example is extensively phosphorylated and cleaved to produce toxic, aggregate-prone C-terminal fragments, while endogenous FUS is maintained at full length, even in disease [114]. The fact that neurodegeneration is induced through the presence of a single point mutation within the *FUS* gene in some cases of ALS, but FUS inclusions are the predominant pathological characteristic of a subset of FTLD cases *despite* lack of mutation to its corresponding gene, has led to the suggestion of each disease being driven by separate pathogenetic mechanisms. Post-translational modification of proteins can drastically alter their function; for example by changing their conformational shape through the addition of charged amino acids at certain residues. Recently, evidence has emerged involving specific post-translational modifications of FUS that suggest a possible explanation for the differences in pathogenesis between the two diseases, whilst simultaneously accounting for their shared FUS immunoreactivity.

Arginine methylation is a common post-translational modification of RNA-binding proteins involving the addition of methyl groups either symmetrically or asymmetrically to nitrogen atoms in the arginine side chain [123](Table 3). At least 20 sites within the FUS protein, mainly located in the RGG3 domain, are arginine methylated, [124], mediated primarily by protein *N*-arginine methyltransferase 1 (PRMT1) [125], inhibition of which limits the capacity of mutant FUS to localize to the cytoplasm to form inclusions [126]. The nuclear import karyopherin protein Transportin-1 strongly co-localizes with FUS in FTLD-FUS [97], however in FTLD-FUS all FET proteins co-localize with Transportin-1, whereas ALS-*FUS* inclusions contain exclusively FUS. In 2012, Dormann

et al [127] showed that arginine methylation impairs Transportin-1 dependent nuclear import of FUS by preventing Transportin-1 binding upstream of the NLS. Using a novel methyl-specific antibody, they also showed that inclusions in ALS-*FUS* are extensively asymmetrically methylated. The authors used this evidence to speculate that mislocalization of FUS in ALS is caused by mutations in the NLS that are then exacerbated by arginine methylation in the RGG3 domain, whereas mislocalization in FTLD-FUS may be caused more broadly by hypomethylation of all FET proteins, mediated by altered Transportin-1 binding. This concept has recently been elaborated through the development of monoclonal antibodies capable of distinguishing individually methylated forms of FUS protein - unmethylated arginine (UMA), monomethylated arginine (MMA) or asymmetrically arginine dimethylated (ADMA) [128]. Using these antibodies, it has been possible to show that FUS inclusions in FTLD-FUS contain UMA and MMA, whilst inclusions in ALS-*FUS* contain only ADMA (Table 3). UMA and MMA show an increased binding capacity to Transportin-1, whilst arginine methylation decreases its binding capacity and thus reduces nuclear import. Together, these studies implicate a role for arginine methylation in FUSopathy, and for the first time provide substantive evidence of each disease being driven, at least in part, by distinct pathogenetic mechanisms.

Phosphorylation is another common post-translational modification involving the covalent addition of a phosphoryl group by a protein kinase. FUS is phosphorylated by DNA protein kinase (DNA-PK) in response to DNA damage, which leads to its cytoplasmic accumulation [129], and there is evidence of DNA damage in FTLD-FUS patients. Additionally, one group has shown that phosphorylation of a specific C-terminal tyrosine residue impairs Transportin binding and prevents nuclear import [130]. Given the multifactorial nature of FUSopathy (and indeed, ALS/FTD in general) it is likely that

both types of post-translational modification contribute to disease pathogenesis. However, the actual pathological significance and contribution of each to human disease is still yet to be demonstrated.

Disease			**ALS-*FUS***	**FTLD-FUS**	**sALS**	**FTLD-TDP**	**References**
Genetics			Over 50 *FUS* mutations described, particularly within Nuclear Localization Signal	No evidence of *FUS* mutations in pure FTLD	No mendelian pattern of inheritance	*GRN*, *VCP* and *C9ORF72* mutations	[28, 91, 109, 119, 131]
Pathological sub-types			N/A	aFTLD-U, NIFID, BIBD	B	A, B, C, D.	[28, 91]
Primary inclusion component			FUS	FUS	TDP-43	TDP-43	[91, 109, 132]
Other inclusion components	FET proteins (EWS, TAF15)		✗	✓	✗	✗	[119]
	Ubiquitin		✓	variable	✓	✓	[133]
	Transportin-1		✗	✓	✗	✗	[128]
Post-translational modifications of main inclusion component	Phosphorylation		✗	✗*	✓	✓	[129, 130]
	Arginine Methylation	Unmethylated (UMA)	✗	✓	✗	✗	[125-128]
		Monomethylated (MMA)	✗	✓	✗	✗	[125-128]
		Dimethylated (ADMA)	✓	✗	✗	✗	[125-128]
	Cleavage		✗	✗	✓	✓	[49, 93]

Table 3: Pathogenetic differences between ALS-*FUS*, FTLD-FUS, sporadic ALS and FTLD-TDP. Under normal physiological conditions, FUS does not appear to undergo any post-translational modifications. Arginine methylation is facilitated by protein methyltransferase 1 (PRMT1), which inhibits binding to Transportin-1 and prevents nuclear re-localization. Hypermethylation of FUS protein only occurs in ALS-*FUS*, and not FTLD-FUS, suggesting possible insight into the way FUS aggregates are the predominant pathological characteristic of FTLD-FUS despite the absence of causative mutations. *= FUS is phosphorylated in response to DNA damage, some evidence of DNA damage in FTLD.

1.3.6 Current rodent models of ALS-*FUS*

Note: Some of this section has been published, see: Publications, page XX.

Significant progress has been made regarding modelling FUSopathies associated with *FUS* mutations *in vivo*; including the development of cellular, vertebrate and invertebrate models. While invertebrate models using *Saccharomyces cerevisiae* [134], *Drosophila melanogaster* [135], and *Caenorhabditis elegans* [136] have yielded various insights, vertebrate models in general provide more translatable results to human disease because of their increased genetic homology - at the notable expense of being considerably more complex and time consuming to generate. Recently several groups have characterised their own ALS-*FUS* rodent models created using a variety of transgenic and viral-mediated methods.

Originally, *FUS* was identified for its role as a fusion oncoprotein in the development of round cell liposarcomas and human myeloid leukaemia's. Nine years before the recognition of its relevance to ALS/FTD, two groups created FUS knock out (KO) mouse models to investigate its functional role and effects of haploinsufficiency. Hicks et al (2000) used insertional site mutagenesis to create a null mutation that effectively caused *FUS* transcriptional silencing. Mice failed to suckle, dying within 16 hours of birth, and affected cells showed an increase in aneuploidy and chromosomal aberrations, which the authors used to highlight the importance of *FUS* in genomic maintenance and chromosomal stability. Another group used a similar non-functional insertional cassette technique to adequately disrupt FUS transcription, albeit resulting in low level expression of a severely truncated, non-functional protein [137]. Kuroda et al analysed their model solely in terms of the reproductive system, and neither group investigated their model neuropathologically. The first neuropathological analysis of *FUS* KO mice was performed

recently [138], utilising the same mice as Hicks but heterozygotes were outcrossed with ICR mice before inter-crossing the F1 progeny. *FUS*$^{-/-}$ mice displayed a reduced body weight but no motor phenotype, and numbers of choline-acetyltransferase positive neurons were normal. Mice did display non-progressive vacuolations, particularly in the hippocampus. The lack of both motor phenotype and neurodegeneration in KO mice suggests that FUS depletion alone is insufficient to cause ALS symptoms or pathology. Interestingly however, a reduction in motor activity has been reported in two zebrafish knock-down models using anti-sense morpholino oligonucleotides [102, 139]. This is perhaps surprising given that morpholinos are generally only capable of partially reducing target gene expression. The reason for this apparent phenotypic discrepancy between species is unclear, but the difficulties in identifying subtle motor impairments in embryonic zebrafish are noted. Alternatively, it may feasibly be due to a more significant functional role played by *FUS* in the developing zebrafish embryo than the adult mouse.

The effects of mutated *FUS* displaying a gain-of-function mechanism of toxicity have been described in various cell culture experiments, and the cellular toxicity of wild-type (WT) Fus overexpression has been documented in yeast [134]. The aggregation propensity of wild-type (WT) FUS was investigated by Mitchell et al (2012) in mice, who overexpressed WT human FUS cDNA under the control of a mouse prion protein gene promoter. FUS$^{+/+}$ mice developed a rapid decline in motor function from four weeks old, and displayed intense FUS perinuclear inclusions in Layer V motor cortex and striatum, with additional diffuse cytoplasmic staining throughout cortical neurons, despite total FUS expression being only 1.7 times higher than non-transgenic mice. Neuronal loss was seen in the spinal cord but not in the brain, with consequent impaired neuromuscular function. Aggregation of structurally normal (i.e. non-mutation affected) FUS is characteristic of FTLD, however the severe motor dysfunction seen in these mice supports

the suggestion that aggregation of WT FUS is sufficient to induce neurodegeneration and the motor phenotype of ALS.

Normal FUS protein contains several distinct functional domains, including multiple RNA binding regions, a C-terminal Zinc-finger motif and a highly-conserved Nuclear Localization Signal (NLS). Recently, several groups have attempted to drive pathology by inducing mutations in the NLS. In perhaps the most extensive characterisation of a *FUS* rodent model to date, Qiu et al (2014) used a prion promoter to drive expression of the human R521C mutation in transgenic mice, leading to severe motor deficits and death within 4-6 weeks of symptom onset. While there was significant and progressive neuronal loss, *FUS* expression was predominantly nuclear, demonstrating that neurodegeneration induced by the mutation was not caused by aggregation of cytoplasmic FUS. Expression analysis identified significant alterations in genes involved in transcription and RNA processing, which were predicted to be the cause of severe dendritic and synaptic defects in spinal and cortical motor neurons. In addition, the authors identified deficiencies in DNA repair caused by R251C mutant FUS being unable to interact with the chromatin re-modelling factor HDAC1. However, this study did not utilise mice expressing human WT FUS, so it is unknown whether these defects were as a result of the mutation or overexpression of FUS protein itself.

Some groups have investigated more dramatic genetic FUS alterations. Shelkovnikova et al (2013) generated transgenic mice that lacked both the entire NLS and RNA binding motifs, while still retaining the N-terminal prion-like domain. This allowed the investigation of FUS pathogenicity independent of its ability to sequester RNA binding proteins and its effect on RNA processing, while still being highly aggregate prone. Mice showed degeneration of motor neurons, neuroinflammatory reactions with abrupt development of a severe motor phenotype, death within a few days of symptom onset, and

distinct FUS inclusions within LMN cell bodies and in the motor cortex. Taken together, these results are significant because they suggest that FUS aggregation and inclusion formation caused by mutant FUS is sufficient to induce neurodegeneration independently of the role of FUS in RNA metabolism. Robinson et al (2015) combined approaches, and created a model that both lacked an RNA recognition motif and contained the R522G point mutation within the NLS. Mice exhibited pronounced tremor followed by early death, and widespread cytoplasmic FUS aggregation in the cortex, brainstem and cerebellum, suggesting that lack of RNA binding to FUS increases its inherent propensity for cytoplasmic aggregation. However, there was no evidence of neuronal loss or astrogliosis. While significant as proof-of-concept, the extent of genetic alteration required to induce pathology in both studies makes the relationship to human disease pathogenesis uncertain.

A different approach has been to use somatic brain transgenesis (SBT) to overexpress human mutant FUS cDNA [140]. Mice were intracerebally injected with an adeno-associated virus vector, incorporating either the R521C mutation or FUS lacking the nuclear localization signal entirely (Δ14). The advantage of this method is its speed - mice can be generated within a few months as opposed to years when using traditional transgenic approaches. Affected mice however showed no phenotype when euthanized at 3 months. Neuropathologically, FUS R521C mice showed a large increase in cytoplasmic FUS without obvious NCI formation or neurodegeneration, while FUS Δ14 mice displayed FUS pathology more closely mimicking human disease including ubiquitin/p62 positive NCI. Additionally, the authors also used this method to overexpress wild-type (WT) human FUS. Unlike those reported previously [141], overexpression of WT FUS did not cause any abnormal pathology or neurodegeneration. Huang et al (2011) created two rat models; one expressing the R521C mutation, and one overexpressing WT human

FUS at comparable levels. Similar to their mice counterparts, R521C rats developed a progressive paralysis resembling human ALS, and also displayed motor neuron axonopathy with motor neuron loss in both the hippocampus and the cortex. NCI were absent, but diffuse cytoplasmic FUS staining was noted in ventral horn motor neurons. Rats overexpressing WT FUS did not develop a significant motor phenotype, but did display deficits in spatial learning and memory, with moderate neuronal loss in the frontal cortex. Consistent with previous studies [141] this suggests that overexpression of WT FUS is sufficient to induce neuronal loss but that mutant FUS is more toxic than WT. The phenotypic differences between the Verbeeck model and other models involving the same mutations/WT-overexpression may be due to the transient expression of the adenovirus before it is cleared, the localized expression of AAV transgenes, or because mice were euthanized before the development of severe NCI formation/phenotype.

Finally, Sephton et al (2014) used a Cre-inducible transgenic approach to create two mice lines, expressing either human WT FUS (FUS^{WT}) or the R521G (FUS^{R521G}) mutation, both at comparably low levels. Nearly all mice developed a severe motor phenotype and early lethality, with some FUS^{R521G} mice escaping this and exhibiting subtle motor impairments and altered sociability. This is in contrast to previous studies mentioned above, which concluded that expression of WT FUS is less pathogenic than mutant. While there was no evidence of FUS cytoplasmic mislocalization, aggregation or neuronal loss in either model, the authors suggested these features are end-stage pathological markers of human disease, precipitated by the denervation of neuromuscular junctions (NMJ) that caused the motor phenotype. Interestingly, differences in gene expression between models suggests that FUS^{WT} exhibits a loss-of-function mechanism through its effects on gene expression, while FUS^{R521G} exhibits gain-of-function toxicity through its disruption of synaptic homeostasis. This is consistent with the effects of the R521C mutation on the

regulation of genes relating to synaptic function in the Qiu et al model. Most recently in an elegant study, Sharma et al (2016) used Cre-LoxP to generate mice expressing a single copy of human WT FUS, (FUS^{WT}), R521C (FUS^{R521C}) or P525L (FUS^{P525L}) at the *MAPT* locus, and an additional knock-out model. Unlike previous over-expression models [104, 141], they demonstrated that overexpression of WT FUS alone was insufficient to induce neurodegeneration, but that mutant FUS is more stable and pathogenic than WT. Additionally, they demonstrated that near-complete removal of endogenous FUS from mice does not lead to motor neuron degeneration, supporting the idea that the neurodegeneration seen in FUS mutant mice is caused by a toxic gain-of-function, not loss-of-function [105, 106]. As in the previous Cre-LoxP model [142] there was also significant denervation of NMJ in both mutant models preceding neurodegeneration, adding weight to the suggestion that neuronal loss is a downstream consequence of NMJ denervation caused by these mutations. However, the survival time of these mice was normal, and there was no NCI formation in any line.

Given its significance in the pathophysiology of ALS/FTD, modelling FUSopathy *in vivo* has been a focus for several groups. However, reproducing both the motor dysfunction phenotype and the distinct neuropathological features of *FUS*-linked ALS has proven challenging in rodents. In particular, while the models discussed here provide clues as to the pathomechanistic role of FUS and its significance in the neurodegeneration of human disease, none of the above completely recapitulate the features of human ALS, and all current models compromise in at least one area of human pathophysiology. To our knowledge there is currently no vertebrate model that mimics the unique post-translational modifications associated with human FTLD-FUS, which are clearly distinct from FUSopathy with *FUS* mutations.

Several of the models described above were created using traditional plasmid-mediated transgenic methods, which have their own methodological limitations. Small cDNA-based transgenes lack the regulatory upstream sequences found as part of many complex mammalian genes. Also, several of the models described here use heterologous promoter sequences that cause expression of the transgene in excess of what would normally be expected in human disease. A Bacterial Artificial Chromosome (BAC) approach may somewhat ameliorate these issues, by allowing the integration of important regulatory sequences some distance upstream of *FUS* in addition to an endogenous mouse promoter, as well as being modifiable to direct cell-type specific gene expression. Unlike small cDNA-based transgenes, the expression of BAC clones also correlates closely with copy number. This approach has already been used in the context of ALS to generate two *C9ORF72* mouse models [80, 143], and the neuropathology associated with a novel ALS-FUS model is described in chapter 4. CRISPR-Cas9 allows for the knock-in of specific point mutations, without extensive off target effects or the need for exogenous regulatory sequences, and it is anticipated that this tool will be used extensively in neurodegenerative disease modelling in the coming years. Finally, of note is that many of the aforementioned studies did not conduct significant transcriptional profiling of their models, which is perhaps surprising given the known role of FUS in the expression regulation of several target genes identified in cell culture experiments. Elucidating the precise normal physiological function of *FUS* and further refinement of vertebrate models will likely aid our understanding of its role in the pathogenesis of both ALS and FUS.

1.3.7 *SOD1*

In 1993, mutations to the superoxide dismutase (*SOD1*) gene were identified as causing ALS [47], making it the first definitively identified gene to be associated with the disease and representing a major step-change in ALS research. Collectively, *SOD1* mutations account for around 20% of genetically-inherited ALS cases [144], and a small number of sporadic cases [145], of which over 100 individual mutations have been identified [146]. Most are heterozygous dominant, although a small number of homozygous dominant and recessive cases have also been reported [147, 148]. The cellular consequences of each mutation are dependent on their location within the protein - mutations at conserved residues such as those at metal binding ligands or the dimer interface are more highly disruptive [146], but all result in the cytoplasmic aggregation of the mutant protein within neurons to varying degrees (Fig 16F). Additionally, the phenotypic effects of each mutation *in-vivo* are also highly variable, with patient survival time and disease course in some mutations (e.g A4V) causing aggressive disease and highly reduced lifespan, while others (e.g G37R) causing a prolonged disease course [149].

Present in both the nucleus and cytosol, SOD1 is a relatively small metalloenzyme comprised of 153 amino acids, coded by just five exons, and whose main physiological function is as a free-radical scavenger through its catalysis of the toxic superoxide anion (O_2^-) to hydrogen peroxide (H_2O_2) and oxygen [146, 150]. Broadly, gain-of-toxicity is thought to be conferred by an increase in cellular oxidative stress, however some mutant forms of the protein exhibit almost the same anti-oxidant activity as wild-type [151], and mutant SOD1 is now thought to contribute to toxicity through a number of non-mutually exclusive mechanisms [152].

1.3.8 *TARDBP*

In 2008 mutations to the corresponding gene of TDP-43, *TARDBP*, were identified as causative in a small percentage of both sporadic and dominantly inherited ALS [153] and FTD cases, further implicating the importance of TDP-43 and RNA processing more broadly in the pathogenesis of both diseases.

TARDBP is highly expressed in most tissue types and conserved across mammalian species. Structurally similar to *FUS*, it possesses two RNA-recognition motifs that are capable of binding both DNA and RNA, as well as a highly conserved, glycine-rich C-terminal region where the majority of mutations occur, clustered around exon 6 [154]. TDP-43 exhibits a variety of cellular functions including in transport of nascent RNA across the nuclear membrane, gene expression and translation. TDP-43 also plays a key role in the promotion of exon splicing or inclusion of several mRNA's, including *SMN2* [155]. Expression of *TARDBP* itself is tightly autoregulated through binding of TDP-43 to specific sequences within its 3' UTR [156], by inhibiting its binding to the most proximal polyadenylation site and causing the splicing of multiple introns leading to its subsequent reduction within the cytoplasm [157]. Functional TDP-43 also represses the splicing of non-conserved 'cryptic exons', maintaining intronic integrity. Evidence from primary mouse neurons suggests that when nuclear TDP-43 is depleted, cryptic exons are spliced into mRNA, often resulting in the translation of premature stop codons or the degradation of the RNA through nonsense mediated decay [158]. Alterations to both mechanisms are thought to contribute to ALS/FTD disease pathogenesis. Spinal motor neurons containing pTDP-43 aggregates show an increased ratio of *TARDBP* mRNA within the cytoplasm [157], which is thought to contribute to a destructive negative-

feedback loop of aberrant RNA homeostasis. However, the transcriptional effect of mislocalized TDP-43 on *TARDBP* within upper motor neurons is unknown.

The mechanism of toxicity conferred by mutations is debated. Knock-out of *tardbp* is embryonic lethal by E8.5 in mice, however heterozygous *tardbp* mice display decreased grip strength and other motor deficits without degeneration of motor neurons [159].

1.3.9 *CHMP2B, OPTN* and *HNRNPA1*

Mutations to genes other than *C9ORF72*, *SOD1*, *FUS* and *TARDBP* comprise <1% of all ALS cases, and often present clinically with a more severe upper/lower motor neuron phenotype. While rare, the functional implication of these genes can be used to highlight potential aberrant processes that exist in the more common forms of ALS.

CHMP2B encodes the multivesicular body protein 2B, which in yeast-based functional studies has been identified as being part of the endosomal ESCRTIII complex, a transport unit involved in the trafficking of proteins between the plasma membrane and Golgi network [160]. Mutations to *CHMP2B* disrupt mRNA splicing and have been strongly implicated in the causation of a small number of both FTD and ALS cases [45, 161]. Notably, several of the identified cases have exhibited a predominance of lower motor neuron pathology [45, 51].

OPTN, located on chromosome 10 encodes the coiled-coil containing protein optineurin. Originally named for its neuroprotective role in the optic nerve and implication in the development of glaucoma, mutations to *OPTN* have since been identified in a small number of ALS cases [50]. OPTN is interesting because it is one of four autophagy receptors that link ubiquitinated cargoes to autophagic membranes and interacts with

TBK1, another gene implicated in ALS/FTD, together highlighting the potential importance of dysregulated autophagy in ALS/FTD.

Recently, mutations to another RNA binding protein, *HNRNPA1*, have been identified as a rare cause of ALS and multisystem proteinopathy [52]. hnRNPA1 is one of a family of ribonucleoproteins whose main functions are in the alternative splicing and processing of nascent pre-mRNA's within the nucleus, and whose importance is underscored by its ubiquitous expression in nearly all cell types (https://www.ncbi.nlm.nih.gov/gene/3178). Like FUS and TDP-43, hnRNPA1 also possesses an N-terminal low-complexity prion like domain, mutations to which contribute to its aberrant phase transition and subsequent accumulation within pathological aggregates [162]. TDP-43 interacts with hnRNPA1 through its glycine-rich C-terminal region, however hnRNPA1 immunoreactivity is reduced in the nuclei of spinal motor neurons with cytoplasmic TDP-43 aggregation [163]. These pathological and genetic implications for hnRNPA1 further confirm the importance of RNA processing and alternative splicing in the pathogenesis of ALS, however the significance of hnRNPA1 function in FTD is less clear.

1.3.10 An 'oligogenic' hypothesis of disease

Over 50 genes have now been implicated in ALS/FTD, either through identification of index cases or GWAS based approaches. However, identification of affected kindreds is reliant on a number of variables for them to be suitably identified, and GWAS studies are only powered to detect associations between common variants and disease.

An interesting feature of ALS genetics is the existence of two or more causative mutations in some ALS patients or families at a higher rate than would be expected by chance. This

has become known as the ‘oligogenic’ hypothesis of disease. This hypothesis is exemplified in lineages containing inherited mutations that display incomplete penetrance in phenotypically normal family members, where affected individuals possess risk factor variants in multiple genes. Such oligogenic variants have the potential to influence the neuropathology or phenotype of a more dominant mutation in ALS/FTD, as has been evidenced in several cases [39-41, 164], with some patients exhibiting altered neuropathology and/or clinical course than would normally be seen with an isolated mutation. This effect is also recognised in the context of several other diseases [165-168]. Interestingly, it has also been suggested that some patients require more than one mutation to express disease [169]. In a recent study, it was demonstrated that there is a higher burden of variants within non-coding regions of *FUS* and *TARDBP* in sporadic ALS cases [170], which potentially have the ability to act as risk or disease modifiers. However, this study was conducted by sequencing peripheral blood, and the defined compartmentality of the CNS means that the relevance of these variants to ALS disease is unclear.

Investigating the relative contribution of these modifier variants to disease pathogenesis is often challenging and requires extensive experimental as well as computational genomic and bioinformatic analysis. Further work is required to elucidate the influence of such genetic modifiers on ALS/FTD.

1.4 Neuropathology

1.4.1 Anatomical vulnerability

Atrophy of affected regions can be seen post mortem, and depending on the severity, also *in vivo* using various imaging modalities [171-173]. The regions of the CNS most obviously affected by the disease are those which physically degenerate and can be visualised histologically, i.e the lower motor neurons within the descending pathway of the spinal cord anterior horn, the trigeminal and hypoglossal cranial nuclei within the brainstem, and the upper motor neurons originating in the primary motor cortex. The frontotemporal and associative cortices are considered pathophysiologically involved (especially with the concomitant development of FTD) but do not necessarily exhibit macroscope evidence of degeneration.

While there is pathological involvement of other regions (e.g hippocampus, cerebellum), their degeneration is not obviously apparent, although it should be noted that their obvious degeneration does not preclude the significance of their involvement. In *C9ORF72* disease for example, large numbers of both RNA foci and dipeptide repeat proteins are found in both the cerebellum and hippocampus, normally considered disease unaffected regions. However, this may simply be as a result of the higher density of neurons in these regions relative to the cortex, and their significance in the pathophysiology of ALS is unclear.

1.4.2 Neuropathology and neurodegeneration

Around 97% of ALS cases are associated with hyperphosphorylated TDP-43 within neurons and glial cells (Fig 2E-G) with the rest being associated with SOD1 and FUS inclusions. In *C9ORF72* disease, pTDP-43 is present in addition to p62-positive dipeptide repeat proteins, as well as RNA foci transcribed in both the sense and antisense directions. However, while the presence of pTDP-43 is observed in a majority of cases, and the toxic effect of TDP-43 has been extensively demonstrated in-vitro [174-176], the relationship between pathology and neurodegeneration is not completely understood. Some have speculated that the presence of pTDP-43 at post-mortem - as an end-stage phenomenon - is actually neuroprotective. In this model, soluble TDP-43 and its subsequent creation of toxic oligomeric species are what drive neurodegeneration, and the aggregation and phosphorylation of the protein is essentially the cell 'doubling down' on the disease process to prevent further spread. However, whether this is actually the case is unknown in part because of a lack of models *in vitro* which develop hyper-phosphorylated TDP-43 inclusions. While some mutations result in a more obvious gain-of-function toxic effect (e.g *SOD1*), the mechanism in sporadic TDP-43 disease is less clear. Prior to the aggregation of TDP-43 within the cytosol there is loss of nuclear TDP which negatively affects multiple functions including DNA damage repair [177] and the proper repression of cryptic exon spicing [158].

1.4.3 TDP-43 proteinopathy

Post-mortem TDP-43 pathology is morphologically heterogeneous and exists in several forms depending on cellular and anatomical location (Fig 2E-G). In neurons, pTDP-43

exists as diffuse skeins, cytoplasmic punctate or as larger discrete inclusions, and these can be restricted to the soma or within dendrites and axons (Fig 2E). In oligodendroglia, which can be identified histologically by the size and shape of their nucleus, pTDP-43 pathology is present as either skeins or characteristic 'cat eye' shaped inclusions (Fig 2F). pTDP-43 inclusions are present in most layers of the cerebral cortex with the exception of layer I, but including the subcortical- and deep layer white matter.

1.4.4 Microglial activation and the neuroinflammatory response

Microglia are the innate immune cells of the CNS, whose main function is the phagocytosis of cells/aggregates as part of the neuroinflammatory response. Microglia robustly express the transmembrane glycoprotein CD68 in response to injury as part of an 'activated' phenotype. Microglial activation and proliferation is commonly implicated in the pathogenesis of ALS [178], and cortical microgliosis is a prominent feature at post-mortem, however whether this response is in itself pathogenic or primarily a subsequent reactive event is debated. Notably, the presence of wild-type glial cells in the $SOD1^{G93A}$ mouse results in the prolonged survival of mutant SOD1 motor neurons [179], suggesting significant non-cell autonomous roles for both microglia and astrocytes.

Both wild-type TDP-43 and its C-terminal fragments initiate CD14-mediated NF-κB activation as well as the intracellular NLRP3 proinflammatory cascade *in vitro*, which is toxic to motor neurons [180, 181]. In addition, loss of TDP-43 within microglia causes severe synaptic loss in knock-down mice, but only rarely do microglia exhibit TDP-43 mislocalisation [182]. However the extent to which TDP-43 aggregation might in itself is responsible for the observed microgliosis has been somewhat clarified in a recent study utilising an inducible TDP-43 mouse model, which demonstrated that the presence of

TDP-43 - not neurodegeneration - is responsible for an increase in microglial proliferation [183]. However, further work is required to establish whether it is intracellular TDP-43, or perhaps TDP-43 aggregates left behind after the destruction of the cell that is responsible for this response.

1.4.5 Inhibitory GABAergic interneurons and the cortical hyperexcitability phenotype

The majority of neurons (~80%) within the cortex are projection neurons, which project distally and use excitatory neurotransmitters such as glutamate to propagate action potentials across the synaptic cleft. However, a smaller population of neurons are inhibitory, utilise γ-aminobutyric acid (GABA) and project intrahemispherically. GABA binds to specific transmembrane receptors in both the pre- and post-synaptic processes, hyperpolarizing the neuron by allowing the flow of negatively charged chloride ions into the neuron and preventing excitation. The main role of interneurons therefore is as a negative-feedback mechanism to prevent the runaway hyperexcitability of the cortex. Small populations of excitatory interneurons utilising glutamine also exist within the spinal cord [184].

Calcium-binding proteins (CBP) protect neurons from excitotoxicity via increased intracellular calcium by regulating $Ca2^{+}$ concentration within the cytosol. CBP are highly expressed in subpopulations of GABAergic inhibitory interneurons, whose degeneration has previously been implicated in several diseases [185-187], including ALS [188]. A cortical hyperexcitability phenotype has been described in ALS patients [189], and has subsequently led to ALS being described as potentially being an ‘interneuronopathy’ [190]. Two neuroimaging studies revealed decreased GABA concentrations and

benzodiazepine receptor unit distribution in the primary motor cortex [191, 192]. Additionally, previous studies have suggested loss of inhibitory interneurons as prominent feature of cortical dysfunction in animal models [193, 194]. However, the assessment of interneuron numbers in the human ALS primary motor cortex post mortem has produced conflicting results [188, 195, 196].

1.4.6 Projection neuron diversity and loss

The functional output of the mammalian neocortex is maintained by the excitation and inhibition of neuronal circuitry initiated by two main classes of neurons – projection neurons, which are largely excitatory, and interneurons, which are largely inhibitory. Projection neurons reach distant targets either intrahemispherically or elsewhere, and can be further subdivided by the target of their axonal projection. Subtypes include cortico-thalamic, cortico-spinal and callosal, the development of which are tightly regulated by the delicate up/down temporal expression of one or more neuronal transcription factors critical for lineage fate, some of which are maintained post-mitotically. T-box brain protein 1 (*TBR1*) is critical for cortico-thalamic projection neuron (CThPN) development [197]. *CTIP2* is a determinant of subcerebral projection neuron fate, which in the case of the motor cortex specifies projection into the corticospinal tract as corticospinal projection neurons (CSPN) [198]. *SATB2* is critical for axonal projection across the corpus callosum into the contralateral hemisphere as callosal projection neurons (CPN) [199, 200]. Finally, *Fezf2* is an essential determinant of cortical laminar migration and is considered a 'master regulator' of projection neuron fate [201].

ALS is typically thought of as a CSMN disease, and studies have indicated that CSMN expressing *CTIP2* undergo early degeneration in the $SOD1^{G93A}$ model [202]. Betz cells

are the largest cell type in the CNS, whose presence define the primary motor cortex. While they are often quoted as projecting solely into the corticospinal tract, much of the work done to identify this has been done in mouse models which display considerable differences in UMN anatomy. Pyramidal Betz cells also selectively degenerate in ALS, but rarely accumulate the disease-defining pTDP-43 aggregation pathology associated with the disease [203]. The degeneration of inhibitory interneuron populations in the ALS primary motor cortex has previously been described [188]. However, the expression of the above genes, and the specification and involvement of these molecularly defined projection neuron subtypes in the human ALS motor cortex is unknown.

1.4.7 Oligodendroglial dysfunction

Oligodendrocytes are a diverse type of glial cell which can be identified histologically by their characteristic round nucleus, chromatin structure and nucleolus, thin rim or perinuclear eosinophilic or clear cytoplasm and laminar position. The main role of oligodendrocyte is support of the neuron, either directly as a metabolically supportive 'satellite' oligodendrocyte or via the production of insulating myelin.

Myelination of axons allows for efficient salutatory conduction and fast transmission of action potentials. Myelinating oligodendrocytes are capable of extending processes to ensheath up to 50 axons [204]. Demeylination of axons is a prominent feature of several neurodegenerative diseases including multiple sclerosis and ALS [205, 206]. After demyelination, small populations of immature oligodendrocyte precursor cells (OPC) retained in the adult CNS are able to migrate to the site of injury and remyelinate [207, 208]. It is therefore plausible that one aspect of autosomal dominant ALS is the detrimental effect of the mutation on the efficiency of OPC migration, differentiation or

remyelination. Inhibiting oligodendrocyte formation in normal mice results both in a lack of myelin production and inability to learn a motor task [209]. Additionally, the selective removal of mutant SOD1 in oligodendrocytes significantly delays disease onset and prolongs survival in the $SOD1^{G93A}$ model, which exhibits early dysfunction of oligodendrocytes [205]. Ferraiuolo *et al* (2016) showed reduced motor neuron (MN) survival and altered axonal architecture when oligodendrocytes from ALS patients were co-cultured with disease free MN, and that this degeneration generally required close cell-to-cell proximity but could also be induced through the secretion of soluble factors [210].

Neuropathologically, oligodendrocyte pTDP-43 inclusions are numerous in both the brain and spinal cord of ALS patients [211], where they have a distinctive morphological phenotype (Fig 2F). However, whether these inclusions represent a primary event or are a subsequent reaction to TDP-43 dysfunction in neighbouring neuron cells is unclear. TDP-43 can be transmitted across axon terminals from neuron-neuron *in vitro* [212], but whether this can occur between non-neuronal cells is unknown, as is the potential relationship between ALS genotype and preponderance to oligodendrocyte pTDP-43 inclusions. Additionally, while oligodendroglial pTDP-43 inclusions are common within the motor and sensory cortices, they are rare within the deep-white matter of the corticospinal tract, corpus callosum and cingulum bundle [213]. This suggests that while they may be affected by local disease, they are unlikely to be involved in the distant spread of pathological TDP-43.

1.5 The nature of disease progression

While ALS is a disease of motor neurons, and the majority of pathology is confined to the motor cortex and spinal cord, the nature of disease progression across the neuraxis is

debated. In such debates a distinction should be made between pathological spread and clinical progression, which may or may not be correlated, as a significant proportion of ALS cases exhibit relatively minor TDP-43 pathology even at the clinical end stage of disease - i.e post mortem [214]. Additionally, the reasons for vulnerability/resistance to the disease across motor neuron populations are not completely understood. Evidence for whether ALS exists because of a cell-type vulnerability that affects regionally distinct cell-types, or as a systems vulnerability that follows a predictable pattern of spread across regions is evaluated here.

1.5.1 Mechanisms of spread

Mislocalization and aggregation of pTDP-43 is the primary pathological observation in around 95% of ALS cases. In a recent study, Brettscheider et al [214] assessed pTDP-43 deposition in a cohort of 76 sporadic ALS cases, analysing 22 regions of the CNS. They suggested that the progression of pTDP-43 aggregation can be considered in four stages, beginning in the clinically affected motor cortex and spinal cord in stage I, and progressing to the clinically unaffected hippocampal formation in stage IV. This staging system is based upon pTDP-43 not only originating in the spinal cord/primary motor cortex, but also getting progressively worse in these areas as disease duration is prolonged. The authors suggest a corticofugal spread of pTDP-43 pathology, where grey matter regions are sequentially involved through white-matter tract spread, and of ultimately ALS being a ‘corticoefferent’ syndrome. This concept was supported in a subsequent study that assessed pTDP-43 pathology within white matter oligodendrocytes [213], which mirrored the pattern of progression in the Brettschneider study. This sequential spread would suggest a systems vulnerability to TDP-43 pathology, if not the disease.

However, there are issues with this staging approach. There is significant variability in pTDP-43 deposition between sporadic cases for example, with some cases of sALS exhibiting very little pTDP-43 within the primary motor cortex at post-mortem, despite all cases presumably being at the same clinical end-stage. This thesis will describe several cases that demonstrate that the aggregation of pTDP-43 pathology within the primary motor cortex - and its relationship to degeneration - is not linear within this genotype. The progression of pTDP-43 pathology described in the aforementioned papers therefore requires validation in an at least one other, independent cohort before it should be considered as robust a staging system as that of Braak staging for Tau. It is noted that the high quality and specificity of available primary antibodies targeting the disease specific, hyper-phosphorylated form of TDP-43, which have been extensively optimised and validated in hundreds of peer-reviewed studies, permits the creation of an accurate TDP-43 neuropathological staging system (see section 1.8 – Antibody validation and usage). Post mortem staging in this way is warranted because there is currently no TDP-43 specific ligand capable of labelling the protein *in vivo* through PET imaging as there is for other neurodegenerative proteins such as tau [215].

Investigations into the transmission of the disease began in experiments in the 1960's, well before the discovery of TDP-43. Saline lysates from the medulla and spinal cord of ALS patients were injected into monkeys, some of whom developed hand and forearm muscular atrophy and decreased weight, leading the authors to hypothesise a viral transmission [216]. However, until recently whether the hyper-phosphorylated insoluble or soluble form of TDP-43 is actually able to spread from cell-to-cell was debated. A recent study demonstrated that oligomeric TDP-43 is able to move across the synapse within microvesicles in both anterograde and retrograde directions [212], and another study has hypothesised that the origin of this movement is from Betz cells within the

primary motor cortex towards spinal cord lower motor neurons [203]. However, given that TDP-43 pathology is often prominent within glial cells, it remains to be seen whether this transmission can occur between neuronal and non-neuronal cell types, or whether pathological TDP-43 is able to influence the WT TDP-43 in the next cell, through a potential prion-like mechanism.

1.5.2 'Dying forward' vs 'Dying back'

While patients commonly present with a combination of lower and pyramidal signs, the nature of disease progression between the spinal cord and cortex is debated and two competing (but not necessarily mutually exclusive) hypotheses have emerged. In the 'dying forward' hypothesis, cortical dysfunction caused by anterograde trans-synaptic, glutamate-mediated excitotoxicity precedes lower motor neuron (LMN) dysfunction [189, 217, 218]. This is supported by a cortical hyperexcitability phenotype apparently preceding significant LMN signs in human sporadic ALS cases [189], as well as presymptomatic cortical neuron defects in both *SOD1* [202, 219] and *TARDBP* [220] mouse models. In the 'dying back' hypothesis, dysfunction and denervation of the neuromuscular junction precedes cortical abnormalities. Despite the prominence of TDP-43 function in ALS, denervation at the neuromuscular junction (NMJ) (which may be occurring up to a meter away from the cell body) is actually what is largely responsible for the symptoms seen in patients. This disconnect between what can be observed mechanistically at the cell body and the realities of localised translation at the synapse are a current focus of research. Partly addressing this, two recent papers from separate groups have identified that knocked down levels of TDP-43 results in the lowered expression of the neuronal growth-associated factor stathmin-2 [221, 222], linking TDP-43 loss-of-

function with dysfunction at the synapse. Additionally, preventing the degeneration of the cell body alone delays onset but is insufficient to prevent progression in *SOD1* mice [223], likely because once denervation at the NMJ has occurred the connection cannot be re-established sufficiently. Given the specific vulnerability of motor neurons in ALS, and the physical distance between the cell body and neuronal growth cone/synapse, identifying localised CSMN proteomes/transcriptomes using novel methods [224] will be illuminative.

The reasons for the apparent UMN/LMN compartmental vulnerability and origin of the disease are unclear. In the autosomal dominant forms of the disease, it is possible that the extent of expression of each mutation determines the site of origin, whereby the mutation is more highly expressed in certain compartments. Within the spinal cord, neurons which innervate fast-twitch muscle fibres are severely affected, while slow twitch neurons degenerate less rapidly [225]. Fast twitch neurons exhibit reduced expression of the ER-homeostasis co-chaperone protein SIL1 relative to slow twitch [226]. Additionally, clues regarding the molecular basis of motor neuron vulnerability in ALS may be found within the oculomotor neurons, which display significant resistance to the disease. Transcriptomic profiling of oculomotor neurons vs spinal motor neurons revealed a differential expression of 1,757 genes, including those involved in synaptic transmission, and also display an upregulation of several GABA and glutamate receptor subunits [227]. This suggests that a resistance to excitotoxity is responsible for their reduced susceptibility in ALS. Notably, the oculomotor neurons also only display pTDP-43 aggregations in around 45% of ALS cases [228]. Further work in understanding the structural and molecular basis of UMN and LMN vulnerabilities in ALS will likely aid in the identification of targets for therapeutic design.

1.5.3 Genotype-phenotype correlations

Notably, some disease-causing autosomal dominant mutations appear to predispose patients to either an upper or lower motor neuron predominant ALS with variable progression rates [42-45]. This suggests that there may be a compartment specific vulnerability to the effects caused by these mutations, or compensatory mechanisms in compartments that are less affected.

1.6 Primary motor cortex

1.6.1 Macroanatomy

The human motor cortex is located on the precentral gyrus, anterior to the central sulcus (Fig 3). Subdivided into primary, premotor and supplementary areas, the primary motor cortex is distinguished from somatosensory at the fundus of the central sulcus, and contributes the majority of output for the stimulation of movement whilst receiving input from the basal ganglia and cerebellum via the ventrolateral nucleus of the thalamus. There are also substantial numbers of projections from motor cortex to lobules VB-VIIIB of the cerebellar vermis [229]. Brodmanns area 4 classification is still largely accepted, although has been revised since its original description [230]. Historical contention regarding the functional division between primary and premotor cortices led to some argue that they are better considered as one, a proposed 'M1' region [231, 232]. While the term is still in common use, it is perhaps an oversimplification and should be avoided.

The primary motor cortex can be represented based on the extent of its involvement and association with particular muscle groupings; the so called 'homunculus' (Fig 4A), with

larger representations such as hand and face signifying higher proportions of cortical involvement and complexity, concomitant with larger numbers of motor receptors in these areas. However, it is not entirely cleanly defined somatotropically, and there is notable representational overlap between areas [233, 234]. This is evidenced by the fact that intracortical stimulation of specific sites within the motor cortex elicits a response from multiple muscle groups, and individual muscles can be stimulated at several sites [233, 235]. However, intracortical stimulation is of course an artificial method, and bears little resemblance to the small scale, localized pattern of neuronal activity that regulates natural in-vivo movement. There is still some debate therefore surrounding whether the primary motor cortex best represents individual muscle groups, or 'movements' of multiple groups. One recent study examining EMG activity of forearm muscles delineated this relationship further by suggesting that muscles performing particular *functions* are activated by distinct cortico-motorneurons from within the primary motor cortex [236].

The motor cortex in humans generally shows a high degree of inter-hemispheric symmetry, however neuropil volume of the hand region is larger in left-hemisphere of the majority of post-mortem brains, consistent with there being a majority of right-handed people [237, 238]. While the primary motor cortex can generally be sufficiently identified topographically, an inherent difficulty is encountered in defining functionally distinct brain regions based on macroanatomical landmarks [239], and cortical regions are more accurately identified through smaller variations in cytoarchitecture.

Focal injury to the motor cortex results in the loss of fine motor movement control and the initiation of limited compensatory mechanisms at both the cellular and systemic levels. Various growth factors are secreted within peri-infarct tissue for example, which possibly guide the creation of new axonal connections, and certain novel intra-cortical connections are generated following injury [240]. However, substantial growth of tissue does not

occur, and recovery of the motor cortex following injury is generally limited to localized reorganization of cortical wiring.

1.6.2 Microanatomy

The motor region of the human brain is arguably the most microanatomically distinct region of the cerebral cortex, containing a variety of heterogeneous classes of neurons of various size/output, but uniquely organised in its cytoarchitecture. Unlike other cortical regions, the human motor cortex is agranular, containing no clear layer IV, whilst also having a diffuse layer VI border (Figure 4F) and displaying a smooth laminar pattern. The most striking feature of the motor cortex at this level is the presence of Betz cells in layer V. There is also a small population of Betz cells in the depth of the anterior cingulate which appear to be morphologically distinct from the rest of the precentral population [241]. The grey-level index (GLI), a measure of quantitative cytoarchitecture, can be used as a method of comparatively distinguishing cellular architecture in order to map cortical layer architecture in regions that are otherwise ill-defined using a combination of cell body fraction volumes, cell size and density [242]. The primary motor cortex has a distinctly low GLI value that indicates low cell body fraction volume but larger space between cell bodies than other cortical areas [239].

1.7 Betz cells

Betz cells are a large type of pyramidal neuron located within layer Vb of the primary motor cortex, across a region corresponding broadly to Brodmann area 4 (Fig 3). Present in several mammalian species, Betz cells are distinguished histologically from other

pyramidal populations by location, morphology, and dendritic architecture. Stereological studies indicate that Betz cell morphology and number vary across the primary motor cortex, with the largest being in the foot and leg representation of the homunculus, and the most densely clustered being in a zone two- thirds from the midline along the mediolateral axis. This regional/spatial distribution suggests that particular Betz cell populations may be implicated in different functional aspects. However, molecular characterisation of these neurons has thus far been limited, in part because of the lack of an antibody capable of specific recognition. Betz cell involvement is noted in several neurodegenerative diseases, including ALS.

Vladimir Betz (1834-94) was a Ukrainian neuroanatomist who published extensively on the cytoarchitecture of the cerebral cortex in the second half of the 19th century. Propelled by his own technological advances in microscopy, fixation and staining, Betz made defining contributions in elucidating the microanatomy of the brain, at a time when the understanding of the relationship between neuroanatomical structure and functional organization was in its earliest infancy. Noting shrewdly that "…there are two cerebral areas which may be designated as two centres, one motor and the other sensory", he built on the previous work of other preeminent neuroanatomists of the time including Broca, Meynert, Baillarger, and Campbell, and laid the foundation for the future understanding of functional neuroanatomy. Reportedly thoroughly meticulous in his approach, Betz collected and studied over 9000 human brain specimens [243] before his death in 1894.

In 1874, Betz made perhaps his most famous contribution through his description of the 'cumulative nests' of 'giant pyramids' of the precentral gyrus, which he originally described as being located in Meynerts layer IV [244]. Subsequent revision identified these giant pyramids as being located in layer V, and were later themselves renamed as 'Betz' cells.

While input from the primary motor cortex comprises around 30% of fibres in the corticospinal tract [245], Betz cells comprise only around 10% of pyramidal neurons in layer V [246], and around 2-3% of pyramidal tract cells in total [247]. The primary projection is to the corticospinal tract, crossing in the brainstem before reaching the contralateral anterior horn of the spinal cord. Betz axons also send shorter collaterals back into the cortex, which are believed to inhibit adjacent regions around where Betz cells discharge in order to 'sharpen' the excitatory response [245]. They also receive relayed input from the somatosensory cortex through layers II and III [248]. Betz cells are primarily distinguished morphologically from neighbouring pyramidal cells through their larger size, accumulation of intracellular lipofuscin and nissl (Fig 4H), and unique dendritic architecture [241, 246, 249]. Lassek (1941) also notes their relatively small nuclear size in proportion to the volume of cytoplasm.

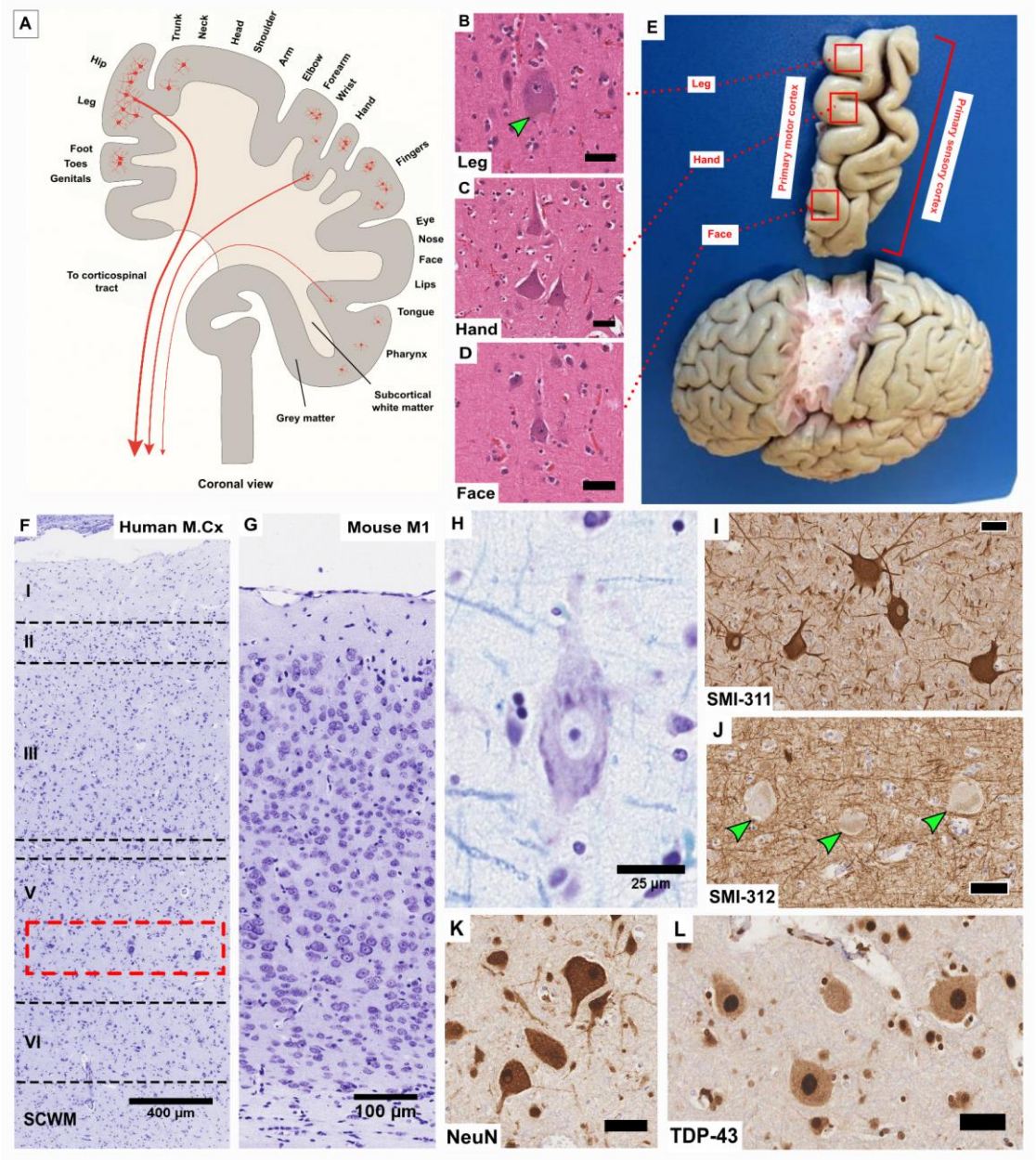

Figure 3: Betz cell size, morphology and distribution in the primary motor cortex. Betz cells are largest and most numerous in the leg representation of the homunculus, decreasing in size and number moving ventrolaterally across the cortex (A), being largest in the leg region (B), mid-sized in the hand region (C), and smallest in the face region (D) of the homunculus. (E) The M1/S1 is removed from the left cerebral hemisphere. The anterior gyrus is therefore the primary motor cortex, next to the primary somatosensory cortex. The regions of the primary motor cortex are somatotropically organised according to axonal projection. Betz cells are present in layer V of the human PMC (F), but not the mouse M1 region (G). CFV stain of single Betz cell, note the large nucleus and dark nucleous (H). Human Betz cells stain strongly for SMI-311 (I), NeuN (K) and pan-TDP-43 (L), but not SMI-312 (J, Betz cells arrowed). Note that the cytoplasmic expression of NeuN is well known [1, 2]. All unlabelled scale bars = 50µm. All images created by the author.

1.7.1 Distribution

Betz cells are the largest neurons in the human CNS, with axonal projections spanning up to one metre in humans. Seen in small clusters or individually, Betz cells account for around 10% of pyramidal neurons in Layer Vb [246]. Early estimates of total cell number ranged from 25,000 - 40,000 per hemisphere [247, 250, 251], however a newer stereological study of six cases found a mean total of 125,290±, albeit with significant inter-case variability [246]. Their distribution follows a mediolateral gradient around the precentral gyrus, with the most densely clustered being in a zone midway from the midline along the mediolateral axis in the paracentral lobule, and the largest being in the foot and leg region of the homunculus, on the most medial part of the cortex [246], decreasing in both size and number moving ventrolaterally along the central sulcus [249](Figure 4B-D). Around 75% of all Betz cells are present in the upper third [246, 247], in the foot and leg representation of the homunculus. While it is commonly believed that Betz cells axonally project primarily into the brainstem, whether in humans they have additional significant projections is unknown, has not been confirmed using lineage tracing in primates and indeed, Betz cell regional/morphological differences suggest that individual populations exhibit specific functional capacities, potentially underlined by molecular or transcriptomic differences.

1.7.2 Morphology

Betz cells are identified histopathologically based on their size and presence in layer Vb. However, it is their unique dendritic architecture which must be used to distinguish them from other layer V pyramidal neurons [246]. Unusually for neurons and unlike other layer

V pyramidal cells, Betz cells have dendritic spines that project locally around the full circumference of the soma, exhibiting a much higher variation in dendritic number than other layer V neurons, but which do not appear to contribute to vertical organisation [249]. A small number of Betz cells appear to be bipolar, with basal dendrites entering the white matter [249], but most have one long apical dendrite that can extend into the superficial layers [241, 249]. In addition, all Betz cell dendrites exhibit numerous spiny appendages and bulbous protrusions surrounding the soma [241]. However there is both inter-regional and inter-individual dendritic variation, with dendritic asymmetry particularly evident in the transitional area between the precentral gyrus and central sulcus [249]. Betz cells are considered pyramidal cells because of their large primary apical dendrite, numerous circumferential dendritic spines and excitatory nature. Like other pyramidal cells, Betz cells are also often surrounded by an extracellular matrix of chondroitin sulphate proteoglycan (CSPG)-immunoreactive perineuronal nets [252].

Stereological estimations of Betz cell somal size vary. Betz himself described their average size as 60x120µm (Betz, 1874), Brodmann reports them as 53x106µm (Brodmann, 1909), while Rivara et al (2003) records an average cell soma volume of 86,685µm^3. However, as noted above, there is considerable Betz cell size variation even within the same cortical plane. Early theories suggested that Betz cell size was proportional to either axonal length or the size of the dependent muscle, as the largest Betz cells are present in the cortical region represented by the lower limb areas of the homunculus [246], despite this involving a relatively small proportion of the total primary motor cortex. However, this appears to be untrue as several smaller animals possess disproportionately large Betz cells (Brodmann, 1909). In humans, while soma size and axonal length increase concomitantly with height, there is no relationship with body weight [253].

Betz cells are also notable for their prominent rough endoplasmic reticulum [246] and accumulation of cytoplasmic lipofuscin [241] which can be readily viewed on H&E stain and has been used practically to distinguish Betz cells from other layer V pyramidal cells [203]. Intracellular lipofuscin accumulation is most commonly associated with ageing, but is also occasionally present in Betz cells of patients under 65. Other ultrastructural features such as bundles of filaments and accumulations of neurofilament appear to occur only rarely in controls [254].

1.7.3 Evolutionary biology of Betz cells

Betz cells have been identified in at least 25 species [230, 255-259], assuming the definitions described above. While their shape, size and number vary considerably across phylogeny, most taxonomic groups can be delineated according to their Betz cell somatodendritic architecture [259]. It is largely accepted that cell body size of neurons is determined by the extent of the total metabolic activity of the neuron, with larger, more dendritically complex neurons requiring higher levels of metabolic support. It has therefore been suggested that Betz cells become proportionally larger with increases in body size, with the largest mean volume in humans. This would align with the specific importance of the sensorimotor capacities of primates, concomitant with evolutionary hierarchies. However, while there is a relative increase in the size and number of Betz cells with larger brain and body size, it is not an entirely linear relationship, and several species exist outside the 95% CI range in this respect [257]. Two examples of this are that of the *Potus flavus* (Kinkajou), which despite weighing on average just 6 lbs, possess Betz cells close to the mean volume of humans [230], and *Erythrocebus patas* (patas monkey), who exhibit an usually high Betz cell ratio despite it's relatively small brain volume [257].

There appears to be no significant relationship between Betz cell ratios and digital dexterity of the species [257, 259].

Recently, Jacobs et al (2017) conducted a comprehensive stereological analysis of gigantopyramidal, superficial and deep-layer pyramidal neurons across 19 mammalian species. Using quantitative measures of neuronal morphology, they found that Gigantopyramidal cell morphology was more varied across species than other pyramidal neurons, and that this variation allowed these taxonomic species to be distinguished statistically based on their particular gigantopyramidal somatodendritic architecture. Interestingly, they also found that Betz cells were larger in Feliforms; the average Betz cell soma area was 2,847μm^2 compared to the average primate soma of 987μm^2. They also found striking differences in the *Panthera* Genus, with their gigantopyramidal neurons being 4.6 and 12.1 times larger than primates, in area and volume, respectively. The authors, using previous hypotheses regarding the direct correlation between soma size and size of dependent muscle, interpreted these large changes as being due to the increased need for fine motor control and muscle composition in predatory behaviour.

1.7.4 Molecular basis and electrophysiology

Relatively little is known about the molecular basis of Betz cells, when compared to other large named neurons such as Purkinje cells, and notably there is no single-cell RNA-seq data available for human Betz cells to date. There are likely two main reasons for this. Firstly, Betz cells are not overly numerous and can be difficult to identify histologically, particularly in terms of their differentiation from surrounding layer V neurons. Secondly, there are currently no antibodies which selectively label Betz cells, preventing their isolation via fluorescent-activated cell sorting (FACS).

Betz cells strongly express the voltage-gated potassium channel kv3.1b protein and mRNA on IHC/ISH, which is localized to the somal and proximal dendritic cytoplasmic membrane [260], collagen XVII [261], a transmembrane protein thought to be involved in synaptic plasticity [262, 263], and also hnRNP-A1, the target for autoimmune IgG antibodies in human T-lymphotropic virus type 1 (HTLV-1)-associated myelopathy/tropical spastic paraparesis (HAM/TSP), a disease that can be difficult to distinguish from MS [264]. A recent study has also shown that Betz cells have an increased immunoreactivity towards DNAJC30 – an auxiliary component of ATP-synthase [265].

In common with other highly metabolically active, fast-firing neurons, they also strongly express the transmembrane-enzyme complex cytochrome oxidase [266]. They are also known to express the calcium-binding protein parvalbumin in synaptic boutons surrounding the cell soma [267]. Expression of calcium-binding proteins such as parvalbumin is more commonly associated with inhibitory interneurons, possibly suggesting that Betz cells possess an uncommon dynamic functionality.

The development of cortical neurons from neural progenitors is driven in part by the lineage-dependent expression of various transcription factors, which drive and maintain differentiation post-mitotically [198, 201, 268]. It could be reasonably speculated that due to their large size and unusual morphology, Betz cells maintain a specific transcriptional/molecular profile, at least relative to other cortical populations. However, how such transcription factors are expressed in Betz cells is currently unknown, hampered by the difficulty in isolating individual cells. While several antibodies are capable of highlighting Betz cells in situ (NeuN etc), currently there exists no specific antibody that can reliably distinguish Betz cells from other neighbouring pyramidal cells immunocytochemically. Such an antibody might feasibly be utilised in gated flow-

cytometry experiments, and the development of such a marker would likely improve isolation of these cells and greatly facilitate their investigation. While excitatory motor neurons can be generated via induced pluripotent stem cells (iPSC), such generated cells are not fully developed motor neurons, and are also unlike Betz cells in both their morphology and their potential for axonal projection length. The identification of specific transcription factors and proteins associated with Betz cells may therefore facilitate their future generation from human iPSC and the advent of *in vitro* Betz cell modelling.

Betz cells are primarily excitatory, glutamatergic neurons, whose primary function is to initiate rapid early phasic input that prepares flexor muscle tone prior to the recruitment of neighbouring pyramidal neurons. Betz cell axons project mainly into the corticospinal tract, which synapse with cells of the spinal cord anterior horn, and subsequently synapse directly with alpha motor neurons which innervate target muscle groups. Betz cells are postulated to be the origin of the thick myelinated axons that form 3% of the corticospinal tract which are capable of conducting rapid impulses at speeds of 60-70m/s [269]. They also receive somatosensory input from area 2 through intracortical associative neurons in layers II and III [270]. Historically, much of the electrophysiological work concerning Betz cells has been conducted on cats [256, 271-273], arguably because of their large size and easy identification rather than an interest in their particular neurophysiological properties. Relatively little evidence exists from primate models. In mice, corticospinal projection neurons show the fastest and most regular action potential firing rate of all layer V projections neurons, with subtle differences in electrophysiological properties between lumbar and cervical corticospinal neurons [274]. Mice layer Vb neurons primarily receive excitatory input from secondary motor cortex and frontal areas, but also from the motor nuclei of the thalamus [275]. However, such neurons do not exhibit the unique circumferential dendritic architecture described above. For this reason, the prevailing

belief is that mice do not possess Betz cells.

1.7.5 Betz cells in development, ageing and disease

1.7.5.1 Development

While the neurodevelopmental progression of the cerebral cortex is now well delineated, the particular cytoarchitecture of the primary motor region suggests its development is governed by distinct molecular/transcriptomic controls. Marin-Padilla (1970) provided a comprehensive Golgi study on the development of the primary motor cortex by investigating the cortical layers of 7 brains (3 foetuses, 4 infants) at different time points. First, he established that Layer I was mostly developed at around 5 months, and fully matured by 7.5 months of gestation. Interestingly, he noted that the arrival of afferent fibres in the motor cortex precedes the organization of the grey matter and laminated structures. Secondly - although not referred to as Betz cells - he identified the large pyramidal neurons in layer V in the 7 month gestational brain. He also noted that they appeared to grow considerably by the 7.5 month time point and that in the new-born infant they were fully matured [276]. In his detailed histological series of post-natal development, J. LeRoy Conel also identified Betz cells in the neocortex of the new-born [277], although unlike Marin-Padilla he found they appeared to be the most developed cells of the motor cortex, suggesting an early stage of differentiation from other pyramidal cells.

1.7.5.2 Ageing

In common with other highly metabolically active neurons, Betz cells undergo morphological alterations through ageing. While somal volume is reduced, axonal size, length and number remain relatively constant throughout life, with the most obvious age-related occurrence being the accumulation of cytoplasmic lipofuscin [278], and the progressive loss of circumferential dendrites [279]. Bunina bodies and dense accumulations of neurofilament are also occasionally present in older patients without neurological disease [254]. However, there is also clear Betz cell involvement in several age-related neurodegenerative diseases. In frontotemporal dementia (FTD), Betz cells degenerate and are replaced by clusters of macrophages containing lipofuscin, whilst also occasionally containing intracellular accumulations of tau (pick bodies) [280]. Lewy bodies composed of α-synuclein are also occasionally seen within Betz cells of Parkinson's disease (PD) patients [281], whilst there is also prominent degeneration of Betz cells and other neurons in layer V in corticobasal degeneration (CBD) [282] and multiple-systems atrophy (MSA) [283]. There have also been isolated reports of marked Betz cell pathology in late-infantile galactosialidosis [284] and Friedreich's ataxia [285]. Given the functionality of Betz cells it seems unlikely that these are primary pathological events in these cases, and more likely they exist as secondary aspects of disease pathogenesis.

1.7.5.3 Motor neuron diseases

Motor neuron diseases such as amyotrophic lateral sclerosis (ALS) are defined by the loss of both lower and upper motor neurons, including Betz cells. However, ALS patients commonly exhibit a predominance of either upper or lower motor neuron signs, with

considerable variation in the extent of upper motor neuron loss across cases. There is debate on the nature of disease progression, with two competing (but not necessarily mutually exclusive) hypotheses suggested. In the first, the so called 'dying-back' hypothesis, lower motor neuron dysfunction occurs as the primary event, prior to cortical dysfunction. This is supported by observations in several transgenic mouse models utilising ALS-associated mutations where prominent neuromuscular junction (NMJ) abnormalities occur early or pre-symptomatically [286-288]. In the second, the so called 'dying-forward' hypothesis, cortical dysfunction occurs as the primary pathophysiological event prior to lower motor neuron degeneration, potentially mediated by an anterograde, trans-synaptic, excitotoxic mechanism of multiple possible aetiologies. This is supported by clinical observations of cortical hyperexcitability occurring early in the progression of ALS patients [189], and pre-symptomatic cortical dysfunction in a $SOD1^{G93A}$ mouse model [202, 219].

While most neuropathologists would expect to identify neuronal loss in the motor cortex of ALS patients to at least some extent, pathological studies of post-mortem cases offer differing perspectives on the specific nature and severity to which this occurs. Two stereological studies found no difference in mean neuronal number, perikaryon volume, mean neuronal nuclear volume, total perikaryon volume or total nuclear volume between ALS and control motor cortex [289, 290], despite neuronal loss/damage being observed in-vivo [291]. This led to speculation that motor cortex dysfunction in ALS is caused by regional metabolic changes, rather than microanatomical alterations. However, these studies quoted were not designed to assess Betz cell alterations specifically, and ultrastructural changes and loss of layer V neurons including Betz cells is acknowledged in most cases of ALS [196, 218, 292, 293]; the discrepancy probably due to sampling methods and the difficulty in quantifying the loss of cells that constitute only a small

proportion of the total. Interestingly, there appears to be significant correlation between the level of neuronal loss, including Betz cells, between M1 and S1 [294], suggesting a degree of interdependence between the two regions. It could be postulated that this interdependence is mediated at least in part by Betz cells connections to the somatosensory cortex through layers II and III [248].

Transactive response DNA-binding protein 43kDa (TDP-43) is a DNA/RNA binding protein involved in several aspects of RNA metabolism including transcriptional repression, splicing and translational regulation [295], and is highly expressed within both the Betz cell nucleus and cytoplasm (Fig 3L). Neuronal and glial cytoplasmic inclusions immunoreactive for mislocalized TDP-43 are the primary neuropathological characteristic of the majority of ALS cases [133]. Despite the loss of nuclear TDP-43, Betz cells appear to be mostly free of the characteristic cytoplasmic aggregation of insoluble, hyper-phosphorylated TDP-43 associated with ALS [203], despite other smaller, neighbouring pyramidal cells being affected. Additionally, there appears to be no correlation between Betz cell loss and the severity of pTDP-43 pathology in motor cortex grey matter [213]. These findings raise interesting questions regarding the specific selective vulnerability of Betz cells in ALS. Are they more vulnerable to the increased toxicity of soluble TDP-43, perhaps because of the higher importance of RNA/protein homeostasis as a consequence of their larger size or metabolic activity? Or are they in fact selectively resistant to the aggregation of insoluble TDP-43, which afflicts neighbouring neurons? Regarding selective resistance, one case report describing two cases of post-operative hypoxic-ischemic encephalopathy notes how Purkinje cells, but not Betz cells, were selectively destroyed under hypoxic conditions [296]. Other additional, non-specific Betz cell alterations are occasionally observed in ALS, including fragmentation of the

Golgi apparatus [297, 298], reduction in expression of neurofilament-200kDa [299] and accumulation of reactive astrocytic gliosis around the soma [300].

Several studies have identified dendritic degeneration as a prominent feature of ALS Betz cell pathology [292, 300-302]. In a recent study, Genc et al (2017) reported profound Betz cell apical dendrite degeneration, including extensive dendritic vacuolation and cytoarchitectural disintegration which appeared to be most severe distally from the soma. Interestingly, they also found differences in Betz cell apical dendrite structure and soma size between two patients who had different SOD1 mutations, raising the possibility of mutation-dependent patterns of Betz cell pathology. The specific pathologies of Betz cells in other genetic forms of ALS are thus far unreported. Betz cell involvement is also noted in other motor neuron diseases, including primary lateral sclerosis (PLS), where patients can exhibit complete Betz cell loss concomitant with an upper motor neuron predominance [303], and to varying degrees in hereditary spastic paraplegia (HSP) [304, 305]. One study also found a reduction in Betz cell number in two cases of juvenile spinal muscular atrophy [306], but which are seemingly unaffected in the adult form [307]. Finally, there are also published reports of prominent Betz cell loss in Spinocerebellar ataxia type 2 (SCA2) [308] and type 6 (SCA6) [309].

1.7.6 Comparative anatomy

Mice are commonly used when investigating the motor cortex. However, there are two reasons why the conclusions drawn from using mice in such a context are perhaps self-limited. Firstly, while much of the neuronal fate mapping of motor cortical neurons has been identified using developing mouse neurons, there are inherent issues when extrapolating these findings to the development of the human motor cortex. Given the

distinctiveness of the human motor cortex, comparative and evolutionary anatomy suggests that the molecular mechanisms which drive upper motor neuron differentiation are unlikely to be the same in mice. Mice, for example, do not possess Betz cells under the definition described previously. Secondly, while the anatomical organization of the corticospinal tract from cortex to brainstem is largely similar across mammalian species, there are distinct differences in anatomical organization at the level of the pyramidal decussation between humans and mice [310] which have evolved to provide humans with a greater degree of fine motor control. Using mice therefore to study the selective vulnerability of upper motor neurons in the context of neurodegenerative diseases like ALS is therefore also perhaps non-ideal.

Other models have therefore been utilised, with varying success. Sloper and Powell (1978) used electron microscopy to study the motor cortex of young Rhesus monkeys. Interestingly, they found that Betz Cells had complex indentations of their nuclear membrane. This indentation was often accompanied with clusters of endoplasmic reticulum. They also commented that the Betz cell soma contained numerous mitochondria and that the nucleus is smaller in relation to the overall size of the Betz cell compared to other pyramidal cell types [311]. Later, Tigges et al (1992b) explored the motor cortex of aged Rhesus Monkeys, and noted novel inclusion bodies within Betz cells that had previously not been seen or bore similarity with human ALS motor neurons. The authors concluded that these bodies had a 10nm filament as their basic unit and suggested that Betz cells for unknown reasons prolifically produced ubiquitous neurofilament, proposing that this be used as a criterion for identifying Betz cells [278].

Like others of the time, Kaiserman-Abramof and Peters (1972) studied the domestic cat to gain further insight into the Betz cell. They found that glial cells usually surround the perikarya of Betz cells, more so than the bases of their dendrites. In any 1 µm section they

counted 2-3 neuroglial cells around the Betz cell soma, and this frequency was unchanged throughout sampling [312]. Similarly to Sloper et al., they also found the nuclear envelope to be folded, with mitochondria being in high concentrations adjacent to these indentations. The most prominent feature of these giant cells was found to be the Nissl substance that is widespread across the cytoplasm, but which was particularly concentrated in the deep folds of the nuclear envelope, under the plasma membrane and at the bases of the dendrites. Kaiserman-Abramof and Peters (1972) also commented that some Betz cells have dendritic spines that are unusually large – with an appearance similar to a large axon terminal with multiple postsynaptic densities. Finally, the authors used crude measurements to calculate that the average Betz cell perikaryon bears approximately 870, broadly symmetrical axon terminals.

1.8 Antibody validation and usage

Most techniques used in this thesis are immunohistochemical in nature and therefore rely upon the specificity and sensitivity of primary antibodies. Monoclonal antibodies are generated from identical B-cells derived from the same parent clone, and subsequently target a single region of an epitope. Polyclonal antibodies, by contrast, are generated from multiple clones and therefore when pooled bind to different regions of the same target. On this basis, monoclonal antibodies should be used for nearly all experiments. However, the signal amplification associated with polyclonal antibodies is usually higher, and these may therefore be more appropriate for the identification of lowly expressed targets. Polyclonal antibodies are also particularly suitable for the identification of denatured proteins, as is the case in formalin-fixed paraffin embedded (FFPE) tissue following heat-mediated epitope retrieval.

The overall goal of all immunohistochemical experiments is to permit the identification of proteins through high signal, low background visualisation of the target, and antibodies can be validated against these goals in several ways. Specificity is defined as the ability of the antibody to correctly identify when the target is not present in the sample, and can be assessed through the use of KO animals/cells to confirm absence of staining in IHC or WB. Sensitivity is defined as the ability of the antibody to correctly identify the target when it is present, and can be confirmed using western blotting to confirm expected molecular weights with minimal smearing, IHC against known control tissue or immunoprecipitation of targets prior to mass spectrometry (IP-MS) [313]. The specificity of secondary antibodies can also be evaluated by omitting the primary antibody in experiments using a known positive control. Additional methods such as pre-adsorption to eliminate cross-reactivity of polyclonal antibodies, and assessment of binding affinity using ELISA can then be used to further optimise and assess the quality of the antibody.

However, despite these approaches, a lack of standard guidelines for validation means that many commercially available antibodies still exhibit non-specificity and cross reactivity, factors which are thought to contribute to the current 'reproducibility crisis' affecting life sciences research [314]. There is also considerable variation in the extent to which antibody manufacturers validate their products. To rectify this, some large scale projects such as the Human Protein Atlas have published their validation methods through a defined set of criteria antibodies must meet before they are considered suitable (https://www.proteinatlas.org/about/antibody+validation) for inclusion.

The antibodies used here are therefore both poly- and monoclonal, depending on the availability and specificity of the antibody and its particular application. All primary antibodies, manufacturers and their dilutions used in this thesis are listed in Table 11. Antibodies were chosen based on their use in previous studies, validation data supplied

by the manufacturer, and through preliminary experiments/optimisation in our lab. The antibody used most often in this study for example, the mouse monoclonal pTDP-43 primary antibody from Cosmo-Bio, is undoubtedly the best antibody available for the target and is viewed as the 'gold standard' for sensitivity and specificity in the field. Prior dilution series experiments in our lab have revealed that this antibody can be used at dilutions of up to 1:80,000 in IHC and still provide high-quality (intense signal, zero background) results. Notably in this case, confirmation of specificity using KO mice or cell lines is not possible because the protein is disease specific and uniquely human in nature. However, staining is entirely absent in all human control samples in WB and IHC (data not shown).

1.9 Novel techniques in histopathology

While some diseases can be investigated using surgically extracted biopsy material from living patients, this is largely not possible in the context of neurodegenerative disease where biopsies of the brain and spinal cord are both invasive and unnecessarily hazardous to the patient. Analysis of post-mortem tissue therefore, through donations made to brain banks, present an important avenue for investigation. However, the use of post-mortem tissue is frequently beset by issues related to effect of detrimental pre-analytical variables such as prolonged fixation, post-mortem delay, RNA-integrity and agonal state of the patient.

Over the last 30 years substantive progress has been made in developing tools for the investigation of post-mortem human tissue that have broad applicability for all aspects of histological research. Here the use of three novel histological techniques: CLARITY, RNAscope and imaging mass-spectrometry, will be briefly reviewed, and later attempts

described in applying these methods in the context of assessing selective vulnerability in the ALS primary motor cortex using post-mortem tissue.

1.9.1 Imaging of intact biological tissue in three-dimensions

Standard immunohistochemical methods are conducted on thin or semi-thin (<100μm) tissue sections. Generally, these allow the visualisation of pathology in a single or shallow-depth plane, limited by both the thickness and opacity of the tissue which refracts light and prevents analysis at depth when using brightfield or fluorescent microscopy. This is particularly relevant when studying brain tissue, which contains significant quantities of compounds which scatter light (e.g lipids), necessitating the need for thin sections and extensive pre-processing before staining.

However, given that tissue and cells are inherently three-dimensional in nature, and that significant information regarding structural biology/pathology is lost when visualising tissue in a two-dimensional plane, several methods have been developed that utilise clearing of intact three-dimensional biological tissues followed by whole-mount staining – negating the need for the cutting and staining of thin serial sections. Combined with newer imaging methods such as optical light-sheet microscopy, which provides additional laser penetration depth, these methods allow the visualisation of whole tissue structures in three-dimensions.

The primary step in these methods is the clearing technique, which involves the removal of material from the tissue that scatters the majority of light, with the aim being complete clearing with minimal damage of structures of interest. The first of these methods was developed as early as 1914, but required significant processing and caused damage to the

superficial aspects of the tissue [315]. Since then, several clearing methods have been devised which cause less tissue damage and can be used on smaller pieces of tissue, with most utilising solvent-based clearing using benzyl alcohol, benzyl benzoate or dibenzyl ether [316]. An additional issue with such methods is the penetration depth of antibodies. As antibodies are comparatively large biological molecules, their penetration through tissue is limited, which affects imaging depth even if the tissue is completely cleared. One way around this is the genetic labelling of cells/proteins of interest using fluorescent tags, but these require the transgenic engineering of the animal and are of obvious incompatibility with human tissue.

1.9.2 CLARITY and FASTClear

In 2013, a method was developed in the lab of Karl Deisseroth at Stanford which involved infusion of formalin-fixed tissue using a hydrogel scaffold, electrophoretic tissue clearing, and prolonged incubation with primary antibodies. They termed this method CLARITY [317, 318]. The use of the hydrogel scaffold in CLARITY offers structural advantages over other methods; the scaffold 'anchors' the architecture of the tissue and prevents tissue expansion which can affect imaging quality. This method has recently been developed further by a group at Imperial College London, who have termed their new method FASTClear [319].

In this thesis, attempts are therefore described to use this FASTClear method for the investigation of post-mortem human ALS tissue, after having learned the method at Imperial in the Summer of 2016.

1.9.3 RNA in-situ hybridization using RNAscope

Like all eukaryotic cells, the structure and function of both neurons and glia is controlled by the regulated expression of proteins. Traditionally, immunohistochemistry (IHC) using either DAB or fluorescent signal has been the neuropathological method of choice for studying the cellular expression of proteins in situ. However, analysis using IHC is inherently limited in its scope as it is only able to describe one level of cellular expression. Firstly, many cells (even of the same type/function) are transcriptionally diverse, with variations based on location and structure within neural tissue. Secondly, both neurons and glia are continually actively responding to localized changes in environment caused by stress and disease etc. Thirdly, protein expression is not always correlated with expression at the RNA level, in part because of localized translational repression. This is particularly pertinent in neurons, whose proper functioning requires a high degree of polarity.

Traditional methods of analysing genetic expression including quantitative reverse-transcriptase PCR (qRT-PCR), microarray analysis and RNA-sequencing. However these methods exhibit notable drawbacks including being relatively complex/expensive methods, the need to maintain and RNase-free environment, and loss of cellular/spatial resolution of the tissue being investigated. RNA in situ-hybridization (RNA-ISH) allows the visualisation and quantification of specific genes using antisense oligonucleotide probes, which can be seen in the context of the cells/tissue they are present in. However traditional RNA-ISH requires the synthesis of these probes as well as extensive quality control experiments. Additionally, retrieval of some target mRNA's can be difficult in FFPE tissue, or where tissue has undergone prolonged fixation.

RNA-ISH is reasonably easily applied to cell cultures and animal tissue, where pre-analytical variables such as RNA-integrity (RIN) and fixation can be completely controlled. However, applying RNA-ISH to human brain tissue presents additional challenges for a number of reasons. The agonal state of brain donors contributes considerably to the RIN and overall quality of the donated tissue for example. Additionally, the most common neuropathological fixative, 10% Neutral buffered formalin (NBF), stably cross-links all nucleic acids making subsequent RNA/DNA probe binding difficult. The required fixation times for human tissue diagnostics are also often well beyond the optimum fixation times for RNA-ISH, meaning that the majority of archival brain tissue stored within brain banks is inappropriate for use in this regard.

In 2012 a RNA-ISH method was developed by Advanced Cell Diagnostics (ACD) and termed RNAscope [320]. The advantages of this method are that it can be used chromogenically, negating the need for fluorescence microscopy, it can be automated on staining platforms from either Leica or Ventana, and ACD manufacture all the probes which have been extensively tested and optimised. Additionally, there are sequential amplification steps built into the protocol, which do not require extra input when used on an automated platform, and when optimised multiple probes can be utilised simultaneously. Specificity of the probes are ensured in part because multiple probes are required to bind to the target before signal amplification can occur, and it is therefore unlikely that a signal will be detected through probes binding next to each other non-specifically. After hybridization, there are then pre-amplification and amplification steps which ensure robustness of the signal [320]. These features combined are said to offer a higher unique signal-noise ration available than other commercially available RNA *in situ* methods. At least one previous study has also demonstrated that expression data generated using RNAscope probes correlate with results from conventional PCR [321]. In this thesis

therefore, we describe efforts to circumvent as far as possible the previously described issues concerning pre-analytical variables, and begin to demonstrate the application of RNAscope in the context of ALS gene expression and projection neuron diversity in the primary motor cortex.

1.9.4 Imaging mass-spectrometry

Primary antibodies conjugated to fluorophores which emit light in the visible/far spectra when excited by their corresponding specific wavelength are commonly utilised in immunohistochemistry, and their use allows the simultaneous staining of multiple targets and subsequent analysis of co-localization patterns. However, certain components of tissue generate significant autofluorescence due to excitation of their molecular structure at multiple or all wavelengths, masking specific signal and creating unwanted background 'noise'. This is a particular issue when using post-mortem brain tissue, which contains large quantities of both lipids and intracellular lipofuscin granules, both of which strongly autofluoresce.

Mass-spectrometry is a proteomic method commonly used to separate proteins in a given sample based on their polarity and mass. A sample is first ionized, and the constituent fragments of the sample are separated by mass-to-charge ratio through the use of an accelerating electromagnetic field. Separated ions are then detected and analysed [322]. However, this method is in general expensive and time consuming, and comes at the expense of cellular resolution. Imaging mass cytometry (IMC) utilising cytometry time-of-flight (CyTOF) is a new method which attempts to circumvent the above issues by using primary antibodies directly conjugated to heavy-metal tags [323] Tissue sections are stained in the normal way using these antibodies before being ionized. Proteins bound

to the heavy metals are picked up by the detector and used to create an image with an accuracy at subcellular resolution. This method avoids the autofluorescence issue entirely, as there is no fluorescent component. It can also be performed in a multiplex fashion allowing the visualisation and co-localization of multiple targets simultaneously [323] and be combined with RNA-ISH through the use of metal-tagged antisense probes [324]. One platform for performing this method is the Hyperion system from Fluidigm.

Elsewhere in this thesis it is shown that pTDP-43 aggregation is present within oligodendrocytes, but not GFAP+ astrocytes (Fig 24 and 25), and that GABAergic inhibitory interneurons degenerate within the ALS primary motor cortex (Fig 21). Expanding this, we hypothesised that GABAergic interneurons were less likely to develop pTDP-43 pathology than excitatory projection neurons. We therefore also attempted to apply this method to post-mortem human ALS brain tissue, but were ultimately unsuccessful.

1.10 Study rationale

The concept of selective vulnerability is not new, having been commented on as far back as Charcot himself, and also exists prominently in other neurodegenerative diseases. However, this vulnerability is particularly apparent in ALS, where we might consider that it exists at several levels. Firstly, it is a systems vulnerability, in that it affects predominantly the motor system (but also the frontotemporal associative cortices to varying degrees). It is also a sub-type vulnerability, in that even within the nosology of motor neurons some are severely affected, while others such as the oculomotor neurons remain relatively undisturbed [227]. Finally, it is a cell-type vulnerability, and the influence of non-cell autonomous factors that contribute to neurodegeneration (e.g

oligodendroglial dysfunction and pathology) are increasingly recognised [204, 205, 210]. However, the degree to which these aspects of vulnerability are responsible for the overall pathotype of ALS is debated [325].

ALS is a disease of both upper and lower motor neurons. Historically, the origin of the disease was believed to be in the lower motor neurons of the spinal cord, however recently, some have advocated the progression of ALS as a 'corticoefferent' syndrome, whereby both the disease and characteristic TDP-43 pathology begins in the primary motor cortex, possibly within the large pyramidal cells of Betz, and spreads along white matter pathways [326]. The primary motor cortex has been somewhat neglected neuropathologically thus far in favour of the spinal cord, possibly in part because the motor cortex is more difficult to delineate from surrounding cortical regions and is in many cases less obviously degenerated. Additionally, much of the work investigating UMN pathology in ALS has been conducted using mice, which exhibit significant UMN anatomical differences to humans, including the absence of Betz cells. While others have assessed selective vulnerability in ALS in the anatomical sense [214], there has been no systematic comparison of cell-type specific neuropathology in the ALS primary motor cortex since the discovery of several key ALS genes/proteins, including TDP-43 and *C9ORF72*. Much of the relevant prior work (and indeed, in human neuropathological research in general) has been completed using semi-quantitative 'scoring' based methods, which depend on agreement between assessors and are therefore more subject to bias. Additionally, the large pyramidal cells of Betz are severely affected in the disease, but relatively little is known about them overall.

Given the above - namely the combination of its prominent disease relevance, lack of detailed systematic study and involvement in controversial hypotheses - there is a need to assess the pathology of the primary motor cortex in isolation in ALS.

1.11 Aims

The aims of this project were therefore as follows:

1. Explore and develop the utility of novel histological methods applicable to post-mortem human brain tissue including CLARITY, RNAscope and multiplexed immunofluorescence
2. To characterise the pathology of the primary motor cortex across the genotypic spectrum of the disease, and begin to assess the existence of human ALS cortical pathology in the context of molecularly defined cellular subtypes
3. To comparatively assess a monogenic human form of upper motor neuron predominant ALS (ALS-*OPTN*) with that of a transgenically engineered (ALS-*FUS*) mouse model utilising the LMN predominant P525L mutation.

1.12 Hypotheses

We are therefore able to formulate two pertinent hypotheses. Firstly, that there is significant variability in pathology within the primary motor cortex across the genotypic spectrum of ALS, which is potentially concordant with clinical phenotypes commonly seen for the various mutations, and secondly, that not all neuronal/glial subtypes equally accumulate the disease defining TDP-43 proteinopathy associated with the disease.

Chapter two

Establishment of novel techniques for the investigation of post-mortem ALS tissue

2. Establishment of novel histopathological techniques for the investigation of post-mortem ALS tissue

2.1 CLARITY

Protocol followed is as previously described [319]. Post-mortem human brain tissue from the primary motor cortex (~ 3mm^3, grey matter) and lumbar spinal cord (~3mm^3) of a single ALS patient was used. In one experiment, tissue that had been stored in 10% NBF solution for a period of 3 months was used. In another experiment, tissue that had been post-fixed for 48 hours from frozen tissue was used. Both sets of tissue were subject to the same processing procedure. After fixation, tissue was passively (i.e, non-electrophoretically) delipidated using 4% SDS buffer at 37°C. Buffer was changed regularly until the grey matter had turned adequately transparent. The tissue was then twice washed in 0.2% PBS-Triton overnight at 37°C to remove excess SDS buffer. Tissue was then blocked in a solution containing 0.6M glycine, 0.2% Triton X-100, 6% Donkey serum and 20% DMSO in 1X PBS overnight at 37°C. Tissue was then washed again in 0.2% Tween-20 to remove excess blocking solution. Tissue was incubated with mouse monoclonal pTDP-43 primary antibody (Cosmo-Bio, Japan) for three days at a concentration of 1:1,000 (3ml) with another 1µl of antibody added on the second day. Primary antibody was then washed from the tissue using 0.2% Tween-20 in 1X PBS three times for one hour, then overnight. Tissue was then incubated with a goat anti-mouse IgG secondary antibody, conjugated to Alexafluor 488 fluorophore (Invitrogen, cat# A11001) at a dilution of 1:200 (2ml) for three days, with an additional 1µl of antibody added on the second day. Tissue was then washed again using 0.2% Tween-20 in 1X PBS five times, then overnight at room temperature. Counterstaining was performed using DAPI at a dilution of 1:10,000. Refractive index matching was performed using 47% TDE v/v in

0.1M PB, pH7.4. Tissue was then placed in an inverted imaging dish with a small amount of refractive-index matching solution and imaged using an inverted confocal microscope.

There was significant variability in the duration of the delipidation step that was related to the fixation duration, where longer time spent in fixative required longer durations to effectively delipidate (Fig 4), effectively precluding the use of tissue that is stored in wet formalin for a period of longer than one week when using passive clearing methods. It is noted however that some groups have been able to effectively clear large pieces of tissue that have been stored in formalin for long periods of time by using electrophoretic clearing methods. Additionally, as this was an exploratory experiment, it is limited to an *n* of 1.

The images in Fig 5 represent the best results gained from the single attempt of the method. However, as it stands the method appears to exhibit several drawbacks which limit its routine histological use. A significant issue with the method is the length of time the protocol takes. Both primary and secondary antibodies must be incubated for long periods (four days plus in some cases), at concentrations far higher than would be necessary using standard IHC which also increases the cost. Without these higher concentrations, penetration of the antibody is insufficient for imaging; penetration also being limited by the relatively large molecular size of most antibodies. However, the use of smaller primary antibodies generated from alpacas (https://www.chromotek.com/about-us/the-alpaca-antibody-advantage/), which lack light-chain fragments, as well as advances in optical light-sheet microscopy which provide higher laser penetration depths, offer potential means of improvement.

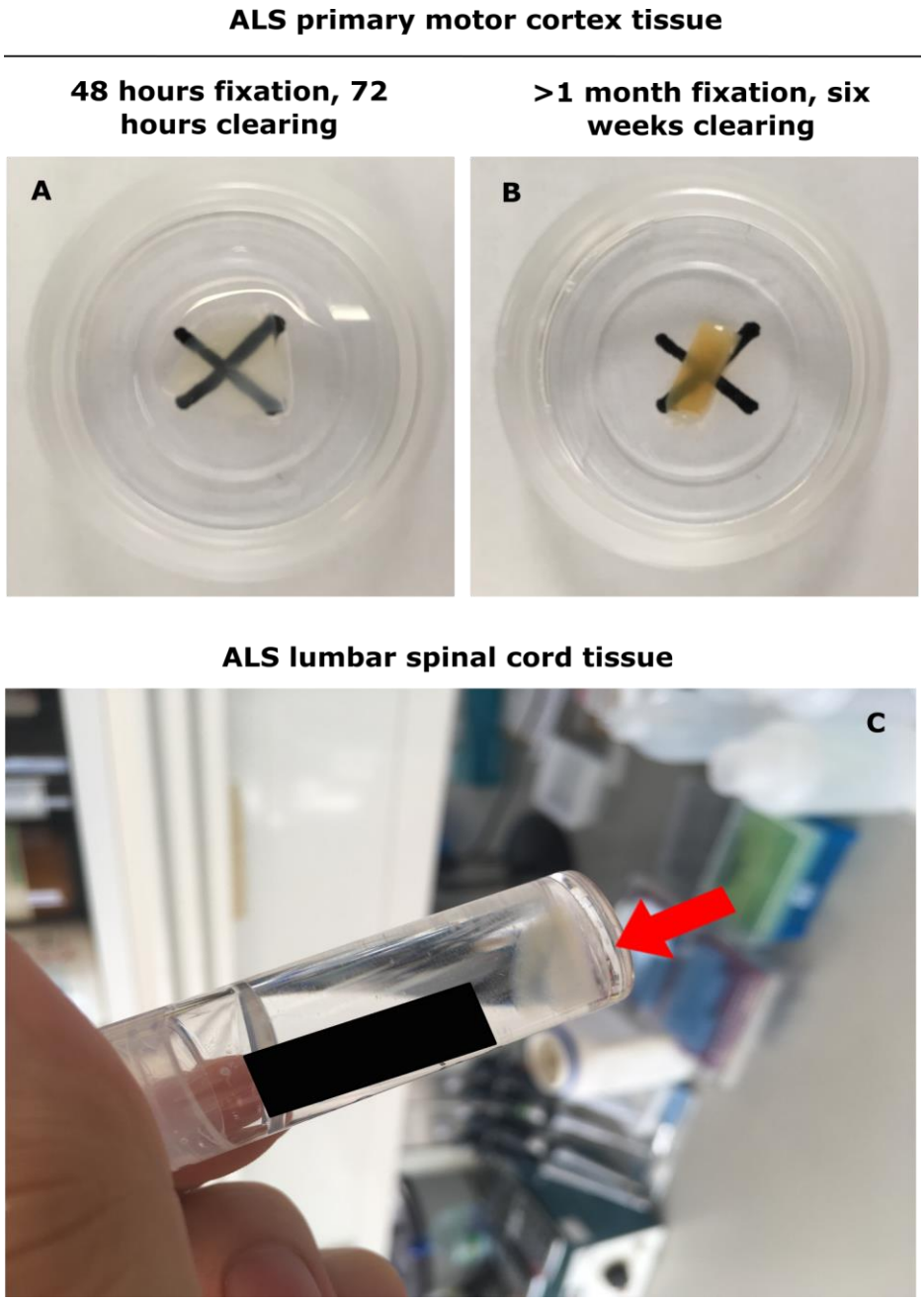

Figure 4*:* Fixation duration is a key determinant in how efficiently tissue is delipidated in preparation for staining using the FASTClear protocol. Motor cortex tissue that is minimally fixed is rapidly cleared using 4% SDS buffer (A), but tissue that has undergone prolonged fixation is not adequately cleared even after clearing for six weeks (B). Human spinal cord is sufficiently cleared but with some concomitant expansion of the tissue (C).

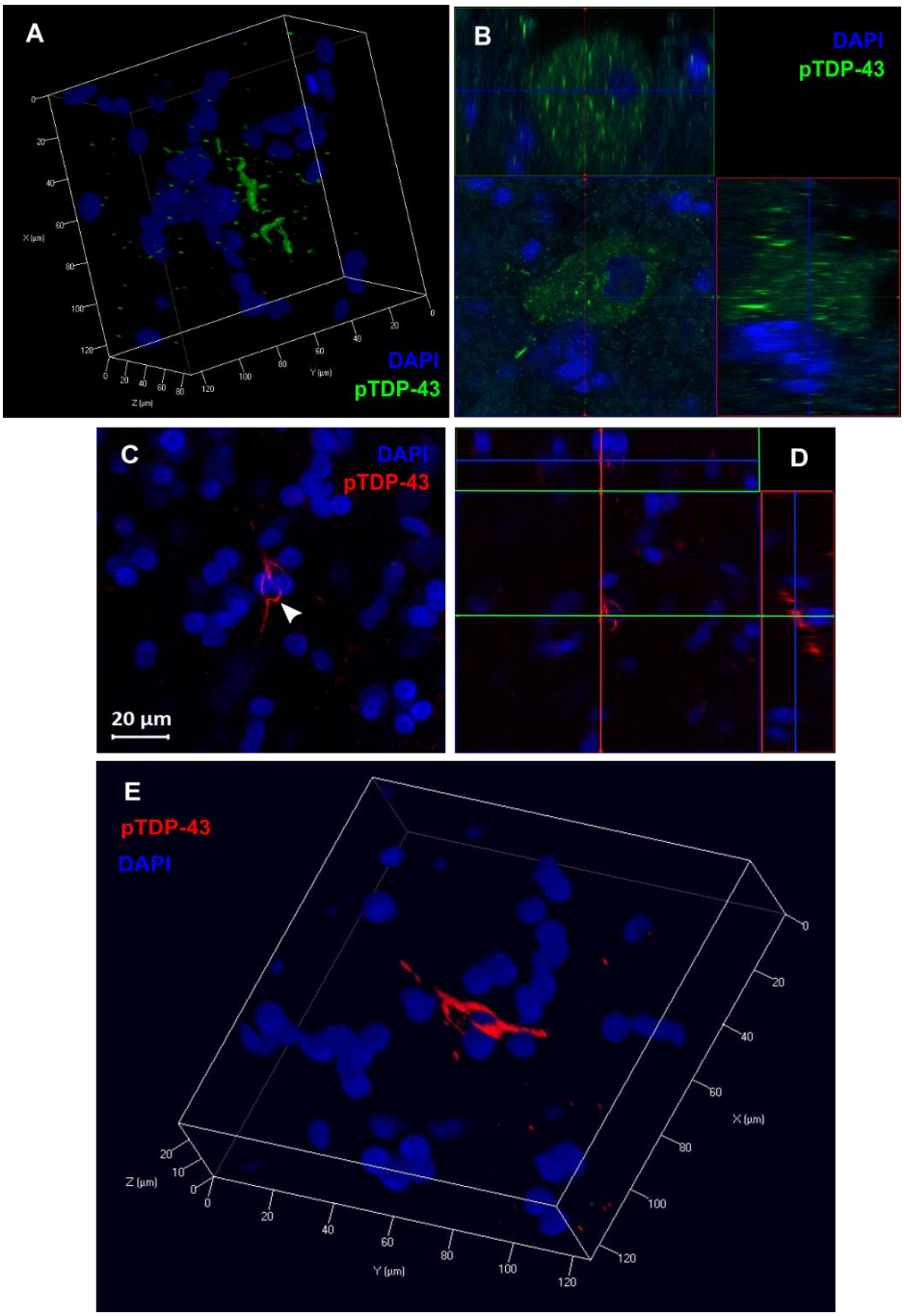

Figure 5: Using FASTClear to visualise pTDP-43 pathology within the anterior horn of the lumbar spinal cord (A,B) and of the primary motor cortex (C-E) in post-mortem human ALS tissue. Skeins and punctate are represented in three dimensions using this method (A). Orthogonal view through the same region shows a single neuron with diffuse and punctate pTDP-43 present throughout the cytosol (B). Maximum intensity projection (C). Orthogonal view through same image (D). 3D reconstruction of skein pathology, possibly through an oligodendrocyte (E).

2.2 RNAscope

2.2.1 Preparation of tissue

Post-mortem brain tissue is particularly susceptible to the effects of pre-analytical variables such as post-mortem delay and pH because of the brain's high metabolic demand and subsequent cellular vulnerability after death. In surgical brain tissue, by contrast, these variables are comparatively easy to limit. Brain biopsies and neuro-oncology tissue are therefore excellent candidates for RNA-ISH investigation.

Variables affecting the suitability of post-mortem brain tissue for use with RNA-ISH include agonal state of the patient (protracted death vs sudden death etc), cause of death (e.g stroke vs heart attack), fixation times and processing schedules. The inherent quality of the tissue is paramount – tissue with a low RNA integrity is unlikely to yield valuable results. For downstream RNA-ISH analysis therefore, it is prudent to measure RIN either by extracting RNA and running on an agarose gel, or, alternatively, using the Agilent 2100 Bioanalyzer from Agilent technologies that also provides additional information such as RNA purity and concentration, whilst also requiring much smaller amounts of RNA.

Fixation is a key concern when performing RNA-ISH. Under-fixed tissue will become over-digested at the protease step causing subsequent loss of signal. Over-fixed tissue will cause under-digestion at the protease step causing inadequate probe accessibility and binding. We have conducted extensive optimization of the protocol below, and have found that human brain tissue becomes unsuitable for use with RNAscope beyond 48hrs fixation in 10% NBF. This means that the majority of archival brain tissue stored within brain tissue banks is unsuitable for RNA-ISH using this method. Alcohol (commonly industrial methylated spirit (IMS) in pathology labs) also has a fixative effect and tissue processing

schedules must therefore be modified from routine diagnostic protocols. The optimised protocol here is based on the use of the RNAscope method with the automated Ventana Benchmark platform from Roche Diagnostics, however prior to this extensive optimisation of the pre-analytical variables involved in using post-mortem FFPE tissue was undertaken.

2.2.2 Tissue processing

Tissue was dissected from either frozen tissue, or was dissected fresh at the point of the donation being received in our lab, and placed into a standard histology cassette before being fixed in 10% NBF. Tissue was fixed for a maximum of 48 hours as optimisation determined that past this mRNA started to become difficult to detect, and tissue fixed for less than this can produce a background signal due to unspecific probe binding. After fixation, tissue was processed using a carousel processor (TP1020, Leica Biosystems). The processing schedule used can be seen in Table 4. A shorter processing schedule was used than is standard for human FFPE brain - this is because of the additional fixative effect of alcohol. Tissue was then embedded in paraffin wax and sectioned onto Superfrost+ slides at 6µm using a rotary microtome. After staining, sections were rinsed in diluted washing up liquid three times to remove residual liquid coverslip, rinsed in running tap water and dried at 37°C for 30 minutes. Sections were then coverslipped using a single drop of xylene and Ecomount (Biocare) mounting medium and viewed using a Zeiss Primo Star microscope before being digitally scanned using the Aperio Scanscope (Leica Biosystems).

Station	Reagent	Time	
		Tissue 1-5mm^3	Tissue 5-10mm^3
1	10% NBF	5 mins (can be delayed as appropriate)	5 mins (can be delayed as appropriate)
2	75% IMS	1 hr	1 hr 30 mins
3	85% IMS	1 hr	1 hr 30 mins
4	95% IMS	1 hr	1 hr 30 mins
5	100% IMS	1 hr	1 hr 30 mins
6	100% IMS	1 hr 30 mins	1 hr 30 mins
7	Xylene	1 hr	1 hr 30 mins
8	Xylene	1 hr	1 hr 30 mins
9	Xylene	1 hr 30 mins	1 hr 30 mins
10	Molten paraffin wax	1 hr	1 hr 30 mins
11	Molten paraffin wax	1 hr	1 hr 30 mins
12	Molten paraffin wax	1 hr	1 hr 30 mins
Total time		12 hr 05 mins	16 hrs 35 mins

Table 4: Optimised tissue processing schedule for use with RNAscope. Total time spent processing is dependent on the size of the tissue, but times are substantially reduced from standard post-mortem brain times to account for the additional fixative effect of alcohol which could potentially reduce mRNA amplification.

The first run of tissue assessed using RNAscope is shown below Table 5.

Slide number	Method
1	FFPE tissue fixed for ~24hrs from fresh, unfrozen tissue @ 6µm
2	FFPE tissue fixed for ~24hrs from tissue that was previously frozen @ 6µm
3	FFPE tissue fixed for ~4 weeks @ 6µm
4	FFPE tissue fixed for years @ 6µm
5	Fixed frozen: Frozen tissue thawed, fixed in 4% PFA for 24hr @ 4C. Immersed in 10% sucrose in 1XPBS, repeated with 20% and 30% sucrose. Frozen @ -80C, sectioned @ 11µm on cryostat

Table 5: Methods of tissue preparation used in preliminary RNAscope optimisation.

2.2.3 Probes

Tissue was stained on the Benchmark Ventana platform (Fig 6) using anti-sense probes described in Table 6. For each run, two control probes were included. A probe for *PPIB*, which encodes a peptidyl isomerase and was chosen as a positive control because it displays a moderate expression across most human tissues including brain (Human Protein Atlas), and was applied to both HeLa cells (Fig 7B) and human tissue (Fig 7C-E). An additional *probe for dapB*, which as a bacterial gene is not expressed in human tissue, was applied and used as a negative control (Fig 7A). In RNAscope, each dot represents a

single transcript of mRNA for the given gene, with specificity ensured by multiple identical probes being required to bind to a single target before amplification and detection can take place [320]. This prevents the amplification of non-specifically bound probes and therefore confidence in target identification.

Using the above tissue (table 5), we were first able to ascertain that the tissue from slide number one offered the best signal/noise ratio and the clearest staining. Tissue from slide 3 and 4 did not stain at all, probably because of their prolonged fixation times preventing the adequate retrieval of the target mRNA. This led to the development of a short-fix protocol when a new ALS or control donation was received into our department, which allows complete control over fixation and ensures it is compatible not just with RNAscope but also with antibodies which may also be susceptible to fixation effects. In each subsequent run (table 7, 8 and 9), further refinements were made to our method so that we could achieve consistency and robustness of staining (Fig 7 and Fig 8). Application of the method using post-fixed frozen tissue was largely unsuccessful because of the significant ice crystal artefact created when defrosting tissue frozen at -80°C. Once the method had been optimised, *C9ORF72* test probes were applied to a single control case as a preliminary experiment (Fig 8). As RNAscope probes can only be designed when there is a >300bp difference in sequence homology between transcripts, and two of the three *C9ORF72* transcript variants exhibit just a 50bp difference, one *C9* probe labelled two variants simultaneously (variants 2 and 3) (Table 6). The *C9ORF72* probes could not (in a single attempt) be used to easily discern RNA foci which are abundant in the cerebellum of the patients with the expansion (Fig 8).

Gene	Human ENSEMBL Transcript ID	Target region (bp)	Accession number
PPIB	ENST00000300026.3	139-989	NM_000942.4
dapB	-	414-862	EF191515
TARDBP	ENST0000024018	2742-4112	NM_007375.3
FUS	ENST00000254108.11	2-1113	NM_004960.3
C9ORF72 (transcript variant 1)	ENST00000379997.7	859-1932	NM_145005.6
C9ORF72 (transcript variants 2 and 3)	ENST00000380003.7	774-2109	NM_018325.3
TBK1	ENST00000331710.9	1234-2321	NM_013254.3
CTIP2	ENST00000357195.7	4771-7609	NM_138576.3
SATB2	ENST00000417098.5	1608-2546	NM_001172509.1
TBR1	ENST00000389554.7	208-1345	NM_006593.2

Table 6: mRNA antisense oligonucleotide probes used in this study. Probes are designed by the company they are purchased from, and subsequently guaranteed. Specificity of the probes is ensured by the particular technology employed in the method, whereby multiple 'Z' pairs of probes are required to bind to the target before amplification and signal detection can occur. This ensures specificity by preventing the amplification of non-specific probe binding. Note that as the current synthesis method can only generate probes with a minimum of 300bp difference in homology, one of the C9ORF72 probes is specific for two transcript variants as they are both highly homologous (50bp difference between transcript variants 2 and 3.

Slide number	Type	Tissue	PM delay	Fixation	Processing	Result
1	Fresh PM	Cerebellum	48 hrs	24 hrs	12 hrs	Positive probe: faint expression but appears to have worked. Staining at different focal planes
						Negative probe: dots are present but far fainter than positive probe
2	Fresh PM	Spinal cord	48 hrs	24 hrs	12 hrs	Not tested
3	Fresh PM	M1 hand	48 hrs	24 hrs	12 hrs	Positive probe: dots present in grey matter, but additional edge effect
						Negative probe: dots fainter than +probe but still with edge effect
4	Fresh PM	Cerebellum	48 Hrs	24 hrs	72 hrs	Positive probe: some faint expression in granular layer, not clear though
						Negative probe: Almost no detectable expression
5	Fresh PM	Spinal cord	48 hrs	24 hrs	72 hrs	Not tested
6	Fresh PM	M1 hand	48 hrs	24 hrs	72 hrs	Positive probe: fairly consistent expression across grey matter, slight edge effect
						Negative probe: No detectable expression
7	Post-fixed frozen (liquid nitrogen)	Cerebellum	<48 hrs	40 hrs	12 hrs	Positive probe: Very clear specific dots in both granular and molecular layer, as well as purkinje cells
						Negative probe: No real detectable expression
8	Surgical	Cerebellum	-	24 hrs	15.5 hrs	Positive probe: clear expression in both granular and molecular layers
						Negative probe: very faint expression in both layers
9	Surgical	Pituitary	-	24 hrs	15.5 hrs	Positive probe: Very clear, obvious expression
						Negative probe: very faint expression in some areas
12	Fresh PM	Cerebellum	72 hrs	24 hrs	7 hrs	Positive probe: clear expression, particularly of purkinje cells (Fig 7 D&E). Slight underprocessing
						Negative probe: very faint expression in some areas

Table 7: Second run of RNAscope. Results on this run were more consistent, and allowed us to focus on using fresh-fixed PM tissue as our source material.

Slide number	Type	Tissue	Freezing method	Frozen since	PM delay	Fixation	Processing	Result
13	Post-fixed frozen	Cerebellum	Slow	July 2012	51 hrs	38 hrs	12 hrs	Positive probe: Inconsistent dots size and intensity across section. Failed
								Negative probe: Inconsistent background staining across whole slide. Failed
								C9ORF72 tv2tv3 probe: Staining is clear in places but mainly inconsistent with high background
14	Post-fixed frozen	Cortex	Slow	July 2012	51 hrs	38 hrs	12 hrs	Positive probe: Moderate but consistent expression and staining
								Negative probe: No expression
								C9ORF72 tv2tv3 probe: Low but consistent expression
15	Post-fixed frozen	Cerebellum	Liquid Nitrogen	Jan 2013	48 hrs	38 hrs	12 hrs	Positive probe: Clear, bright staining of granule layer and purkinje cells
								Negative probe: High background in granule cell layer
								C9ORF72 tv2tv3: Clear expression in granule layers
16	Post fixed frozen	Cerebellum	Liquid Nitrogen	Oct 2013	48 hrs	38 hrs	12 hrs	Positive probe: Good staining, but some inconsistency. Purkinje cell staining excellent
								Negative probe: No expression
								C9ORF72 tv1 probe: Maybe some specific staining, but difficult to distinguish from background which is fairly high
17	Post-fixed frozen	Cortex	Liquid Nitrogen	Oct 2013	48 hrs	38 hrs	12 hrs	Positive probe: Clear, consistent expression across grey matter
								Negative probe: No expression or background staining
								C9ORF72 tv1 probe: Low (1 or 2 transcripts per cell), but consistent expression
18	Post-fixed frozen	Cerebellum	Liquid Nitrogen	June 2015	24 hrs	38 hrs	12 hrs	Positive probe: Some staining but overall fairly weak. Freezing/fixation artefact
								Negative probe: background staining. Freezing/fixation artefact
								C9ORF72 tv2tv3 probe: Inconsistent across slide. Freezing/fixation artefact
19	Post-fixed frozen	Cerebellum	Liquid Nitrogen	March 2016	17 hrs	38 hrs	12 hrs	Positive probe: Clear but inconsistent specific dots
								Negative probe: Some weak background staining
								C9ORF72 tv1 probe: Some expression but difficult to distinguish from background
20	Post-fixed frozen	Cortex	Liquid Nitrogen	March 2016	17 hrs	38 hrs	12 hrs	Positive probe: Clear, consistent expression
								Negative probe: No expression
								C9ORF72 tv1 probe: Low but consistent and clear expression

Table 8: Third run of RNAscope. This run consisted of tissue that had been post-fixed from frozen tissue.

Slide number	Type	Tissue	Freezing method	Frozen since	PM delay	Fixation	Processing	Result
21	Post-fixed frozen	Cerebellum	Slow	July 2012	51 hrs	48 hrs	12 hrs	Positive probe: Some staining of granular layer, but no dots present in purkinje cell layer, little in molecular layer
								Negative probe: Little to no background but freezing/processing artefact within tissue
22	Post-fixed frozen	Cortex	Slow	July 2012	51 hrs	48 hrs	12 hrs	Positive probe: Consistent staining with some artefact
								Negative probe: No expression, haematoxylin patchy
23	Post-fixed frozen	Cerebellum	Liquid Nitrogen	Jan 2013	48 hrs	48 hrs	12 hrs	Positive probe: Consistent, clear staining across slide
								Negative probe: No staining
24	Post fixed frozen	Cerebellum	Liquid Nitrogen	Oct 2013	48 hrs	48 hrs	12 hrs	Positive probe: Expression is slightly inconsistent across slide but strong in most areas
								Negative probe: No background staining at all
25	Post-fixed frozen	Cortex	Liquid Nitrogen	Oct 2013	48 hrs	48 hrs	12 hrs	Positive probe + immuno: RNAscope staining good, no IHC staining
								Negative probe: No staining
26	Post-fixed frozen	Cerebellum	Liquid Nitrogen	June 2015	24 hrs	48 hrs	12 hrs	Positive probe + IHC: RNAscope staining good, but slight reduction in staining of Purkinje cells, no IHC staining
								Negative probe: No expression, under fixed/under processed?
27	Post-fixed frozen	Cerebellum	Liquid Nitrogen	March 2016	17 hrs	48 hrs	12 hrs	Positive probe + IHC: Good morphology. Slight decrease in RNAscope signal intensity, no IHC staining
								Negative probe: No staining
28	Post-fixed frozen	Cortex	Liquid Nitrogen	March 2016	17 hrs	48 hrs	12 hrs	Positive probe + IHC: RNAscope staining good, no IHC staining
								Negative probe: Very light background staining, barely noticeable

Table 9: Fourth run of RNAscope. This run consisted of tissue that had been post-fixed from frozen tissue, but the AMP5 time was made slightly longer to increase the size of the signal.

2.2.4 Set up of the Ventana Benchmark protocol and critical steps

While RNAscope is a multi-step process, there are certain steps (aside from pre-processing of the tissue) which are key to successful outcomes (Fig 6B). Firstly, the target retrieval conditions, namely the boiling and protease steps. Sufficient target retrieval is crucial to obtaining subsequent adequate RNA amplification, and was optimised based on the length of time the tissue had been fixed. In our experience, boiling times of 16 minutes and protease incubation times of 24 minutes gave the best results when the fixation of the tissue had been limited to 48 hours or less. Longer fixation times require longer pretreatment conditions, but as with all such methods, too long in pretreatment will damage the tissue and create artefactual damage. Secondly, the probe hybridization time. Prolonging the probe amplification times resulted in more efficient probe binding and better staining quality, at the compromise of vastly increased protocol times. Additionally, the automated platform does not allow hybridization times beyond two hours – the manual version of the assay allows much more flexibility in this regard. We found that hybridization of the probe for one hour was optimal. There are multiple amplification steps embedded within the RNAscope protocol, however the most important of these is the AMP5 time ('amplification' steps in Fig 6B, see also extended protocol in supplementary information) which is a critical aspect of the subsequent size of the dot staining. Increased AMP5 times allow each mRNA transcript to be visualised larger, however this is not necessarily desirable, especially for genes that are highly expressed.

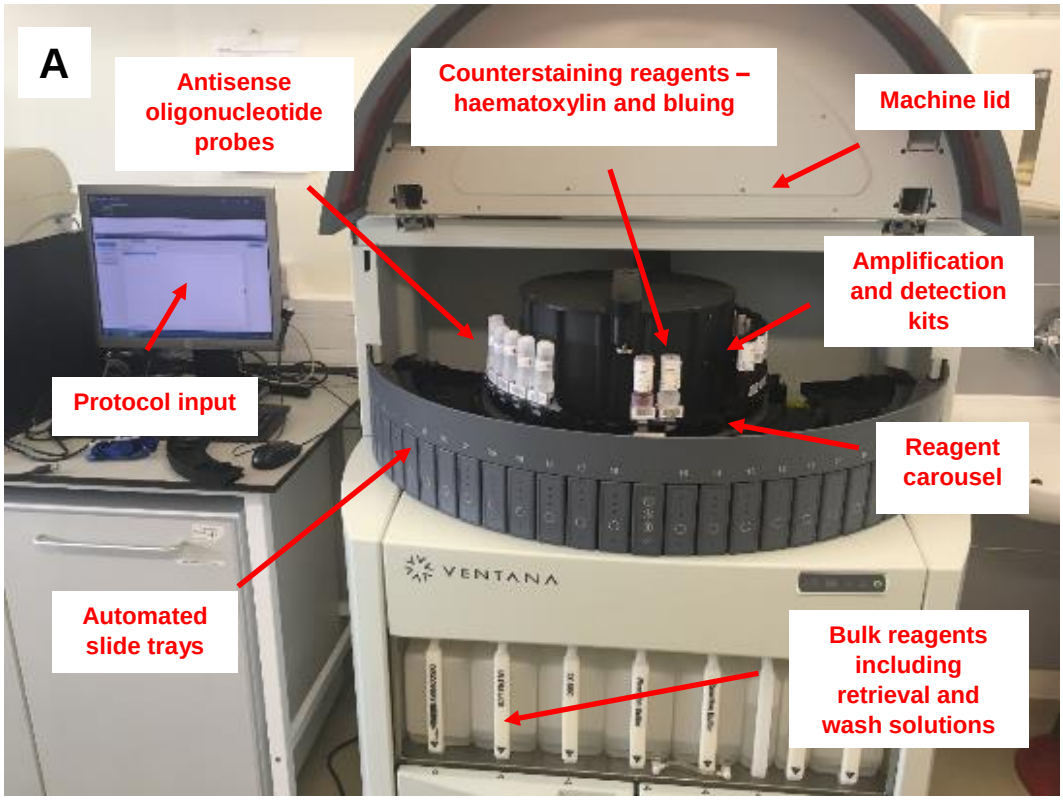

Critical step: Retrieval step including 24 minutes boiling

Alkaline phosphatase detection step

Critical step: Probe hybridization and amplification (including AMP5 time)

Counter staining

B

Protocol Summary

Procedure: mRNA Universal (v0.00.0210)

Discovery ULTRA Staining Module

Neuropathology Department, John Radcliffe Hospital Oxford, UK

Protocol No	Protocol Name	Creation Date
161	FUS - Amp 1HR	08/01/2018

1 Wet Slide Load [Selected]
2 Cell Conditioning [Selected]
3 8 Minutes [Selected]
4 Warmup Slide to [97 Deg C] from All Temperatures (Cycle 1)
5 16 Minutes [Selected]
6 24 minutes [Selected]
7 mRNA AP Detection [Selected]
8 AP detection 3rd Pretreatment [Selected]
9 Warmup Slide to [37 Deg C], and Incubate for [0 Hr 16 Min] (Pretreatment #3 Temp RB)
10 Apply Two Drops of [PROBE 10] (Probe #1), Apply Coverslip, and Incubate for 4 Minutes
11 Warmup Slide to [43 Deg C], and Incubate for 2 Hours (Hybridization)
12 Warmup Slide to [39 Deg C], and Incubate for 32 Minutes (Hybridization #2)
13 Warmup Slide to [39 Deg C], and Incubate for 32 Minutes (Hybridization #4)
14 Incubate for [1 Hour] (Hybridization #5)
15 Counterstain [Selected]
16 Apply One Drop of [HEMATOXYLIN II] (Counterstain), Apply Coverslip, and Incubate for [12 Minutes]
17 Post Counterstain [Selected]
18 Apply One Drop of [BLUING REAGENT] (Post Counterstain), Apply Coverslip, and Incubate for [8 Minutes]

Figure 6: Ventana Discovery machine set-up. (A) The slides remain in position on heat pads while the reagent carousel sequentially applies the reagents specified in the protocol. (B) The specific automated protocol and critical steps in the RNAscope staining method. The expanded protocol is included in the supplementary information.

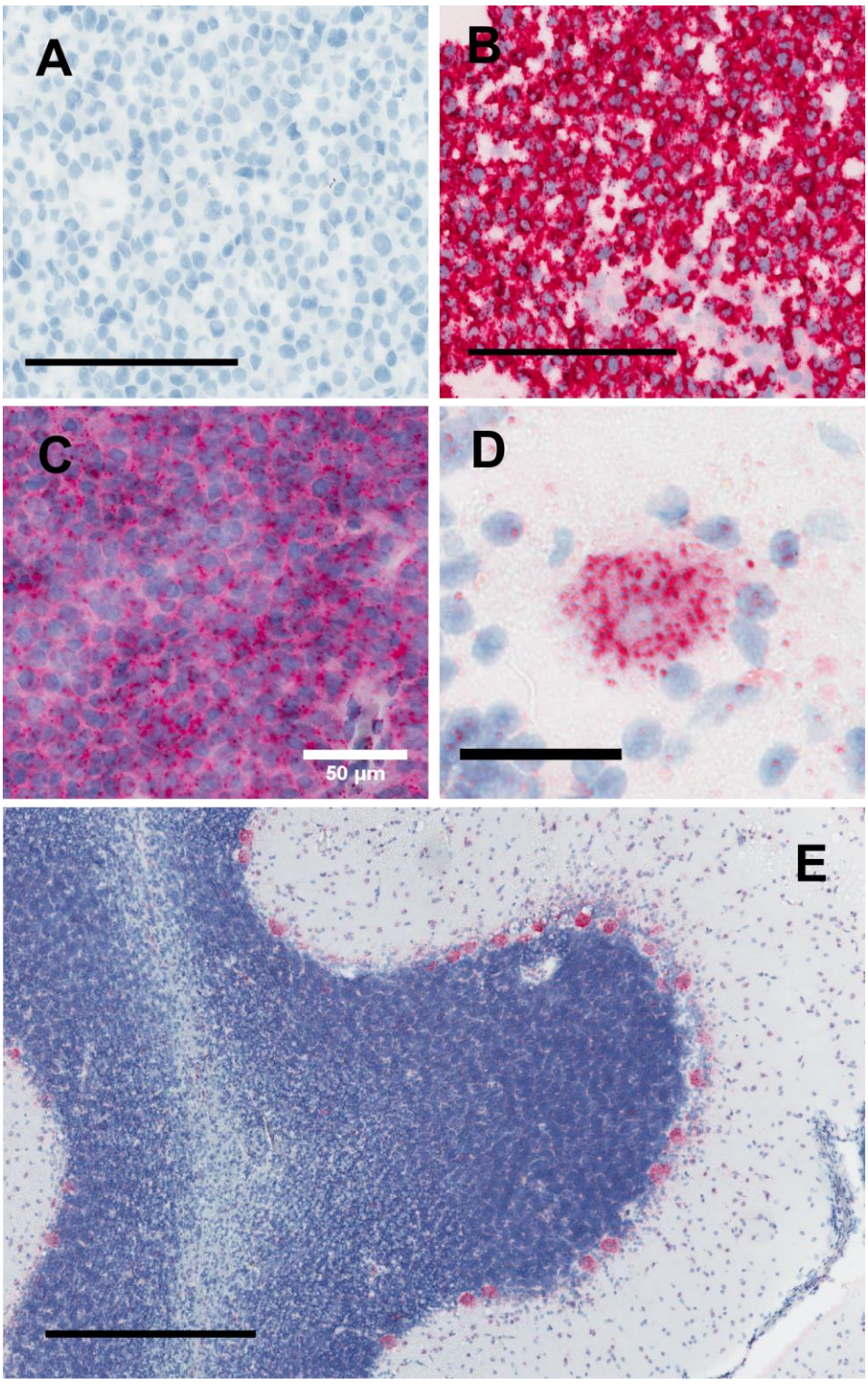

Figure 7: Optimization of RNAscope using the PPIB positive control probe. A probe targeted against the bacterial gene DapB, does not detect staining in HeLa cells (A), but the PPIB positive control probe is highly expressed in HeLa cells (B), and in frozen tissue from a pituitary adenoma surgical biopsy (C). The PPIB gene is also highly expressed in Purkinje cells of the cerebellum (D and E).

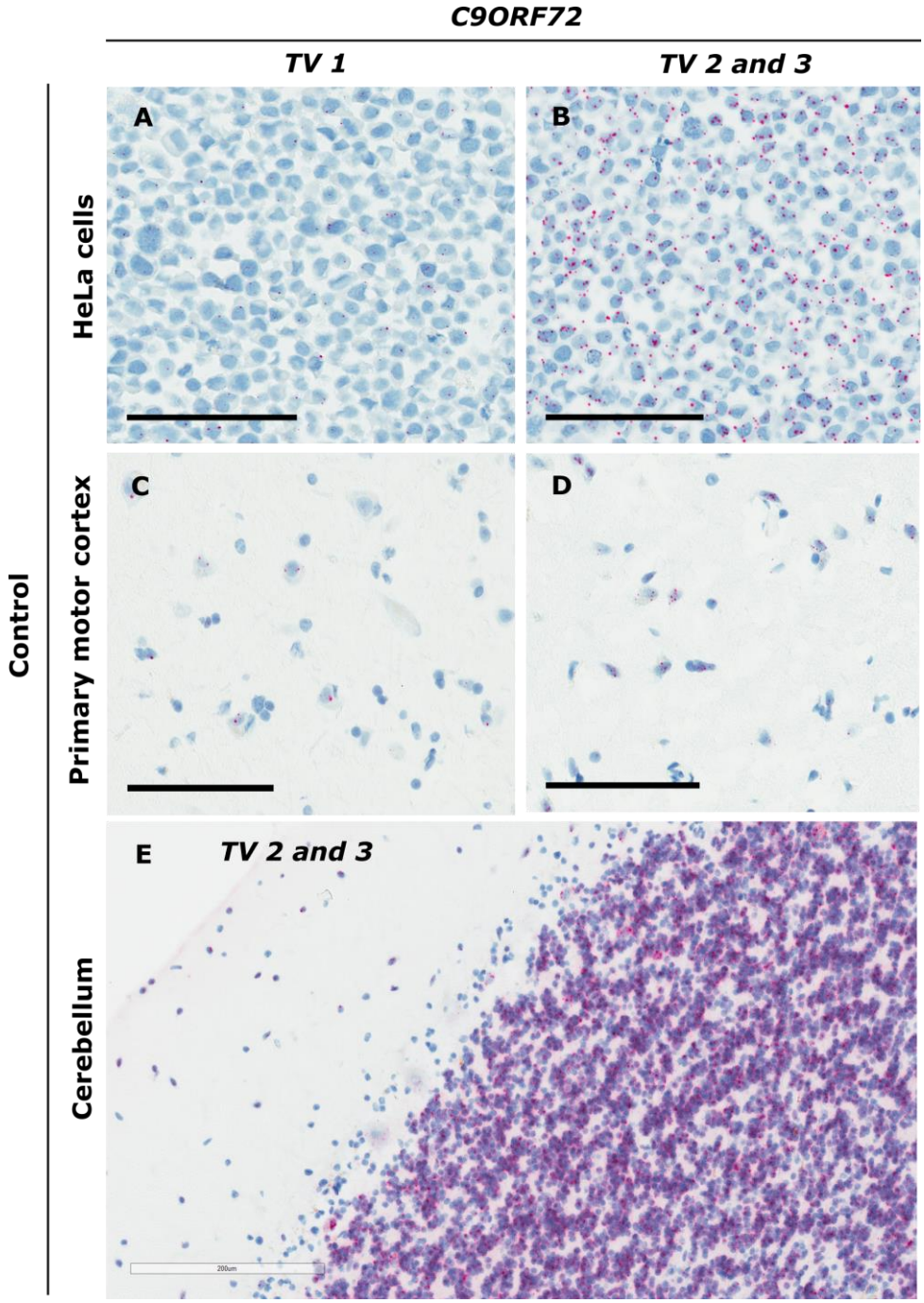

Figure 8: Expression of C9ORF72 using RNAscope. As transcript variants 2 and 3 are highly homologous, probes can only be synthesised that match both. There is relatively low expression of all transcripts in HeLa cells (A and B), and very low expression in human primary motor cortex (C and D). However, expression of transcript variants 2 and 3 are highly expressed in the granular layer of the human cerebellum (E). We were unable to confidently detect the sense RNA foci unique to C9ORF72 ALS/FTD within the cerebellum using either anti-sense RNAscope probe.

2.2.5 Final RNAscope protocol

1. Dissect fresh tissue into piece no larger than 10 x 5 x 5mm. This ensures adequate penetration of fixative and processing reagents
2. Immersion fix tissue in 10ml 10% NBF for 24-48 hours
3. Place tissue in labelled tissue processing cassette
4. Process tissue through increasing concentrations of alcohol and xylene followed by penetration using molten paraffin wax. See Table 4 for processing schedules
5. Embed processed tissue in paraffin wax and leave to cool on cold plate for at least 2 hours
6. Section tissue using rotary microtome at 5-7µm and pick up from water bath on Superfrost+ slides
7. Dry sections overnight at 37°C
8. 'Burn' sections to slide by incubating at 80°C for 1 hr
9. Dewax sections immediately through three washes in xylene, 5 min each
10. Take sections to water through rinsing in decreasing (100%, 100%, 90%, 74%) concentrations of IMS
11. Rinse sections in tap water
12. Add label to slide printed from Ventana software
13. Place slide in Ventana benchmark machine on slide pad and run on relevant protocol.
14. Ventana RNAscope protocols applied to post mortem tissue should use the following setup for critical steps, as in Fig 6B. The expanded protocol is included in the supplementary information:

- Wet slide load
- Protease time: 24 mins @ 97°C
- Boiling time: 16 mins @ 97°C
- AMP5 time: 32 mins
- Total amplification time: 1 hr
- Haematoxylin: 12 mins
- Bluing reagent: 8 mins

15. Remove slides from machine and rinse in cold tap water containing a small amount of washing up liquid to remove liquid coverslip (oil)
16. Rinse in cold water
17. Allow to dry completely in 37°C oven for at least 30 mins
18. Mount using EcoMount (NOT DPX) and coverslip

Note: Reagents containing alcohol (e.g DPX) cannot be applied after staining has been conducted as AP signal is soluble in alcohol.

2.2.6 Practical utility of RNAscope

RNAscope is a robust method that produces high quality, reproducible results, as long as the pre-analytical variables associated with post-mortem human tissue are suitably controlled for. Overall, the RNAscope protocol itself is standardised as a result of the software used to run the platform, however there is some scope for it to be modified for particular tissues. The difficulty in its implementation therefore comes not from the protocol itself, but from accounting for the presence of extensive pre-analytical variables involved in using post-mortem tissue, particularly sub-optimal, prolonged fixation times. Ultimately, once these factors are controlled for through fixing tissue for <48 hours and optimising staining itself, the results generated in preliminary experiments were consistent and of high enough quality that it was felt other probes listed in table 6 could be used in future experiments with confidence.

2.3 Quantification

Despite the high degree of specificity achieved through the need for multiple probes to bind simultaneously before amplification can occur, some transcripts will be overlapping and some will exhibit larger dots than others, meaning algorithms are required that can distinguish between these. Quantification of expression was performed using QuPath analysis software [327]. Algorithms were designed that allowed the quantification of the signal in several contexts. Firstly, the raw number of dots per annotation region could be counted. A concomitant algorithm was also run in parallel that counted the number of viable cells using haematoxylin staining as the criteria, providing an accurate quantitation of cell nuclei. This allowed the number of transcripts per cell, per annotation region to be

quantified. This algorithm could then be used to assess the average number of transcripts per cell, and each cell could then be designated as 'positive' if the minimum number of transcripts per cell was met. In this study, we designated a 'positive' cell as containing at least three times the average number of transcripts per cell. Finally, where dots were identified as being overlapping, the algorithm was trained to recognise this and output an average of dots counted using minimum dot size as a criteria. Quantification was achieved more accurately by inverting the colours used in the image analysis software, so that a greyscale image was used (Fig 9C). The algorithms created and used in QuPath are listed below.

2.3.1 Source code for RNAscope quantification and analysis

The code below performs three functions. First, the parameters required for the identification of the dots are input. This includes colour deconvolution to identify the fast-red signal, optimization of dot parameters, and assessment of the cytoplasm-to-nuclear dot ratio. The output for this algorithm includes the number of dots in the annotation region, the number of dots per cell, and the nuclear vs cytoplasmic ratio of dots. The algorithm was designed in conjunction with the creators of the QuPath software via github (https://github.com/qupath/qupath/issues/119).

```
--setImageType('BRIGHTFIELD_H_DAB');

setColorDeconvolutionStains('"Name" : "H-Fast Red ISH", "Stain 1" :
"Hematoxylin", "Values 1" : "0.76196 0.55713 0.33018 ", "Stain 2" :
"DAB", "Values 2" : "0.21428 0.75316 0.62196 ", "Background" : " 255
255 255 "');
runPlugin('qupath.imagej.detect.nuclei.WatershedCellDetection',
'{"detectionImageBrightfield": "Hematoxylin OD",
"requestedPixelSizeMicrons": 0.5,  "backgroundRadiusMicrons": 8.0,
"medianRadiusMicrons": 0.0,  "sigmaMicrons": 1.5,  "minAreaMicrons":
10.0,  "maxAreaMicrons": 400.0,  "threshold": 0.1,  "maxBackground":
```

```
2.0,  "watershedPostProcess": true,  "excludeDAB": false,
"cellExpansionMicrons": 7.0,  "includeNuclei": true,
"smoothBoundaries": true,  "makeMeasurements": true');
runPlugin('qupath.imagej.detect.cells.SubcellularDetection',
'"detection[DAB]": 0.175,  "doSmoothing": true,  "splitByIntensity":
true,  "splitByShape": true,  "spotSizeMicrons": 1.0,
"minSpotSizeMicrons": 0.5,  "maxSpotSizeMicrons": 12.0,
"includeClusters": false');
setCellIntensityClassifications("Subcellular: DAB: Num spots
estimated", 6)
// Note: This sets the class according to spot/cluster location,
// but does not try to set meaningful colors at this point

// Get all spots/clusters
def clusters = getObjects({p -> p.class ==
qupath.imagej.detect.cells.SubcellularDetection.SubcellularObject.class
}

// Loop through all clusters
for (c in clusters) {
    // Find the containing cell
    def cell = c.getParent()
    // Check the current classification - remove the last part if it
    // was generated by a previous run of this command
    def pathClass = c.getPathClass()
    if (["Nuclear", "Cytoplasmic"].contains(c.getName())) {
        pathClass = pathClass.getParentClass()
    }
    // Check the location of the cluster centroid relative to the
nucleus,
    // and classify accordingly
    def nucleus = cell.getNucleusROI()
    if (nucleus != null && nucleus.contains(c.getROI().getCentroidX(),
c.getROI().getCentroidY())) {
        c.setPathClass(getDerivedPathClass(c.getPathClass(),
"Nuclear"))
    } else
        c.setPathClass(getDerivedPathClass(c.getPathClass(),
"Cytoplasmic"))
}
fireHierarchyUpdate()
// Loop through the detections (we assume cells...)
for (detection in getDetectionObjects()) {
    // Request cell measurements & calculate integrated density
    double cellMean = measurement(detection, "Cell: DAB OD mean")
    double nucleusmean = measurement(detection, "Nucleus: DAB OD mean")
    double cellnucleusDABratio = cellMean / nucleusmean
    // Only add measurement if it's not 'Not a Number' - this implies
both mean & area were available
    if (!Double.isNaN(cellnucleusDABratio)) {
        // Add new measurement to the measurement list of the detection
        detection.getMeasurementList().addMeasurement("Cell-Nucleus DAB
ratio", cellnucleusDABratio)
        // It's important for efficiency reasons to close the list
        detection.getMeasurementList().closeList()
    }
}

// Make sure to update the hierarchy
fireHierarchyUpdate()
print("Done!")
```

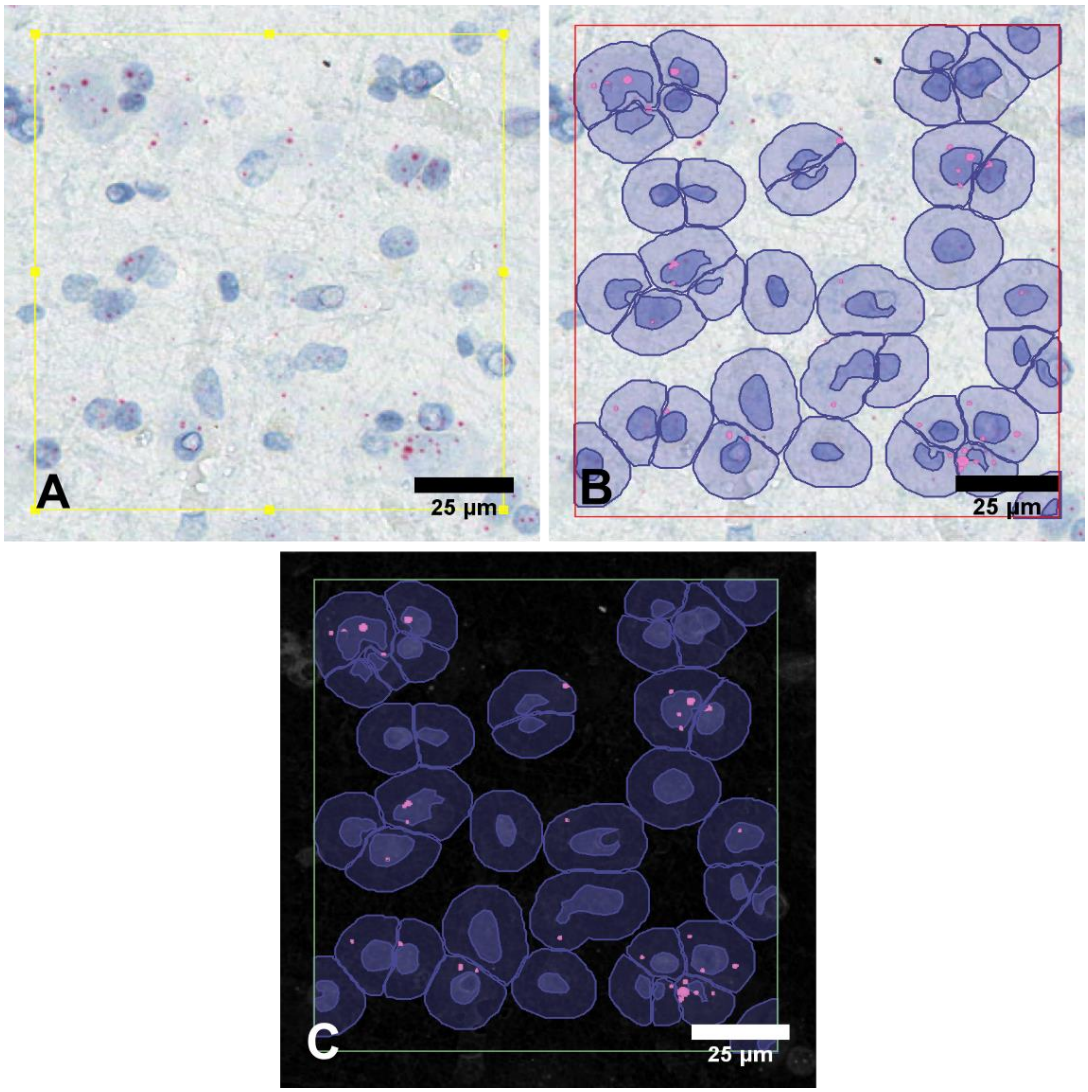

Figure 9: Quantification of RNAscope using QuPath image analysis software. Annotation region of RNAscope staining shown three ways. Individual dots (transcripts) can be distinguished using a custom algorithm after optimising colour deconvolution (A). The algorithm then accurately identifies cell nuclei/cytoplasm, as well as detecting RNAscope positive signal, i.e gene expression (B). This can be seen more clearly when the image is subsequently converted to greyscale (C).

2.4 Imaging mass cytometry

Antibodies used in IMC must be conjugated by the user or bought pre-conjugated from Fluidigm. Antibodies were conjugated to the metals based on their expression level in DAB-immunohistochemistry, i.e the lowest expressed protein was conjugated to the metal considered to give the most intense signal from the platform manufacturer literature and using the protocol from the manufacturer exactly. Antibodies were validated by positive identification of the relevant signal using the Helios cytometer system (Fluidigm) and by standard DAB-IHC post-conjugation. Sections were treated prior to primary antibody staining as previously described. Primary antibodies against NeuN (Merck Millipore, MAB377, 1:500), GAD67 (Merck Millipore, MAB5406, 1:700) and pTDP-43 (Cosmo-Bio, TIP-PTD-M01, 1:5000) were applied and incubated at 4°C overnight. Sections were then rinsed with TDS-T and intercalator (Fluidigm, cat #201192A**)** was applied at a dilution of 1:400, before insertion into the Fluidigm Hyperion platform. The GAD67 primary was chosen based on the high quality results gained when visualised using DAB-IHC in preliminary experiments (data not shown), and because of the hypothesis that inhibitory interneurons aggregate pTDP-43 pathology less frequently than their excitatory counterparts, which is explored elsewhere in chapter 3 (Fig 26).

Preliminary results from a single use of the Hyperion platform were not successful (Fig 10), hampered by insufficient image resolution and inadequate conjugation of antibodies. Additionally, acquiring the correct antibodies at sufficient purity and concentration so that they were suitable for conjugation made the protocol difficult to implement within the allotted time. The manufacturer of the platform produces a line of antibodies conjugated by themselves in house, however their range is limited and they do not currently stock a significant number of neuroscience related targets. The promise in the platform lies in its

ability to handle multiple simultaneously stained targets, as well avoiding the autofluorescence issue so inherent when using human brain tissue. It is noted that the platform is being used successfully in the investigation of cancer tissue and has also been used in conjunction with RNAscope to visualise RNA-protein relationships [324]. However, until the above issues are rectified its utility in routine neuroscience lab settings will be limited, and ultimately our preliminary application of the method was unsuccessful.

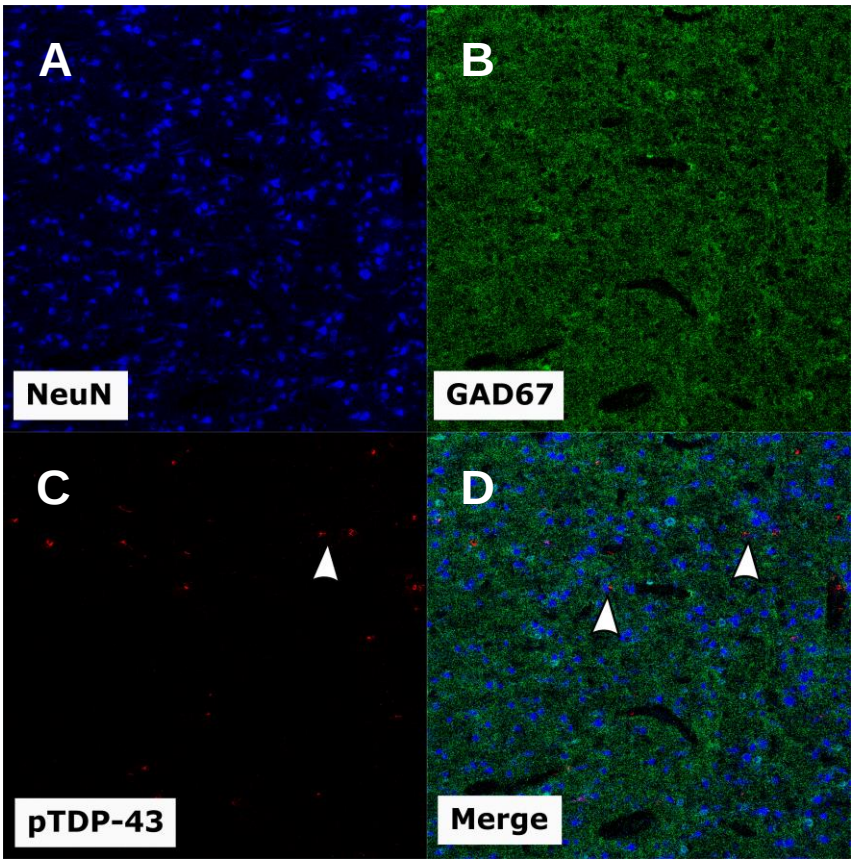

Figure 10: Preliminary results from imaging mass spectrometry. Three antibodies – NeuN (A), GAD67 (B) and pTDP-43 (C) were tagged to specific heavy metals and the tissue ablated using the Hyperion platform from Fluidigm. The resolution of the images is low and the GAD67 antibody has not worked efficiently, and staining is difficult to discern (D). White arrows indicate pTDP-43 inclusions stained red. This is the maximum practical resolution possible for the method, which is unsuitable for the applications required in this thesis.

Chapter three

Neuropathological substrates of selective vulnerability in the ALS primary motor cortex

3. Neuropathological substrates of selective vulnerability in the ALS primary motor cortex

3.1 Introduction

The term ‘selective vulnerability’ describes the differential susceptibility of cells or anatomically defined regions to disease pathomechanisms, which is generally recognised as the basis for the heterogeny of features across the spectrum of neurodegenerative disease. In this context, selective vulnerability can be further delineated as vulnerability to cellular proteinopathy or vulnerability to degeneration itself; a relationship which cannot be assumed to be linear, as microscopically visible aggregate formation may be an indicator of a successful cellular response to proteotoxicity [328-331].

The concept of selective vulnerability defines the classical neurodegenerative diseases. The clear progressive loss of dopaminergic neurons in the substantia nigra pars compacta of Parkinson’s disease [332], or the susceptibility of hippocampal neurons to tau and β-amyloid pathology in Alzheimer’s disease for example have provided ways in which these diseases can be accurately neuropathologically staged. However in ALS, this selectivity is particularly apparent as even functionally-related but regionally distinct motor neuron sub-types are differentially involved; e.g the trigeminal and hypoglossal nuclei of the brain stem are severely affected, whereas oculomotor neurons remain generally undisturbed throughout disease course [109, 227].

While patients commonly present with a combination of lower motor neuron and pyramidal signs, the nature of disease initiation and progression between the spinal cord and cortex is debated and two competing (but not necessarily mutually exclusive) hypotheses have emerged. In the ‘dying-back’ hypothesis, denervation at the

neuromuscular junction precedes lower motor neuron (LMN) degeneration, which in turn precedes cortical dysfunction. In the 'dying forward' hypothesis, cortical dysfunction caused by anterograde trans-synaptic, glutamate-mediated excitotoxicity precedes LMN dysfunction [189, 217, 218]. This is supported by a cortical hyperexcitability phenotype apparently manifesting before significant LMN signs in human sporadic ALS cases [189], as well as presymptomatic cortical neuron defects in both *SOD1* [202, 219] and *TARDBP* [220] mouse models. Degeneration of GABAergic, inhibitory interneurons has been suggested as the cause of the aforementioned hyperexcitability and subsequently of ALS potentially being an 'interneuronopathy' [190]. The histological basis for this is supported by studies detailing interneuron loss in various ALS mouse and zebrafish models [193, 194, 333-335].

However, differences in comparative anatomy make using such models to study selective vulnerability and upper motor neuron pathology challenging, and several studies utilising human tissue for this purpose have described conflicting results [188, 195, 196]. To our knowledge, there have been no studies attempting to reconcile motor cortex degeneration to the presence of cortical pathology since the discovery of the main ALS driver genes and their protein products (e.g TDP-43, FUS, SOD1 and *C9ORF72*). Finally, while atrophy of the ALS primary motor cortex relative to other cerebral regions can be identified *in-vivo* using various neuroimaging methods [171-173, 336, 337], two stereological studies found no evidence of total neuronal loss [290] or a significant change in neuronal morphology [289].

We hypothesized that not all cell-types are equally affected by the specific proteinopathies that define the major neuropathologically recognised disease entities of ALS-TDP, C9-ALS, ALS-FUS and ALS-SOD1. Here, we use both standard immunohistochemistry and multiplexed immunofluorescence (MxIF) in conjunction with multilevel statistical

modelling to characterise the pathology of the motor cortex across the spectrum of ALS genotypes, and assess the existence of this pathology in the context of molecularly-defined cellular sub-types.

3.2 Materials and methods

3.2.1 Cases

Post-mortem human brain tissue in the form of 10µm sections was obtained from the Oxford Brain bank, the MRC London Neurodegenerative Diseases Brain Bank and the Sheffield Brain Tissue Bank. Consent and ethical approval for the use of tissue was provided by the generic REC of each bank respectively according to institutional guidelines. Details of the cases used in this study are included in Table 10.

Patients were diagnosed during life by experienced clinicians according to standard diagnostic criteria. All cases were diagnosed post-mortem by an experienced neuropathologist and confirmed genetically via next-generation sequencing. For the purposes of this study, we therefore use the term 'sporadic' to refer to cases with no known high-penetrance mutations and an absence of characteristic genetically-linked pathology. Two cases could not be confirmed genetically but were diagnosed through the presence of characteristic SOD1 and FUS pathology respectively. Sample sizes were largely determined by the availability of cases from each genotype. Cases caused by *OPTN*, *CHMP2B*, *HNRNPA1* and *TARDBP* mutations are present in <1% ALS patients and therefore we were unable to obtain sufficient power for these genotypes, but were included because of their potential for interesting comparisons and clarification of their pathotype.

Genotype	Age (Years)				PMD (Hours)			Fixation (Weeks)		
	***n*=**	**Range**	**Mean**	**Std. Dev.**	**Range**	**Mean**	**Std. Dev.**	**Range**	**Mean**	**Std. Dev.**
Control	19	36-95	62.7	13.5	18-73	42.9	15.2	0.2-32	6.4	9.0
Sporadic	43	44-90	64.3	12.1	2-120	45.0	24.4	0.2-28	5.6	8.2
C9ORF72	18	42-76	60.6	9.4	4-96	47.6	30.6	0.2-17	7.6	4.8
SOD1	11	34-78	55.9	14.7	5-96	39.0	31.9	3-20	11.8	5.8
FUS	9	18-64	37.9	15.2	3-71	39.3	21.9	3-45	12.6	12.8
CHMP2B	2	51-69	60.0	12.7	12-22	17.0	7.1	3-4.5	3.8	1.1
HNRNPA1	1	62	62.0	-	48	48.0	-	12.0	12.0	-
OPTN	1	54	54.0	-	3	3.0	-	12.0	12.0	-
TARDBP	1	57	57.0	-	48	48.0	-	9.0	9.0	-

Table 10: Summary details of all cases used in the selective vulnerability study. PMD = Post Mortem Delay.

3.2.2 Tissue sampling

10µm sections containing underlying white matter were cut from archival formalin-fixed paraffin-embedded blocks from the primary motor cortex, corresponding to the 'hand knob' region of the homunculus where available. 5µm sections from the same region were used in MxIF experiments. 10µm sections of FFPE lumbar spinal cord were also cut from each case. All sections were cut using a rotary microtome and harvested on Superfrost + slides.

3.2.3 Single immunohistochemistry

For single-stain immunohistochemistry (sIHC), de-identified sections from sporadic (*n* = 19), *C9ORF72* (*n* = 16), *SOD1* (*n* = 11), *FUS* (*n* = 9), *CHMP2B* (*n* = 2), *TARDBP* (*n* = 1), *HNRNPA1* (*n* = 1), *OPTN* (*n* = 1) and control (*n* = 11) cases were dewaxed through xylene, and rehydrated through decreasing concentrations of alcohol before being pre-treated for 30 min in 10% concentrated (30%) H_2O_2 and distilled water to block endogenous peroxidase. Heat-induced epitope-retrieval was performed using autoclave boiling at 121°C for 10 minutes. Sections were then rinsed with Tris-buffered saline and blocked with normal goat serum (1:10 in TBS-T) for 30 min. The primary antibodies used are listed in Table 11. Primary antibodies were incubated overnight at 4°C and visualised using the Dako Envision+ kit and HRP-DAB signal. Primary antibody dilutions were optimised extensively prior to testing, with criteria for success being intense signal staining and minimisation of background and artefact. In order to assess the relative extent of upper vs lower motor neuron involvement, an additional three sections from the lumbar spinal cord region were cut at 10µm from each case and stained with pTDP-43, CD68 and SMI-312 using the same method. Positive and negative controls were used for each

antibody. No staining was seen when the primary antibody was omitted. For all cases, an additional section was stained using haematoxylin and eosin (H&E) to confirm the presence of Betz cells in layer Vb. Stained sections were then dehydrated, cleared, mounted (Histomount, Thermo-Fisher Scientific, Germany) and coverslipped. All sections were viewed using a Zeiss Primo Star microscope (Zeiss, Oberkochen, Germany).

Antigen	Supplier	Catalogue #	Host	Clone	Dilution
pTDP-43	Cosmo-bio	TIP-PTD-M01	Mouse	Monoclonal	1:40,000
p62	Abcam	ab91526	Rabbit	Polyclonal	1:1,000
FUS	Sigma-Aldrich	HPA008784	Rabbit	Polyclonal	1:300
SOD1	StressMarq Bio	SPC-206	Rabbit	Polyclonal	1:1,000
HuC/D	Merck Millipore	MABN153	Mouse	Monoclonal	1:2,000
NeuN	Merck Millipore	MAB377	Mouse	Monoclonal	1:1,000
SMI312	Sternberger monoclonals	837904	Mouse	Monoclonal	1:2,000
Calbindin	Swant	300	Mouse	Monoclonal	1:4,000
Calretinin	Swant	7697	Rabbit	Polyclonal	1:4,000
Parvalbumin	Swant	235	Mouse	Monoclonal	1:7,500
GFAP	Sigma-Aldrich	C9205	Mouse	Monoclonal	1:500
Olig2	Abcam	ab109186	Rabbit	Monoclonal	1:400
TPPP/p25	Win-Fest Ltd	-	Mouse	Monoclonal	1:2,000
Iba1	WAKO	019-19741	Rabbit	Polyclonal	1:1,000
CD68	Dako	M0876	Mouse	Monoclonal	1:200
Collagen IV	Millipore	MAB3326	Mouse	Monoclonal	5µg/ml
OPTN	Proteintech	10837-1-AP	Rabbit	Polyclonal	1:3,000
CTIP2	Abcam	ab18465	Rat	Monoclonal	1:500
SATB2	Abcam	ab51502	Mouse	Monoclonal	1:400
TBR1	Abcam	ab183032	Rabbit	Monoclonal	1:100

Table 11: Antibodies used to investigate neuropathological substrates of vulnerability.

3.2.4 Multiplexed immunofluorescence

Multiplexed fluorescence staining and imaging was performed at GE Global Research, Niskayuna, USA using previously described methodologies [338], optimized for FFPE neurological specimens. In brief, fluorescent antibodies against 21 markers were applied two or three at a time across nine sequential staining-and-dye-deactivation rounds to a subsection of our cohort (sporadic n = 18, *C9ORF72* n = 3, controls n = 5). Antibodies were detected either by directly conjugated fluorophores, by pre-bound fluorophore-labelled antibody binders, or using fluorophore-labelled secondary antibodies (Table 11 and Fig 11). Using the MxIF methodology, staining is performed for all antibodies on a single slide per case, allowing the analysis of a number of targets within a single section, without the loss of spatial colocalization inherent when staining different markers across multiple sequential sections. The staining of each antibody was imaged on separate channels after each staining round. Images were collected on custom Olympus IX81 inverted microscopes (Olympus, Tokyo, Japan) using 20x objectives, with multi-round image acquisition driven by automated, custom software. Autofluorescence signal was removed during automated, post-acquisition processing by subtracting an earlier, unstained image from each corresponding stained image. Regions of interest (ROIs) for MxIF acquisition were selected manually on the whole-tissue tissue sections to cover from the pial surface to the subcortical white matter of each case. Image analysis on a single ROI composed of ~15 fields of view per case was completed at the University of Oxford using a custom plugin for ImageJ [339] enabling review of the multi-channel MxIF image data.

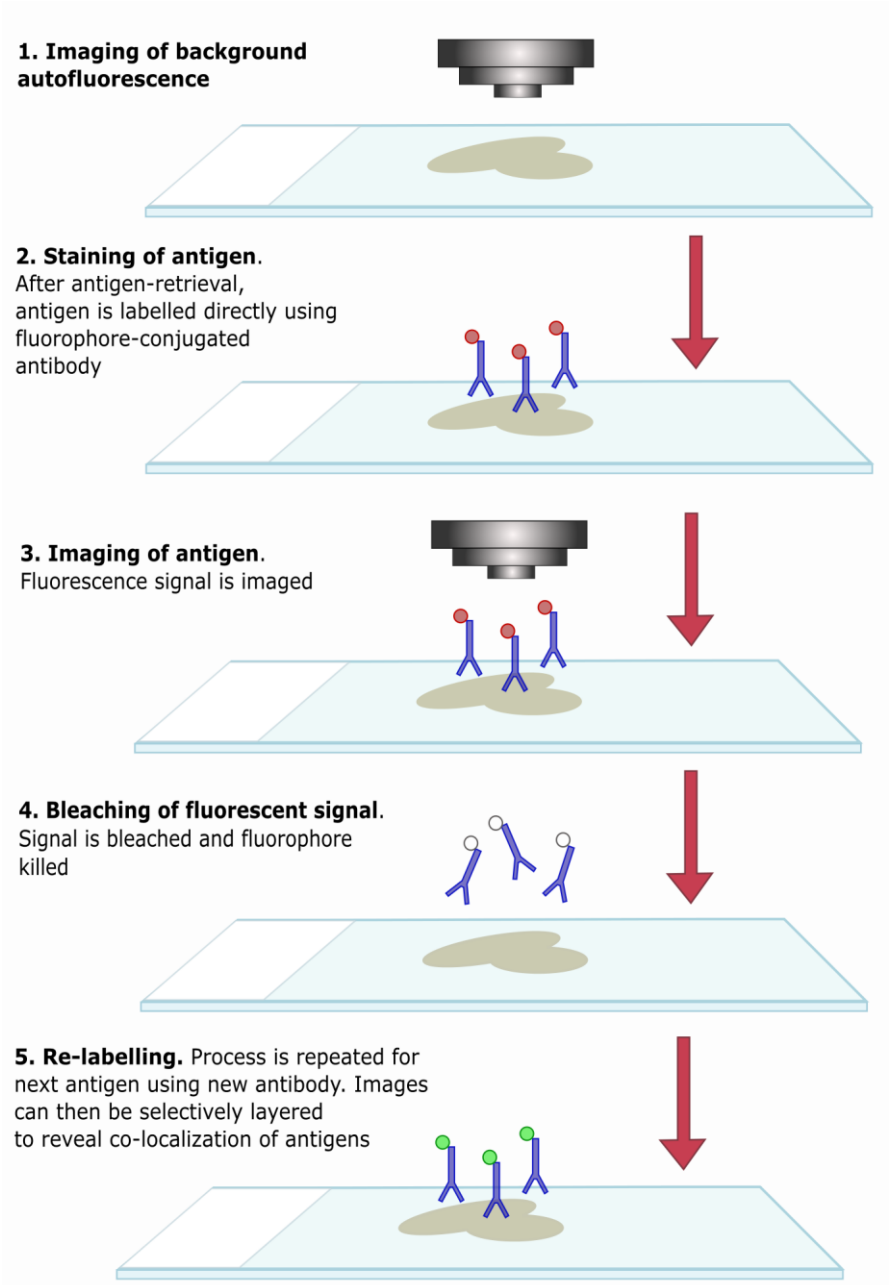

Figure 11: Sequential staining using the MxIF proprietary method from GE. Directly conjugated monoclonal primary antibodies are sequentially applied, followed by image acquisition and processing. Autofluorescence is removed by imaging the unstained section and subtracting this fluorescence from the stained image. MxIF staining was conducted by GE Global Research, and image analysis conducted by the author at the University of Oxford.

3.2.5 Single IHC quantification

Single stained IHC slides were digitally scanned using the Aperio ScanScope AT Turbo system (Leica Biosystems, Germany). Anterior horn neuron size was measured using QuPath software [327]. 10 anterior horn neurons (5 from each half of the spinal column) from the lumbar region of each case were measured by drawing around the perimeter of each neuron at x40 mag. These measurements were then averaged and log transformed for statistical testing. For oligodendrocyte analysis, criteria for designation as an oligodendrocyte were small size, close proximity to neurons within grey matter, a densely stained, round nucleus, 'Fried egg' sign or the presence of 'cat's eye' TDP-43 inclusion. Neuronal criteria were a large cell body, presence of Nissl substance, a round nucleus with pale homogenous nucleoplasm and a single dark nucleolus.

For pathological quantification of the primary motor cortex, ROI measuring 1000µm x 3000µm were defined and quantified using QuPath pathology analysis software with thresholding and algorithms manually optimized for each stain. Algorithms were applied consistently throughout. CD68, TPPP/p25, Olig2, Calbindin, Calretinin and Parvalbumin were quantified using a positive cell (pc) count. Because of the morphological heterogeneity of pTDP-43 and p62 pathology, these were quantified using a positive pixel (pp) count tool. Both algorithms measured the number of positive cells/pixels above a defined DAB optical density (OD) threshold (Fig 12B). Five ROI were assessed per slide, and placed where the short edge of each ROI was touching the pial surface whilst parallel with underlying white matter. ROI were placed evenly around a single gyrus on each slide, and measurements averaged across the five ROI (Fig 12A). For CD68, three additional ROI within the white matter of a single gyrus were also defined and measurements averaged. For lumbar spinal cord sections, one circular ROI measuring 1,757,000µm^2 and one square ROI measuring 2,250,000µm^2 was placed in the lateral corticospinal tract

region and anterior horn region respectively, on each side of a single lumbar spinal cord slice (Fig 12C). CD68 and pTDP-43 were both quantified in the spinal cord using the same algorithms as the motor cortex. The algorithms used to quantify the single-IHC can be seen below. All analyses were conducted blind to case details including genotype and other IHC results.

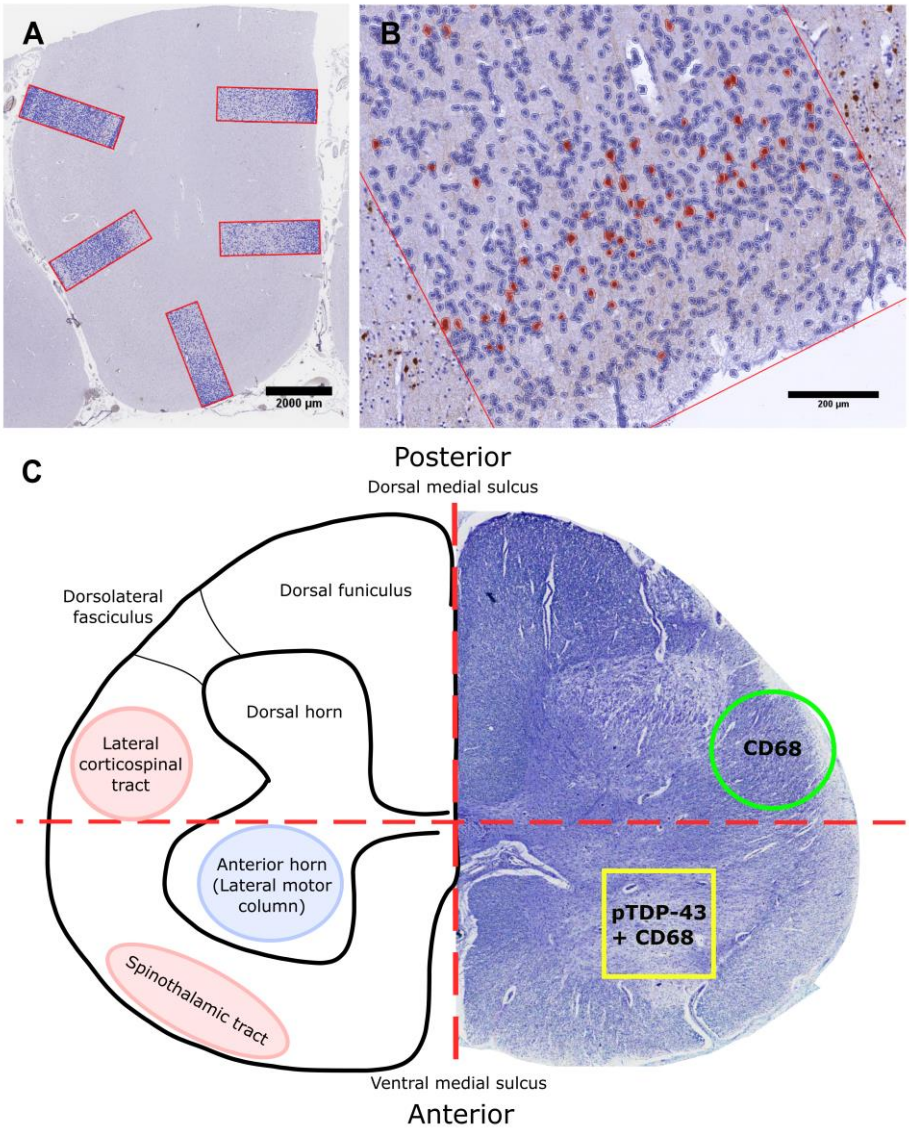

Figure 12: Quantitative assessment of pathology in the primary motor cortex and at the level of the lumbar spinal cord. IHC staining was quantified in the motor cortex using DAB optical-density based algorithms on five ROI, each measuring 3,000,000µm^2. ROI were spread evenly around a single gyrus where the top edge of the ROI was at the pial surface (A). An optimised algorithm for Calbindin counts the number of grey matter positive interneurons (B). CD68 and pTDP-43 pathology was also quantified in the anterior horn and corticospinal tract of the lumbar spinal cord (C, yellow and green box respectively), using guidelines bisecting the section in each direction across the central canal.

3.2.6 Statistical analysis

Statistical analysis and graphing was performed using a combination of GraphPad Prism (California, USA) and RStudio (Boston, USA). The results of this study were analysed using multi-level generalized linear models (GLM) [340, 341]. This is because the measurements, being counts, were neither normally distributed nor homoscedastic and ordinary parametric ANOVA or ANCOVA analyses were therefore inappropriate. The procedure used is analogous to a 3-way ANOVA where each individual *Case* is a block, *Protein* is a grouping variable and *Genotype* is a treatment, but in order to avoid over-parameterisation *Case* was incorported as a random effect in a 2-level multilevel model; thus within-*Case* correlation is accounted for. Goodness-of-fit chi-squared test revealed the data was negatively-binomially distributed. If the mean *Count* is μ, a negative-binomial GLM fits the model:

$$\log \mu = \alpha + \sum_{i} \beta_i Genotype_i + \sum_{j} \beta_j Protein_j + \sum_{i,j} \beta_{ij} Genotype_i : Protein_j$$

Comparisons were assessed for all proteins across all genotypes, only statistically significant results are reported in the figures and text. If a *p* value is not reported for any two treatments, then $p>0.05$. For calcium-binding protein analysis, fixation $time_{log}$ and predominance were included as covariates in a negative-binomial GLM, to examine whether any potential loss in expression was affected by either a more severe neurodgeneerative phenotype overall or decreased immunoreactivity caused by prolonged fixation. Covariates were added as log(*Fixation*) and *Predominance* with their interactions with *Genotype* and *Protein*; *Fixation* needed to be log-transformed to remove excessive

skewness. In practice there was no evidence of a *Genotype*:*Predominance* interaction and it was dropped from the model. A plot of log(*Count*) obtained from the fitted negative-binomial GLM versus values of recorded log(*Count*) shows that the overall model fit is good and therefore appropriate (Fig 13). *Fixation* and *Predominance* were both highly significant covariates. A Wald test of the model with and without *Fixation* resulted in a *p*-value of 2.4×10^{-10}; a Wald test of the model with and without *Predominance* resulted in $p = 3.6 \times 10^{-10}$.

Scatterplots are formatted on a logarithmic base 2 scale and labelled as exponents of the base value. Levels for quoted confidence intervals are set at 95% and *p*-values in the figures are indicated as follows: * $p < 0.05$, ** $p < 0.01$, *** $p < 0.001$, **** $p < 0.0001$.

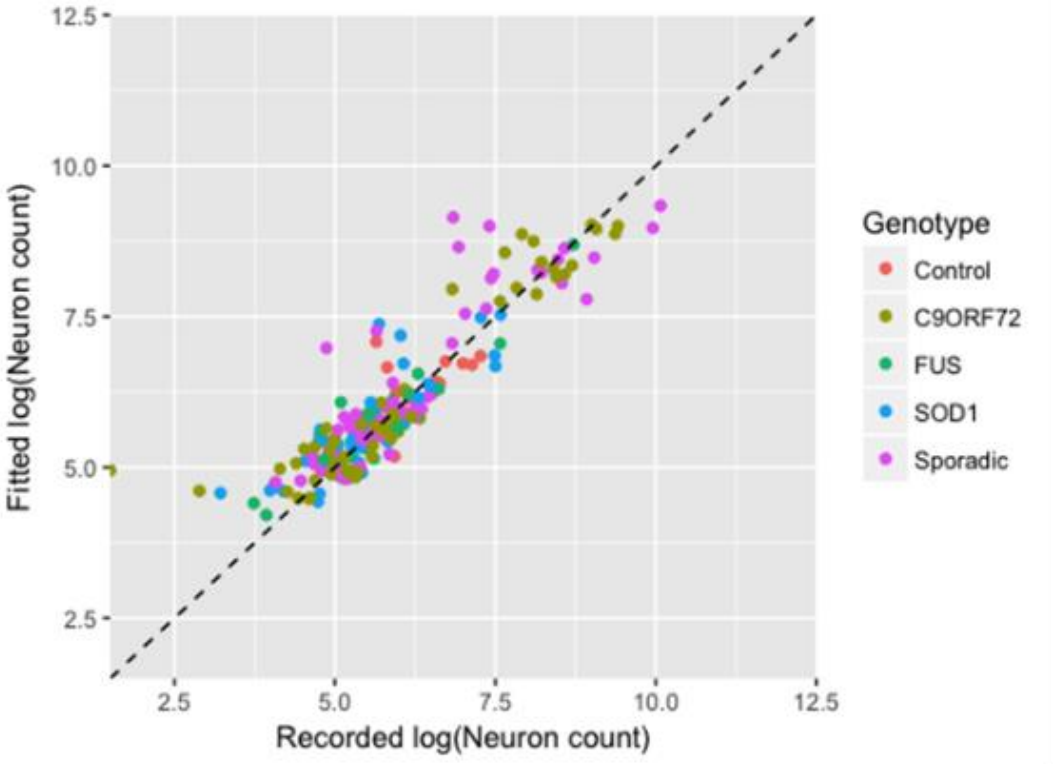

Figure 13: Plot of fitted count against recorded count. A generalized linear model was used to assess interneuron counts against controls, with and without predominance and fixation as covariates. A plot of log(Count) obtained from the fitted negative-binomial GLM versus values of recorded log(Count) shows that the overall model fit is good and therefore appropriate.

3.3 Results

3.3.1 ALS pathology in the primary motor cortex is highly variable both within and across the spectrum of ALS genotypes

To assess the relative extent of pathology within the primary motor cortex across ALS genotypes, we performed immunohistochemical staining on our cohort using antibodies for the common pathological markers pTDP-43, p62 and CD68, which was then quantified using digital image analysis (Table 12).

The primary neuropathological observation in ~95% ALS cases is the cytoplasmic mislocalization and aggregation of hyper-phosphorylated TDP-43 (pTDP-43) within neurons and glia [133]. In our cohort, pTDP-43 staining was present mainly within layers II-VI, but many cases showed inclusions within the subcortical white matter. Morphology of staining was varied, with both neuronal and glial staining present across cases (Fig 14). No pTDP-43 staining was detected in any of the *SOD1*, *FUS* or control cases. pTDP-43 staining was highest in the *OPTN* case (n = 1, 40,668 pp/ROI). Interestingly, this case also negatively stained for OPTN protein (which is highly expressed in controls, Fig 16A, D), concomitant with the knock-out effect of the mutation resulting from the termination of the protein through a premature stop codon. Among suitably powered genotypes, pTDP-43 staining was highest in sporadic cases (n = 18, μ = 14662 pp/ROI, CI = [9088, 23655]), followed by *C9ORF72* cases (n = 16, μ = 7143 pp/ROI, CI = [4300, 11863]). A formal goodness-of-fit test of a negative-binomial GLM fit for pTDP-43 staining was satisfactory ($\chi^2(32) = 39.577$, $p = .167$). Interestingly, pTDP-43 staining was moderately but significantly higher in sporadic cases than *C9ORF72* disease (p = .043) (Fig 14G).

Microglia are the innate immune cells of the central nervous system, and robustly express the transmembrane glycoprotein CD68 in response to inflammatory injury as part of an 'activated' phenotype, a process which is commonly implicated in the pathogenesis of ALS (for review, see: [178]. CD68 staining was therefore performed to assess the relative levels of microglial activation in both the grey and white matter within the primary motor cortex across our cohort (Fig 17C and E). The extent of CD68 staining between the subcortical white matter and grey matter correlated in all genotypes (Fig 18). Within the grey matter, CD68 was highest in sporadic cases (n = 19, μ = 707.7 pc/ROI, CI = [477, 1048]), and lowest in *SOD1* cases (n = 11, μ = 123.6 pc/ROI, CI = [73, 206]). The differences in grey matter CD68 staining were significant between genotypes (Fig 14I). Staining was higher in sporadic cases than *C9ORF72* (p = .037) and *SOD1* cases (p = < .0001). White matter staining was highest within the *OPTN* case (n = 1, 1954 pc/ROI). Among other genotypes, white matter CD68 staining was highest in sporadic cases (n = 19, μ = 1613 pc/ROI, CI = [1089, 2390]), followed by *C9ORF72* cases (n = 16, μ = 1353 pc/ROI, CI = [882, 2076]). There was a significant difference in white matter CD68 staining between genotypes. Staining was significantly higher in sporadic cases than *SOD1* (p = <.0001) and *FUS* cases (p = .0006). White matter staining was also significantly higher in *C9ORF72* cases than *SOD1* cases (p = .0001) (Fig 14I). Finally, CD68 staining in both the white and grey matter correlated with levels of pTDP-43 in both sporadic and *C9ORF72* cases (Fig 17K and L).

Grey matter p62 staining was quantified using a positive-pixel count image analysis algorithm. p62 was highest in the *OPTN* case (n = 1, 3514 pp/ROI). Among other genotypes, p62 was highest in *C9ORF72* cases (n = 16, μ =1020 pp, CI = [649, 1604]), and lowest in *HNRNPA1* (n = 1, 142 pp/ROI)(Fig 14H). There was a significant difference in p62 staining between genotypes, and was significantly higher in sporadic than *FUS* (p

= .0004) and *SOD1* (p = < .0001) cases but not *C9ORF72* disease (p = .92). p62 staining was correlated with pTDP-43 in sporadic cases [Pearson $r(16) = 0.61$, $p = .006$], and less strongly in *C9ORF72* cases [Pearson $r(14) = 0.53$, $p = .03$](Fig 15), reflecting the existence of p62-positive dipeptide repeat proteins in C9-ALS.

The single ALS-*OPTN* case was unusual in both its pathological severity and apparent absence of *OPTN* protein expression (Fig 16A&D), and is analysed in more detail later in chapter 4. ALS-*FUS* and ALS-*SOD1* cases were also stained for their respective proteinopathies (Fig 16), but quantification of these was not possible due to the heterogeneity of pathology, lack of available disease specific FUS antibodies, and significant astrocytic staining when using the SEDI-SOD1 antibody. Our results broadly highlight the significant variability of pathology within the ALS primary motor cortex across the spectrum of ALS genotypes.

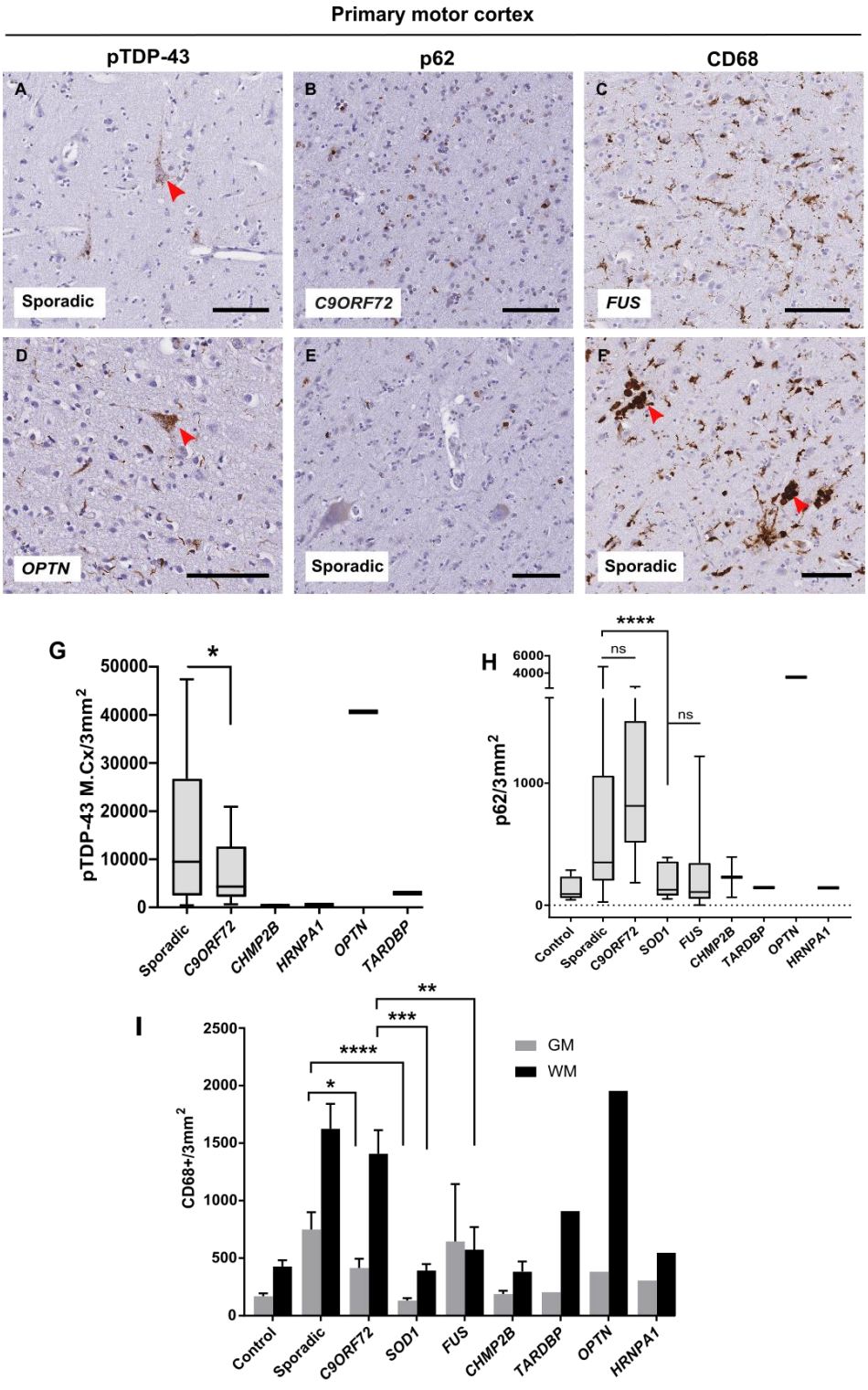

Figure 14: Pathology of the primary motor cortex is highly variable in ALS, both within and across the genotypic spectrum of disease. Other than in a single OPTN case, (D), the average highest pTDP-43 deposition was seen in sporadic cases (A,G) and was statistically higher than in C9-ALS (G). Quantification of p62 (B, E, H) reveals p62 aggregations are most severe in C9-ALS, probably reflective of the additional p62-positive dipeptide repeat proteins unique to the genotype. Microglial activation (C,F) was highly variable between genotypes (I), and was most severe in the TDP-43 genotypes.

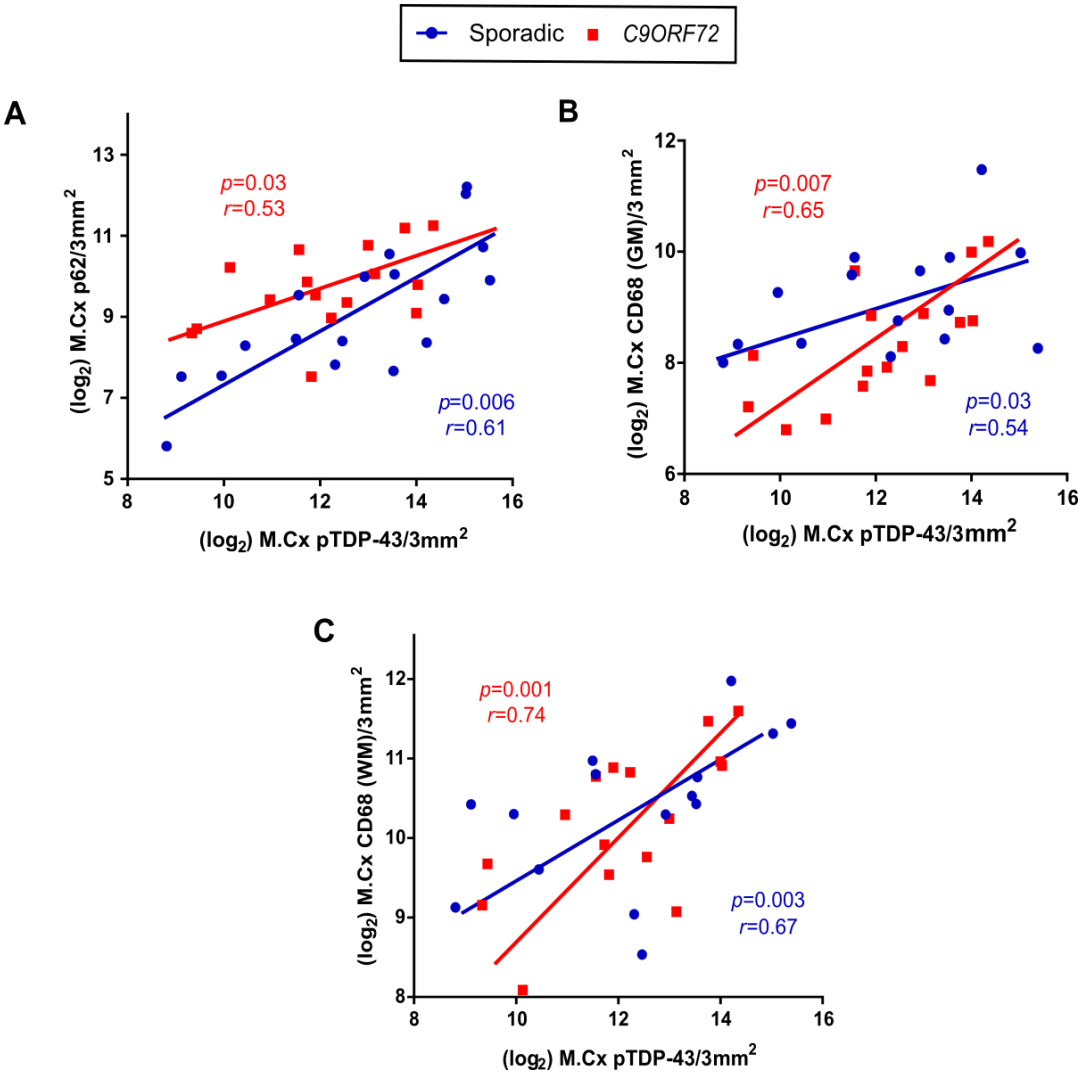

Figure 15: The extent of microglial activation correlates closely with the severity of TDP-43 proteinopathy. pTDP-43 levels correlate with p62 in sporadic ALS, suggesting that all pTDP inclusions are also p62 positive (A). CD68 correlated with the extent of pTDP-43 deposition in both the white and grey matter (B,C) of both sporadic and *C9ORF72* cases [Pearson r correlations, results as on figure] suggesting that pTDP-43 aggregation is a driver of microglial activation in the ALS primary motor cortex. All scale bars = 50µm. Best-fit lines are manually added for illustrative purposes to visually indicate the angle of the slope.

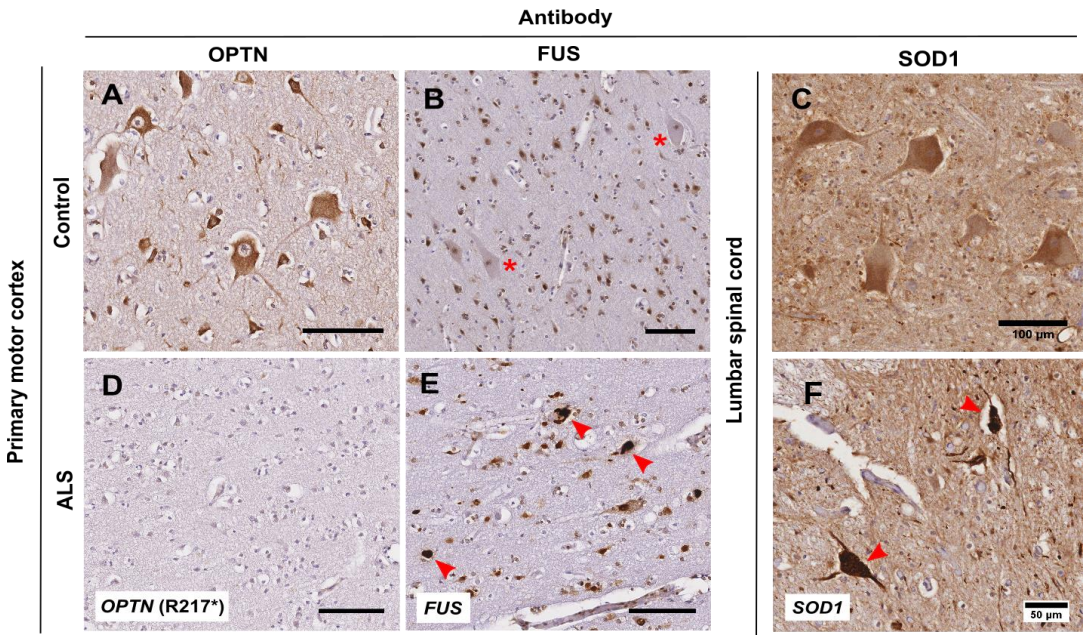

Figure 16: Supplementary pathology in the primary motor cortex of the cohort. OPTN protein is highly expressed in controls including within Betz cells (A), but not in the primary motor cortex of the OPTN mutation case (D) concomitant with the location of the mutation (Fig 36A) and its truncation effect upstream of the antibody binding site. Betz cell nuclei stain positive for FUS (B, starred). Cytoplasmic FUS inclusions in the ALS-FUS primary motor cortex (E)(arrowed). SOD1 is highly expressed in the CNS, including within the lumbar spinal cord anterior horn (C). Aggregated SOD1 is present in the large anterior horn motor neurons in SOD1-ALS (F, arrowed).

		Primary motor cortex				Anterior horn			Corticospinal tract
		Positive pixel count/3,000,000µm²		Positive cell count/3,000,000µm²		Neuron size (µm²)	Positive pixel count/positive cell count per 2,250,000µm²		Positive cell count/1,175,000µm²
Genotype	**Stat**	**pTDP-43**	**p62**	**CD68 (GM)**	**CD68 (WM)**		**pTDP-43**	**CD68**	**CD68**
	Mean	-	139.0	164.3	399.4	2163.0	-	271.2	140.3
Control	95% CI	-	76.0-254.0	93.2-289.6	226.6-703.8	1429.0-2897.0	-	174.3-421.9	90.1-218.3
	Mean	14662.3	989.3	707.7	1613.6	763.9	11626.9	1104.5	993.6
Sporadic	95% CI	9088.2-23655.1	653.4-1497.9	477.6-1048.5	1089.1-2390.7	495.5-1032	7612.5-17758.19	850.5-1434.3	765.1-1290.4
	Mean	7143.1	1020.8	389.3	1353.8	794.9	10068.0	1228.3	1179.0
C9ORF72	95% CI	4300.9-11863.4	649.6-1604.1	253.8-597.2	882.6-2076.5	494.4-1095	6346.1-15972.9	917.1-1645.0	880.3-1579.0
	Mean	-	186.1	123.6	366.0	469.5	-	987.3	837.7
SOD1	95% CI	-	107.8-321.0	73.9-206.8	219.0-611.9	258.1-681.0	-	694.1-1404.4	588.9-1191.6
	Mean	-	264.1	471.0	490.0	404.4	-	1489.1	782.0
FUS	95% CI	-	144.5-482.7	267.3-829.9	278.1-863.4	190.9-618.0	-	1008.7-2198.3	529.7-1154.5
	Mean	259.5	229.0	188.5	382.5	217.5	5673.0	1251.0	679.0
CHMP2B	95% CI	-	-	-	-	71.38-363.6	-	-	-
	Mean	2970.0	144.0	205.0	910.0	853.0	7779.0	881.5	649.0
TARDBP	95% CI	-	-	-	-	-	-	-	-
	Mean	463.0	142.0	305.0	547.0	325.0	10975.0	2149.0	1189.0
HNRNPA1	95% CI	-	-	-	-	-	-	-	-
	Mean	40668.0	3514.0	383.0	1954.0	1363.0	1649.0	28.5	85.0
OPTN	95% CI	-	-	-	-	-	-	-	-

Table 12: Primary motor cortex IHC results. CI = Confidence interval, GM = Grey matter, WM = White matter.

3.3.2 Sporadic ALS exhibits broad pathological homogeneity across the cortico-spinal neuraxis

As ALS patients commonly present clinically with a combination of upper and lower motor neuron signs and concomitant pathology, we performed additional immunohistochemical staining on sections from the lumbar spinal cord region of each case in order to assess relative upper/lower pathological predominance in our cohort. pTDP-43 within the anterior horn region was highest in sporadic cases (n = 19, μ = 11626 pp/ROI, CI = [7612, 17758]), and lowest in the *OPTN* case (n = 1, 1649 pp/ROI). There was no significant difference in spinal cord pTDP-43 deposition between sporadic and *C9ORF72* cases (p = .65)(Fig 17B). The lateral corticospinal tract is composed of white matter axons that descend from the cortex and decussate at the level of the medullary pyramids, synapsing with lower motor neurons in the contralateral spinal cord. CD68 staining within the corticospinal tract was highest in *C9ORF72* cases (n = 19, μ = 2552 pp/ROI, CI = [1643, 3963]), however similar to within the motor cortex, there was no significant difference between sporadic and *C9ORF72* cases (p = .91)(Fig 17F)(Table 10).

Staining from the lumbar spinal cord from each case was next compared to its equivalent stain within the primary motor cortex. pTDP-43 staining in the anterior horn correlated with pTDP-43 staining in the primary motor cortex in sporadic cases [Pearson $r(17)$= 0.62, p = .0044], but not C9-ALS [Pearson $r(14)$= -0.03, p = .89](Fig 19). CD68 staining within the lateral corticospinal tract correlated with CD68 staining in the primary motor cortex in sporadic [Pearson $r(17)$= 0.63, p = .0037] and *FUS* cases [Pearson $r(7)$= 0.89, p = .0013], but not other genotypes (Fig 19B). Note that, with 3 out of 4 correlations being highly significant, simultaneous inference corrections do not modify the conclusions.

We next sought to assess the relative predominance of upper/lower motor neuron involvement in our cases by comparing the extent of pathology in the primary motor cortex to the anterior horn using CD68 as a surrogate marker of neurodegeneration. The extent of CD68 staining between motor cortex and spinal cord was expressed as a ratio and used as a covariate in subsequent analyses, where smaller ratios represent a tendency towards a higher burden of CD68 in the anterior horn (Fig 19C). Ratios were calculated as:

$$\frac{M.Cx\ grey\ matter\ CD68/1{,}000{,}000\mu m^2{}_{(\log)}}{Anterior\ horn\ CD68/1{,}000{,}000\mu m^2{}_{(\log)}}$$

Many *FUS* and *SOD1* cases exhibited very little cortical CD68, but significant staining within the anterior horn (Fig 19G). 80% of all non-TDP-43 proteinopathies assessed fell below the calculated median predominance ratio of our cohort (Fig 19C).

Together, our results show that while sporadic ALS cases exhibit the most severe cortical pathology on average, they also exhibit a large degree of inter-case variance and also the highest pathological homogeneity across the cortico-spinal neuraxis. Additionally, we show that non-TDP-43 proteinopathies are more likely to display significant lower motor neuron predominance than TDP-43 proteinopathies, broadly corresponding to clinical phenotypes commonly seen for these cases.

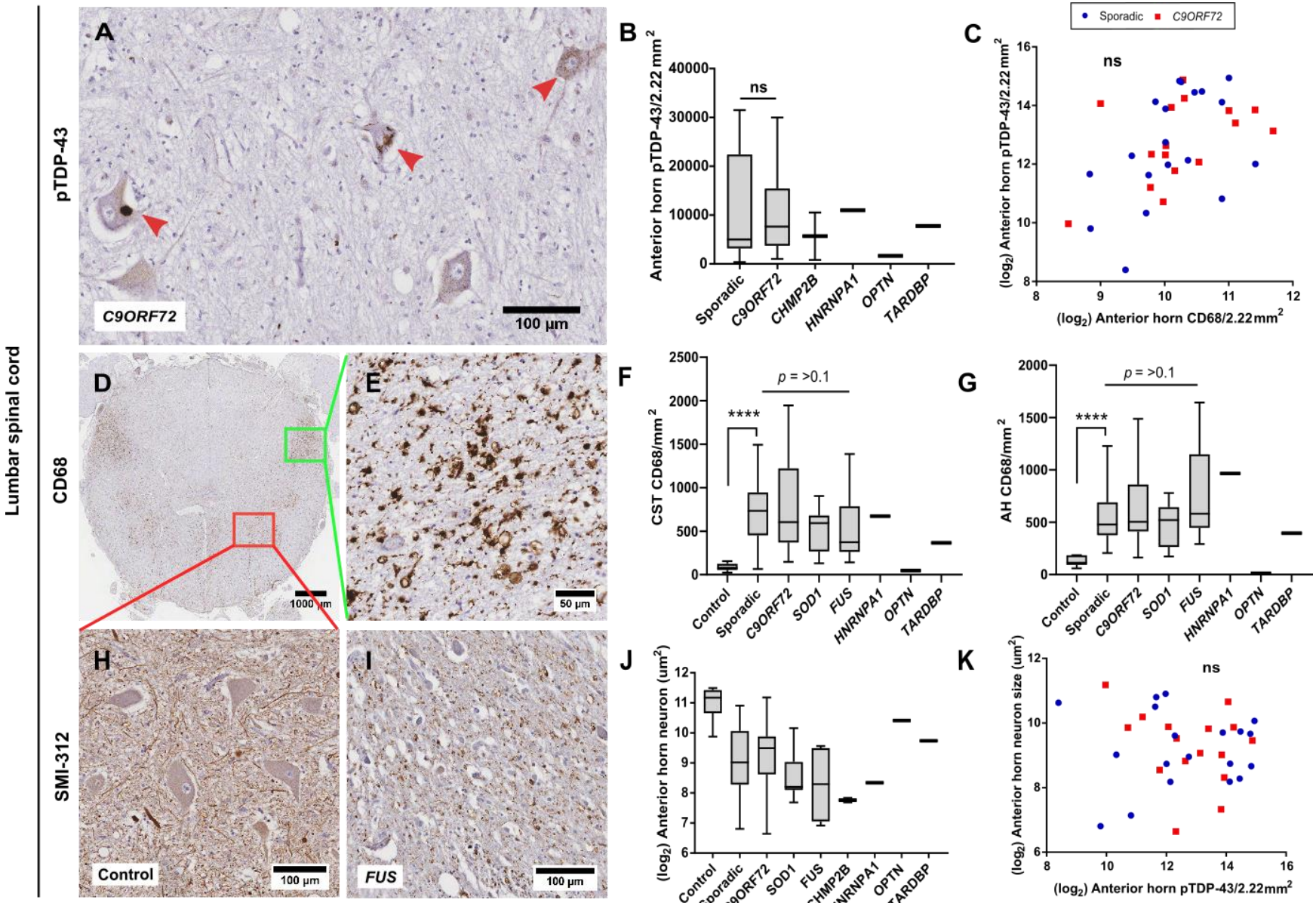
Lumbar spinal cord
pTDP-43
CD68
SMI-312
A
C9ORF72
100 µm
B
Anterior horn pTDP-43/2.22 mm2
ns
Sporadic
C9ORF72
CHMP2B
HNRNPA1
OPTN
TARDBP
C
Sporadic
C9ORF72
ns
(log2) Anterior horn pTDP-43/2.22 mm2
(log2) Anterior horn CD68/2.22mm2
D
1000 µm
E
50 µm
F
CST CD68/mm2
p = >0.1
****
Control
Sporadic
C9ORF72
SOD1
FUS
HNRNPA1
OPTN
TARDBP
G
AH CD68/mm2
p = >0.1
****
H
Control
100 µm
I
FUS
100 µm
J
(log2) Anterior horn neuron (um2)
Control
Sporadic
C9ORF72
SOD1
FUS
CHMP2B
HNRNPA1
OPTN
TARDBP
K
ns
(log2) Anterior horn neuron size (um2)
(log2) Anterior horn pTDP-43/2.22mm2

Figure 17 (previous page): Assessment of ALS pathology in the anterior column and the corticospinal tract. The morphology of pTDP-43 pathology was varied in anterior horn lower motor neurons, with large discrete inclusions and diffuse punctate staining present (A, red arrows). Mean highest pTDP-43 in anterior horn neurons was in sporadic cases (B), mirroring the finding in the motor cortex. pTDP-43 aggregation in the spinal cord did not correlate with numbers of activated microglia in the anterior horn (C). CD68 was quantified both within the anterior horn (D, red box) and corticospinal tract (D, green box and E), with the severity of both varying across genotypes (F,G). CD68 in both the anterior horn and corticospinal tract was significantly higher in all ALS genotypes than controls ($p = < .0001$), but there was no difference in either between ALS genotypes ($p = > 0.1$). Anterior horn degeneration and shrinkage was most prominent in FUS and SOD1 cases (H-J). pTDP-43 aggregation in the anterior horn did not correlate with neuron shrinkage/loss (K). (Red squares and blue dots represent *C9ORF72* and sporadic cases respectively in C and K).

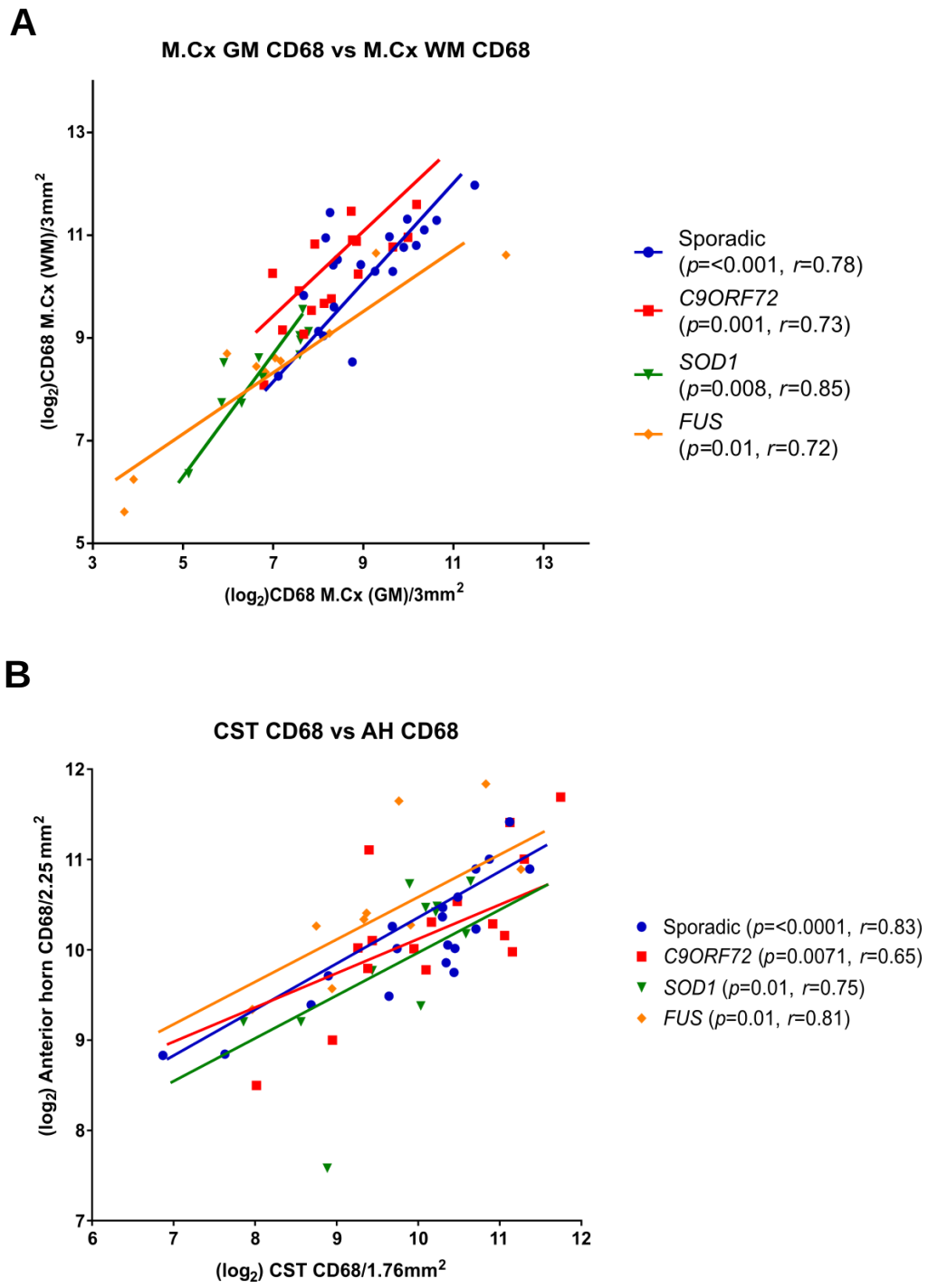

Figure 18: Microglial activation as measured by CD68 correlates across the white and grey matter in both the primary motor cortex (A) and spinal cord (B) across all genotypes. Best-fit lines are added manually for illustrative purposes to visually indicate the angle of the slope more clearly.

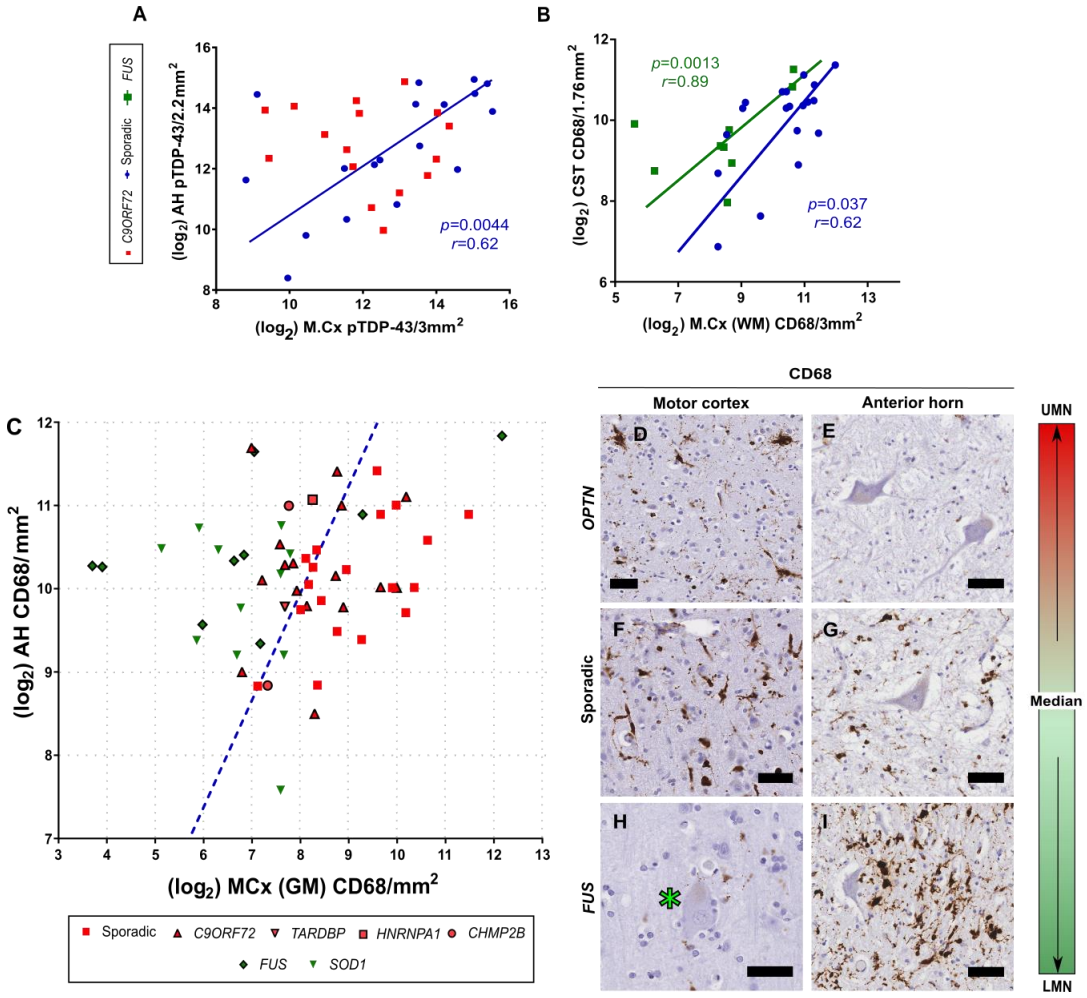

Figure 19: Sporadic ALS displays broad pathological homogeneity across the motor cortex-spinal cord neuraxis. pTDP-43 in the motor cortex correlated with pTDP-43 in the anterior horn in sporadic disease [Pearson r(17)=0.62, p = .0044] but not C9-ALS [Pearson r(14)=0.001, p =.89] (A) and CD68 correlates between the corticospinal white matter tract and the subcortical white matter in both FUS and sporadic cases (B). CD68 in the lower anterior horn neuron was plotted against grey matter CD68 in the motor cortex (C). This was used to create a predominance ratio for each case that could be used as a covariate in subsequent models, where a lower ratio represents a tendency towards a burden of CD68 in the anterior horn. The dotted blue line in (C) represents the approximate median ratio of our cohort. Therefore, the further each case is from this line, the more extreme the relative UMN/LMN burden of CD68 the case exhibits. Cases are coloured according to whether they are TDP-proteinopathies (red) or not (green), showing that non-TDP-proteinopathies are more likely to exhibit a LMN neuropathological predominance when assessed via levels of activated microglia. Representative images of this variation across the neuraxis between genotypes, with OPTN and FUS mutations representing upper and lower motor neuron spectral extremes, respectively (D-I). Green-red UMN/LMN bar pictured to visualise predominance according to each genotype in D-I.

3.3.3 Calbindin+ and Parvalbumin+, but not Calretinin+ interneurons, are reduced in the ALS primary motor cortex

Calcium-binding proteins (CBP) protect neurons from excitotoxicity via increased intracellular calcium by regulating $Ca2^{+}$ concentration within the cytosol. CBP are highly expressed in subpopulations of GABAergic inhibitory interneurons, whose degeneration has previously been implicated in several diseases [185-187], including ALS [188]. A cortical hyperexcitability phenotype has been described in ALS patients [189], and two neuroimaging studies revealed decreased GABA concentrations and benzodiazepine receptor unit distribution in the primary motor cortex [191, 192]. Additionally, previous studies have suggested loss of inhibitory interneurons as prominent feature of cortical dysfunction in animal models [193, 194]. We therefore sought to assess the significance of interneuron loss in the primary motor cortex of ALS patients using antibodies targeted to three calcium-binding proteins – Calbindin, Calretinin and Parvalbumin (Fig 20, Fig 21, table 13).

The distribution pattern of interneurons in our control cohort was consistent with previous studies [188, 342, 343]. Interneuron analysis was conducted on both unadjusted and adjusted results, with the adjustment being for the covariates fixation and predominance described in the statistical methods. This was to clarify whether any reduction in interneurons was related to a more severe degenerative phenotype overall or a specific loss of interneurons. Calretinin+ interneurons were present in all cortical layers including sparse staining within the subcortical white matter, but were predominantly within layers II-III. We found no significant difference in Calretinin staining between ALS and control cases (Fig 21A-C). Parvalbumin+ interneurons were predominantly located in layers II-IV. We found a small reduction in Parvalbumin+ interneurons in *FUS* cases against

controls (p = .026), which was present even after adjustment for fixation and predominance (Fig 21D-F). Calbindin+ interneurons were mainly present in layers II/III, with smaller populations within the deeper layers and the subcortical white matter. We found a small reduction in Calbindin+ interneurons between controls, *C9ORF72* (p = .039) and *SOD1* (p = .036) cases after covariate adjustment (Fig 21G-I). However, we found no correlation between interneuron number and extent of pTDP-43 deposition in sporadic or *C9ORF72* cases (Fig 22), suggesting that the toxic effects of TDP-43 pathology alone is not responsible for the selective degeneration of the interneuron populations tested. These results demonstrate a moderate, genotype-specific reduction in the numbers of inhibitory interneurons within the ALS primary motor cortex, which may contribute to the existence of the cortical hyperexcitability phenotype in ALS patients.

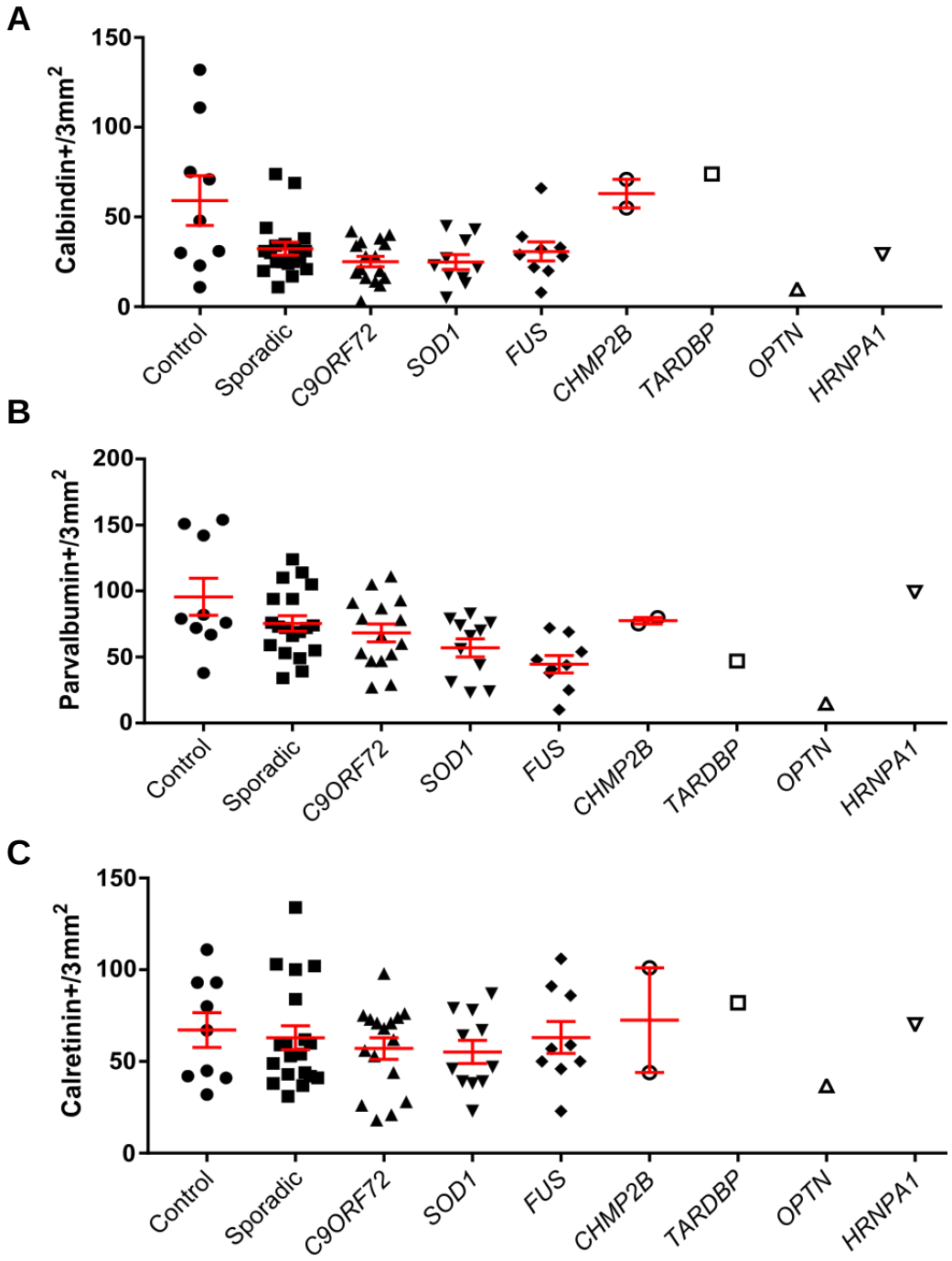

Figure 20: Raw interneuron counts within the primary motor cortex across the genotypic spectrum of disease. Calbindin+ (A) and Parvalbumin+ (B), but not Calretinin+ (C) interneurons degenerate in the ALS primary motor cortex. Red bars indicate means and 95% confidence intervals.

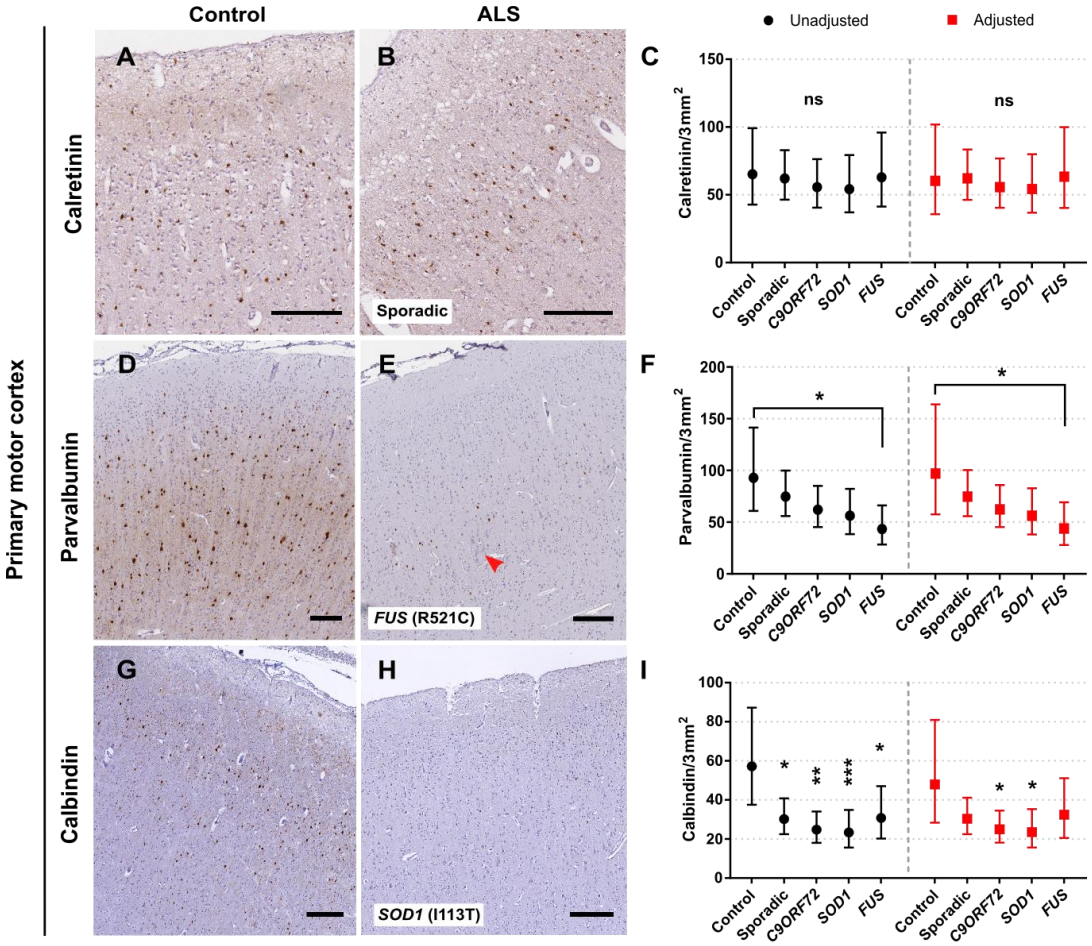

Figure 21: Parvalbumin and Calbindin positive, but not Calretinin positive interneurons degenerate in the ALS primary motor cortex. Data on graphs represent means and confidence intervals. Immunohistochemical staining for three calcium-binding proteins reveals a modest reduction of interneuron number, and that this reduction is genotype-dependent. We found no evidence of Calretinin+ interneuron loss in the ALS primary motor cortex (p = >.05) (A-C). Parvalbumin+ interneurons were reduced in several of the genotypes tested, but only ALS-FUS cases (unadjusted p = .013, adjusted p = .026) showed a statistically significant difference against controls (D-F, red arrow indicates Betz cells). Calbindin+ interneurons were reduced in all the genotypes tested that were suitably powered, however after adjustment for fixation and predominance this was only maintained in C9ORF72 (adjusted p = .039) and SOD1 cases (adjusted p = .036). All scale bars = 100µm.

Primary Motor Cortex									
		Calbindin							
		Unadjusted				Adjusted			
Genotype	*n*=	Mean	CI	Contrast	*p*-value	Mean	CI	Contrast	*p*-value
Control	9	57.21	37.54-87.17	-	-	47.93	28.36-80.99	-	-
Sporadic	19	30.24	22.44-40.76	0.5287	0.0164	30.37	22.42-41.13	0.6337	0.1377
C9ORF72	16	24.78	18.04-34.04	0.4332	0.0024	24.99	18.10-34.51	0.5215	0.0390
SOD1	11	23.36	15.64-34.87	0.4083	0.0031	23.50	15.64-35.32	0.4905	0.0363
FUS	9	30.82	20.20-47.02	0.5387	0.0424	32.44	20.57-51.15	0.6769	0.2660

		Parvalbumin							
		Unadjusted				Adjusted			
Genotype	*n*=	Mean	CI	Contrast	*p*-value	Mean	CI	Contrast	*p*-value
Control	9	92.85	60.97-141.40	-	-	97.11	57.53-163.91	-	-
Sporadic	19	74.76	55.96-99.88	0.8052	0.3993	74.77	55.70-100.36	0.7700	0.3876
C9ORF72	16	62.09	45.27-85.14	0.6686	0.1310	62.36	45.24-85.96	0.6424	0.1547
SOD1	11	56.24	38.42-82.33	0.6057	0.0823	56.19	38.15-82.77	0.5787	0.0984
FUS	9	43.41	28.48-66.19	0.4676	0.0132	43.96	27.90-69.25	0.4527	0.0260

		Calretinin							
		Unadjusted				Adjusted			
Genotype	*n*=	Mean	CI	Contrast	*p*-value	Mean	CI	Contrast	*p*-value
Control	9	65.12	42.75-99.21	-	-	60.31	35.70-101.87	-	-
Sporadic	19	62.05	46.44-82.91	0.9529	0.8509	62.14	46.29-83.43	1.0305	0.9210
C9ORF72	16	55.63	40.56-76.30	0.8543	0.5515	55.72	40.42-76.82	0.9239	0.7977
SOD1	11	54.20	37.03-79.34	0.8324	0.5204	54.31	36.87-79.99	0.9004	0.7487
FUS	9	62.98	41.34-95.96	0.9672	0.9110	63.44	40.29-99.89	1.0519	0.8844

Table 13: Calcium binding protein analysis, including adjusted and unadjusted values. Contrast for each genotype is against control cases.

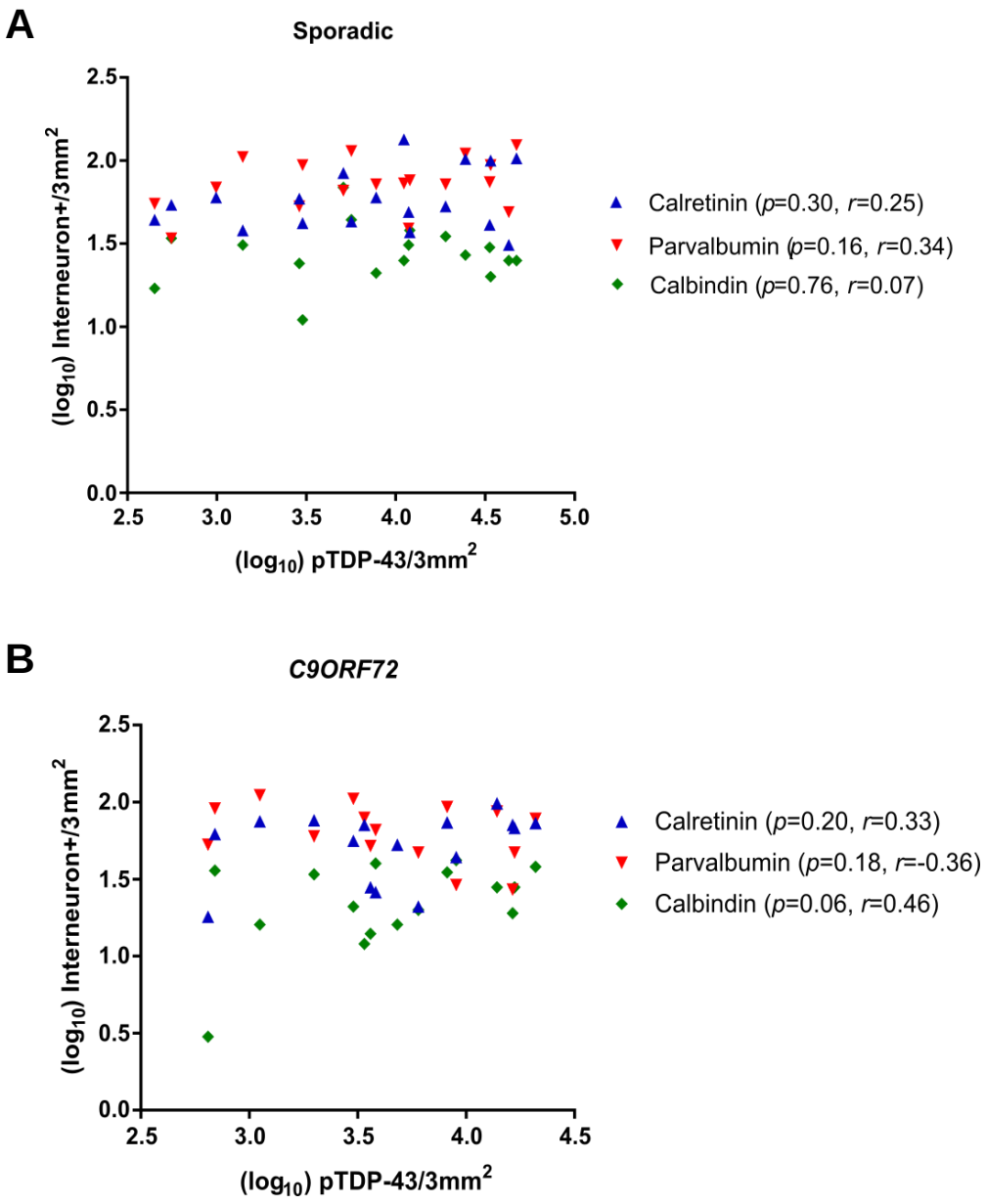

Figure 22: Interneuron numbers do not correlate with the severity of pTDP-43 deposition in the sporadic (A) or C9-ALS (B) primary motor cortex.

3.3.4 Cortical oligodendrocyte pTDP-43 pathology is a defining feature of ALS-TDP

The main role of oligodendroglia is the support of neurons via the production of insulating myelin. As pTDP-43 accumulation is present within oligodendrocytes and their dysfunction has been implicated in pathogenesis of ALS [204], we sought to assess the numbers of oligodendrocytes within the primary motor cortex as well as the relative abundance of oligodendrocytes containing pTDP-43 inclusions in a small subset of our cohort.

Olig2 is a transcription factor highly expressed in immature oligodendrocyte precursor cells (OPC)(Fig 23A) while Tubulin polymerization-promoting protein (TPPP/p25) is highly expressed in mature oligodendrocytes (Fig 23B) [344]. Similar to a previous study in the spinal cord [211], we found no significant difference in mature or immature oligodendrocyte numbers within the ALS motor cortex grey matter (Fig 23C and D). We next assessed the prevalence of oligodendrocyte inclusions across our cohort. We found at least one obvious instance of an oligodendrocyte pTDP-43 inclusion in all ALS-TDP cases assessed (40/40), even in cases that exhibited low levels of pTDP-43 pathology overall. With the exception of layer I, this pathology was found across all grey-matter layers as well as the subcortical white matter, but was particularly evident within oligodendrocytes in the deeper layers V/VI and at the grey-white matter border. We next assessed the relative abundance of oligodendrocyte pTDP-43 pathology in genotypes with the highest mean pTDP-43 deposition (sporadic $n = 10$, *C9ORF72* $n = 10$). Both the mean number of oligodendrocyte inclusions and the ratio of oligo/neuron inclusions was highest in *C9ORF72* cases but neither was significantly higher than in sporadic disease (Fig 23G and H). These results highlight cortical pTDP-43 oligodendrocyte pathology as a defining

feature of ALS, and support the notion that any potential dysfunction caused by their pTDP-43 accumulation contributes to neurodegeneration via non-cell autonomous mechanisms.

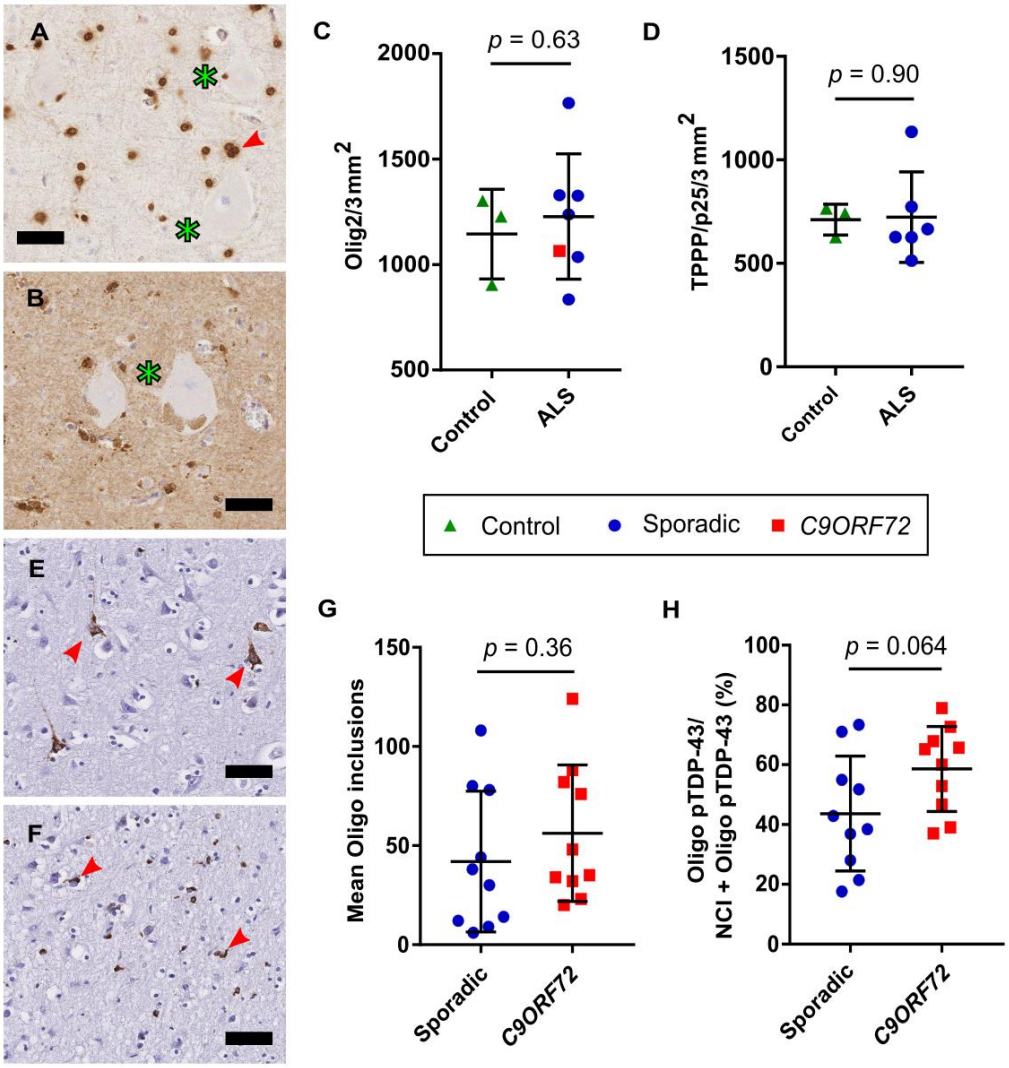

Figure 23: Assessment of cortical oligodendrocyte pathology. Olig2+ OPC (A) and mature TPPP/p25+ oligodendrocytes (B) were present in all layers of the primary motor cortex. Green star in (A) indicates Betz cell, with red arrow indicating and immature oligodendrocyte satellite surrounding its apical dendrite. Green star in (B) indicates Betz cells. However there was no difference in the numbers of mature or immature oligodendrocytes between ALS and control cases (C and D). pTDP-43 inclusions are present in neurons (E) and oligos (F, red arrows indicate characteristic 'cateye' shaped inclusions). Both the mean numbers of oligo inclusions and the relative predominance of pTDP-43 oligo pathology was higher in C9-ALS, but was not statistically higher than in sporadic disease (G and H).

3.3.5 Cell-type specific vulnerability to pathological aggregation

Given our previous results, we next sought to reconcile the presence of ALS pathology to individual cell types within the primary motor cortex using a MxIF method in a subset of our cohort. This method allowed the co-localization of antigens to be visualised without the associated loss of anatomical resolution caused by serial sections.

Microglia phagocytose inclusions/cells that have been suitably marked for destruction as part of the innate immune system. As the extent of microglial activation correlates with pTDP-43 deposition, we first analysed whether pTDP-43 inclusions could be visualised within microglia. Similar to other studies [182], we found several examples (Fig 24A-D) of Iba1+ microglia either actively phagocytosing or containing pTDP-43 in several of the TDP-43 proteinopathy cases analysed, although this was not universally true across all cases. Astrocytes are a diverse glial sub-type whose roles include mediation of potassium ions across the synapse and the provision of neurotrophic support. Cortical astrogliosis is a prominent feature of ALS [345]. However, we were unable to find clear evidence of pTDP-43 within astrocytes (Fig 25), even in cases with extensive pTDP-43 deposition. We were also unable to find significant evidence of pTDP-43 inclusions within HuC/D-parvalbumin+ interneurons (Fig 26).

Similar to a previous study [203], we were unable to find significant evidence of pTDP-43 accumulation within Betz cells (Fig 27A-C). However, we did find evidence in several cases of severe microgliosis surrounding large pyramidal neurons in layer V (Fig 27D), suggesting that processes within these large neurons may induce a selective vulnerability to the microglial response. Together, these results suggest a clear cell-type specific vulnerability to pathological aggregation within the ALS primary motor cortex.

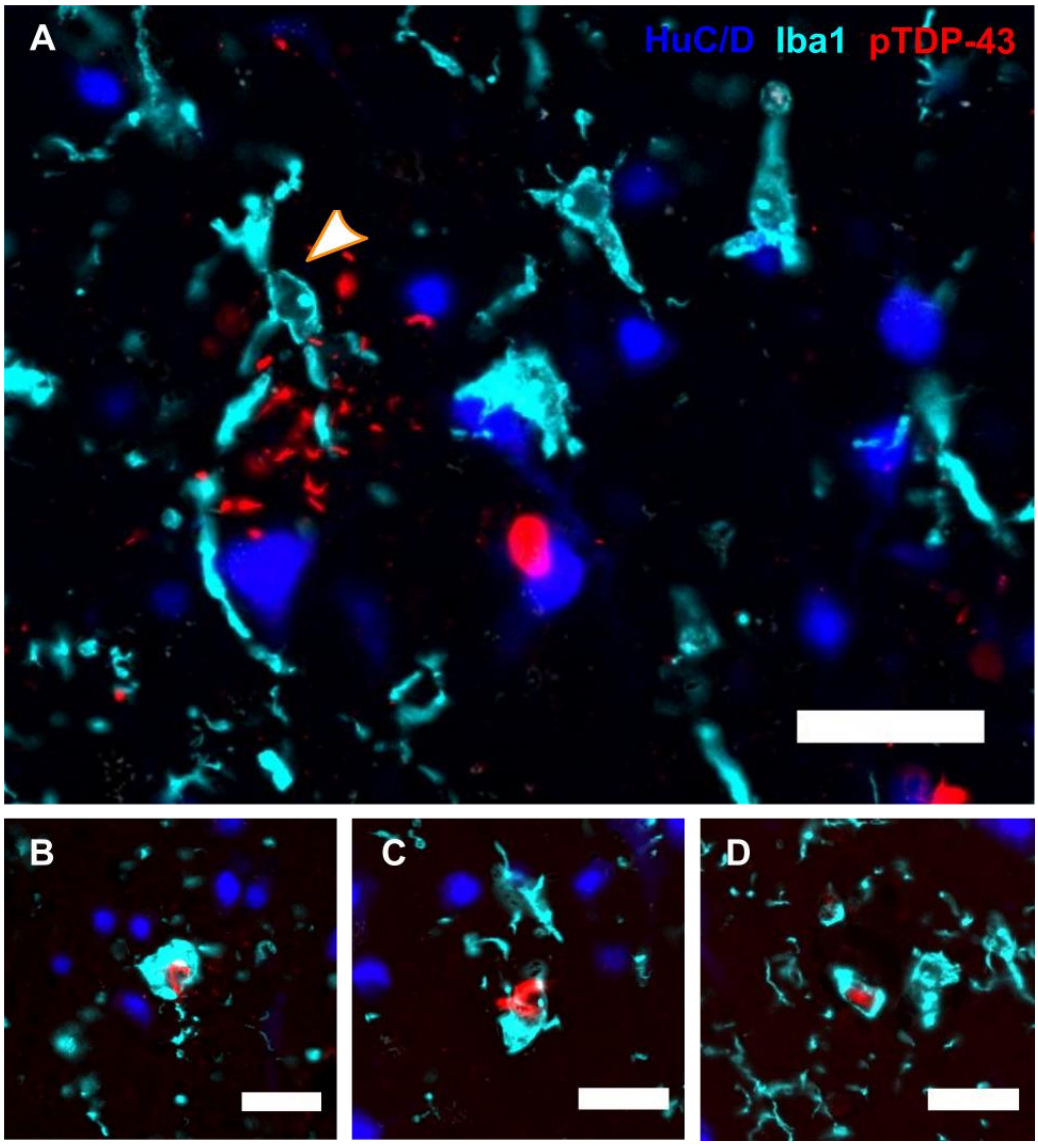

Figure 24: pTDP-43 inclusions are found within Iba1+ microglia. Mx-IF allows the staining and identification of multiple antigens on a single slide, without the concomitant loss of anatomical resolution caused by serial sections. We found several examples of pTDP-43 aggregates within Iba1+ microglia (A-D), however it is unknown whether the microglia phagocytosed the aggregates, or they arose within the microglia themselves. We also found examples of elongated microglial processes reaching the apical dendrites of neurons containing smaller pTDP-43 aggregations (A, orange arrow). All scale bars = 50µm.

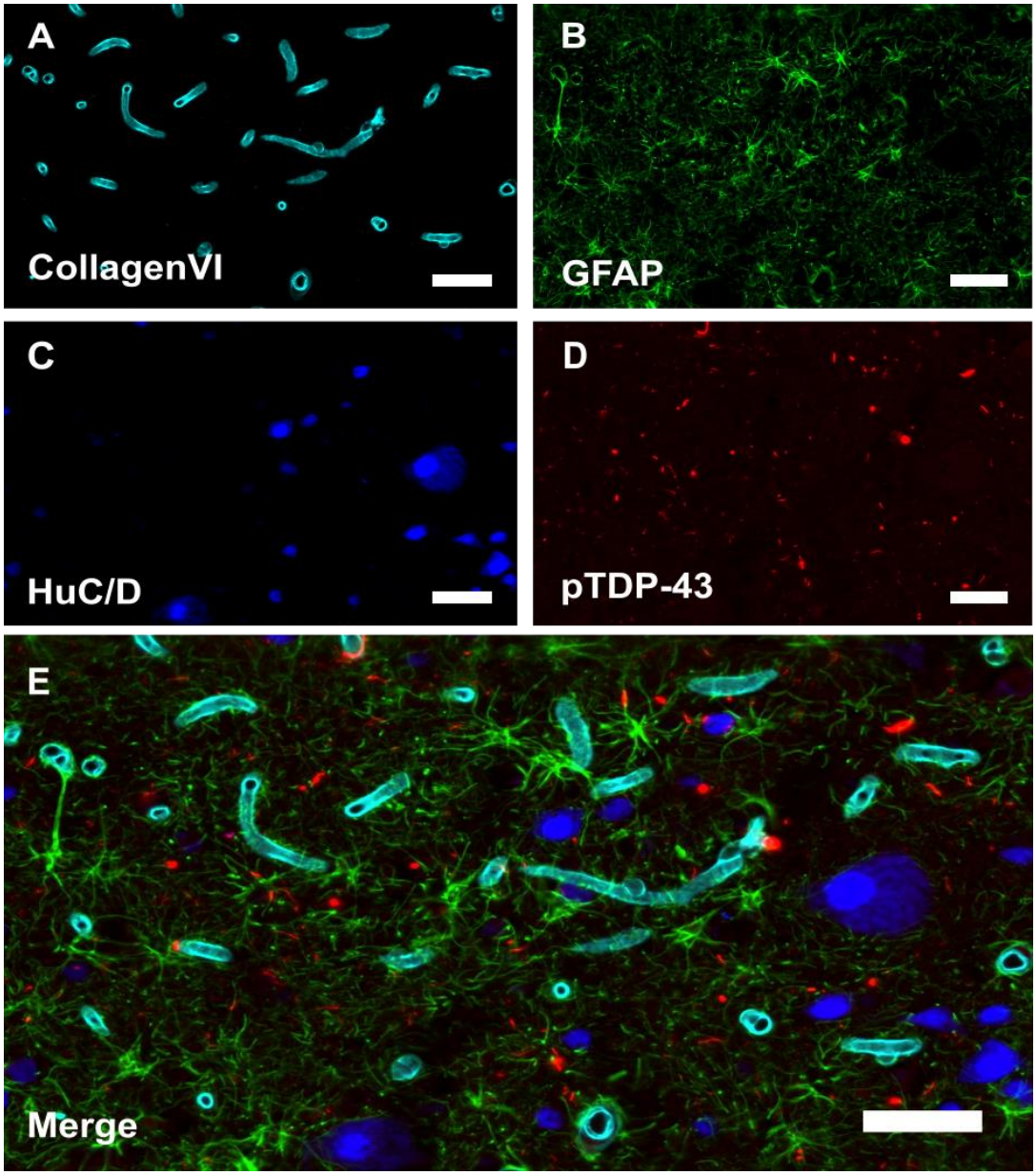

Figure 25: pTDP-43 inclusions are not present within GFAP+ astrocytes. Staining for CollagenIV (A, blood vessels), pTDP-43 (B), GFAP (C, astrocytes) and HuC/D (D, neurons) was simultaneously conducted on a single section using MxIF (E, merge). There was no clear evidence of pTDP-43 within GFAP+ astrocytes, even in cases with extensive pTDP-43 deposition and despite cortical astrogliosis being a prominent neuropathological feature of ALS. Scale bar = 50μm.

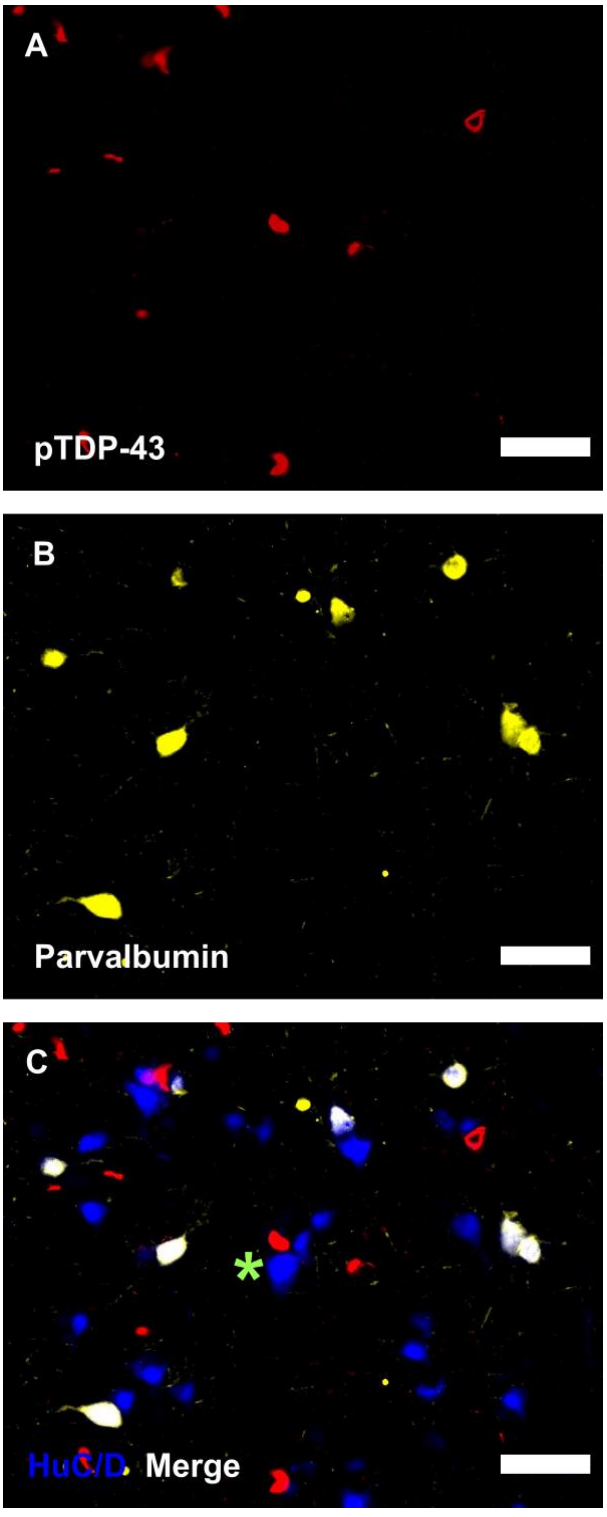

Figure 26: We find no evidence of pTDP-43 inclusions are not present within parvalbumin+ interneurons. Co-localization staining for pTDP-43 (A), parvalbumin (B) and HuC/D (C, merge) revealed no evidence of pTDP-43 inclusions within parvalbumin+ interneurons in the cases assessed. Green star indicates pTDP-43 inclusion within HuC/D+, parvalbumin- neuron. Scale bar = 100µm.

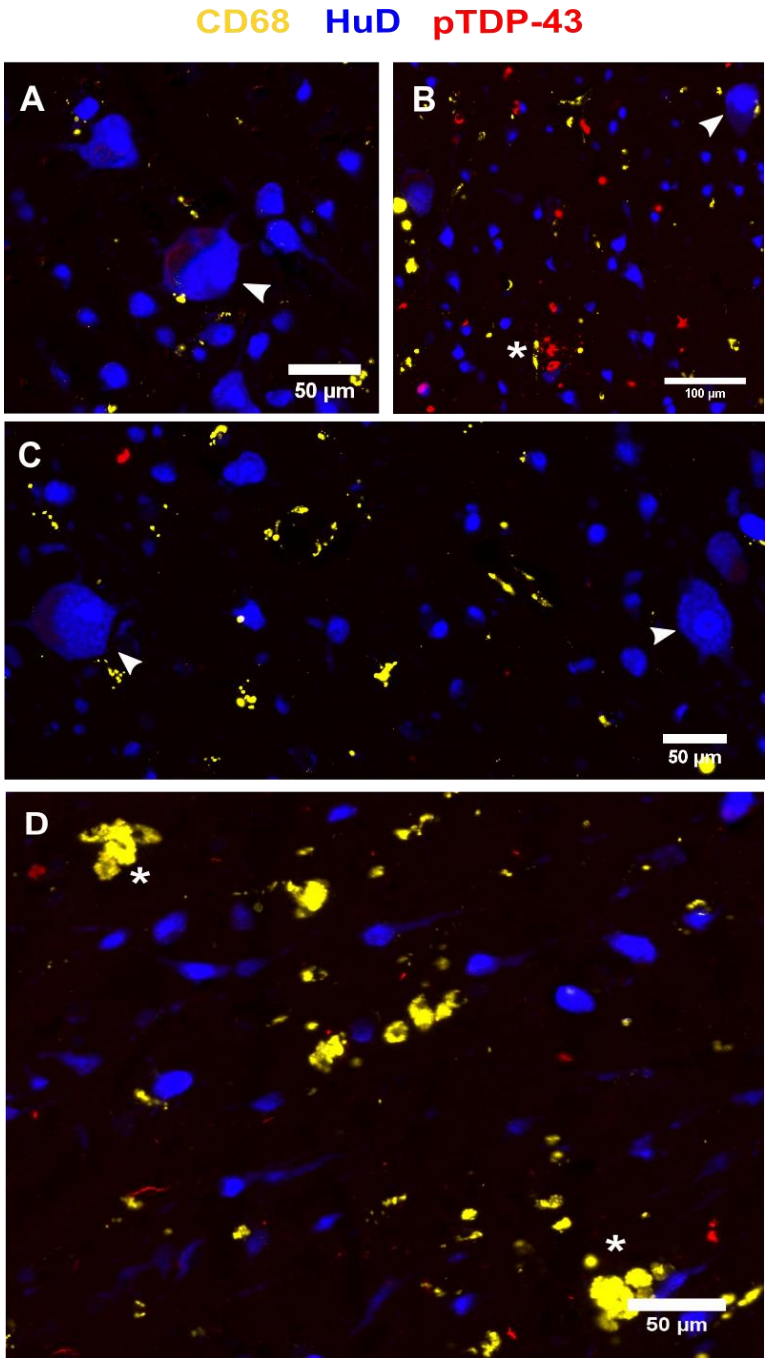

Figure 27: pTDP-43 is rare within large pyramidal cells of Betz. Using MxIF and layering of the digital images, we found almost no evidence of pTDP-43 inclusions within layer Vb Betz cells (A-C, arrows), but did find several examples of severe microgliosis surrounding these cells (D, starred and Fig 14F), suggesting that neuronophagia is occurring in some cases even in the clinical end stage of disease.

3.4 Expression and localisation of *FUS* and *TARDBP* in the human primary motor cortex

Previous studies have identified differing expression levels of genes involved in ALS across the human brain, however these studies were performed using methods such as RT-PCR and RNA-seq, which while highly specific and quantitative, come at the cost of cellular resolution, and offer no contextual information such as the localization of transcripts. The *in situ* cortical expression of two core genes involved in ALS, *FUS* and *TARDBP*, is unknown. We therefore sought to assess the expression of genes involved in ALS in the primary motor cortex using RNAscope and quantitative digital image analysis. Anti-sense probes (Table 6) targeted to *FUS (*Fig 28A*)* and *TARDBP* (Fig 28B) were applied to post-mortem human brain tissue cut at 6µm from the primary motor cortex of a small cohort of short fixed ALS (*n*=7) and control cases (*n*=3) (Table 14). We also sought to begin to assess the RNA-protein interaction between pTDP-43 and its gene, *TARDBP*, by using a dual IHC/ISH approach (Fig 29C&D). The expression and localisation of transcripts was then assessed and quantified using the algorithms described previously (see section 2.3).

We found that *FUS* is significantly more highly expressed than *TARDBP* in the primary motor cortex (Fig 29A&B, Fig 30A&B), but that there was no reduction in the expression of either gene between ALS and control cases (Fig 30). We found several instances of strong *FUS* expression within Betz cells (Fig 29C), but there were also several examples of Betz cells in the same case which expressed only very low levels of *FUS* (Fig 29C, orange star). This suggests a highly dynamic expression of at least one ALS gene within Betz cells. In contrast, *TARDBP* expression was relatively low within the primary motor cortex (Fig 29B) and within Betz cells (Fig 29D). This is perhaps surprising, given that

IHC staining using a pan-TDP-43 antibody reveals nuclear staining within almost every cortical cell [133]. However, expression of an individual gene does not correlate strongly with the expression of its relevant protein [346] particularly in neurons where there is a significant requirement for dynamic translation/repression and subsequently a high degree of polarity. This difference in *FUS* and *TARDBP* expression is notable because both are RNA binding proteins closely involved in ALS pathogenesis, have similar structures and functions, and yet exhibit very different expression and localisation patterns.

We also attempted to assess the interaction of pTDP-43 with *TARDBP* mRNA using a combined ISH/IHC approach. This is warranted because a previous study demonstrated that the aggregation and mislocalisation of TDP-43 in spinal motor neurons increases the numbers of *TARDBP* transcripts localised to the cytosol via disruptions to *TARDBP* autoregulation [157]. However, we were unable to comment on this or draw conclusions more generally due to the limited number of runs and cases (n = 2) involved here. Additionally, the red-ISH and brown-DAB made it difficult to discern individual signals, and the use of fluorescently bound probes and antibodies would facilitate their identification in future studies.

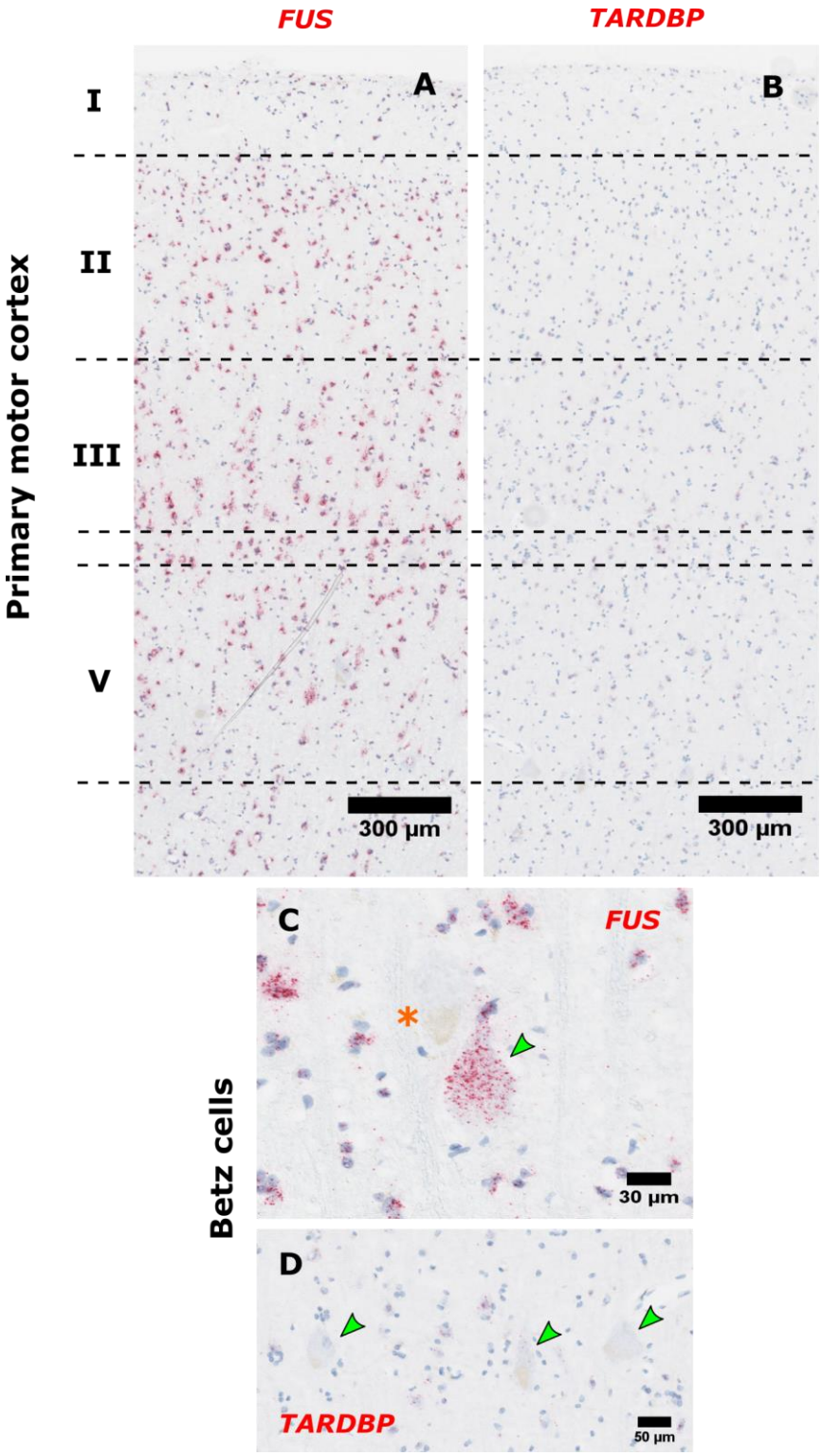

Figure 28: *FUS*, but not *TARDBP*, is highly expressed in the human control primary motor cortex. *FUS* is highly expressed in all cortical layers (A) and in some Betz cells (C). *TARDBP* is expressed at lower levels relative to *FUS* (B and D). There appears to be significant differences in the extent that Betz cells express both *FUS* (C) and *TARDBP* (D). Betz cells are designated with green arrows. Orange asterisk in C denotes Betz cell that is not expressing *FUS*. Betz cells were identified solely by their size, morphology and presence in layer V.

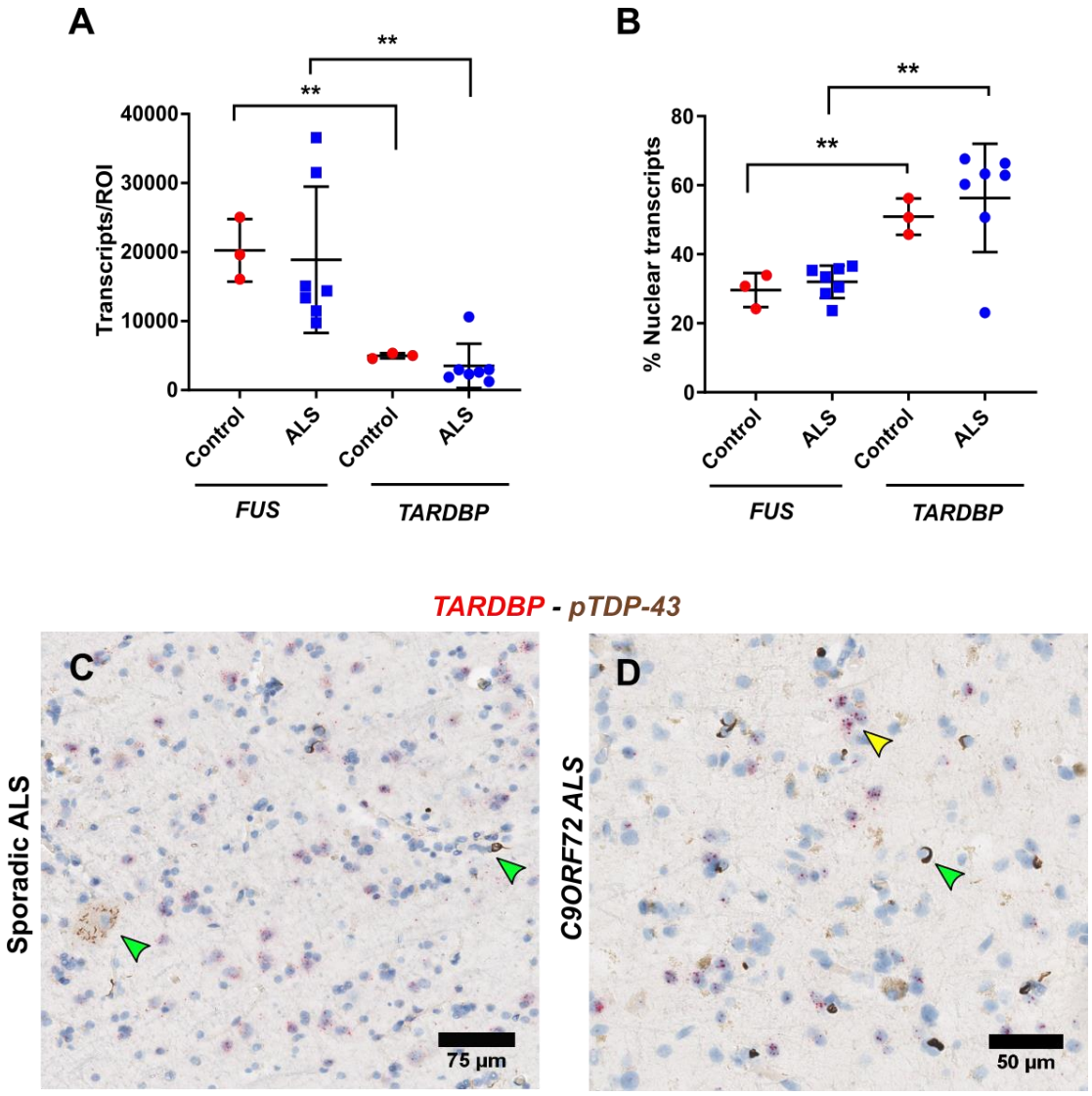

Figure 29: Quantification of *FUS* and *TARDBP* gene expression in the primary motor cortex and dual *TARDBP*-pTDP-43 expression. *FUS* is highly expressed in the primary motor cortex, while *TARDBP* is not. There is no significant difference in expression of *FUS* or *TARDBP* between ALS and control cases (A). However proportionally, significantly more *TARDBP* transcripts are localized to the nucleus than in *FUS* (B). A Betz cell containing pTDP-43 skein pathology can be seen in (C, left green arrow). No obvious co-localization of *TARDBP* probes and pTDP-43 deposition can be seen in either the sporadic (C) or *C9ORF72* case tested (D). Green arrows indicate pTDP-43 pathology, yellow arrow indicates clustering of *TARDBP* transcripts.

	RNA-ISH							DAB-IHC		
	Average transcripts/3mm^2					Nuclear: cytoplasm ratio %		Average positive cells/3mm^2		
Case	***CTIP2***	***SATB2***	***TBR1***	***FUS***	***TARDBP***	***FUS***	***TARDBP***	**CTIP2**	**SATB2**	**TBR1**
Control	4804	20501	14925	16070	4587	24.2	45.7	125.3	729.0	523.0
Control	1220	8409	10371	25059	5336	30.7	56.2	143.6	610.0	600.3
Control	271	7266	10257	19626	5018	33.9	50.7	44.0	388.3	319.3
C9-ALS	1925	16813	14561	11499	2629	35.8	67.6	40.3	288.6	433.0
sALS	3628	17480	13686	9744	2995	23.6	50.7	121.0	582.3	651.3
sALS	1535	14545	17086	15070	2305	36.5	63.3	41.3	621.3	939.0
sALS	665	20819	10620	14375	1887	30.5	60.3	39.0	642.0	623.3
sALS	1048	7814	6648	31521	10614	35.3	66.3	105.0	468.3	421.6
sALS	359	3509	4047	13398	1245	28.6	23.0	68.3	608.3	578.0
sALS	599	7270	-	36572	2959	33.4	62.9	75.3	386.3	467.0

Table 14: Quantification of RNA-ISH and DAB-IHC for *CTIP2, SATB2, TBR1, FUS* and *TARDBP*.

3.5 Specification of neurons expressing transcription factors associated with projection neuron diversity

We previously demonstrated that inhibitory interneurons degenerate within the ALS primary motor cortex (Fig 21), however the majority of neurons within the cortex are excitatory pyramidal neurons. *CTIP2*, *SATB2* and *TBR1* are critical transcription factors required for projection neuron fate determination in mice [197-199]. However, the expression pattern of genes associated with projection neuron diversity is unknown in the human motor cortex. We therefore next sought to assess projection neuron diversity in the human ALS motor cortex, and attempt to reconcile these neurons to the presence of characteristic ALS pTDP-43 pathology using a combination of anti-sense *in situ* probes (Table 6) and IHC.

Using a small subset of short fixed ALS (n = 7) and control (n = 3) cases (Table 14), we were unable to find a difference in either the numbers of cells expressing the above transcription factors in either IHC (Fig 30) or by using RNAscope (Fig 31) in the ALS primary motor cortex. IHC for CTIP2, SATB2 and TBR1 revealed very little staining within layer I. IHC for CTIP2 revealed that CTIP2+ neurons appeared to be concentrated within layers II and V, but SATB2 and TBR1 IHC revealed expression that was present across all cortical layers (Fig 30). This was largely recapitulated using probes for each antibody in RNAscope, and the expression of each probe appears to correlate fairly closely with the extent of protein expression in Betz cells and surrounding layer V neurons (Fig 32G-L). However the expression of each gene/protein was not assessed in a layer wise manner. The results of additional ISH/IHC experiments using these probes in conjunction with pTDP-43 antibody (Fig 32A-F) were also inconclusive, in part because of the difficulty in observing red-brown co-localization. Together, while conducted on a small

number of cases and therefore largely inconclusive, these results are an example of how RNAscope and combined IHC/ISH could potentially be utilised and expanded upon in the future to answer defined hypotheses regarding gene/protein expression dynamics using post-mortem human tissue, which is relevant in the context of neurodegenerative diseases like ALS.

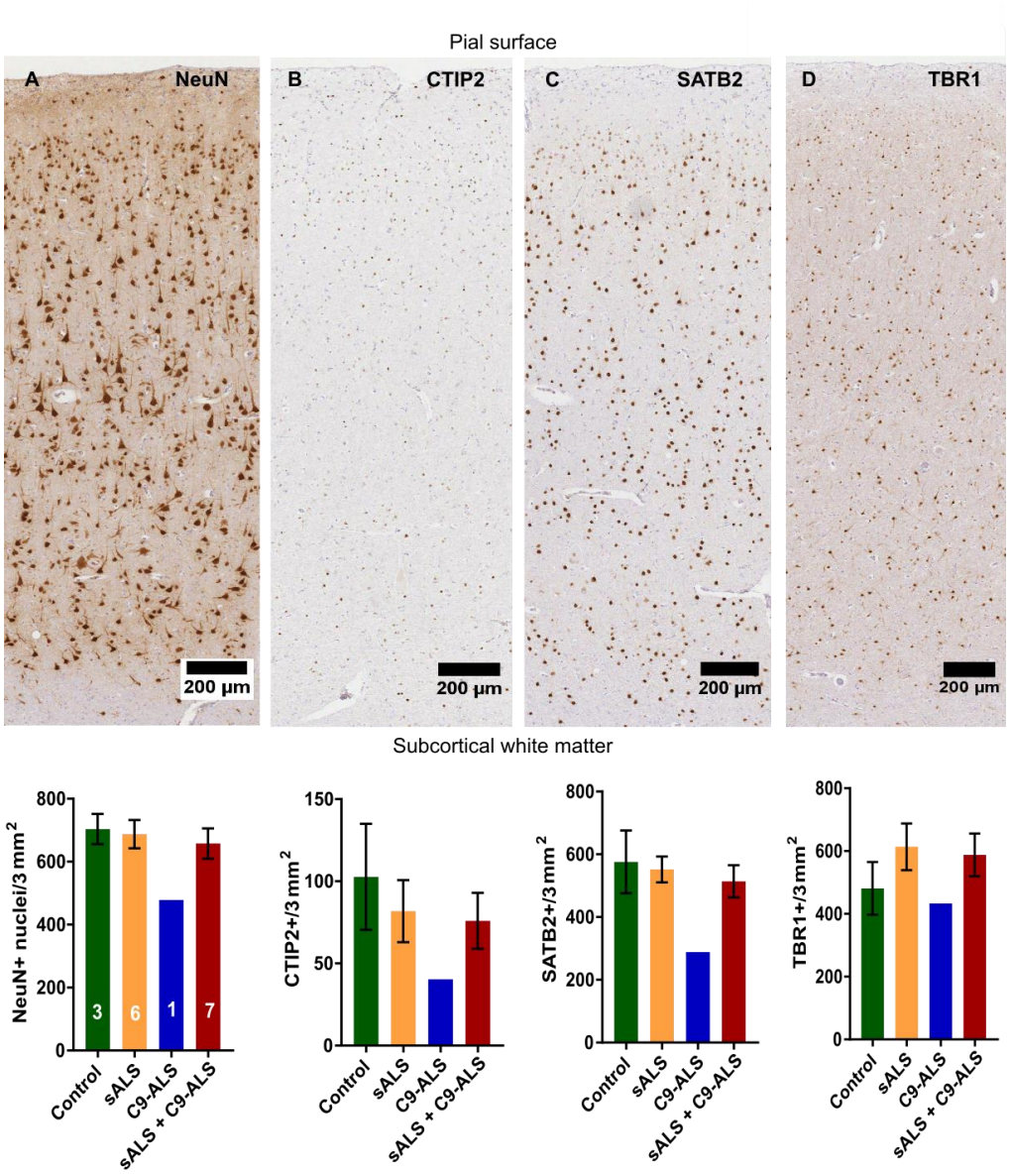

Figure 30: Analysis of expression of neuronal transcription factors associated with projection neuron fate in the primary motor cortex using DAB-IHC. Pictured is a single control case. NeuN labels all neurons and is highly expressed in all layers (A). CTIP2 largely labels CSMN in layers II and V (B). SATB2 labels callosal projection neurons which are present in all layers (C). TBR1 labels corticothalamic projection neurons which are also present in all layers (D). From these cases, there appears to be no significant reductions in these positive neurons within the ALS primary motor cortex. White numbers within bars highlight number of cases included, error bars indicate SEM.

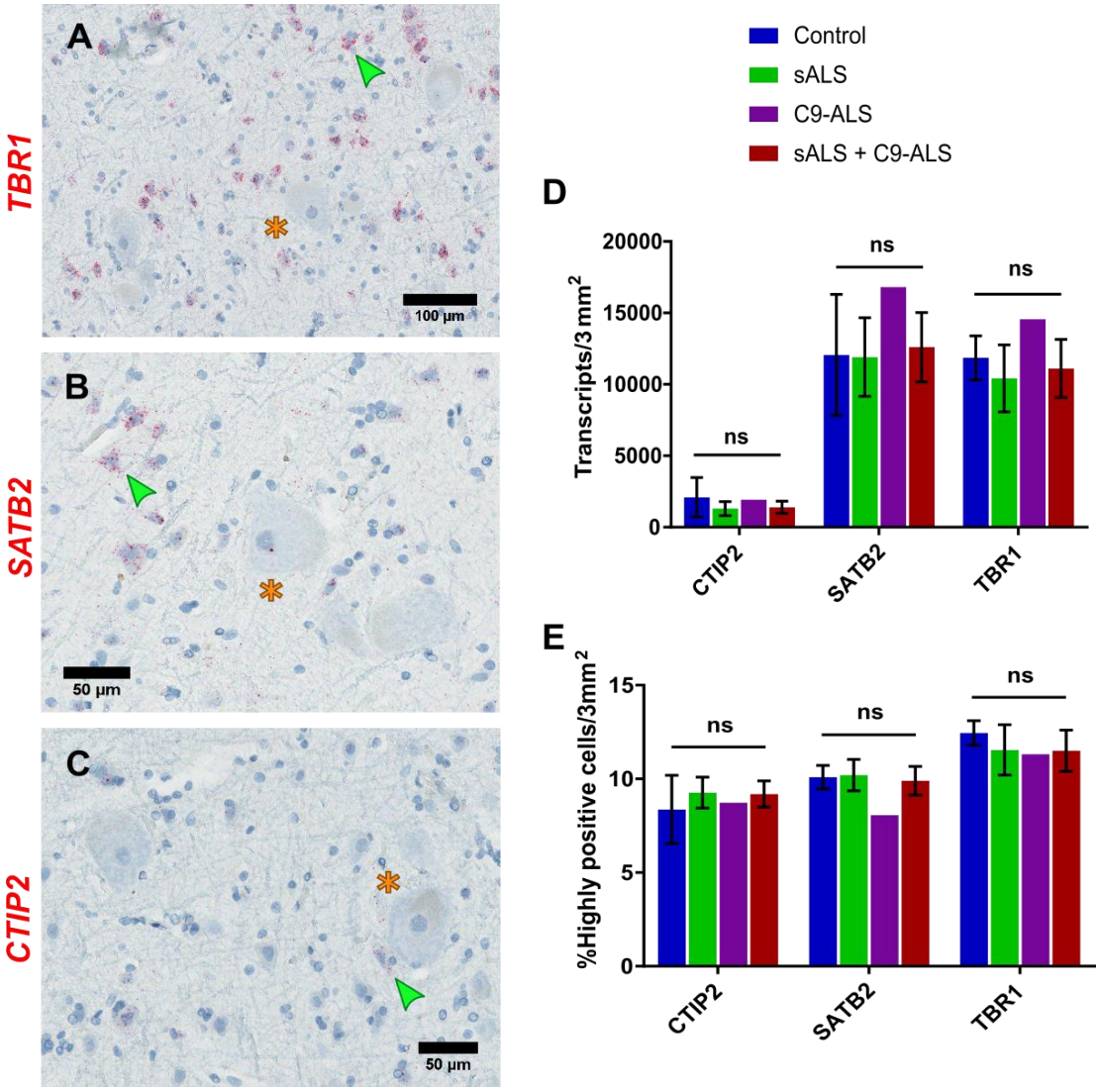

Figure 31: Expression of genes involved in projection neuron diversity in the human primary motor cortex assessed using RNAscope. Images are from layer Vb of a single control case. Areas of expression are arrowed green, Betz cells are highlighted by orange stars. TBR1 (A) and SATB2 (B) are more significantly more highly expressed than CTIP2 (C and D). However the relative expression of each gene is similar (E) when normalised against the number of cells highly expressing (at least 3x the average number of transcripts per cell) each gene. There was no significant difference in expression between ALS and control cases in any gene. Error bars represent SEM.

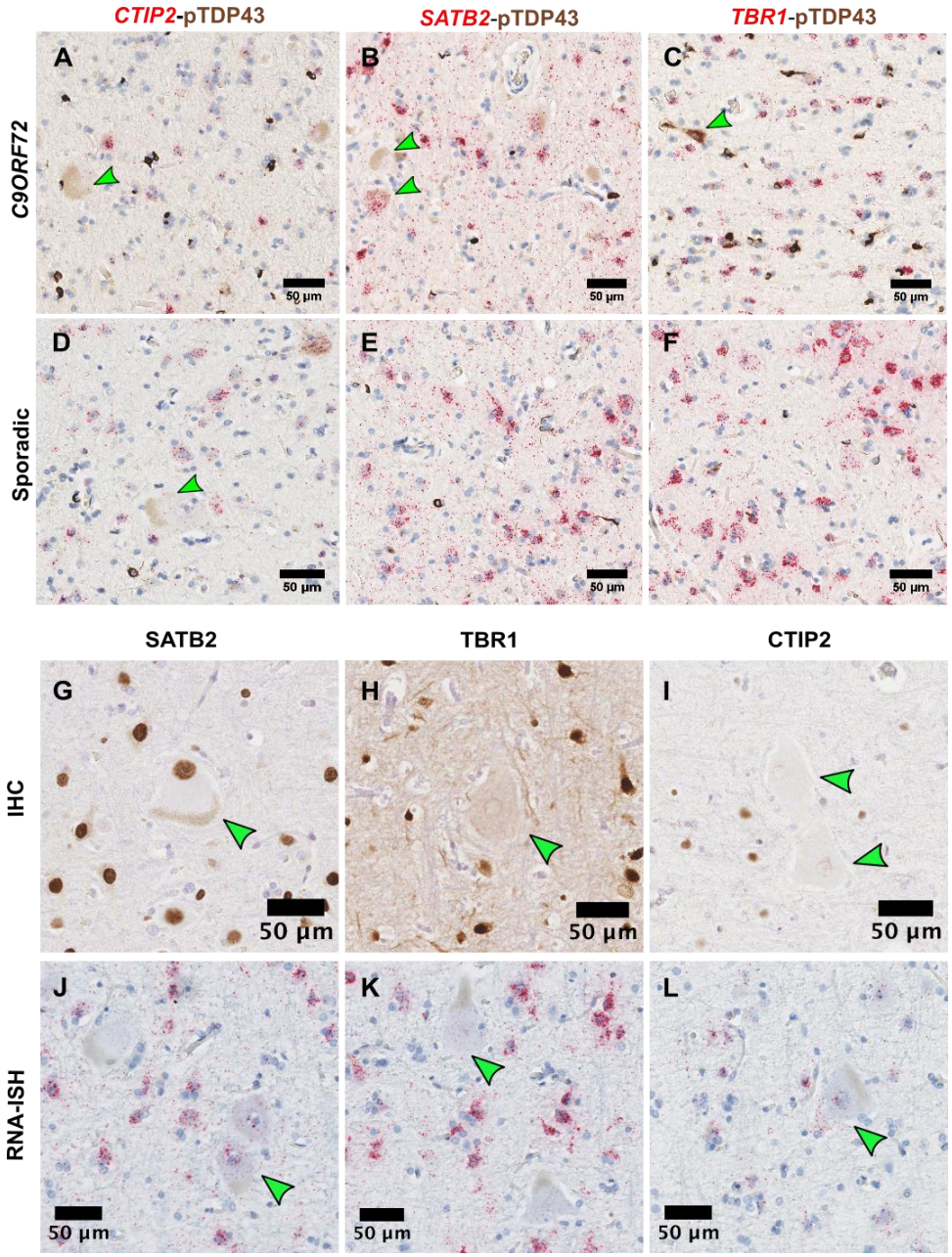

Figure 32: ISH-IHC using probes targeted to specific neuronal transcription factors in conjunction with IHC for pTDP-43 pathology. Probes against *CTIP2* (A,D), *SATB2* (B,E) and *TBR1* (C,F) were applied to human tissue from the primary motor cortex in conjunction with pTDP-43 antibody. Green arrows highlight Betz cells. No obvious correlation could be seen between expression of these transcription factors and the likelihood of aggregative pTDP-43 pathology in either sporadic of C9ORF72 ALS cases. Quantification in these cases was not possible because the colour deconvolution between the red and brown signal was too similar to make identification of each possible. RNAscope results observed in ~20 Betz cells per case suggests that *SATB2* is expressed reasonably highly in Betz cells (G,J), but surprisingly *CTIP2* is not (I,L). *TBR1* does not appear to be significantly expressed in Betz cells either at the protein or RNA level (H,K). Green arrows highlight Betz cells in all panels. Images A-C and D-F taken from a single C9-ALS and sporadic case, respectively. Images G-L taken from a single control case. All scale bars = 50µm.

Chapter four

Upper and lower motor neuron predominant monogenic ALS

4. Upper and lower motor neuron predominant monogenic forms of ALS

In 2009, mutations to the Fused-in-Sarcoma (*FUS*) gene were identified as causative in a small number of ALS cases [48, 347]. This was followed in 2010 by the discovery that mutations to the autophagic adapter *OPTN* also cause ALS [50]. This section assesses the neuropathology of a novel mouse model of ALS-*FUS* utilising the P525L mutation, which in humans causes a LMN predominant syndrome, and contrasts with another monogenic form of the disease (ALS-*OPTN*) assessed through the identification and description of an UMN predominant index case donated to the Oxford Brain Bank. A comparison of the pathotypes is included in the discussion (Chapter 5).

4.1 Neuropathological characterisation of a novel BAC transgenic mouse model of ALS-*FUS* utilising the P525L mutation

A novel mouse model of ALS-FUS was generated which uses a Bacterial artificial chromosome (BAC) transgene containing the P525L mutation. The generation of the transgene, insertion into the mouse, animal husbandry and phenotyping were performed by other members of the lab. Described here is the neuropathological characterisation of the mouse. The mice were culled at 3, 9, 12 and 20 months of age. Three strains were generated: WT, expressing the full-length human wild-type FUS, PL1, a low copy-number variant expressing the P525L mutation, and PL3, a high copy-number variant expressing the P525L mutation. Within the BAC transgene, the human FUS gene was tagged to mCherry to allow the distinction between human and endogenous mouse FUS expression.

4.1.1 Methods

Mice were anaesthetised using ketamine prior to transcardial perfusion using 4% paraformaldehyde (PFA). The brain and spinal column were dissected and immersion fixed in 4% PFA for a further 48 hours. Fixed tissue was then dissected by slicing the brain into separate hemispheres along the midline. One hemisphere was then coronally sliced. The spinal cord was removed from the spinal column and transected into small enough pieces to fit into a standard histology cassette. The bisected hemisphere, coronal sections and transected spinal cord were then all placed cut surface down into the same cassette. Tissue was then processed on a carousel-based tissue processor through increasing concentrations of alcohol, followed by four xylene changes, followed by infiltration using paraffin wax, for a total processing time of 24 hours. Processed tissue was then embedded within paraffin wax and sectioned using a rotary microtome at 4µm.

Sections were dewaxed through xylene, and rehydrated through decreasing concentrations of alcohol before being pre-treated for 30 min in 10% concentrated (30%) H_2O_2 and distilled water to block endogenous peroxidase. Heat-induced epitope-retrieval was performed using autoclave boiling at 121°C for 10 minutes. Sections were then rinsed with Tris-buffered saline and blocked with normal goat serum (1:10 in TBS-T) for 30 min. Primary antibodies including Iba1 (Wako, 1:1000), FUS (Sigma-Aldrich, 1:300), FUS (Bethyl labs, 1:500), mCherry (Abcam, 1:1000), p62 (BD Transduction labs, 1:3000), NeuN (Merck Millipore, 1:1000) and mutant specific P525L FUS (gift from Elke Bogaert, KU Leuven, 1:200) were incubated overnight at 4°C and visualised using the Dako Envision+ kit and HRP-DAB signal.

NeuN and Iba1 staining was quantified using digital image analysis algorithms optimised for each stain using ImageScope software. Graphing and statistical analysis was performed using GraphPad prism software.

4.1.2 Results

mCherry staining was consistent across mice of same genotype and age. Overall, expression of the mCherry-tagged mutant FUS increased in both a time and genetic level expression dependant manner, across brain and spinal cord, with complete nuclear clearance caused by the mutation preventing nuclear re-localization even in PL1 3M mutant mice (Fig 33B). Progression of staining was clear, with 12M PL3 mice exhibiting granular mCherry-FUS inclusions, however these were not large or discrete enough to be considered inclusions in the human sense (Fig 33F). mCherry staining was most intense in the spinal cord, in keeping with mutation being LMN predominant in humans. In WT mice, mCherry staining is nuclear as expected, which supports the hypothesis that full length, WT human FUS is not pathogenic in mice when expressed at near physiological levels (Fig 33A, D, G and Fig 34 A, D, G). In the spinal cord some larger anterior horn neurons contained small aggregations, but most had diffuse mCherry.

Staining was also conducted using two different FUS antibodies which recognise different epitopes of the FUS protein (Bethyl labs antibody 200-250aa, Sigma antibody 1-122aa). FUS staining was broadly similar for both antibodies, staining both nuclear and to a lesser extent cytoplasmic FUS. However in PL3 spinal cord there was additional intense diffuse cytoplasmic staining as well as nuclear (Fig 35 A&B). Staining using an antibody targeted against the P525L mutation in the 20M PL3 mice exclusively highlights the mislocalized

mCherry-FUS in most cells, but did not appear to be as sensitive as standard mCherry staining (ie, inclusions etc cannot be identified)(Fig 35C). As with mCherry-FUS, the most intensive pathology identified using the mutation specific antibody is in the spinal cord, in keeping with the effect of the mutation in humans. Aggregated granulations of FUS protein could be seen in the spinal cord and thalamus of 12M PL3 mice at higher magnifications (Fig 34). However, there does not appear to be clear neuronal selectivity, and most neurons are affected.

Staining for p62 revealed only a small amount of staining across mice, which was mainly moderate diffuse cytoplasmic staining with some granularity/punctate inclusions in motor cortex and cerebellum. The spinal cord (Fig 35F) and brainstem most severely affected in terms of number of p62 inclusions. Staining and quantification of the microglial marker Iba1 (Fig 35E) and the pan-neuronal marker NeuN (Fig 35D) revealed no indication of microglial activation or neuronal loss in the motor cortex, spinal cord or cerebellum in any of the mice tested (Fig 35).

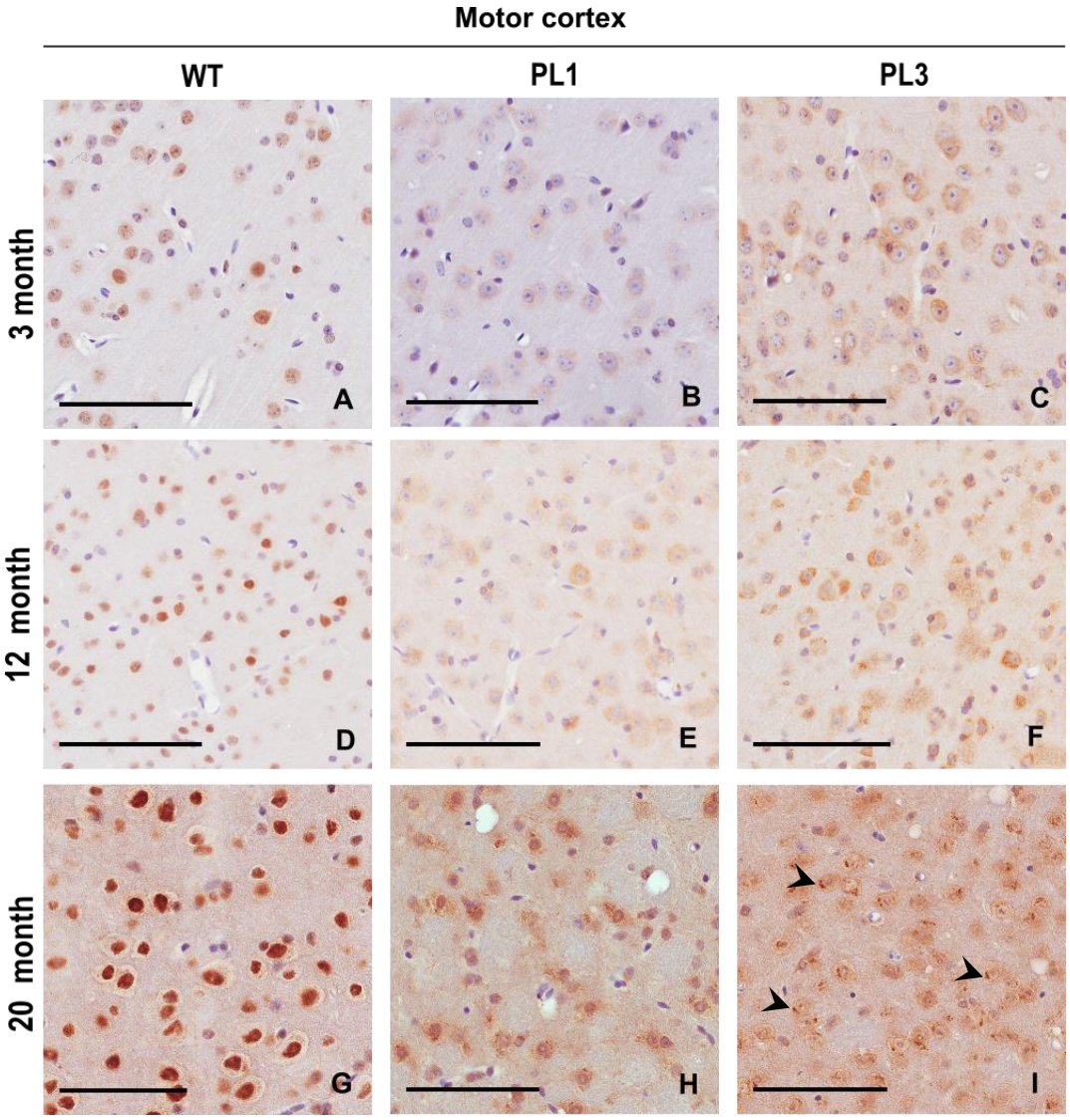

Figure 33: Mutant FUS pathology assessed using mCherry antibody progresses in an age and expression level dependent manner in the motor cortex of the transgenic P525L mice. The mutant transgene causes the cytoplasmic mislocalization of mCherry-FUS in all regions of the brain including the motor cortex. However this remains more diffuse mislocalization until around 12 months (E,F). At 20 months there are small inclusions within neurons in the high-expressing PL3 mice (I, arrowed), but this begins as early as 3 months in the PL1 mice (B). The full length wild-type human protein was retained within the nucleus in all lines/ages (A,D,G). All scale bars at 100µm.

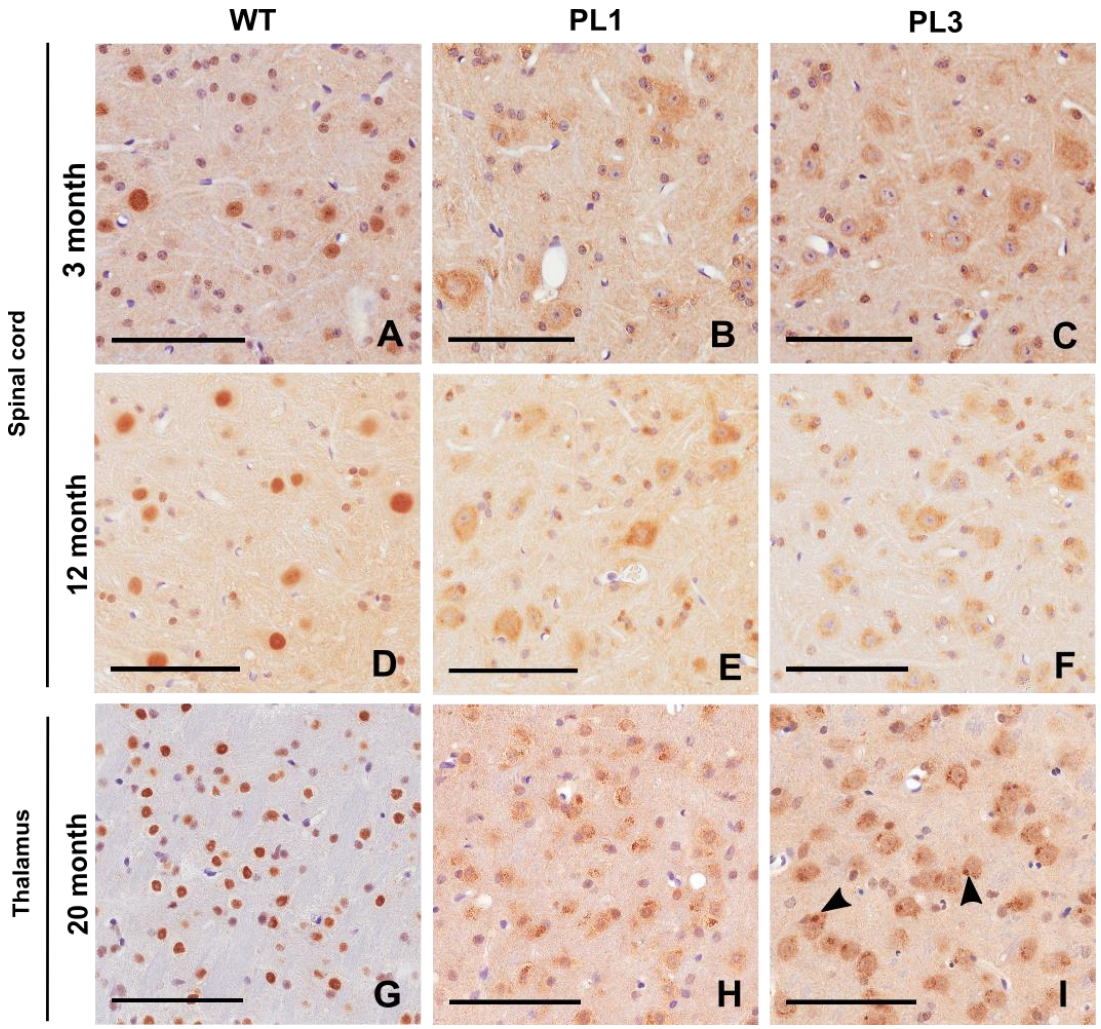

Figure 34: mCherry IHC reveals mutant FUS pathology progresses in an age and expression level dependent manner in the spinal cord and thalamus of the P525L mice. The mutant transgene causes the cytoplasmic mislocalization of mCherry-FUS in all regions of the CNS including spinal cord (A-F) and thalamus (G-I). At 20 months, there are small inclusions within thalamic neurons in the high-expressing PL3 mice, arrowed (I). The wild-type human protein was retained within the nucleus in all lines/ages (A,D,G). All scale bars at 100µm.

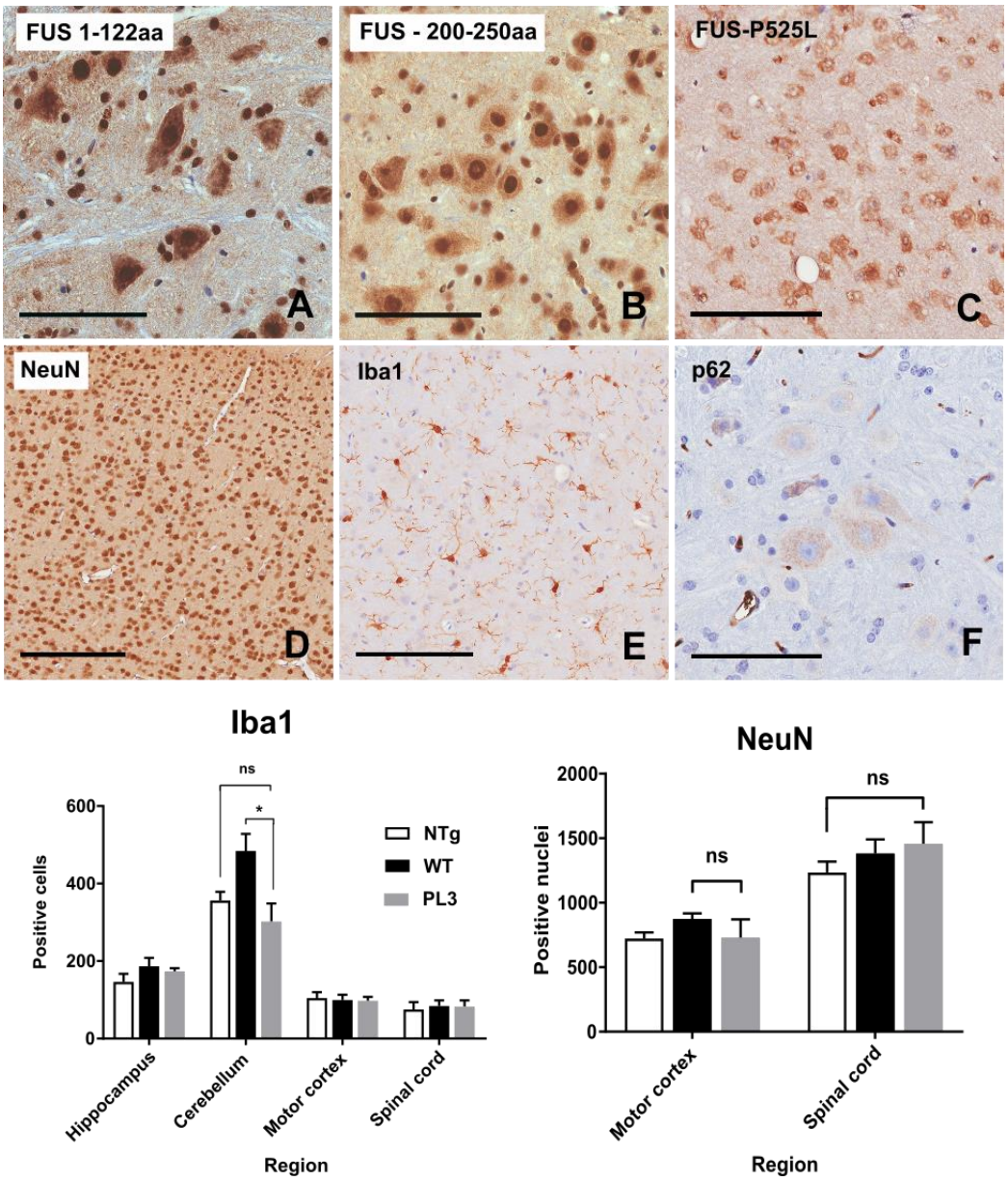

Figure 35: Transgenic mice display no evidence of microgliosis or neurodegeneration. Neuronal numbers of various regions were quantified using NeuN staining (D, 12M PL3 cortex) which revealed no statistically significant neuronal loss in any line at 12 months. Microgliosis was assessed using Iba1 staining (E, 12M PL3 Thalamus), which revealed no evidence of increased microglial activation at 12 months. Staining using an antibody targeted at the full-length FUS protein (A, 3M PL3 spinal cord and B, 20M PL3 spinal cord) revealed some mislocalization of transgenic FUS plus staining of the endogenous mouse FUS within the nucleus. Staining using an antibody targeted to the P525L mutation selectively stains the mislocalized mCherry-FUS within the cytoplasm (C, 20M PL3 motor cortex). There was also some evidence of punctate p62 staining within large anterior horn neurons in the spinal cord (F, 20M PL3 spinal cord). Scale = A,B,C,E,F 100µm, D 200µm.

4.1.3 Discussion

A novel transgenic mouse model of ALS-FUS was generated which utilised the full-length human FUS gene, plus the P525L mutation which in humans causes a severe, juvenile onset form of ALS [104]. The main advantage of this mouse is the use of the BAC transgene, which unlike smaller cDNA based transgenes, allows for the inclusion of all the human upstream regulatory elements including the human promoter, allowing expression of the transgene at near physiological levels. The mutant FUS was also tagged to a mCherry reporter, to allow for the distinction between endogenous mouse FUS and mutant human FUS. mCherry-FUS staining exhibited a clear age- and genetic- dependent progression, with mislocalization of the mutant protein increasing accordingly. WT mice displayed no mislocalization of the human FUS protein, with no concomitant phenotype (data not published), demonstrating that full-length human WT FUS is not pathogenic in mice. mCherry-FUS is clearly mislocalized, with total nuclear clearance at fairly juvenile ages. However, these mice display no overt motor phenotype (data not published). Additionally, there is no evidence of neuronal loss or overt microglial activation in any of the lines. This suggests that the expression of the transgene at this level is insufficient to induce neurodegeneration, or that the existence of the endogenously expressed mouse FUS is sufficient for the physiological role of the gene in mice, essentially overriding any negative cellular effects caused by the human gene.

FUS, like TDP-43, exhibits substantial autoregulatory capacity whereby FUS protein is able to bind to the C-terminal domain of *FUS* mRNA to prevent translation. This allows the temporal and spatial expression of the *FUS* gene. However, the effect of the mutation described here on the autoregulatory capacity of FUS is unknown. Additionally, recent studies have highlighted the role that TDP-43 plays in the alternative splicing of other target exons including *MAPT* [335, 348, 349], providing a further pathophysiological link

between ALS and FTD. However, whether this is also the case for *FUS* is also largely unknown.

4.2 Novel homozygous R217X *OPTN* mutation causes knock-out of functional C-terminal domains and upper motor neuron predominant amyotrophic lateral sclerosis.

The following is a case report of an *OPTN* mutation case that was donated to the Oxford Brain Bank in 2009. The case described is the same ALS-*OPTN* patient used in the neuropathological selective vulnerability component of this study. Elaboration on the case is included as a direct comparator to ALS-*FUS* which has been described previously, and because it stands as an example of the extreme UMN vulnerability that can be induced by genotypic background.

4.2.1 Introduction

Mutations to the autophagy adaptor gene *OPTN* are a rare cause of ALS and also the related but clinically distinct disease frontotemporal dementia (FTD). Here, we describe an ALS autopsy case of a 54 year old male who presented initially with isolated dysarthria and subsequently developed only limited lower motor neurone symptoms. There was no family history of ALS or dementia. Whole-exome sequencing revealed a novel homozygous recessive mutation (c.649A>T, p.R217X) within the *OPTN* gene. No other mutations within known ALS/FTD genes were found. At post-mortem there was prominent cortical atrophy of the primary motor region and relative sparing of the spinal cord. Neuropathology revealed a striking upper motor neuron predominant motor neuron

disease with widespread neuronal and glial pTDP-43 proteinopathy, as well as extensive reactive gliosis, without significant β-amyloid or α-synuclein pathology. C-terminal OPTN protein was undetectable across the brain and spinal cord in both IHC and western blotting. RT-qPCR analysis of three CNS regions revealed around a 75% reduction in *OPTN* expression against control, together suggesting loss-of-function through both truncation of functional C-terminal domains and reduced gene expression via nonsense mediated decay. This is the first reported human case of ALS resulting from the R217X mutation, with implications for our understanding of the OPTN-mediated autophagy pathway in ALS.

4.2.2 Background

Optineurin, coded by the *OPTN* gene and most frequently associated with its role in primary open-angle glaucoma [350], is one of five autophagy adaptor proteins whose primary role is the linking of ubiquitinated cargo to autophagic membranes. TANK-binding kinase 1 (TBK1) phosphorylates OPTN at its ubiquitin binding domain and enhances the autophagic clearing of both damaged mitochondria and cytoplasmic aggregates [351, 352](Fig 38). OPTN also suppresses the receptor-interacting kinase-1 (RIPK1) signalling pathway [353], and acts as an adaptor between myosin-VI and secretory vesicles [354]. Conditional deletion of *optn* from oligodendrocytes and myeloid cells in mice results in progressive dysmyelination and axonal degeneration without significant motor neuron cell body loss [353], however global deletion of its C-terminal is embryonic lethal [355]. Mutations to *OPTN* in humans are an infrequent cause of ALS and the genetically/pathologically related but clinically distinct disease, frontotemporal

dementia (FTD), of which over 30 individual mutations of varying predicted pathogenicity have been described (Table 15) [40, 44, 50, 356-358].

Pathologically, wild-type OPTN is occasionally found in the inclusions present in both sporadic and autosomal dominant forms of ALS [50, 359-361]. However, there have been few neuropathological descriptions of *OPTN* mutation cases themselves. Ayaki *et al* (2018) recently characterised three cases which were found to exhibit multiple proteinopathies including one case which positively immunostained for tau, pTDP-43 and α-synuclein within a single neuron [362]. Bury et al (2015) described OPTN-positive, TDP-43-negative inclusions in an *OPTN* mutation case, however the patient also carried a hexanucleotide repeat expansion within *C9ORF72* [40]. Other reports have also described *OPTN* mutations existing in conjunction with other known ALS/FTD mutations, contributing to the discussion of ALS as an 'oligogenic' disease [356].

The combination of these genetic and neuropathological factors highlight the functional importance of *OPTN* and its role in the autophagic clearance pathway in ALS. Here, we present an autopsy case of upper motor neuron predominant sporadic ALS caused by a novel homozygous recessive c.649A>T mutation within *OPTN*, existing independently of all other known ALS/FTD mutations.

Study	Mutations		Zygosity	Effect	Location	Diagnosis	Notes
	DNA	**Protein**					
	c.1502C>T	Q398X	Homozygous	Nonsense	Coil-Coiled domain	ALS	-
	c.1743A>G	E478G	Heterozygous	Missense	Ubiquitin-binding domain	ALS	OPTN+ and pTDP-43 inclusions, see Ayaki et al (2018)
[50]	Exon 5 deletion	N/A	Homozygous	Deletion	-	ALS	58-aa truncated protein
	c.703C>T	Q235X	Heterozygous	Nonsense	Coil-Coiled domain		Same patient. Prominent focal cortical atrophy. TDP-43 and p62 positive inclusions. No pathology in motor neurons. Reduction of *OPTN* expression in cerebellum
[356]	c.1442C>T	A481V	Heterozygous	Missense	Ubiquitin-binding domain	FTD	
	c.495C>T	Q165X	Heterozygous	Nonsense	Coil-Coiled domain	FTD	72% truncation of protein
[358]	c.1362C>G	Q454E	Heterozygous	Missense	Ubiquitin-binding domain	ALS	Possibly damaging (PolyPhen-2)
[44]	c.493C>T	Q165X	Heterozygous	Nonsense	Coil-Coiled domain	ALS	Predicted truncation of the protein
	c.1242+1GA_insA	-	Heterozygous	Unknown	Intronic	ALS	Possible frameshift and protein truncation
[357]	c.1442C>T	A481V	Heterozygous	Missense	Ubiquitin-binding domain	ALS	-
	c.785C>A	S262X	Heterozygous	Nonsense	Coil-Coiled domain		
[363]	c.1289_1290del	L430Rfs*16	Heterozygous	Frame shift	Ubiquitin-binding domain	ALS-FTD	Same patient. 75-80% reduction in *OPTN* expression in blood
[364]	c.1320delA	K440Nfs*8	Heterozygous	Frame shift	Coil-Coiled domain	ALS	Frameshift resulting in premature stop codon
[365]	c.691_692insAG	D128Rfs*21	Homozygous	Insertion	Exon 6	ALS	Frameshift resulting in premature stop codon
	c.844A>C	T282P	Heterozygous	Missense	Coil-Coiled domain	PLS	Possible pathogenicity
	c.941A>T	Q314L	Heterozygous	Missense	Coil-Coiled domain	ALS	Within highly-conserved region, predicted pathogenicity (PMUT, PolyPhen and SNPs3D)
	c.1670A>C	K557T	Heterozygous	Missense	Zinc Finger domain	ALS	Within highly-conserved region, predicted pathogenicity (PMUT, PolyPhen and SNPs3D)
	c.67G>T	G23X	Heterozygous	Nonsense	Intronic	ALS	Creates very premature stop codon
	c.552+1delG	148_184del	Heterozygous	Deletion	Intronic	ALS	Induces activation of exonic cryptic donor splice site, leading to 111 nucleotide skipping within exon 6
[366]	c.1401+4A>G	-	Heterozygous	Unknown	Intronic	ALS	Predicted splice site insertion. Patient also carried T343T variant
	c.277G>C	A93P	Heterozygous	Missense	Coil-Coiled domain	ALS	Highly conserved region, predicted pathogenicity (PolyPhen, SMART)
[367]	c.1433A>G	E478G	Homozygous	Missense	Ubiquitin-binding domain	ALS	-
[368]	c.481G>A	V161M	Heterozygous	Missense	Leucine Zipper domain	ALS	-
	c.658delG	D220Mfs*12	Heterozygous	Frame shift	Intronic	ALS	
[369]	c.493C>T	Q165X	Heterozygous	Nonsense	Coil-Coiled domain	ALS	Two siblings with identical mutations
	c.407C>T	A136V	Heterozygous	Missense	Coil-Coiled domain	ALS	-
	c.1184A>G	K395R	Heterozygous	Missense	Coil-Coiled domain	ALS	-
	c.1352T>C	I451T	Heterozygous	Missense	Ubiquitin-binding domain	ALS	-
[370]	c.1546G>C	E516Q	Heterozygous	Missense	Exon 14	ALS	-
[40]	c.964G>A	E322K	Heterozygous	Missense	Coil-Coiled domain	ALS	Concurrent *C9ORF72* expansion
[371]	c.1403T>G	M468R	Heterozygous	Missense	Ubiquitin-binding domain	ALS-FTD	Concurrent *C9ORF72* and *ATXN* expansions

Table 15: Selection of previously reported OPTN mutations associated with ALS/FTD. Only mutations for which reasonable evidence of pathogenicity is available (e.g absence in controls) are included.

4.2.3 Genetic screening

Next-generation whole exome sequencing was conducted on DNA extracted from frozen brain tissue as part of a separate study [372]. A novel homozygous recessive nonsense mutation (c.649A>T, p.R217X) was found within exon 8 of the *OPTN* gene (Fig 36A&B). which was absent from 368 simultaneously sequenced controls and from both the NCBI dbSNP and ExAC databases. No other obviously penetrant within known ALS/FTD genes, including *TBK1* and *SQSTM1*, were found [372]. Only two other non-synonymous SNP's have been described at the 217 codon (rs1328890259, 649A>G, Arg>Gly and rs755695303, 650G>C, Arg>Thr)(NCBI dbSNP database). Nonsense mutations cause the translation of a premature stop codon which generally disrupt gene function through lack of transcription, degradation of mRNA via nonsense-mediated decay or protein truncation. *In-silico* analysis predicted a stop-gain effect (SIFT, PolyPhen2) for the mutation, with a concomitant 62.4% reduction in protein length (Fig 36A) where translation occurs. The mutation meets multiple effect criteria making its pathogenic significance 'very strong' according to ACMG guidelines [373].

4.2.4 Immunohistochemistry

For immunohistochemistry (IHC), 6µm FFPE sections from fourteen regions (medulla oblongata, pons, midbrain, cerebellar vermis, primary motor cortex, parietal cortex, occipital cortex, anterior cingulate, amygdala, hippocampus, basal ganglia, thalamus, trigeminal ganglion and cervical spinal cord) of the index case were assessed. Sections were dewaxed through xylene, and rehydrated through decreasing concentrations of alcohol before being pre-treated for 30 min in 10% concentrated (30%) H_2O_2 and distilled water to block endogenous peroxidase. Heat-induced epitope-retrieval was performed

using autoclave boiling at 121°C for 10 minutes. Sections were then rinsed with Tris-buffered saline and blocked with normal goat serum (1:10 in TBS-T) for 30 min. The primary antibodies used were against pTDP-43 (Cosmo-bio, 1:10,000), CD68 (Wako, 1:250), α-synuclein (BD Transduction labs, 1:1000), Tau (Launch Diagnostics 1:1500), β-amyloid (Biolegend, 1:24000), p62 (Abcam, 1:1000) and OPTN (Proteintech, 1:3000). Primary antibodies were incubated overnight at 4°C and visualised using the Dako Envision+ kit and HRP-DAB signal. Additional sections from the lumbar spinal cord, cerebellum and primary motor cortex of one sporadic ALS and one neurologically normal case were also assessed via OPTN IHC. No staining was seen when the primary antibody was omitted. Stained sections were then dehydrated, cleared, mounted (Histomount, Thermo-Fisher Scientific, Germany) and coverslipped. All sections were viewed using a Zeiss Primo Star microscope (Zeiss, Oberkochen, Germany). Slides were digitally scanned at 40X using the Aperio ScanScope AT Turbo system (Leica Biosystems, Germany), and analysed using QuPath pathology analysis software [327].

4.2.5 Western blotting

Proteins were extracted from fresh-frozen tissue of three regions (frontal cortex, spinal cord and cerebellum) of the index case, one sporadic ALS case and one neurologically normal control (Fig 36C) and yield assessed using Pierce™ BCA Protein Assay Kit (Thermo Fisher). The same amount of proteins (20 μg) was mixed with 4X Sample Blue buffer (Invitrogen) and 10X Reducing agent (Invitrogen), boiled at 95°C for 5 minutes and loaded onto a 4-12% Bis-Tris gel (Life Technologies). Samples were run at 140 V for one hour, before being transferred to PVDF membrane and blocked using 5 % skim milk (Sigma) dissolved in TBS-T for one hour at room temperature. After blocking, membranes

were exposed to primary using HRP-conjugated anti rabbit or anti-mouse IgG at a dilution of 1:5000 (Amersham). Protein bands were visualized using the ChemiDoc™ Imaging System (BioRad).

4.2.6 RT-qPCR

qPCR was performed on total RNA extracted from three regions (frontal cortex, spinal cord and cerebellum) of the index case, one sporadic ALS case and one neurologically normal control (Fig 36D). After TRIzol extraction (Invitrogen), total RNA was treated with DNaseI (Invitrogen) and retro-transcribed (High capacity cDNA reverse transcription kit, Applied Biosystems). The qPCR reagent used was Fast SYBR® Green Master Mix (Applied Biosystems). qPCR was run on a Roche LightCycler and melting curve analysis was performed on LightCycle Multicolor software. Target transcripts were *OPTN* and *TBK1*, and the internal reference was the combined *TOPI*, *RPL13A* and *ATP5B* whose stability has been previously described [374]. The primers were designed based on the reference sequences in National Centre for Biotechnology Information (NCBI) database. The relative mRNA expression was calculated as $2^{-(\Delta Ct)}$ and plotted as a percentage.

4.2.7 Neuropathology

On external post-mortem examination there was very prominent focal cortical atrophy involving the entire motor region but without significant atrophy outside of the motor area. Coronal slices revealed the grey/white matter was generally well demarcated. The lateral horn of the ventricle was not dilated and the hippocampi were of normal bulk. The substantia nigra was well pigmented. The aqueduct was patent and both the pons and

medulla were within normal limits. The spinal cord was not particularly thin and the greying of anterior roots was not pronounced. Microscopic examination of pTDP-43, tau, β-amyloid, α-synuclein, CD68 and p62 on fourteen regions was performed (Fig 37). No evidence of β-amyloid or α-synuclein was seen. There was severe reactive gliosis and transcortical spongiosis in the primary motor area, associated with significant neuronal loss including prominent depletion of the layer V Betz cells. p62 and pTDP-43 immunohistochemistry showed extensive white matter pathology which was at least as pronounced as grey matter pathology and consisted of neurites and perinuclear cytoplasmic inclusions as well as widespread glial inclusions. No nuclear inclusions were seen. The hippocampus showed some intracellular neuronal tau accumulation (Fig 37I) but there was no apparent loss of neurons. There was very mild loss of substantia nigra neurons in the lateral pars compacta. The loci coerulei show no clear loss of pigmented neurons and there were no Lewy bodies. The cerebellum was relatively well preserved with possible mild Purkinje cell loss only, but with an abundance of p62 positive corpora amylacea within the molecular layer (Fig 37G). The spinal cord showed severe degeneration of the corticospinal tract. Anterior horn cells were mildly depleted and there were only rare granular or cytoplasmic compact pTDP-43 inclusions (Fig 37D). p62 highlighted glial aggregates which seem to be particularly prominent in the degenerated corticospinal tract. Staining for C-terminal OPTN in the index case was entirely absent in primary motor cortex, cerebellum and spinal cord in both IHC and WB (Fig 36C, Fig 36G, J, M), however cytoplasmic OPTN-ir inclusions were occasionally seen in the sporadic ALS comparative case (Fig 36F, I).

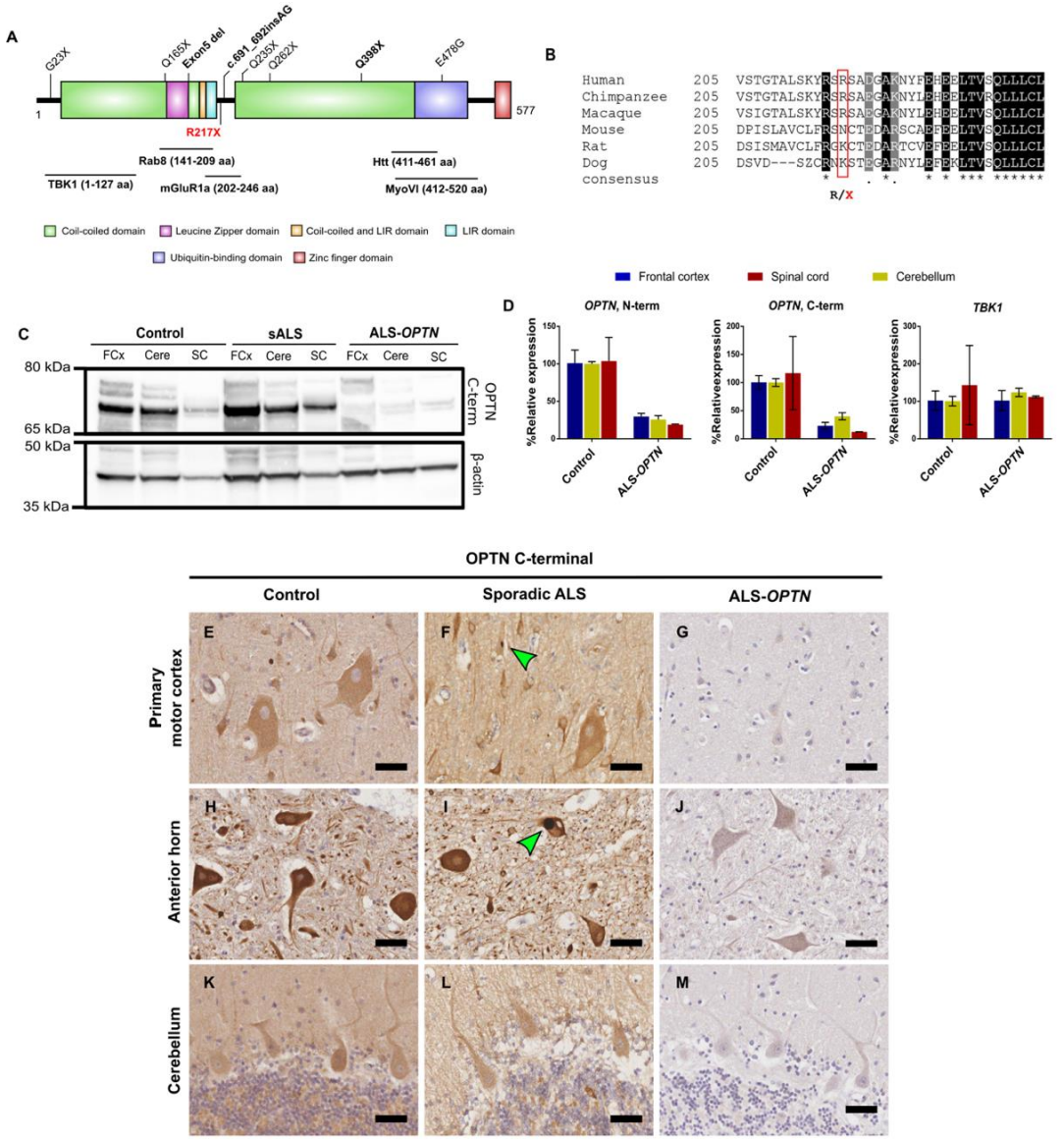

Figure 36: Expression analysis of the R217X mutation. The mutation exists at the non-conserved 217aa residue, between the LIR domain and the largest coil-coiled domain. Previously reported nonsense mutations are shown, homozygous mutations are shown in bold. OPTN possesses several key functional domains, with defined binding-regions for Rab8, Htt and MyoVI. The c.649A>T mutation (highlighted in red) results in a premature stop codon, truncating the protein by 62.4% and preventing the translation of three functional domains. (A). The mutation occurs within a region conserved across primates but not other mammals (B). Expression of the C-terminal OPTN fragment is absent/significantly reduced in both IHC (G, J, M) and WB (C). RT-qPCR using primers mapping both the C- and N-terminal regions reveals a 75% reduction in OPTN, but not TBK1 gene expression across the CNS (D). OPTN is highly expressed in a control (E,H,K) and sporadic ALS (F,I,L) case but not the ALS-OPTN index case (G,J,M). Arrows highlight OPTN-immunoreactive inclusions. All scale bars = 50μm.

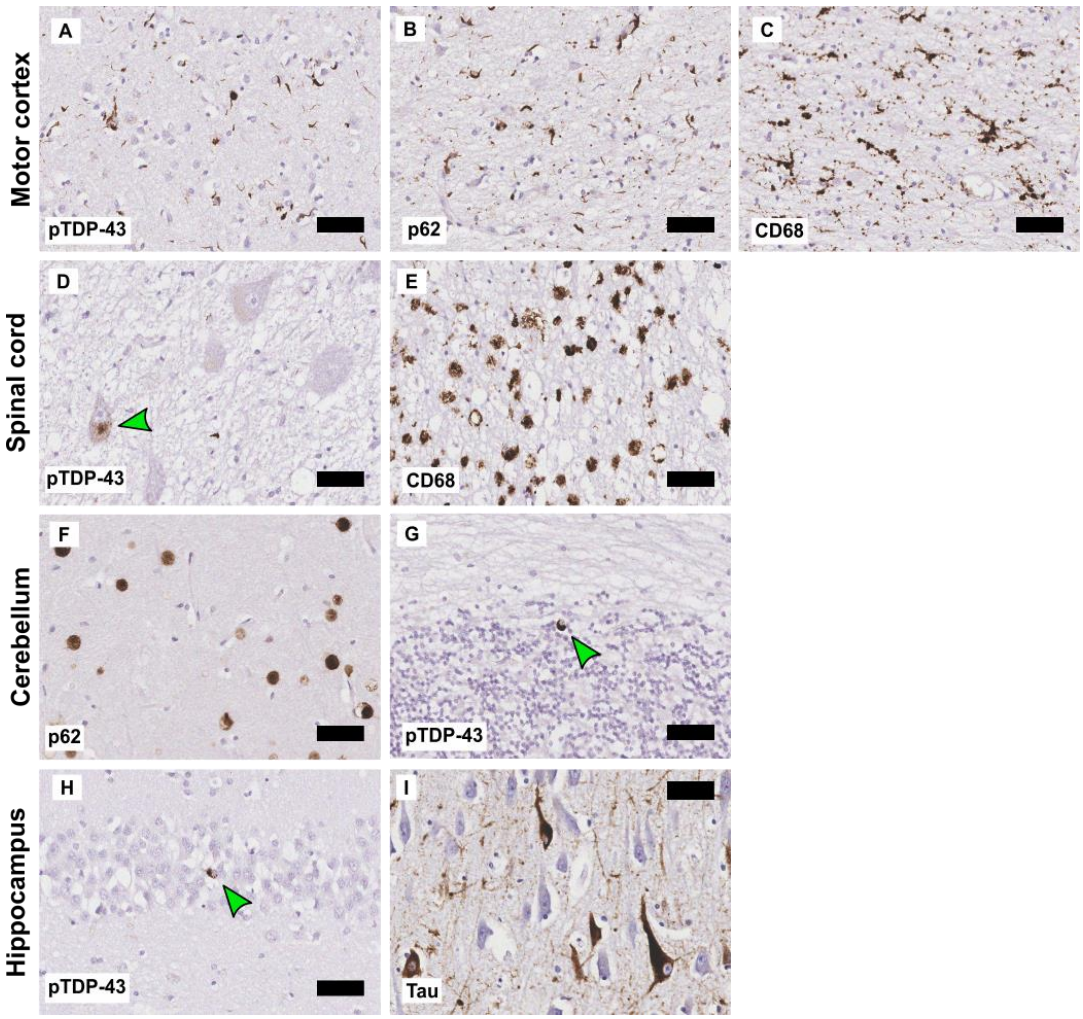

Figure 37: Neuropathology of the index case is defined by widespread TDP-proteinopathy, reactive gliosis and tau aggregation within hippocampal neurons. Extensive neuronal and oligodendroglial pTDP-43 aggregation in the primary motor cortex (A), but also limited glial inclusions within the cerebellum (F), hippocampus (H) and spinal cord α-motoneurons (D). There was also evidence of neuronal intracellular Tau aggregation within the dentate gyrus and CA regions (I). Extensive reactive microgliosis within the primary motor cortex, which was particularly prominent within the subcortical white matter (C) as well as within the lateral corticospinal tract (E). Extensive p62 aggregations in the primary motor cortex (B) and p62-positive corpora amylacea were also seen within the molecular layer of the cerebellum (G). There was no evidence of α-synuclein+ Lewy bodies, or significant β-amyloid accumulation in any of the assessed regions. Arrows highlight pTDP-43 inclusions. All scale bars = 50μm.

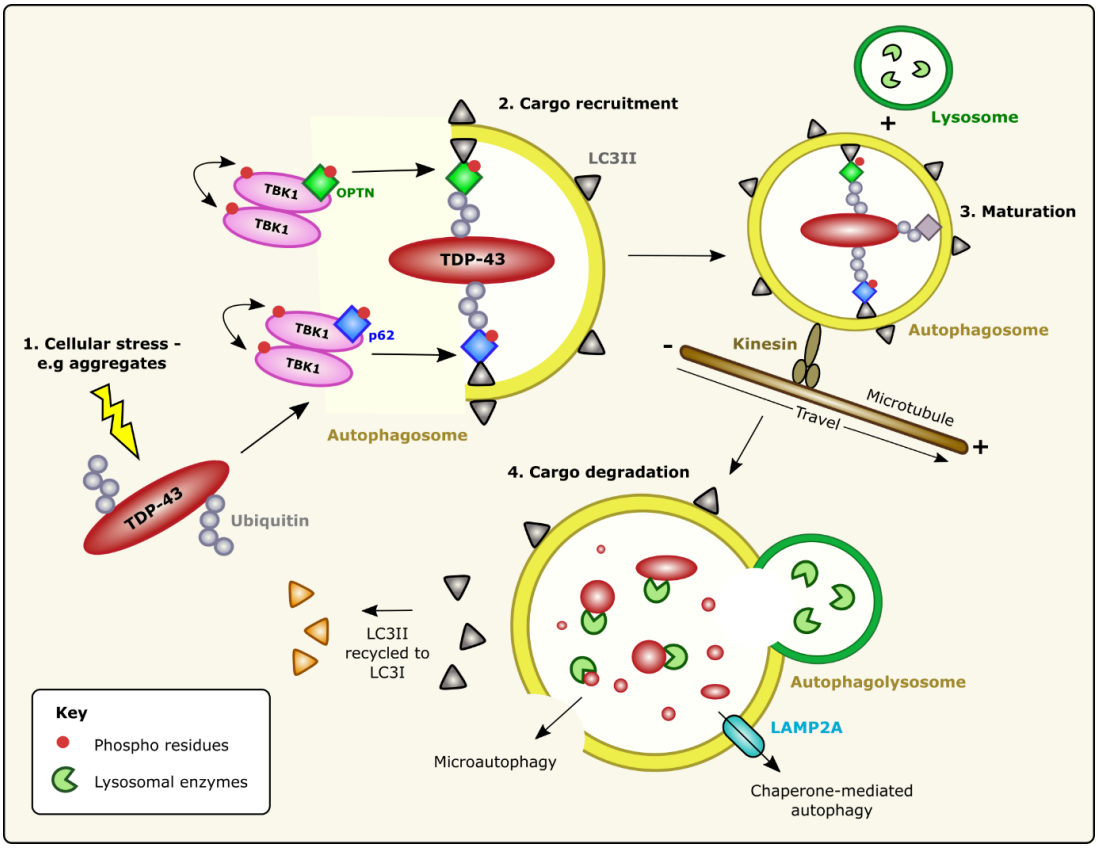

Figure 38: OPTN mediates the endosomal-lysosomal autophagy pathway through its interaction with TBK1. Cellular stress caused by pathogens, damaged mitochondria or aggregation pathology initiates the ubiquitination of the target cargo, in this case TDP-43 (1). Phosphorylation of TBK1 and one of four autophagic adaptor proteins (OPTN, p62, TAX1BP1, NDP52) facilitates the binding of the ubiquitinated cargo to LC3II on the immature autophagosome membrane (2). The autophagosome matures and is transported from the centre of the cell to the membrane along microtubules via the kinesin-dyenin motor unit (3). The lysosome merges with the autophagosome, where lysosomal enzymes degrade the target cargo (4). Some smaller cargos are taken up by the late-stage phagosome and excreted (microautophagy and chaperone-mediated autophagy). LC3II is delipidated and recycled as LC3I. C-terminal OPTN mutations prevent it's binding to ubiquitin and subsequently reduce the efficiency of its role in the endosomal-lysosomal pathway.

4.2.8 Conclusion

This case is unusual for two reasons. First, the vast majority of previously reported ALS-*OPTN* cases are heterozygous (Table 15), and the R217X mutation itself has never before been described. The effect of the mutation is likely loss-of-function through prevention of functional C-terminal domain translation as well as haploinsufficiency through nonsense mediated decay of affected transcripts. Secondly, both the atypical clinical progression pattern and neuropathology appear to be unique among previous reports. We describe the first case of UMN predominant ALS caused by the homozygous nonsense R217X mutation, which exists independently of all other known ALS/FTD mutations, and is one of the few ALS-*OPTN* cases with reported post-mortem neuropathology thus far. Our results strongly suggest that the mutation is LOF via degradation of affected transcripts via NMD and truncation of functional C-terminal protein domains, with the primary neuropathological consequence being a severe TDP-43 proteinopathy (Fig 37). This case has implications for our understanding of the role of *OPTN*-mediated autophagy pathway in ALS.

Chapter five

Discussion

5. Discussion

5.1 Main findings

The main findings in this thesis can be summarised as follows:

1. There is significant variability of motor cortex neuropathology both within and across the genotypic spectrum of ALS. Overall, sporadic cases display the most severe accumulation of pTDP-43 and activation of microglia. pTDP-43 deposition is moderately but significantly higher in sporadic cases than in *C9ORF72* disease, and the extent of the microglial response correlates with the severity of pTDP-43 deposition in both sporadic and C9 genotypes.
2. Sporadic ALS demonstrates the highest level of pathological homogeneity across the motor cortex-spinal cord neuraxis in terms of pTDP-43 aggregation and microglial proliferation.
3. There is a moderate but significant reduction of parvalbumin+ and calbindin+, but not calretinin+ interneurons within the ALS primary motor cortex, and this may be a contributor to the cortical hyperexcitability phenotype seen in ALS patients. Our results show this reduction is genotype specific and present even after statistical adjustment for fixation time and neuropathological predominance.
4. There is a clear vulnerability of specific cell types within the primary motor cortex to the aggregation of pTDP-43. Oligodendrocytes and excitatory neurons appear to be most severely affected, with parvalbumin+ interneurons and Betz cells less likely. At the glial cell level, microglia occasionally contain pTDP-43, but we found no evidence of pTDP-43 within GFAP+ astrocytes.
5. *FUS* is more highly expressed than *TARDBP* in the primary motor cortex, but *TARDBP* exhibits a higher proportion of transcripts localised to the nucleus.

5.2 Discussion

To the best of our knowledge, this is the largest post-mortem study to date on the primary motor cortex in ALS. A particular strength of the study is the use of digital image-analysis algorithms to provide a comprehensive, fully quantitative approach to pathological assessment. This provides a more defined readout of pathological burden than quasi-logarithmic 'scoring' methods - which are also more subject to human bias - and allows for the comparison of multiple pathologies with high-specificity. Our approach uses neuropathological readouts as quantitative traits which we consider to be more proximally related to genetic variables and pathobiology than dichotomous clinical data (e.g. ALS vs. control), which were limited, not quantitative and unlikely to be reflective of neuraxis involvement at the end stage of the disease. Given the multiple molecular and cellular pathways disrupted in ALS it is challenging to describe an overall hypothesis that accounts for all aspects of disease heterogeneity in humans, however a theoretical scenario is presented in Fig 39, that attempts to link preclinical and molecular evidence with the findings described in this thesis.

The first major finding from this study is that on average, sporadic patients demonstrate the most severe primary motor cortex pTDP-43 pathology, and that this is significantly higher than in *C9ORF72* disease (Fig 14G) which comprises the second largest group of ALS TDP-proteinopathies. Sporadic patients also display the highest microglial activation within the primary motor cortex (Fig 14I) which correlates closely with pTDP-43 severity (Fig 15). This suggests that sporadic ALS patients demonstrate on average a more severe cortical disease than *C9ORF72* patients. However, both the pTDP-43 and CD68 data is significantly skewed, showing that there is a high interindividual variance in pathology within each genotype. We presume that all of the cases used in this study, being post-

mortem, represent end-stage disease. While it is conceptually unclear why there should be such a variance in pathology, this variance can possibly be explained by the duration of the disease that the patient experiences. However detailed clinical information was not available for all cases, and this relationship could not be tested.

Microglial activation and proliferation is a prominent feature of ALS. Notably, the largest degree of microglial activation was found within the white matter of each genotype (Fig 14I). However the extent of activation between the white and grey matter was also closely correlated in all genotypes, i.e cases that demonstrated high microglial activation within the grey matter, also demonstrated high microglial activation in the white matter (Fig 18). The non-TDP-proteinopathies (i.e *SOD1* and *FUS* cases) demonstrated the lowest levels of microglial activation (Fig 14I). However, as we were unable to quantify the severity of the *FUS* and *SOD1* inclusions in these cases owing to the specificity of the antibodies, it is unclear whether this is a reflection of these cases being lower motor neuron predominant, or there being lower numbers of inclusions within the primary motor cortex. The extent of microglial activation correlated closely with the severity of pTDP-43 pathology in the primary motor cortex (Fig 15B and C). Given that pTDP-43 aggregation is the dominant pathology in 97% of ALS cases, it can be reasonably suggested that the mislocalisation and aggregation of TDP-43 is a driver of cortical microgliosis in ALS. However, it is acknowledged that by using post mortem human tissue we are ultimately only able to observe their correlation.

A key point in discussions concerning selective vulnerability is the distinction between cellular vulnerability to proteinopathy, and vulnerability to degeneration itself. The toxicity of TDP-43 has been demonstrated *in vitro* through a range of mechanisms including its effects on endocytosis, autophagy and stress-granule formation [174-176]. However, the cellular effect of this toxicity in humans is less well understood. On average,

in our cohort the most severe motor cortex pTDP-43 deposition was in sporadic ALS cases (Fig 14G), a finding which was also recapitulated at the level of the lumbar spinal cord within the anterior horn (Fig 17B). Our results show that of all the genotypes analysed, sporadic cases demonstrate the highest level of pathological homogeneity across the motor cortex-spinal cord neuraxis at post-mortem (Fig 19A&B). C9-ALS cases did not exhibit this homogeneity to the same degree. We also found that non-TDP-proteinopathies exhibit the highest levels of neuronal shrinkage/loss in the anterior horn (Fig 17J) and that the severity of pTDP-43 deposition does not correlate with anterior horn neuron degeneration (Fig 17K). This mirrors findings at the other end of the neuraxis in Betz cells [213], where the degeneration of Betz cells does not correlate with the severity of pathology. Similar to a previous study [203], we found little evidence of pTDP-43 aggregates within Betz cells themselves (Fig 27A-C) , although we did find evidence of severe microgliosis surrounding layer V neurons in several cases (Fig 27D), which has also been previously reported [375]. This raises interesting questions regarding whether Betz cells are perhaps selectively vulnerable to the toxicity conferred by soluble TDP-43 and its effects on microglia, selectively resistant to the aggregation of pTDP-43 which afflicts neighbouring neurons, or both. It is possible that Betz cells lack the capacity to insolubilize TDP-43, perhaps because of their larger size or metabolic activity, which precludes their vulnerability. In this hypothesis, the capacity of a cell to aggregate insoluble pTDP-43 actually represents a neuroprotective mechanism, a concept which has previously been suggested [328, 330]. Molecular characterisation of this anatomically unique cell will likely yield further insights.

Previous studies using $SOD1^{G93A}$ mice have strongly implicated oligodendrocyte dysfunction in ALS [204, 205]. Using human cortical tissue, we found evidence of oligodendrocyte pathology in nearly every case assessed in this study, demonstrating

cortical oligodendroglial proteinopathy as a defining feature of the disease. However, the mechanisms by which these aggregations cause dysfunction are unclear. Ferraiuolo et al (2016) showed reduced MN survival and altered axonal architecture when oligodendrocytes from ALS patients were co-cultured with disease free MN, and that this degeneration generally required close cell-to-cell proximity but could also be induced through the secretion of soluble factors [210]. It is plausible that a combination of both mechanisms occurs *in-vivo*, whereby pTDP-43 oligodendroglial pathology is an end stage result preceded by both cell-to-cell transmission and secretion of soluble TDP-43 which is toxic to surrounding motor neurons. Neuronal transmission of soluble TDP-43 has been demonstrated [212], but at the time of writing there have been no studies demonstrating its transmission either glia-glia or glia-neuron.

Whether the microglial response is in itself pathogenic in ALS or primarily a subsequent reactive event is debated. Our results show that the extent of this response in the primary motor cortex varies significantly between ALS genotypes (Fig 14I), and confirms findings *in vivo* concerning the difference in microglial burden between upper and lower motor neurons in sporadic ALS [376, 377](Fig 19). It is notable that comparably low numbers of cortical activated microglia were seen in *SOD1* and *FUS* cases, which are not TDP-proteinopathies, while the highest microglial response was seen in sporadic and *C9ORF72* cases, implicating TDP-43 as a driver of the microglial-based cortical inflammatory response. Both wild-type TDP-43 and its C-terminal fragments initiate CD14-mediated NF-κB activation as well as the intracellular NLRP3 proinflammatory cascade *in-vitro*, which is toxic to motor neurons [180, 181]. A recent study in mice found that the presence of TDP-43, not neurodegeneration, is responsible for an increase in microglial proliferation [183], however conversely, repressing mutant SOD1 within microglia in the $SOD1^{G93A}$ model does not delay disease onset but does significantly slow progression in

the later stages of disease [378]. It may therefore be speculated that the microglial response is both a primary pathogenic instigator and secondary reactive event, dependent on disease genotype, perhaps whereby a dominant mutation (presumably present in all cells including microglia) alters the microglial response to its corresponding proteinaceous inclusion. Functional *in vitro* studies utilising microglia conditionally expressing mutations in the various ALS genes will be required to ascertain this.

However, we demonstrate that the pTDP-43-microglial relationship is not entirely linear, because their correlation is not recapitulated in spinal cord lower motor neurons (Fig 17C). We also found several examples of pTDP-43 aggregates within microglia (Fig 24), though we cannot say whether these cells actively phagocytosed the aggregates, or the inclusions arose within the microglia as result of the disease process itself. Notably, we found no evidence of pTDP-43 inclusions within astroglia (Fig 25A-E) despite cortical astrogliosis being a prominent feature in ALS [345]. Further mechanistic studies will be required to determine the specificity of the microglial response in the various ALS genotypes.

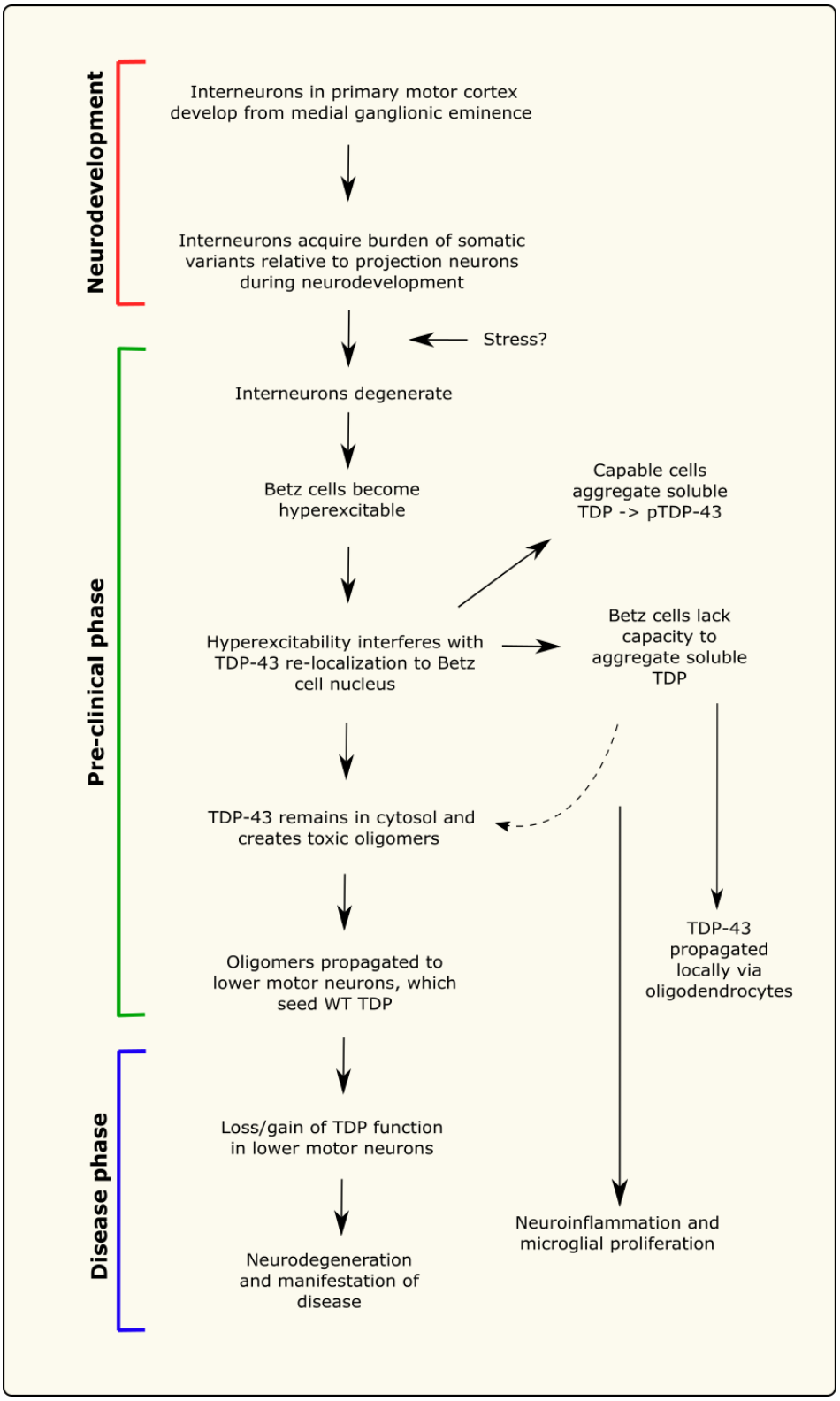

Figure 39: Suggested overall hypothesis of ALS pathogenesis, linking preclinical observations with post-mortem findings elaborated within this thesis.

The loss of GABAergic inhibitory interneurons within the cortex has been postulated to be the cause of a cortical hyperexcitability phenotype in ALS patients. Similar to a previous study using human cortical tissue [188], we demonstrate that there is a modest reduction of Calbindin+, but not Calretinin+ interneurons within the primary motor cortex in ALS (Fig 20 and Fig 21). However, given that ALS patients exhibit varying degrees of cortical involvement, we also attempted to reconcile interneuron numbers with the relative extent of upper/lower MN involvement to clarify whether interneuron loss was simply related to more severe cortical disease in general. Our results show that there is still a small, but statistically significant loss of interneurons in the primary motor cortex in some genotypes, even after adjustment for UMN/LMN predominance and fixation (Fig 21). The effect of this adjustment suggests that UMN/LMN predominance is a fairly large determinant of interneuron loss– i.e that ALS patients with a more severe motor cortical phenotype overall (the subtleties of which are not likely to be identifiable *in-vivo*) tend to exhibit a more severe interneuron loss in the cortex. However unexpectedly, we found the largest degree of interneuron loss in *SOD1*/*FUS* cases which are predominantly LMN disease genotypes. Conversely, we found only a moderate loss of interneurons in sporadic and *C9ORF72* cases, genotypes associated with the highest mean deposition of pTDP-43 (Fig 14G and Fig 21). There was no correlation between the severity of pTDP-43 deposition and the degree of interneuron loss in these cases (Fig 22), and we found almost no evidence of pTDP-43 inclusions occurring within parvalbumin+ interneurons themselves (Fig 26), which is consistent with a lack of TDP-43 mislocalization in parvalbumin+ interneurons in a recently published *tardbp* knock-in mouse model [335]. Together, this suggests that the reduction of interneurons in the ALS primary motor cortex is not dependent on the accumulation of pTDP-43, and that non-TDP genotypes demonstrate a larger selectively vulnerability to the degeneration of inhibitory

interneurons. This may be because it is not hyperphosporylated TDP but soluble C-terminal fragments of TDP which are the most damaging, or because dysfunction of *FUS/SOD1* is more detrimental to interneurons.

RNAscope is a novel RNA in-situ method which has only recently begun to be applied to human tissue in a significant way. Originally designed for use with surgical oncology and mouse tissue, the method presents significant challenges when used with human post-mortem material. Following optimisation and development of *in situ* specific algorithms it was possible to use the method to assess aspects of primary motor cortex histopathology. Firstly, it was found that *FUS* and *TARDBP* – two RNA binding proteins with similar structures and functions and both implicated in ALS – display very different expression and localisation patterns within the primary motor cortex (Fig 28 and 29). Relatively, *FUS* is far more highly expressed than *TARDBP*, but *TARDBP* displays a higher retention of transcripts within the nucleus. Unlike in a previous study, we found that this localisation of transcripts was unchanged between ALS and controls (Fig 29A&B)[157]. However, the aforementioned study analysed spinal neurons, and the expression and localisation of *TARDBP* transcripts was only quantified in a small number of cells. Here, the localisation of transcripts was quantified in >10,000 cells per case. Our results suggest that dysregulation of *TARDBP* expression may occur in the ALS primary motor cortex, but that the consequence of this dysregulation does not manifest as aberrant localisation. This is in sharp contrast to the pathological consequence of TDP-43 protein expression which is the mislocalisation and aggregation of pTDP-43 within the cytosol. The difference in expression between *FUS* and *TARDBP* is interesting, because both have similar functions, but *FUS* mutations are only implicated in a very small number of total ALS cases. It might be postulated that the relatively low expression of *TARDBP* makes it more vulnerable to physiological alterations. We could also find no clear interaction between *TARDBP* and

pTDP-43 aggregates (Fig 29C&D). However, assessment of this interaction was hampered by only chromogenic detection signals being available. Repeating these experiments using fluorescent-conjugates would allow the distinction between channels and facilitate more detailed analysis.

Next, the expression of three neuronal transcription factors (*CTIP2*, *SATB2* and *TBR1*) associated with projection neuron diversity was assessed within the primary motor cortex (Fig 30 & Fig 31). This was indicated in part because the projection patterns of Betz cells have not been molecularly defined in humans. However, it is noted that the expression of these transcription factors becomes more promiscuous during ageing to the point where they lose fidelity in adult mice. *CTIP2* is a transcription factor essential for the proper migration and development of corticospinal projection neurons [198, 201], and it has been previously shown that CTIP2-positive neurons degenerate early and specifically in the *SOD1* G93A mouse model [202]. However, while the SOD1 G93A model is probably the best available in terms of its recapitulation of an overt motor neuron phenotype, it is arguably not a good model of the underlying pathophysiological disease process because of a high copy number of transgene insertions leading to 4-fold overexpression of the mutant protein. We did not find any reduction in CTIP2+ neurons in the ALS primary motor cortex, when assessed by either IHC (Fig 30) or RNAscope (Fig 31). This is possibly because of the fairly low number of cases that were available at low fixation times, which was a prerequisite for the method. We also found preliminary evidence that all three transcription factors assessed are expressed in Betz cells at low levels relative to surrounding cells (Fig 32), suggesting that Betz cells are a distinct class of neuron which express a unique combination of genes post-mitotically. Further analysis, possibly using RNA-seq/proteomics, will increase our understanding of this unique cell.

The usage of novel methods such as CLARITY and Imaging Mass Cytometry (IMC) represent a glimpse of the future of tissue histopathology and their application in research. However, their implementation was challenging and produced sub-optimal results when attempted here. Both methods will require further adaptation and optimisation for use with human brain tissue before they are used on a wider scale.

The ALS-*OPTN* patient described in chapter 4 suffered a predominantly upper motor neuron syndrome with limited lower motor neuron involvement, but with some mild deficits in cognitive function. Post-mortem neuropathology was consistent with these features and was dominated by widespread TDP-43 proteinopathy within both white and grey matter neurons/oligodendroglia, as well as extensive cortical reactive microgliosis and transcortical spongiosis (Fig 37). The primary motor cortex was severely affected, with prominent depletion of layer V Betz cells and concomitant degeneration of the lateral corticospinal tract, but there was only limited TDP-43 pathology and degeneration of α-motoneurons within the spinal cord ventral grey column (Fig 37D). There was however evidence of predominantly intracellular neuronal AT8 accumulation within the dentate gyrus (Fig 37I) without obvious neurodegeneration, consistent with the mild cognitive deficit exhbited during life. OPTN contributes to the autophagic destruction of damaged mitochondria through the PINK1-Parkin mitophagy pathway [351]. Mutations to Parkin cause genetic Parkinsons disease (PD) [379], normally without Lewy body formation, implicating mitophagy as a pathomechanism in PD. However, in contrast to previous descriptions of 'multiple-proteinopathy' [362], there was no significant evidence of either α-synuclein or β-amyloid pathology, and no parkinsonian features in our patient.

As in previous studies [359-361], we found some evidence of OPTN-immunoreactive inclusions in a single comparitive sporadic ALS case (Fig 36F&I). However, it is unclear how many of these are OPTN-positive, TDP-43-negative inclusions. Co-localization of

OPTN with other proteinopathies has been reported in a number of neurodegenerative diseases [380] - including ALS [50] - however results are conflicting. Others haved noted the combined TDP-43, OPTN, ubiquitin- immunoreactivity of inclusions in sporadic ALS [50] and of OPTN with FUS in ALS-*FUS* [381], but not with SOD1 in ALS-*SOD1* [359], suggesting that OPTN does possesses some capacity to interact with RNA-binding proteins. Conversely, two studies using human tissue have reported that OPTN and TDP-43 co-localize only rarely [40, 361], and OPTN and TBK1 do occasionally co-localize with SOD1 aggregates in the $SOD1^{G93A}$ mouse [382]. No OPTN-ir inclusions were found in the index case described here. OPTN also possesses a C-terminal huntingtin (Htt) binding region, and infrequently co-localizes with Htt in the p62-positive intranuclear inclusions associated with Huntingtons disease [383, 384]. However, despite the location of the R217X mutation upstream of the Htt binding site, there was no indication of such intranuclear inclusions in our patient.

A primary role of OPTN is as an adapter protein in the autophagic clearance pathway, where it is phosphorylated and binds to TBK1 to facilitate the attachment of ubiquinated cargo to the autophagic membrane [351, 352]. TBK1 is known to interact with and phosphorylate OPTN at three serine residues (S177, S473 and S513) enhancing its ubiquitin (UBQ) binding capacity [351, 385]. Mutations in TBK1 have also been associated with ALS/FTD [356, 386, 387], however immunostaining for TBK1 revealed no obvious difference between case and controls (data not shown). One study described a UBQ-independent role for OPTN in autophagy, but this was configured on inclusion interaction with the OPTN C-terminal coiled-coil domain, which also lies downstream of the R217X mutation site. Additionally the authors did not investigate the role of this mechanism in the clearing of TDP-43 [382], which is the disease-defining pathology in around 95% ALS of cases and the main proteinopathy described here. As OPTN binds to

LC3II via its LIR domain and contributes to autophagosome maturation [388], we suggest that in this case the endosomal-lysosomal autophagy pathway itself is only inhibited as far as the role of OPTN within it is rendered impotent.

Given the site of the R217X mutation upstream of the coiled-coil, ubiquitin-binding and zinc finger domains, it seems likely that its effect is to prevent ubiquitin binding and subsequently inhibit the autophagic destruction of cytoplasmic TDP-43, as has been demonstrated *in vitro* for other *OPTN* mutations [389](Fig 38). A previous study also reported a homozgous *OPTN* nonsense mutation (Q398X) in a single patient, whose consanguineous parents were unaffected heterozygous carriers [50]. However its location would be likely to leave a majority of the ubiquitin-binding domain intact and therefore potentially functional. Notably however, homozygous mice lacking the entire UBQ C-terminal binding region of the mouse OPTN homologue display early embryonic lethality [355], suggesting possible compensatory mechanisms in the human autophagic process. Conditional deletion of mouse *optn* from oligodendrocytes and myeloid cells also results in progressive axonal degeneration without significant motor neuron cell body loss [353] suggesting a larger role within myelinating Schwann cells. Notably in our case, pTDP-43 aggregative pathology was at least as pronounced in oligodendroglia than in neurons. Nonsense mutations cause degradation of affected transcripts via nonsense mediated decay (NMD). Consistent with this, we also found a significant reduction in *OPTN* mRNA (~75%) across three regions of the CNS (Fig 36D), strongly implicating reduced *OPTN* gene expression as a pathogenic effect of the homozygous R217X mutation.

The neuroinflammatory response is a common feature of neurodegenerative disease, however whether this response is in itself pathogenic or a primary reactive event is debated. A recent ultrastructural study found that the OPTN ubiquitin binding domain is crucial for NF-κB supression [390], however mice lacking the entire OPTN C-terminal

domain exhibit normal NF-κB activation [355]. It is possible that the R217X mutation inhibits the normal suppression of RIPK1, enhancing necroptosis induced via tumour necrosis factor-α signalling [353], which would be consistent with the extensive reactive microgliosis in our patient. However at the time of writing the RIPK1 binding site for OPTN is unknown.

Interestingly, we found examples of p62-positive corpora amylacea (CA) across both cortical and subcortical regions, which were particularly prominent within the cerebellar molecular layer (Fig 37G). These glycoproteinaceous structures have been described in several neurological diseases [391, 392] including ALS [393], but also normal ageing [394], making their role and sigificance unclear. The age and genetic background in this index case however suggests that their presence may be disease related. It is unsual that CA would be present within the molecular layer, as this is mainly comprised of granular neuropil and purjkinje cell dendrites. It is possible that the majority of autophagy within these neurons is OPTN-mediated under normal conditions, such that p62 adaption alone is insufficient for the disposal of ubiquitinated cellular waste. Previous studies have associated CA with waste product recycling and disposal [392, 395]. OPTN also regulates intracellular vesicle trafficking as an adapter protein between myosin VI and specific cargoes [354]. As there appears to be increased OPTN expression in purkinje cells relative to other cerebellar neurons (Fig 36), and the R217X mutation is present upstream of the myosin VI binding site (Fig 36A), it is feasible that the disruption of these two roles combined contributes to the accumulation of CA in this case.

While mutations to both *FUS* and *OPTN* ultimately cause the degeneration of motor neurons and ALS as a broad phenotype, their molecular mechanisms, pathologies and specific clinical presentations are distinct. *FUS* is an RNA binding protein with a predominantly nuclear protein localization (Fig 16B), while *OPTN* is an autophagic

adapter with an almost exclusively cytosolic localization (Fig 36E&H). *FUS* mutations result in the mislocalization and aggregation of cellular FUS, while the primary neuropathological finding from the *OPTN* case described here is of an extreme TDP-43 proteinopathy. Additionally, the BAC-transgenic mutant *FUS* mouse described previously exhibits mislocalised FUS in every cell (Fig 33 and Fig 34) but does not develop a severe motor phenotype (data not shown). This is surprising because in humans the P525L mutation causes a severe phenotype and juvenile onset [105]. The discrepancy may be due to the BAC transgene not altering the expression of the endogenous mouse FUS, and it is possible that directly engineering the P525L mutation into the mouse gene itself (using CRISPR for example) may result in a more severe phenotype.

Conversely, the pathology of human *OPTN* case, while severe, does not affect every cell in the same way, despite the homozygous R217X mutation essentially causing a deletion of the functional C-terminal region. The seemingly completely different molecular basis for these two monogenic pathotypes - despite both specifically ultimately resulting in motor neuron degeneration – highlights the multi-factorial nature of sporadic ALS, and also suggests that the predominant mechanisms (if they exist) causing the sporadic form of the disease may vary from patient to patient.

The *FUS* cases assessed in this thesis, and those caused by the P525L mutation, are normally heterozygous and generally result in LMN predominant ALS with a severe disease progression, while the R217X *OPTN* mutation produced a distinct UMN phenotype with only limited LMN involvement and the patient dying in middle age. The reasons for this difference in onset, severity and distinct compartmental vulnerability to particular gene mutations are unclear, but may in part be due to the level of expression of each gene within upper and lower motor neurons, or differences in the requirements for the proper functioning of each gene between cells. However notably, we also found a

significant reduction in *OPTN* expression within the spinal cord of our index case (Fig 40D), suggesting that there are other factors (genetic or otherwise) influencing disease expression. While there is significant publicly available data regarding the expression of wild type genes across the human system (EBI, ENSEMBL, Human Protein Atlas etc) this is not true for the expression of ALS/FTD mutants in most tissues. A future study using RNA-seq or RT-qPCR to assess the expression levels of various ALS/FTD mutations in different tissue types across the human system is therefore warranted. Together, these observations pose considerable difficulties in developing treatments capable of biologically modifying the various levels of selective vulnerability in ALS, and lend weight to the idea that in future the distinct genetic forms of ALS should be considered separate diseases for the purposes of therapeutic design.

5.3 Methodical considerations

Our study contains several limitations. We analysed a region of the primary motor cortex corresponding to the hand region of the homunculus wherever possible, however we cannot guarantee that this region was analysed in every case, and it is possible that the expression of genes and proteins described in this paper vary across the somatotopically defined regions of the primary motor cortex. Secondly, we used IHC to measure the expression of proteins associated with three species of interneurons. However, although we used image-analysis algorithms that quantified staining above a certain OD threshold, we cannot say definitively whether we have measured a reduction in the number of these neurons, or a simple loss of expression of the protein in our cases. Additionally, we have not stratified our cases by hemisphere sampled, and it is possible that ALS pathology varies between the same region of different hemispheres. In the spinal cord, we have

attempted to circumvent this issue by assessing both aspects and averaging the results (Fig 12). We note that there is some evidence of asymmetrical TDP-43 pathology in Alzheimer's disease [396], but such asymmetry was not found in two cases of ALS-FTD [397]. The precise variation of ALS pathology across hemispheres is therefore of an unknown significance.

We also used CD68 to create a predominance ratio for each case that reflected the comparable levels of involvement between the primary motor cortex and lumbar spinal cord and could be used as a covariate in subsequent models (Fig 19). This was necessary because there is a degree of corticospinal motor neuron loss even in patients that display almost purely LMN signs [398]. Ideally neuronal loss itself would have been used to create a predominance indicator. However NeuN, the most commonly used pan-neuronal marker in mouse studies, displays a strong fixation dependency and is unsuitable for use with the kind of archival material used in the single-IHC of this study. We attempted to quantify the total numbers of neurons in each case using HuC/HuD, which has been shown previously to exhibit a similar staining pattern to NeuN [399]. However we found that HuC/HuD was also somewhat fixation dependent and quantification using HuC/HuD was unsuccessful (data not shown).

5.4 Conclusions

We used a quantitative immunohistochemical approach to comprehensively analyse pathology within the primary motor cortex in a large cohort of genetically-defined ALS cases, and our results refine the concept of selective vulnerability within the cortex at both the pathological and glial cell levels. We show that a key factor governing the vulnerability of the motor cortex is the overall genotype of the patient, but that pathology varies significantly both within and across the genotypic spectrum. At the cellular level, we show that while interneurons degenerate in the ALS motor cortex, they are less likely to demonstrate the aggregation of pTDP-43 pathology, demonstrating the distinction between cellular susceptibility to the development of proteinopathy and vulnerability to degeneration itself. This is of importance because aggregative pathology – of all kinds – may simply represent a successful cellular response to proteotoxicity. These results may provide targets for the design of future therapeutics through genotype-specific amelioration of cortical pathology.

6. References

1. Lind, D., et al., *Characterization of the neuronal marker NeuN as a multiply phosphorylated antigen with discrete subcellular localization.* J Neurosci Res, 2005. **79**(3): p. 295-302.

2. Gusel'nikova, V.V. and D.E. Korzhevskiy, *NeuN As a Neuronal Nuclear Antigen and Neuron Differentiation Marker.* Acta Naturae, 2015. **7**(2): p. 42-7.

3. Charcot, J., Joffroy, A. , *Deux cas d'atrophie musculaire progressive avec lesions de la substance grise et des faisceaux antero-lateraux de la moelle epiniere.* Arch. Physiol. Neurol. Pathol, 1869. **2**: p. 10.

4. Chio, A., et al., *Global epidemiology of amyotrophic lateral sclerosis: a systematic review of the published literature.* Neuroepidemiology, 2013. **41**(2): p. 118-30.

5. Huisman, M.H., et al., *Population based epidemiology of amyotrophic lateral sclerosis using capture-recapture methodology.* J Neurol Neurosurg Psychiatry, 2011. **82**(10): p. 1165-70.

6. del Aguila, M.A., et al., *Prognosis in amyotrophic lateral sclerosis: a population-based study.* Neurology, 2003. **60**(5): p. 813-9.

7. Al-Chalabi, A. and O. Hardiman, *The epidemiology of ALS: a conspiracy of genes, environment and time.* Nat Rev Neurol, 2013. **9**(11): p. 617-28.

8. Sutedja, N.A., et al., *Beneficial vascular risk profile is associated with amyotrophic lateral sclerosis.* J Neurol Neurosurg Psychiatry, 2011. **82**(6): p. 638-42.

9. Armon, C., *Smoking may be considered an established risk factor for sporadic ALS.* Neurology, 2009. **73**(20): p. 1693-8.

10. Sutedja, N.A., et al., *Exposure to chemicals and metals and risk of amyotrophic lateral sclerosis: a systematic review.* Amyotroph Lateral Scler, 2009. **10**(5-6): p. 302-9.

11. Plato, C.C., et al., *Amyotrophic lateral sclerosis and parkinsonism-dementia complex of Guam: changing incidence rates during the past 60 years.* Am J Epidemiol, 2003. **157**(2): p. 149-57.

12. Hirano, A., et al., *Amyotrophic lateral sclerosis and Parkinsonism-dementia complex on Guam. Further pathologic studies.* Arch Neurol, 1966. **15**(1): p. 35-51.

13. Ishiura, H., et al., *C9ORF72 repeat expansion in amyotrophic lateral sclerosis in the Kii peninsula of Japan.* Arch Neurol, 2012. **69**(9): p. 1154-8.

14. Kiernan, M.C., et al., *Amyotrophic lateral sclerosis.* Lancet, 2011. **377**(9769): p. 942-55.

15. Garg, N., et al., *Differentiating lower motor neuron syndromes.* J Neurol Neurosurg Psychiatry, 2017. **88**(6): p. 474-483.

16. Ludolph, A., et al., *A revision of the El Escorial criteria - 2015.* Amyotroph Lateral Scler Frontotemporal Degener, 2015. **16**(5-6): p. 291-2.

17. Turner, M.R. and K. Talbot, *Mimics and chameleons in motor neurone disease.* Pract Neurol, 2013. **13**(3): p. 153-64.

18. Foerster, B.R., R.C. Welsh, and E.L. Feldman, *25 years of neuroimaging in amyotrophic lateral sclerosis.* Nat Rev Neurol, 2013. **9**(9): p. 513-24.

19. Manole, A., P. Fratta, and H. Houlden, *Recent advances in bulbar syndromes: genetic causes and disease mechanisms.* Curr Opin Neurol, 2014. **27**(5): p. 506-14.

20. Wijesekera, L.C., et al., *Natural history and clinical features of the flail arm and flail leg ALS variants.* Neurology, 2009. **72**(12): p. 1087-94.

21. Kim, W.K., et al., *Study of 962 patients indicates progressive muscular atrophy is a form of ALS.* Neurology, 2009. **73**(20): p. 1686-92.

22. Ince, P.G., et al., *Corticospinal tract degeneration in the progressive muscular atrophy variant of ALS.* Neurology, 2003. **60**(8): p. 1252-8.

23. Tartaglia, M.C., et al., *Differentiation between primary lateral sclerosis and amyotrophic lateral sclerosis: examination of symptoms and signs at disease onset and during follow-up.* Arch Neurol, 2007. **64**(2): p. 232-6.

24. Turner, M.R., M.J. Parton, and P.N. Leigh, *Clinical trials in ALS: an overview.* Semin Neurol, 2001. **21**(2): p. 167-75.

25. Writing, G. and A.L.S.S.G. Edaravone, *Safety and efficacy of edaravone in well defined patients with amyotrophic lateral sclerosis: a randomised, double-blind, placebo-controlled trial.* Lancet Neurol, 2017. **16**(7): p. 505-512.

26. Al-Chalabi, A., et al., *July 2017 ENCALS statement on edaravone.* Amyotroph Lateral Scler Frontotemporal Degener, 2017. **18**(7-8): p. 471-474.

27. Ferrari, R., et al., *Frontotemporal dementia and its subtypes: a genome-wide association study.* Lancet Neurol, 2014. **13**(7): p. 686-99.

28. Bang, J., S. Spina, and B.L. Miller, *Frontotemporal dementia.* Lancet, 2015. **386**(10004): p. 1672-82.

29. Neary, D., et al., *Frontotemporal lobar degeneration: a consensus on clinical diagnostic criteria.* Neurology, 1998. **51**(6): p. 1546-54.

30. Rascovsky, K., et al., *Sensitivity of revised diagnostic criteria for the behavioural variant of frontotemporal dementia.* Brain, 2011. **134**(Pt 9): p. 2456-77.

31. Pressman, P.S. and B.L. Miller, *Diagnosis and management of behavioral variant frontotemporal dementia.* Biol Psychiatry, 2014. **75**(7): p. 574-81.

32. Shaw, P.J. and R. Williams, *Serum and cerebrospinal fluid biochemical markers of ALS.* Amyotroph Lateral Scler Other Motor Neuron Disord, 2000. **1 Suppl 2**: p. S61-7.

33. Phukan, J., N.P. Pender, and O. Hardiman, *Cognitive impairment in amyotrophic lateral sclerosis.* Lancet Neurol, 2007. **6**(11): p. 994-1003.

34. Talbot, K. and O. Ansorge, *Recent advances in the genetics of amyotrophic lateral sclerosis and frontotemporal dementia: common pathways in neurodegenerative disease.* Hum Mol Genet, 2006. **15 Spec No 2**: p. R182-7.

35. Rodriguez de Rivera, F.J., H.A. Rambold, and E. Diez-Tejedor, *Assessment of cognitive impairment in amyotrophic lateral sclerosis.* J Neurol Sci, 2014. **337**(1-2): p. 1-2.

36. Olney, R.K., et al., *The effects of executive and behavioral dysfunction on the course of ALS.* Neurology, 2005. **65**(11): p. 1774-7.

37. Van Langenhove, T., J. van der Zee, and C. Van Broeckhoven, *The molecular basis of the frontotemporal lobar degeneration-amyotrophic lateral sclerosis spectrum.* Ann Med, 2012. **44**(8): p. 817-28.

38. King, A., et al., *ALS-FUS pathology revisited: singleton FUS mutations and an unusual case with both a FUS and TARDBP mutation.* Acta Neuropathol Commun, 2015. **3**: p. 62.

39. van Blitterswijk, M., et al., *VAPB and C9orf72 mutations in 1 familial amyotrophic lateral sclerosis patient.* Neurobiol Aging, 2012. **33**(12): p. 2950 e1-4.

40. Bury, J.J., et al., *Oligogenic inheritance of optineurin (OPTN) and C9ORF72 mutations in ALS highlights localisation of OPTN in the TDP-43-negative inclusions of C9ORF72-ALS.* Neuropathology, 2015.

41. van Blitterswijk, M., et al., *Evidence for an oligogenic basis of amyotrophic lateral sclerosis.* Hum Mol Genet, 2012. **21**(17): p. 3776-84.

42. Hara, M., et al., *Lower motor neuron disease caused by a novel FUS/TLS gene frameshift mutation.* J Neurol, 2012. **259**(10): p. 2237-9.

43. Restagno, G., et al., *The rare G93D mutation causes a slowly progressing lower motor neuron disease.* Amyotroph Lateral Scler, 2008. **9**(1): p. 35-9.

44. Tumer, Z., et al., *Novel heterozygous nonsense mutation of the OPTN gene segregating in a Danish family with ALS.* Neurobiol Aging, 2012. **33**(1): p. 208 e1-5.

45. Parkinson, N., et al., *ALS phenotypes with mutations in CHMP2B (charged multivesicular body protein 2B).* Neurology, 2006. **67**(6): p. 1074-7.

46. Renton, A.E., et al., *A hexanucleotide repeat expansion in C9ORF72 is the cause of chromosome 9p21-linked ALS-FTD.* Neuron, 2011. **72**(2): p. 257-68.

47. Rosen, D.R., et al., *Mutations in Cu/Zn superoxide dismutase gene are associated with familial amyotrophic lateral sclerosis.* Nature, 1993. **362**(6415): p. 59-62.

48. Vance, C., et al., *Mutations in FUS, an RNA processing protein, cause familial amyotrophic lateral sclerosis type 6.* Science, 2009. **323**(5918): p. 1208-11.

49. Sreedharan, J., et al., *TDP-43 mutations in familial and sporadic amyotrophic lateral sclerosis.* Science, 2008. **319**(5870): p. 1668-72.

50. Maruyama, H., et al., *Mutations of optineurin in amyotrophic lateral sclerosis.* Nature, 2010. **465**(7295): p. 223-6.

51. Cox, L.E., et al., *Mutations in CHMP2B in lower motor neuron predominant amyotrophic lateral sclerosis (ALS).* PLoS One, 2010. **5**(3): p. e9872.

52. Kim, H.J., et al., *Mutations in prion-like domains in hnRNPA2B1 and hnRNPA1 cause multisystem proteinopathy and ALS.* Nature, 2013. **495**(7442): p. 467-73.

53. DeJesus-Hernandez, M., et al., *Expanded GGGGCC hexanucleotide repeat in noncoding region of C9ORF72 causes chromosome 9p-linked FTD and ALS.* Neuron, 2011. **72**(2): p. 245-56.

54. Ravits, J., et al., *Deciphering amyotrophic lateral sclerosis: what phenotype, neuropathology and genetics are telling us about pathogenesis.* Amyotroph Lateral Scler Frontotemporal Degener, 2013. **14 Suppl 1**: p. 5-18.

55. van Blitterswijk, M., De-Jesus-Hernandez, M. and Rademakers, R. , *How do C9ORF72 repeat expansions cause ALS and FTD: can we learn from other non-coding repeat expansion disorders?* Current Opinions in Neurology, 2012. **25**(6): p. 689-700.

56. Rizzu, P., et al., *C9orf72 is differentially expressed in the central nervous system and myeloid cells and consistently reduced in C9orf72, MAPT and GRN mutation carriers.* Acta Neuropathol Commun, 2016. **4**(1): p. 37.

57. Levine, T.P., et al., *The product of C9orf72, a gene strongly implicated in neurodegeneration, is structurally related to DENN Rab-GEFs.* Bioinformatics, 2013. **29**(4): p. 499-503.

58. Farg, M.A., et al., *C9ORF72, implicated in amytrophic lateral sclerosis and frontotemporal dementia, regulates endosomal trafficking.* Hum Mol Genet, 2014. **23**(13): p. 3579-95.

59. Aoki, Y., et al., *C9orf72 and RAB7L1 regulate vesicle trafficking in amyotrophic lateral sclerosis and frontotemporal dementia.* Brain, 2017. **140**(4): p. 887-897.

60. Dols-Icardo, O., et al., *Characterization of the repeat expansion size in C9orf72 in amyotrophic lateral sclerosis and frontotemporal dementia.* Hum Mol Genet, 2014. **23**(3): p. 749-54.

61. Nordin, A., et al., *Extensive size variability of the GGGGCC expansion in C9orf72 in both neuronal and non-neuronal tissues in 18 patients with ALS or FTD.* Hum Mol Genet, 2015. **24**(11): p. 3133-42.

62. Gijselinck, I., et al., *The C9orf72 repeat size correlates with onset age of disease, DNA methylation and transcriptional downregulation of the promoter.* Mol Psychiatry, 2016. **21**(8): p. 1112-24.

63. Ng, A.S.L. and E.K. Tan, *Intermediate C9orf72 alleles in neurological disorders: does size really matter?* J Med Genet, 2017. **54**(9): p. 591-597.

64. Waite, A.J., et al., *Reduced C9orf72 protein levels in frontal cortex of amyotrophic lateral sclerosis and frontotemporal degeneration brain with the C9ORF72 hexanucleotide repeat expansion.* Neurobiol Aging, 2014. **35**(7): p. 1779 e5-1779 e13.

65. Belzil, V.V., et al., *Reduced C9orf72 gene expression in c9FTD/ALS is caused by histone trimethylation, an epigenetic event detectable in blood.* Acta Neuropathol, 2013. **126**(6): p. 895-905.

66. Ciura, S., et al., *Loss of function of C9orf72 causes motor deficits in a zebrafish model of amyotrophic lateral sclerosis.* Ann Neurol, 2013. **74**(2): p. 180-7.

67. Therrien, M., et al., *Deletion of C9ORF72 results in motor neuron degeneration and stress sensitivity in C. elegans.* PLoS One, 2013. **8**(12): p. e83450.

68. Shi, Y., et al., *Haploinsufficiency leads to neurodegeneration in C9ORF72 ALS/FTD human induced motor neurons.* Nat Med, 2018.

69. Koppers, M., et al., *C9orf72 ablation in mice does not cause motor neuron degeneration or motor deficits.* Ann Neurol, 2015. **78**(3): p. 426-38.

70. Sudria-Lopez, E., et al., *Full ablation of C9orf72 in mice causes immune system-related pathology and neoplastic events but no motor neuron defects.* Acta Neuropathol, 2016. **132**(1): p. 145-7.

71. Atanasio, A., et al., *C9orf72 ablation causes immune dysregulation characterized by leukocyte expansion, autoantibody production, and glomerulonephropathy in mice.* Sci Rep, 2016. **6**: p. 23204.

72. Zhang, Y.J., et al., *C9ORF72 poly(GA) aggregates sequester and impair HR23 and nucleocytoplasmic transport proteins.* Nat Neurosci, 2016. **19**(5): p. 668-677.

73. Lopez-Gonzalez, R., et al., *Poly(GR) in C9ORF72-Related ALS/FTD Compromises Mitochondrial Function and Increases Oxidative Stress and DNA Damage in iPSC-Derived Motor Neurons.* Neuron, 2016. **92**(2): p. 383-391.

74. Zhang, Y.J., et al., *Aggregation-prone c9FTD/ALS poly(GA) RAN-translated proteins cause neurotoxicity by inducing ER stress.* Acta Neuropathol, 2014. **128**(4): p. 505-24.

75. Mizielinska, S., et al., *C9orf72 repeat expansions cause neurodegeneration in Drosophila through arginine-rich proteins.* Science, 2014. **345**(6201): p. 1192-1194.

76. Mackenzie, I.R., et al., *Quantitative analysis and clinico-pathological correlations of different dipeptide repeat protein pathologies in C9ORF72 mutation carriers.* Acta Neuropathol, 2015. **130**(6): p. 845-61.

77. Saberi, S., et al., *Sense-encoded poly-GR dipeptide repeat proteins correlate to neurodegeneration and uniquely co-localize with TDP-43 in dendrites of repeat-expanded C9orf72 amyotrophic lateral sclerosis.* Acta Neuropathol, 2018. **135**(3): p. 459-474.

78. Gomez-Deza, J., et al., *Dipeptide repeat protein inclusions are rare in the spinal cord and almost absent from motor neurons in C9ORF72 mutant amyotrophic lateral sclerosis and are unlikely to cause their degeneration.* Acta Neuropathol Commun, 2015. **3**: p. 38.

79. O'Rourke, J.G., et al., *C9orf72 BAC Transgenic Mice Display Typical Pathologic Features of ALS/FTD.* Neuron, 2015. **88**(5): p. 892-901.

80. Peters, O.M., et al., *Human C9ORF72 Hexanucleotide Expansion Reproduces RNA Foci and Dipeptide Repeat Proteins but Not Neurodegeneration in BAC Transgenic Mice.* Neuron, 2015. **88**(5): p. 902-9.

81. Liu, Y., et al., *C9orf72 BAC Mouse Model with Motor Deficits and Neurodegenerative Features of ALS/FTD.* Neuron, 2016. **90**(3): p. 521-34.

82. Vatsavayai, S.C., et al., *Timing and significance of pathological features in C9orf72 expansion-associated frontotemporal dementia.* Brain, 2016. **139**(Pt 12): p. 3202-3216.

83. McGoldrick, P., et al., *Unaffected mosaic C9orf72 case: RNA foci, dipeptide proteins, but upregulated C9orf72 expression.* Neurology, 2018. **90**(4): p. e323-e331.

84. Zu, T., et al., *RAN proteins and RNA foci from antisense transcripts in C9ORF72 ALS and frontotemporal dementia.* Proc Natl Acad Sci U S A, 2013. **110**(51): p. E4968-77.

85. Lee, Y.B., et al., *Hexanucleotide repeats in ALS/FTD form length-dependent RNA foci, sequester RNA binding proteins, and are neurotoxic.* Cell Rep, 2013. **5**(5): p. 1178-86.

86. Lagier-Tourenne, C., et al., *Targeted degradation of sense and antisense C9orf72 RNA foci as therapy for ALS and frontotemporal degeneration.* Proc Natl Acad Sci U S A, 2013. **110**(47): p. E4530-9.

87. Gendron, T.F., et al., *Mechanisms of toxicity in C9FTLD/ALS.* Acta Neuropathol, 2014. **127**(3): p. 359-76.

88. Conlon, E.G., et al., *The C9ORF72 GGGGCC expansion forms RNA G-quadruplex inclusions and sequesters hnRNP H to disrupt splicing in ALS brains.* Elife, 2016. **5**.

89. Cooper-Knock, J., et al., *Sequestration of multiple RNA recognition motif-containing proteins by C9orf72 repeat expansions.* Brain, 2014. **137**(Pt 7): p. 2040-51.

90. Cooper-Knock, J., et al., *Antisense RNA foci in the motor neurons of C9ORF72-ALS patients are associated with TDP-43 proteinopathy.* Acta Neuropathol, 2015. **130**(1): p. 63-75.

91. Deng, H., K. Gao, and J. Jankovic, *The role of FUS gene variants in neurodegenerative diseases.* Nat Rev Neurol, 2014. **10**(6): p. 337-48.

92. Tan, A.Y., et al., *TLS/FUS (translocated in liposarcoma/fused in sarcoma) regulates target gene transcription via single-stranded DNA response elements.* Proc Natl Acad Sci U S A, 2012. **109**(16): p. 6030-5.

93. Lagier-Tourenne, C., et al., *Divergent roles of ALS-linked proteins FUS/TLS and TDP-43 intersect in processing long pre-mRNAs.* Nat Neurosci, 2012. **15**(11): p. 1488-97.

94. Wang, W.Y., et al., *Interaction of FUS and HDAC1 regulates DNA damage response and repair in neurons.* Nat Neurosci, 2013. **16**(10): p. 1383-91.

95. Mastrocola, A.S., et al., *The RNA-binding protein fused in sarcoma (FUS) functions downstream of poly(ADP-ribose) polymerase (PARP) in response to DNA damage.* J Biol Chem, 2013. **288**(34): p. 24731-41.

96. Andersson, M.K., et al., *The multifunctional FUS, EWS and TAF15 proto-oncoproteins show cell type-specific expression patterns and involvement in cell spreading and stress response.* BMC Cell Biol, 2008. **9**: p. 37.

97. Brelstaff, J., et al., *Transportin1: a marker of FTLD-FUS.* Acta Neuropathol, 2011. **122**(5): p. 591-600.

98. Bosco, D.A., et al., *Mutant FUS proteins that cause amyotrophic lateral sclerosis incorporate into stress granules.* Hum Mol Genet, 2010. **19**(21): p. 4160-75.

99. Bentmann, E., et al., *Requirements for stress granule recruitment of fused in sarcoma (FUS) and TAR DNA-binding protein of 43 kDa (TDP-43).* J Biol Chem, 2012. **287**(27): p. 23079-94.

100. Daigle, J.G., et al., *RNA-binding ability of FUS regulates neurodegeneration, cytoplasmic mislocalization and incorporation into stress granules associated with FUS carrying ALS-linked mutations.* Hum Mol Genet, 2013. **22**(6): p. 1193-205.

101. Vance, C., et al., *ALS mutant FUS disrupts nuclear localization and sequesters wild-type FUS within cytoplasmic stress granules.* Hum Mol Genet, 2013. **22**(13): p. 2676-88.

102. Kabashi, E., et al., *FUS and TARDBP but not SOD1 interact in genetic models of amyotrophic lateral sclerosis.* PLoS Genet, 2011. **7**(8): p. e1002214.

103. Rademakers, R., et al., *Fus gene mutations in familial and sporadic amyotrophic lateral sclerosis.* Muscle Nerve, 2010. **42**(2): p. 170-6.

104. Huang, E.J., et al., *Extensive FUS-immunoreactive pathology in juvenile amyotrophic lateral sclerosis with basophilic inclusions.* Brain Pathol, 2010. **20**(6): p. 1069-76.

105. Baumer, D., et al., *Juvenile ALS with basophilic inclusions is a FUS proteinopathy with FUS mutations.* Neurology, 2010. **75**(7): p. 611-8.

106. Mochizuki, Y., et al., *Familial ALS with FUS P525L mutation: two Japanese sisters with multiple systems involvement.* J Neurol Sci, 2012. **323**(1-2): p. 85-92.

107. Kent, L., et al., *Autosomal dominant inheritance of rapidly progressive amyotrophic lateral sclerosis due to a truncation mutation in the fused in sarcoma (FUS) gene.* Amyotroph Lateral Scler Frontotemporal Degener, 2014. **15**(7-8): p. 557-62.

108. Mackenzie, I.R., et al., *Pathological heterogeneity in amyotrophic lateral sclerosis with FUS mutations: two distinct patterns correlating with disease severity and mutation.* Acta Neuropathol, 2011. **122**(1): p. 87-98.

109. Al-Chalabi, A., et al., *The genetics and neuropathology of amyotrophic lateral sclerosis.* Acta Neuropathol, 2012. **124**(3): p. 339-52.

110. Corrado, L., et al., *Mutations of FUS gene in sporadic amyotrophic lateral sclerosis.* J Med Genet, 2010. **47**(3): p. 190-4.

111. Ticozzi, N., et al., *Analysis of FUS gene mutation in familial amyotrophic lateral sclerosis within an Italian cohort.* Neurology, 2009. **73**(15): p. 1180-5.

112. Snowden, J.S., Hu, Q., Rollinson, S., Halliwell, N., Robinson, A., Davidson, Y.S., Momeni, P., Baborie, A., Griffiths, T.D., Jaros, E., Perry, R.H., Richardson, A., Pickering-Brown, S.M., Neary, D., Mann, D.M., *The most common type of FTLD-FUS (aFTLD-U) is associated with a distinct clinical*

form of frontotemporal dementia but is not related to mutations in the FUS gene. Acta Neuropathologica, 2011. **122**(1): p. 99-110.

113. Mackenzie, I.R., R. Rademakers, and M. Neumann, *TDP-43 and FUS in amyotrophic lateral sclerosis and frontotemporal dementia.* Lancet Neurol, 2010. **9**(10): p. 995-1007.

114. Neumann, M., et al., *A new subtype of frontotemporal lobar degeneration with FUS pathology.* Brain, 2009. **132**(Pt 11): p. 2922-31.

115. Huey, E.D., et al., *FUS and TDP43 genetic variability in FTD and CBS.* Neurobiol Aging, 2012. **33**(5): p. 1016 e9-17.

116. Van Langenhove, T., et al., *Genetic contribution of FUS to frontotemporal lobar degeneration.* Neurology, 2010. **74**(5): p. 366-71.

117. Mackenzie, I.R., et al., *Nomenclature and nosology for neuropathologic subtypes of frontotemporal lobar degeneration: an update.* Acta Neuropathol, 2010. **119**(1): p. 1-4.

118. Yokota, O., et al., *Basophilic inclusion body disease and neuronal intermediate filament inclusion disease: a comparative clinicopathological study.* Acta Neuropathol, 2008. **115**(5): p. 561-75.

119. Mackenzie, I.R., et al., *Distinct pathological subtypes of FTLD-FUS.* Acta Neuropathol, 2011. **121**(2): p. 207-18.

120. Neumann, M., et al., *Abundant FUS-immunoreactive pathology in neuronal intermediate filament inclusion disease.* Acta Neuropathol, 2009. **118**(5): p. 605-16.

121. Munoz, D.G., et al., *FUS pathology in basophilic inclusion body disease.* Acta Neuropathol, 2009. **118**(5): p. 617-27.

122. Tateishi, T., et al., *Multiple system degeneration with basophilic inclusions in Japanese ALS patients with FUS mutation.* Acta Neuropathol, 2010. **119**(3): p. 355-64.

123. Bedford, M.T. and S.G. Clarke, *Protein arginine methylation in mammals: who, what, and why.* Mol Cell, 2009. **33**(1): p. 1-13.

124. Rappsilber, J., et al., *Detection of arginine dimethylated peptides by parallel precursor ion scanning mass spectrometry in positive ion mode.* Anal Chem, 2003. **75**(13): p. 3107-14.

125. Du, K., et al., *TLS and PRMT1 synergistically coactivate transcription at the survivin promoter through TLS arginine methylation.* Biochem Biophys Res Commun, 2011. **404**(4): p. 991-6.

126. Tradewell, M.L., et al., *Arginine methylation by PRMT1 regulates nuclear-cytoplasmic localization and toxicity of FUS/TLS harbouring ALS-linked mutations.* Hum Mol Genet, 2012. **21**(1): p. 136-49.

127. Dormann, D., et al., *Arginine methylation next to the PY-NLS modulates Transportin binding and nuclear import of FUS.* EMBO J, 2012. **31**(22): p. 4258-75.

128. Suarez-Calvet, M., et al., *Monomethylated and unmethylated FUS exhibit increased binding to Transportin and distinguish FTLD-FUS from ALS-FUS.* Acta Neuropathol, 2016.

129. Deng, Q., et al., *FUS is phosphorylated by DNA-PK and accumulates in the cytoplasm after DNA damage.* J Neurosci, 2014. **34**(23): p. 7802-13.

130. Darovic, S., et al., *Phosphorylation of C-terminal tyrosine residue 526 in FUS impairs its nuclear import.* J Cell Sci, 2015. **128**(22): p. 4151-9.

131. Guerreiro, R., J. Bras, and J. Hardy, *SnapShot: Genetics of ALS and FTD.* Cell, 2015. **160**(4): p. 798 e1.

132. Arai, T., et al., *TDP-43 is a component of ubiquitin-positive tau-negative inclusions in frontotemporal lobar degeneration and amyotrophic lateral sclerosis.* Biochem Biophys Res Commun, 2006. **351**(3): p. 602-11.

133. Neumann, M., et al., *Ubiquitinated TDP-43 in frontotemporal lobar degeneration and amyotrophic lateral sclerosis.* Science, 2006. **314**(5796): p. 130-3.

134. Ju, S., et al., *A yeast model of FUS/TLS-dependent cytotoxicity.* PLoS Biol, 2011. **9**(4): p. e1001052.

135. Lanson, N.A., Jr., et al., *A Drosophila model of FUS-related neurodegeneration reveals genetic interaction between FUS and TDP-43.* Hum Mol Genet, 2011. **20**(13): p. 2510-23.

136. Murakami, T., et al., *ALS mutations in FUS cause neuronal dysfunction and death in Caenorhabditis elegans by a dominant gain-of-function mechanism.* Hum Mol Genet, 2012. **21**(1): p. 1-9.

137. Kuroda, M., et al., *Male sterility and enhanced radiation sensitivity in TLS(-/-) mice.* EMBO J, 2000. **19**(3): p. 453-62.

138. Kino, Y., et al., *FUS/TLS deficiency causes behavioral and pathological abnormalities distinct from amyotrophic lateral sclerosis.* Acta Neuropathol Commun, 2015. **3**: p. 24.

139. Armstrong, G.A. and P. Drapeau, *Loss and gain of FUS function impair neuromuscular synaptic transmission in a genetic model of ALS.* Hum Mol Genet, 2013. **22**(21): p. 4282-92.

140. Verbeeck, C., et al., *Expression of Fused in sarcoma mutations in mice recapitulates the neuropathology of FUS proteinopathies and provides insight into disease pathogenesis.* Mol Neurodegener, 2012. **7**: p. 53.

141. Mitchell, J.C., et al., *Overexpression of human wild-type FUS causes progressive motor neuron degeneration in an age- and dose-dependent fashion.* Acta Neuropathol, 2013. **125**(2): p. 273-88.

142. Sephton, C.F., et al., *Activity-dependent FUS dysregulation disrupts synaptic homeostasis.* Proc Natl Acad Sci U S A, 2014. **111**(44): p. E4769-78.

143. O'Rourke, J.G., et al., *C9orf72 BAC Transgenic Mice Display Typical Pathologic Features of ALS/FTD.* Neuron, 2015. **88**(5): p. 892-901.

144. Pasinelli, P. and R.H. Brown, *Molecular biology of amyotrophic lateral sclerosis: insights from genetics.* Nat Rev Neurosci, 2006. **7**(9): p. 710-23.

145. Jones, C.T., et al., *Cu/Zn superoxide dismutase (SOD1) mutations and sporadic amyotrophic lateral sclerosis.* Lancet, 1993. **342**(8878): p. 1050-1.

146. Valentine, J.S., P.A. Doucette, and S. Zittin Potter, *Copper-zinc superoxide dismutase and amyotrophic lateral sclerosis.* Annu Rev Biochem, 2005. **74**: p. 563-93.

147. Andersen, P.M., et al., *Amyotrophic lateral sclerosis associated with homozygosity for an Asp90Ala mutation in CuZn-superoxide dismutase.* Nat Genet, 1995. **10**(1): p. 61-6.

148. Hand, C.K., et al., *Compound heterozygous D90A and D96N SOD1 mutations in a recessive amyotrophic lateral sclerosis family.* Ann Neurol, 2001. **49**(2): p. 267-71.

149. Radunovic, A. and P.N. Leigh, *Cu/Zn superoxide dismutase gene mutations in amyotrophic lateral sclerosis: correlation between genotype and clinical features.* J Neurol Neurosurg Psychiatry, 1996. **61**(6): p. 565-72.

150. Battistini, S., et al., *SOD1 mutations in amyotrophic lateral sclerosis. Results from a multicenter Italian study.* J Neurol, 2005. **252**(7): p. 782-8.

151. Borchelt, D.R., et al., *Superoxide dismutase 1 with mutations linked to familial amyotrophic lateral sclerosis possesses significant activity.* Proc Natl Acad Sci U S A, 1994. **91**(17): p. 8292-6.

152. Dion, P.A., H. Daoud, and G.A. Rouleau, *Genetics of motor neuron disorders: new insights into pathogenic mechanisms.* Nat Rev Genet, 2009. **10**(11): p. 769-82.

153. Kabashi, E., et al., *TARDBP mutations in individuals with sporadic and familial amyotrophic lateral sclerosis.* Nat Genet, 2008. **40**(5): p. 572-4.

154. Gendron, T.F., R. Rademakers, and L. Petrucelli, *TARDBP mutation analysis in TDP-43 proteinopathies and deciphering the toxicity of mutant TDP-43.* J Alzheimers Dis, 2013. **33 Suppl 1**: p. S35-45.

155. Bose, J.K., et al., *TDP-43 Overexpression Enhances Exon 7 Inclusion during the Survival of Motor Neuron Pre-mRNA Splicing.* Journal of Biological Chemistry, 2008. **283**(43): p. 28852-28859.

156. Ayala, Y.M., et al., *TDP-43 regulates its mRNA levels through a negative feedback loop.* EMBO J, 2011. **30**(2): p. 277-88.

157. Koyama, A., et al., *Increased cytoplasmic TARDBP mRNA in affected spinal motor neurons in ALS caused by abnormal autoregulation of TDP-43.* Nucleic Acids Res, 2016. **44**(12): p. 5820-36.

158. Ling, J.P., et al., *TDP-43 repression of nonconserved cryptic exons is compromised in ALS-FTD.* Science, 2015. **349**(6248): p. 650-5.

159. Kraemer, B.C., et al., *Loss of murine TDP-43 disrupts motor function and plays an essential role in embryogenesis.* Acta Neuropathol, 2010. **119**(4): p. 409-19.

160. Martin-Serrano, J., et al., *Divergent retroviral late-budding domains recruit vacuolar protein sorting factors by using alternative adaptor proteins.* Proc Natl Acad Sci U S A, 2003. **100**(21): p. 12414-9.

161. Skibinski, G., et al., *Mutations in the endosomal ESCRTIII-complex subunit CHMP2B in frontotemporal dementia.* Nat Genet, 2005. **37**(8): p. 806-8.

162. Guo, L., et al., *Nuclear-Import Receptors Reverse Aberrant Phase Transitions of RNA-Binding Proteins with Prion-like Domains.* Cell, 2018. **173**(3): p. 677-692 e20.

163. Honda, H., et al., *Loss of hnRNPA1 in ALS spinal cord motor neurons with TDP-43-positive inclusions.* Neuropathology, 2015. **35**(1): p. 37-43.

164. Cady, J., et al., *Amyotrophic lateral sclerosis onset is influenced by the burden of rare variants in known amyotrophic lateral sclerosis genes.* Ann Neurol, 2015. **77**(1): p. 100-13.

165. Aston, C.E., et al., *Oligogenic combinations associated with breast cancer risk in women under 53 years of age.* Hum Genet, 2005. **116**(3): p. 208-21.

166. Priest, J.R., et al., *De Novo and Rare Variants at Multiple Loci Support the Oligogenic Origins of Atrioventricular Septal Heart Defects.* PLoS Genet, 2016. **12**(4): p. e1005963.

167. Sykiotis, G.P., et al., *Oligogenic basis of isolated gonadotropin-releasing hormone deficiency.* Proc Natl Acad Sci U S A, 2010. **107**(34): p. 15140-4.

168. Zaghloul, N.A., et al., *Functional analyses of variants reveal a significant role for dominant negative and common alleles in oligogenic Bardet-Biedl syndrome.* Proc Natl Acad Sci U S A, 2010. **107**(23): p. 10602-7.

169. Kenna, K.P., et al., *Delineating the genetic heterogeneity of ALS using targeted high-throughput sequencing.* Journal of Medical Genetics, 2013. **50**(11): p. 776-783.

170. Morgan, S., et al., *A comprehensive analysis of rare genetic variation in amyotrophic lateral sclerosis in the UK.* Brain, 2017. **140**(6): p. 1611-1618.

171. Udaka, F., et al., *MRI and SPECT findings in amyotrophic lateral sclerosis. Demonstration of upper motor neurone involvement by clinical neuroimaging.* Neuroradiology, 1992. **34**(5): p. 389-93.

172. Douaud, G., et al., *Integration of structural and functional magnetic resonance imaging in amyotrophic lateral sclerosis.* Brain, 2011. **134**(Pt 12): p. 3470-9.

173. Schuster, C., et al., *Focal thinning of the motor cortex mirrors clinical features of amyotrophic lateral sclerosis and their phenotypes: a neuroimaging study.* J Neurol, 2013. **260**(11): p. 2856-64.

174. Johnson, B.S., et al., *TDP-43 is intrinsically aggregation-prone, and amyotrophic lateral sclerosis-linked mutations accelerate aggregation and increase toxicity.* J Biol Chem, 2009. **284**(30): p. 20329-39.

175. Liu, G., et al., *Endocytosis regulates TDP-43 toxicity and turnover.* Nat Commun, 2017. **8**(1): p. 2092.

176. Kim, H.J., et al., *Therapeutic modulation of eIF2 alpha phosphorylation rescues TDP-43 toxicity in amyotrophic lateral sclerosis disease models.* Nature Genetics, 2014. **46**(2): p. 152-+.

177. Mitra, J., et al., *Motor neuron disease-associated loss of nuclear TDP-43 is linked to DNA double-strand break repair defects.* Proc Natl Acad Sci U S A, 2019.

178. Philips, T. and W. Robberecht, *Neuroinflammation in amyotrophic lateral sclerosis: role of glial activation in motor neuron disease.* Lancet Neurol, 2011. **10**(3): p. 253-63.

179. Clement, A.M., et al., *Wild-type nonneuronal cells extend survival of SOD1 mutant motor neurons in ALS mice.* Science, 2003. **302**(5642): p. 113-7.

180. Zhao, W., et al., *TDP-43 activates microglia through NF-kappaB and NLRP3 inflammasome.* Exp Neurol, 2015. **273**: p. 24-35.

181. Frakes, A.E., et al., *Microglia induce motor neuron death via the classical NF-kappaB pathway in amyotrophic lateral sclerosis.* Neuron, 2014. **81**(5): p. 1009-1023.

182. Paolicelli, R.C., et al., *TDP-43 Depletion in Microglia Promotes Amyloid Clearance but Also Induces Synapse Loss.* Neuron, 2017. **95**(2): p. 297-308 e6.

183. Spiller, K.J., et al., *Microglia-mediated recovery from ALS-relevant motor neuron degeneration in a mouse model of TDP-43 proteinopathy.* Nat Neurosci, 2018. **21**(3): p. 329-340.

184. Cramer, G.D., Darby, S.A. , *Clinical Anatomy of the Spine, Spinal Cord and ANS*. 3rd ed. 2014: Elsevier.

185. Kook, S.Y., et al., *Crucial role of calbindin-D28k in the pathogenesis of Alzheimer's disease mouse model.* Cell Death Differ, 2014. **21**(10): p. 1575-87.

186. Chance, S.A., M. Walker, and T.J. Crow, *Reduced density of calbindin-immunoreactive interneurons in the planum temporale in schizophrenia.* Brain Res, 2005. **1046**(1-2): p. 32-7.

187. Marin, O., *Interneuron dysfunction in psychiatric disorders.* Nat Rev Neurosci, 2012. **13**(2): p. 107-20.

188. Maekawa, S., et al., *Cortical selective vulnerability in motor neuron disease: a morphometric study.* Brain, 2004. **127**(Pt 6): p. 1237-51.

189. Menon, P., M.C. Kiernan, and S. Vucic, *Cortical hyperexcitability precedes lower motor neuron dysfunction in ALS.* Clin Neurophysiol, 2015. **126**(4): p. 803-9.

190. Turner, M.R. and M.C. Kiernan, *Does interneuronal dysfunction contribute to neurodegeneration in amyotrophic lateral sclerosis?* Amyotroph Lateral Scler, 2012. **13**(3): p. 245-50.

191. Foerster, B.R., et al., *An imbalance between excitatory and inhibitory neurotransmitters in amyotrophic lateral sclerosis revealed by use of 3-T proton magnetic resonance spectroscopy.* JAMA Neurol, 2013. **70**(8): p. 1009-16.

192. Lloyd, C.M., et al., *Extramotor involvement in ALS: PET studies with the GABA(A) ligand [(11)C]flumazenil.* Brain, 2000. **123 (Pt 11)**: p. 2289-96.

193. Zhang, W., et al., *Hyperactive somatostatin interneurons contribute to excitotoxicity in neurodegenerative disorders.* Nat Neurosci, 2016. **19**(4): p. 557-559.

194. Clark, R.M., et al., *Calretinin and Neuropeptide Y interneurons are differentially altered in the motor cortex of the SOD1G93A mouse model of ALS.* Sci Rep, 2017. **7**: p. 44461.

195. Ince, P., et al., *Parvalbumin and calbindin D-28k in the human motor system and in motor neuron disease.* Neuropathol Appl Neurobiol, 1993. **19**(4): p. 291-9.

196. Nihei, K., A.C. McKee, and N.W. Kowall, *Patterns of neuronal degeneration in the motor cortex of amyotrophic lateral sclerosis patients.* Acta Neuropathol, 1993. **86**(1): p. 55-64.

197. Bedogni, F., et al., *Tbr1 regulates regional and laminar identity of postmitotic neurons in developing neocortex.* Proc Natl Acad Sci U S A, 2010. **107**(29): p. 13129-34.

198. Arlotta, P., et al., *Neuronal subtype-specific genes that control corticospinal motor neuron development in vivo.* Neuron, 2005. **45**(2): p. 207-21.

199. Alcamo, E.A., et al., *Satb2 regulates callosal projection neuron identity in the developing cerebral cortex.* Neuron, 2008. **57**(3): p. 364-77.

200. Britanova, O., et al., *Satb2 is a postmitotic determinant for upper-layer neuron specification in the neocortex.* Neuron, 2008. **57**(3): p. 378-92.

201. Molyneaux, B.J., et al., *Neuronal subtype specification in the cerebral cortex.* Nat Rev Neurosci, 2007. **8**(6): p. 427-37.

202. Ozdinler, P.H., et al., *Corticospinal motor neurons and related subcerebral projection neurons undergo early and specific neurodegeneration in hSOD1G(9)(3)A transgenic ALS mice.* J Neurosci, 2011. **31**(11): p. 4166-77.

203. Braak, H., et al., *Pathological TDP-43 changes in Betz cells differ from those in bulbar and spinal alpha-motoneurons in sporadic amyotrophic lateral sclerosis.* Acta Neuropathol, 2017. **133**(1): p. 79-90.

204. Philips, T., et al., *Oligodendrocyte dysfunction in the pathogenesis of amyotrophic lateral sclerosis.* Brain, 2013. **136**(Pt 2): p. 471-82.

205. Kang, S.H., et al., *Degeneration and impaired regeneration of gray matter oligodendrocytes in amyotrophic lateral sclerosis.* Nat Neurosci, 2013. **16**(5): p. 571-9.

206. Filippi, M., et al., *Multiple sclerosis.* Nat Rev Dis Primers, 2018. **4**(1): p. 43.

207. Whalley, K., *Repair: Mobilizing stem cells.* Nat Rev Neurosci, 2015. **16**(11): p. 646.

208. Li, Q., et al., *Nexilin Regulates Oligodendrocyte Progenitor Cell Migration and Remyelination and Is Negatively Regulated by Protease-Activated Receptor 1/Ras-Proximate-1 Signaling Following Subarachnoid Hemorrhage.* Front Neurol, 2018. **9**: p. 282.

209. McKenzie, I.A., et al., *Motor skill learning requires active central myelination.* Science, 2014. **346**(6207): p. 318-22.

210. Ferraiuolo, L., et al., *Oligodendrocytes contribute to motor neuron death in ALS via SOD1-dependent mechanism.* Proc Natl Acad Sci U S A, 2016. **113**(42): p. E6496-E6505.

211. Rohan, Z., et al., *Oligodendroglial response in the spinal cord in TDP-43 proteinopathy with motor neuron involvement.* Neurodegener Dis, 2014. **14**(3): p. 117-24.

212. Feiler, M.S., et al., *TDP-43 is intercellularly transmitted across axon terminals.* J Cell Biol, 2015. **211**(4): p. 897-911.

213. Fatima, M., et al., *Spread of pathology in amyotrophic lateral sclerosis: assessment of phosphorylated TDP-43 along axonal pathways.* Acta Neuropathol Commun, 2015. **3**: p. 47.

214. Brettschneider, J., et al., *Stages of pTDP-43 pathology in amyotrophic lateral sclerosis.* Ann Neurol, 2013. **74**(1): p. 20-38.

215. Saint-Aubert, L., et al., *Tau PET imaging: present and future directions.* Mol Neurodegener, 2017. **12**(1): p. 19.

216. Zilber, L.A., et al., *Study of the Etiology of Amyotrophic Lateral Sclerosis.* Bull World Health Organ, 1963. **29**: p. 449-56.

217. Geevasinga, N., et al., *Pathophysiological and diagnostic implications of cortical dysfunction in ALS.* Nat Rev Neurol, 2016. **12**(11): p. 651-661.

218. Kiernan, J.A. and A.J. Hudson, *Changes in sizes of cortical and lower motor neurons in amyotrophic lateral sclerosis.* Brain, 1991. **114 (Pt 2)**: p. 843-53.

219. Fogarty, M.J., P.G. Noakes, and M.C. Bellingham, *Motor cortex layer V pyramidal neurons exhibit dendritic regression, spine loss, and increased synaptic excitation in the presymptomatic hSOD1(G93A) mouse model of amyotrophic lateral sclerosis.* J Neurosci, 2015. **35**(2): p. 643-7.

220. Fogarty, M.J., et al., *Cortical synaptic and dendritic spine abnormalities in a presymptomatic TDP-43 model of amyotrophic lateral sclerosis.* Sci Rep, 2016. **6**: p. 37968.

221. Melamed, Z., et al., *Premature polyadenylation-mediated loss of stathmin-2 is a hallmark of TDP-43-dependent neurodegeneration.* Nat Neurosci, 2019. **22**(2): p. 180-190.

222. Klim, J.R., et al., *ALS-implicated protein TDP-43 sustains levels of STMN2, a mediator of motor neuron growth and repair.* Nat Neurosci, 2019. **22**(2): p. 167-179.

223. Gould, T.W., et al., *Complete dissociation of motor neuron death from motor dysfunction by Bax deletion in a mouse model of ALS.* J Neurosci, 2006. **26**(34): p. 8774-86.

224. Poulopoulos, A., et al., *Subcellular transcriptomes and proteomes of developing axon projections in the cerebral cortex.* Nature, 2019. **565**(7739): p. 356-360.

225. Nijssen, J., L.H. Comley, and E. Hedlund, *Motor neuron vulnerability and resistance in amyotrophic lateral sclerosis.* Acta Neuropathol, 2017. **133**(6): p. 863-885.

226. Filezac de L'Etang, A., et al., *Marinesco-Sjogren syndrome protein SIL1 regulates motor neuron subtype-selective ER stress in ALS.* Nat Neurosci, 2015. **18**(2): p. 227-38.

227. Brockington, A., et al., *Unravelling the enigma of selective vulnerability in neurodegeneration: motor neurons resistant to degeneration in ALS show distinct gene expression characteristics and decreased susceptibility to excitotoxicity.* Acta Neuropathol, 2013. **125**(1): p. 95-109.

228. Mizuno, Y., et al., *Comparison of phosphorylated TDP-43-positive inclusions in oculomotor neurons in patients with non-ALS and ALS disorders.* J Neurol Sci, 2012. **315**(1-2): p. 20-5.

229. Coffman, K.A., R.P. Dum, and P.L. Strick, *Cerebellar vermis is a target of projections from the motor areas in the cerebral cortex.* Proc Natl Acad Sci U S A, 2011. **108**(38): p. 16068-73.

230. Brodmann, K., *Vergleichende Lokalisationslehre der Grosshirnrinde in ihren Prinzipien dargestellt auf Grund des Zellenbaues*. 1909, Leipzig: Johann Ambrosius Barth.

231. Woolsey, C.N., et al., *Patterns of localization in precentral and "supplementary" motor areas and their relation to the concept of a premotor area.* Res Publ Assoc Res Nerv Ment Dis, 1952. **30**: p. 238-64.

232. Penfield, W., *The interpretive cortex; the stream of consciousness in the human brain can be electrically reactivated.* Science, 1959. **129**(3365): p. 1719-25.

233. Schieber, M.H. and L.S. Hibbard, *How somatotopic is the motor cortex hand area?* Science, 1993. **261**(5120): p. 489-92.

234. Rathelot, J.A. and P.L. Strick, *Muscle representation in the macaque motor cortex: an anatomical perspective.* Proc Natl Acad Sci U S A, 2006. **103**(21): p. 8257-62.

235. Silverstein, J., *Mapping the motor and sensory cortices: a historical look and a current case study in sensorimotor localization and direct cortical motor stimulation.* Neurodiagn J, 2012. **52**(1): p. 54-68.

236. Griffin, D.M., D.S. Hoffman, and P.L. Strick, *Corticomotoneuronal cells are "functionally tuned".* Science, 2015. **350**(6261): p. 667-70.

237. Amunts, K., et al., *Interhemispheric asymmetry of the human motor cortex related to handedness and gender.* Neuropsychologia, 2000. **38**(3): p. 304-12.

238. Volkmann, J., et al., *Handedness and asymmetry of hand representation in human motor cortex.* J Neurophysiol, 1998. **79**(4): p. 2149-54.

239. Amunts, K., A. Schleicher, and K. Zilles, *Cytoarchitecture of the cerebral cortex--more than localization.* Neuroimage, 2007. **37**(4): p. 1061-5; discussion 1066-8.

240. Dancause, N., et al., *Extensive cortical rewiring after brain injury.* J Neurosci, 2005. **25**(44): p. 10167-79.

241. Braak, H. and E. Braak, *The pyramidal cells of Betz within the cingulate and precentral gigantopyramidal field in the human brain. A Golgi and pigmentarchitectonic study.* Cell Tissue Res, 1976. **172**(1): p. 103-19.

242. Schleicher, A. and K. Zilles, *A quantitative approach to cytoarchitectonics: analysis of structural inhomogeneities in nervous tissue using an image analyser.* J Microsc, 1990. **157**(Pt 3): p. 367-81.

243. Kushchayev, S.V., et al., *The discovery of the pyramidal neurons: Vladimir Betz and a new era of neuroscience.* Brain, 2012. **135**(Pt 1): p. 285-300.

244. Betz, W., *Anatomischer Nachweis zweier Gehirncentra.* Centralblatt für die medizinischen Wissenschaften., 1874. **12**: p. 578-580, 595-599.

245. Hall, J.E., *Textbook of Medical Physiology*. 13th ed. 2015: Elsevier. 1168.

246. Rivara, C.B., et al., *Stereologic characterization and spatial distribution patterns of Betz cells in the human primary motor cortex.* Anat Rec A Discov Mol Cell Evol Biol, 2003. **270**(2): p. 137-51.

247. Lassek, A.M., *The human pyramidal tract. II. A numerical investigation of the Betz cells of the motor area.* Arch Neurol Psychiatry, 1940. **46**: p. 718-724.

248. Kaneko, T., M.A. Caria, and H. Asanuma, *Information processing within the motor cortex. II. Intracortical connections between neurons receiving somatosensory cortical input and motor output neurons of the cortex.* J Comp Neurol, 1994. **345**(2): p. 172-84.

249. Meyer, G., *Forms and spatial arrangement of neurons in the primary motor cortex of man.* J Comp Neurol, 1987. **262**(3): p. 402-28.

250. Campbell, A.W., *Histological studies on the localization of cerebral function*. 1905, London: Cambridge University Press.

251. Scheibel, M.E. and A.B. Scheibel, *The dendritic structure of the human Betz cell*. Architectonics of the cerebral cortex, ed. P.H. Brazier MAB. 1978, New York: Raven Press.

252. Hausen, D., et al., *Pyramidal cells ensheathed by perineuronal nets in human motor and somatosensory cortex.* Neuroreport, 1996. **7**(11): p. 1725-9.

253. Ho, K.C., et al., *Correlation of neuronal cell body size in motor cortex and hippocampus with body height, body weight, and axonal length.* Int J Neurosci, 1992. **65**(1-4): p. 147-53.

254. Sasaki, S. and M. Iwata, *Ultrastructural study of Betz cells in the primary motor cortex of the human brain.* J Anat, 2001. **199**(Pt 6): p. 699-708.

255. Groos, W.P., et al., *Organization of corticospinal neurons in the cat.* Brain Res, 1978. **143**(3): p. 393-419.

256. Phillips, C.G., *Actions of antidromic pyramidal volleys on single Betz cells in the cat.* Q J Exp Physiol Cogn Med Sci, 1959. **44**(1): p. 1-25.

257. Sherwood, C.C., et al., *Evolution of specialized pyramidal neurons in primate visual and motor cortex.* Brain Behav Evol, 2003. **61**(1): p. 28-44.

258. Takeuchi, T. and S. Sugita, *Cytoarchitectonic study of the cerebral cortex in the horse brain--classification of the cortex area.* Kaibogaku Zasshi, 2001. **76**(2): p. 213-21.

259. Jacobs, B., et al., *Comparative morphology of gigantopyramidal neurons in primary motor cortex across mammals.* J Comp Neurol, 2017.

260. Ichinohe, N., et al., *A voltage-gated potassium channel, Kv3.1b, is expressed by a subpopulation of large pyramidal neurons in layer 5 of the macaque monkey cortex.* Neuroscience, 2004. **129**(1): p. 179-85.

261. Seppanen, A., et al., *Distribution of collagen XVII in the human brain.* Brain Res, 2007. **1158**: p. 50-6.

262. Claudepierre, T., et al., *Collagen XVII and BPAG1 expression in the retina: evidence for an anchoring complex in the central nervous system.* J Comp Neurol, 2005. **487**(2): p. 190-203.

263. Franzke, C.W., P. Bruckner, and L. Bruckner-Tuderman, *Collagenous transmembrane proteins: recent insights into biology and pathology.* J Biol Chem, 2005. **280**(6): p. 4005-8.

264. Levin, M.C., et al., *Autoimmunity due to molecular mimicry as a cause of neurological disease.* Nat Med, 2002. **8**(5): p. 509-13.

265. Tebbenkamp, A.T.N., et al., *The 7q11.23 Protein DNAJC30 Interacts with ATP Synthase and Links Mitochondria to Brain Development.* Cell, 2018. **175**(4): p. 1088-1104 e23.

266. Matelli, M., G. Luppino, and G. Rizzolatti, *Patterns of cytochrome oxidase activity in the frontal agranular cortex of the macaque monkey.* Behav Brain Res, 1985. **18**(2): p. 125-36.

267. Preuss, T.M. and J.H. Kaas, *Parvalbumin-like immunoreactivity of layer V pyramidal cells in the motor and somatosensory cortex of adult primates.* Brain Res, 1996. **712**(2): p. 353-7.

268. Shen, Q., et al., *The timing of cortical neurogenesis is encoded within lineages of individual progenitor cells.* Nat Neurosci, 2006. **9**(6): p. 743-51.

269. Lance, J.W. and R.L. Manning, *Origin of the pyramidal tract in the cat.* J Physiol, 1954. **124**(2): p. 385-99.

270. Daroff, R., Aminoff, M.J. , *Encyclopaedia of the Neurological Sciences*. 2nd ed. 2014: Elsevier. 4740.

271. Schwindt, P.C., W.J. Spain, and W.E. Crill, *Calcium-dependent potassium currents in neurons from cat sensorimotor cortex.* J Neurophysiol, 1992. **67**(1): p. 216-26.

272. Schwindt, P.C., W.J. Spain, and W.E. Crill, *Influence of anomalous rectifier activation on afterhyperpolarizations of neurons from cat sensorimotor cortex in vitro.* J Neurophysiol, 1988. **59**(2): p. 468-81.

273. Phillips, C.G., *Intracellular records from Betz cells in the cat.* Q J Exp Physiol Cogn Med Sci, 1956. **41**(1): p. 58-69.

274. Oswald, M.J., et al., *Diversity of layer 5 projection neurons in the mouse motor cortex.* Front Cell Neurosci, 2013. **7**: p. 174.

275. Hooks, B.M., et al., *Organization of cortical and thalamic input to pyramidal neurons in mouse motor cortex.* J Neurosci, 2013. **33**(2): p. 748-60.

276. Marin-Padilla, M., *Prenatal and early postnatal ontogenesis of the human motor cortex: a golgi study. I. The sequential development of the cortical layers.* Brain Res, 1970. **23**(2): p. 167-83.

277. Conel, J.L., *The Postnatal Development of the Human Cerebral Cortex*

The Postnatal Development of the Human Cerebral Cortex. 1939-1947, Oxford, UK: Harvard University Press.

278. Tigges, J., J.G. Herndon, and A. Peters, *Axon terminals on Betz cell somata of area 4 in rhesus monkey throughout adulthood.* Anat Rec, 1992. **232**(2): p. 305-15.

279. Scheibel, M.E., U. Tomiyasu, and A.B. Scheibel, *The aging human Betz cell.* Exp Neurol, 1977. **56**(3): p. 598-609.

280. Tsuchiya, K., et al., *Pathological heterogeneity of the precentral gyrus in Pick's disease: a study of 16 autopsy cases.* Acta Neuropathol, 2006. **112**(1): p. 29-42.

281. Wakabayashi, K., et al., *Lewy bodies in Betz cells of the motor cortex in a patient with Parkinson's disease.* Acta Neuropathol, 2003. **105**(2): p. 189-92.

282. Tsuchiya, K., et al., *Constant and severe involvement of Betz cells in corticobasal degeneration is not consistent with pyramidal signs: a clinicopathological study of ten autopsy cases.* Acta Neuropathol, 2005. **109**(4): p. 353-66.

283. Tsuchiya, K., et al., *Constant involvement of the Betz cells and pyramidal tract in multiple system atrophy: a clinicopathological study of seven autopsy cases.* Acta Neuropathol, 2000. **99**(6): p. 628-36.

284. Oyanagi, K., et al., *Galactosialidosis: neuropathological findings in a case of the late-infantile type.* Acta Neuropathol, 1991. **82**(5): p. 331-9.

285. Koeppen, A.H. and J.E. Mazurkiewicz, *Friedreich ataxia: neuropathology revised.* J Neuropathol Exp Neurol, 2013. **72**(2): p. 78-90.

286. Fischer, L.R., et al., *Amyotrophic lateral sclerosis is a distal axonopathy: evidence in mice and man.* Exp Neurol, 2004. **185**(2): p. 232-40.

287. Sharma, A., et al., *ALS-associated mutant FUS induces selective motor neuron degeneration through toxic gain of function.* Nat Commun, 2016. **7**: p. 10465.

288. Magrane, J., et al., *Abnormal mitochondrial transport and morphology are common pathological denominators in SOD1 and TDP43 ALS mouse models.* Hum Mol Genet, 2014. **23**(6): p. 1413-24.

289. Toft, M.H., O. Gredal, and B. Pakkenberg, *The size distribution of neurons in the motor cortex in amyotrophic lateral sclerosis.* J Anat, 2005. **207**(4): p. 399-407.

290. Gredal, O., et al., *Unchanged total number of neurons in motor cortex and neocortex in amyotrophic lateral sclerosis: a stereological study.* J Neurosci Methods, 2000. **95**(2): p. 171-6.

291. Pioro, E.P., et al., *Detection of cortical neuron loss in motor neuron disease by proton magnetic resonance spectroscopic imaging in vivo.* Neurology, 1994. **44**(10): p. 1933-8.

292. Hammer, R.P., Jr., U. Tomiyasu, and A.B. Scheibel, *Degeneration of the human Betz cell due to amyotrophic lateral sclerosis.* Exp Neurol, 1979. **63**(2): p. 336-46.

293. Coan, G. and C.S. Mitchell, *An Assessment of Possible Neuropathology and Clinical Relationships in 46 Sporadic Amyotrophic Lateral Sclerosis Patient Autopsies.* Neurodegener Dis, 2015. **15**(5): p. 301-12.

294. Mochizuki, Y., et al., *Proportional neuronal loss between the primary motor and sensory cortex in amyotrophic lateral sclerosis.* Neurosci Lett, 2011. **503**(1): p. 73-5.

295. Kuo, P.H., et al., *Structural insights into TDP-43 in nucleic-acid binding and domain interactions.* Nucleic Acids Res, 2009. **37**(6): p. 1799-808.

296. Murayama, S., T.W. Bouldin, and K. Suzuki, *Selective sparing of Betz cells in primary motor area in hypoxic-ischemic encephalopathy.* Acta Neuropathol, 1990. **80**(5): p. 560-2.

297. Fujita, Y., et al., *Fragmentation of the Golgi apparatus of Betz cells in patients with amyotrophic lateral sclerosis.* J Neurol Sci, 1999. **163**(1): p. 81-5.

298. Fujita, Y. and K. Okamoto, *Golgi apparatus of the motor neurons in patients with amyotrophic lateral sclerosis and in mice models of amyotrophic lateral sclerosis.* Neuropathology, 2005. **25**(4): p. 388-94.

299. Sasaki, S. and S. Maruyama, *Immunocytochemical and ultrastructural studies of the motor cortex in amyotrophic lateral sclerosis.* Acta Neuropathol, 1994. **87**(6): p. 578-85.

300. Udaka, F., M. Kameyama, and M. Tomonaga, *Degeneration of Betz cells in motor neuron disease. A Golgi study.* Acta Neuropathol, 1986. **70**(3-4): p. 289-95.

301. Genc, B., et al., *Apical dendrite degeneration, a novel cellular pathology for Betz cells in ALS.* Sci Rep, 2017. **7**: p. 41765.

302. Jara, J.H., et al., *AAV2 mediated retrograde transduction of corticospinal motor neurons reveals initial and selective apical dendrite degeneration in ALS.* Neurobiol Dis, 2012. **47**(2): p. 174-83.

303. Pringle, C.E., et al., *Primary lateral sclerosis. Clinical features, neuropathology and diagnostic criteria.* Brain, 1992. **115 (Pt 2)**: p. 495-520.

304. Fink, J.K., *Hereditary spastic paraplegia: clinico-pathologic features and emerging molecular mechanisms.* Acta Neuropathol, 2013. **126**(3): p. 307-28.

305. Seidel, K., et al., *Widespread thalamic and cerebellar degeneration in a patient with a complicated hereditary spastic paraplegia (HSP).* Ann Anat, 2009. **191**(2): p. 203-11.

306. Araki, S., et al., *Neuropathological analysis in spinal muscular atrophy type II.* Acta Neuropathol, 2003. **106(**5): p. 441-8.

307. Huang, K. and Y. Luo, *Adult spinal muscular atrophy. A report of four cases.* J Neurol Sci, 1983. **61**(2): p. 249-59.

308. Hoche, F., et al., *Spinocerebellar ataxia type 2 (SCA2): identification of early brain degeneration in one monozygous twin in the initial disease stage.* Cerebellum, 2011. **10**(2): p. 245-53.

309. Gierga, K., et al., *Spinocerebellar ataxia type 6 (SCA6): neurodegeneration goes beyond the known brain predilection sites.* Neuropathol Appl Neurobiol, 2009. **35**(5): p. 515-27.

310. Welniarz, Q., I. Dusart, and E. Roze, *The corticospinal tract: Evolution, development, and human disorders.* Dev Neurobiol, 2017. **77**(7): p. 810-829.

311. Sloper, J.J. and T.P. Powell, *Gap junctions between dendrites and somata of neurons in the primate sensori-motor cortex.* Proc R Soc Lond B Biol Sci, 1978. **203**(1150): p. 39-47.

312. Kaiserman-Abramof, I.R. and A. Peters, *Some aspects of the morphology of Betz cells in the cerebral cortex of the cat.* Brain Res, 1972. **43**(2): p. 527-46.

313. Uhlen, M., et al., *A proposal for validation of antibodies.* Nat Methods, 2016. **13**(10): p. 823-7.

314. Baker, M., *Reproducibility crisis: Blame it on the antibodies.* Nature, 2015. **521**(7552): p. 274-6.

315. Spalteholz, W., *Uber das Durchsichtigmachen von menschlichen und tierischen Praparaten* S. Hierzel, 1914.

316. Richardson, D.S. and J.W. Lichtman, *Clarifying Tissue Clearing.* Cell, 2015. **162**(2): p. 246-257.

317. Chung, K. and K. Deisseroth, *CLARITY for mapping the nervous system.* Nat Methods, 2013. **10**(6): p. 508-13.

318. Chung, K., et al., *Structural and molecular interrogation of intact biological systems.* Nature, 2013. **497**(7449): p. 332-7.

319. Perbellini, F., et al., *Free-of-Acrylamide SDS-based Tissue Clearing (FASTClear) for three dimensional visualization of myocardial tissue.* Sci Rep, 2017. **7**(1): p. 5188.

320. Wang, F., et al., *RNAscope: a novel in situ RNA analysis platform for formalin-fixed, paraffin-embedded tissues.* J Mol Diagn, 2012. **14**(1): p. 22-9.

321. Wang, Z., et al., *Automated quantitative RNA in situ hybridization for resolution of equivocal and heterogeneous ERBB2 (HER2) status in invasive breast carcinoma.* J Mol Diagn, 2013. **15**(2): p. 210-9.

322. Aebersold, R. and M. Mann, *Mass spectrometry-based proteomics.* Nature, 2003. **422**(6928): p. 198-207.

323. Giesen, C., et al., *Highly multiplexed imaging of tumor tissues with subcellular resolution by mass cytometry.* Nat Methods, 2014. **11**(4): p. 417-22.

324. Schulz, D., et al., *Simultaneous Multiplexed Imaging of mRNA and Proteins with Subcellular Resolution in Breast Cancer Tissue Samples by Mass Cytometry.* Cell Syst, 2018. **6**(4): p. 531.

325. Talbot, K., *Amyotrophic lateral sclerosis: cell vulnerability or system vulnerability?* J Anat, 2014. **224**(1): p. 45-51.

326. Braak, H., et al., *Amyotrophic lateral sclerosis--a model of corticofugal axonal spread.* Nat Rev Neurol, 2013. **9**(12): p. 708-14.

327. Bankhead, P., et al., *QuPath: Open source software for digital pathology image analysis.* Sci Rep, 2017. **7**(1): p. 16878.

328. Guo, T., W. Noble, and D.P. Hanger, *Roles of tau protein in health and disease.* Acta Neuropathol, 2017. **133**(5): p. 665-704.

329. Cowan, C.M. and A. Mudher, *Are tau aggregates toxic or protective in tauopathies?* Front Neurol, 2013. **4**: p. 114.

330. Baloh, R.H., *TDP-43: the relationship between protein aggregation and neurodegeneration in amyotrophic lateral sclerosis and frontotemporal lobar degeneration.* FEBS J, 2011. **278**(19): p. 3539-49.

331. Sidhu, A., et al., *The role of alpha-synuclein in both neuroprotection and neurodegeneration.* Ann N Y Acad Sci, 2004. **1035**: p. 250-70.

332. Kalia, L.V. and A.E. Lang, *Parkinson's disease.* Lancet, 2015. **386**(9996): p. 896-912.

333. McGown, A., et al., *Early interneuron dysfunction in ALS: insights from a mutant sod1 zebrafish model.* Ann Neurol, 2013. **73**(2): p. 246-58.

334. Hossaini, M., et al., *Spinal inhibitory interneuron pathology follows motor neuron degeneration independent of glial mutant superoxide dismutase 1 expression in SOD1-ALS mice.* J Neuropathol Exp Neurol, 2011. **70**(8): p. 662-77.

335. White, M.A., et al., *TDP-43 gains function due to perturbed autoregulation in a Tardbp knock-in mouse model of ALS-FTD.* Nat Neurosci, 2018. **21**(4): p. 552-563.

336. Bede, P., et al., *Grey matter correlates of clinical variables in amyotrophic lateral sclerosis (ALS): a neuroimaging study of ALS motor phenotype heterogeneity and cortical focality.* J Neurol Neurosurg Psychiatry, 2013. **84**(7): p. 766-73.

337. Chio, A., et al., *Neuroimaging in amyotrophic lateral sclerosis: insights into structural and functional changes.* Lancet Neurol, 2014. **13**(12): p. 1228-40.

338. Gerdes, M.J., et al., *Highly multiplexed single-cell analysis of formalin-fixed, paraffin-embedded cancer tissue.* Proc Natl Acad Sci U S A, 2013. **110**(29): p. 11982-7.

339. Schneider, C.A., W.S. Rasband, and K.W. Eliceiri, *NIH Image to ImageJ: 25 years of image analysis.* Nat Methods, 2012. **9**(7): p. 671-5.

340. Nelder, J.A., Wedderburn, W. M., *Generalized Linear Models.* Journal of the Royal Statistical Society: Series A (General), 1972. **135**(3): p. 15.

341. Wolfinger, R., O'Connell, M., *Generalized linear mixed models: a pseudo-likelihood approach.* Journal of Statistical Computation and Simulation, 1993. **48**: p. 10.

342. Kobayashi, K., et al., *Cerebral cortical calbindin D28K and parvalbumin neurones in Down's syndrome.* Neurosci Lett, 1990. **113**(1): p. 17-22.

343. Ferrer, I., et al., *Calbindin immunoreactivity in normal human temporal neocortex.* Brain Res, 1992. **572**(1-2): p. 33-41.

344. Bradl, M. and H. Lassmann, *Oligodendrocytes: biology and pathology.* Acta Neuropathol, 2010. **119**(1): p. 37-53.

345. Kushner, P.D., D.T. Stephenson, and S. Wright, *Reactive astrogliosis is widespread in the subcortical white matter of amyotrophic lateral sclerosis brain.* J Neuropathol Exp Neurol, 1991. **50**(3): p. 263-77.

346. Vogel, C. and E.M. Marcotte, *Insights into the regulation of protein abundance from proteomic and transcriptomic analyses.* Nat Rev Genet, 2012. **13**(4): p. 227-32.

347. Kwiatkowski, T.J., Jr., et al., *Mutations in the FUS/TLS gene on chromosome 16 cause familial amyotrophic lateral sclerosis.* Science, 2009. **323**(5918): p. 1205-8.

348. Gu, J., et al., *Transactive response DNA-binding protein 43 (TDP-43) regulates alternative splicing of tau exon 10: Implications for the pathogenesis of tauopathies.* J Biol Chem, 2017. **292**(25): p. 10600-10612.

349. Conlon, E.G., et al., *Unexpected similarities between C9ORF72 and sporadic forms of ALS/FTD suggest a common disease mechanism.* Elife, 2018. **7**.

350. Rezaie, T., et al., *Adult-onset primary open-angle glaucoma caused by mutations in optineurin.* Science, 2002. **295**(5557): p. 1077-9.

351. Richter, B., et al., *Phosphorylation of OPTN by TBK1 enhances its binding to Ub chains and promotes selective autophagy of damaged mitochondria.* Proc Natl Acad Sci U S A, 2016. **113**(15): p. 4039-44.

352. Moore, A.S. and E.L. Holzbaur, *Dynamic recruitment and activation of ALS-associated TBK1 with its target optineurin are required for efficient mitophagy.* Proc Natl Acad Sci U S A, 2016. **113**(24): p. E3349-58.

353. Ito, Y., et al., *RIPK1 mediates axonal degeneration by promoting inflammation and necroptosis in ALS.* Science, 2016. **353**(6299): p. 603-8.

354. Sundaramoorthy, V., et al., *Defects in optineurin- and myosin VI-mediated cellular trafficking in amyotrophic lateral sclerosis.* Hum Mol Genet, 2017. **26**(17): p. 3452.

355. Munitic, I., et al., *Optineurin insufficiency impairs IRF3 but not NF-kappaB activation in immune cells.* J Immunol, 2013. **191**(12): p. 6231-40.

356. Pottier, C., et al., *Whole-genome sequencing reveals important role for TBK1 and OPTN mutations in frontotemporal lobar degeneration without motor neuron disease.* Acta Neuropathol, 2015. **130**(1): p. 77-92.

357. Belzil, V.V., et al., *Analysis of OPTN as a causative gene for amyotrophic lateral sclerosis.* Neurobiol Aging, 2011. **32**(3): p. 555 e13-4.

358. van Blitterswijk, M., et al., *Novel optineurin mutations in sporadic amyotrophic lateral sclerosis patients.* Neurobiol Aging, 2012. **33**(5): p. 1016 e1-7.

359. Deng, H.X., et al., *Differential involvement of optineurin in amyotrophic lateral sclerosis with or without SOD1 mutations.* Arch Neurol, 2011. **68**(8): p. 1057-61.

360. Keller, B.A., et al., *Co-aggregation of RNA binding proteins in ALS spinal motor neurons: evidence of a common pathogenic mechanism.* Acta Neuropathol, 2012. **124**(5): p. 733-47.

361. Hortobagyi, T., et al., *Optineurin inclusions occur in a minority of TDP-43 positive ALS and FTLD-TDP cases and are rarely observed in other neurodegenerative disorders.* Acta Neuropathol, 2011. **121**(4): p. 519-27.

362. Ayaki, T., et al., *Multiple Proteinopathies in Familial ALS Cases With Optineurin Mutations.* J Neuropathol Exp Neurol, 2018. **77**(2): p. 128-138.

363. Pottier, C., et al., *Identification of compound heterozygous variants in OPTN in an ALS-FTD patient from the CReATe consortium: a case report.* Amyotroph Lateral Scler Frontotemporal Degener, 2018. **19**(5-6): p. 469-471.

364. Weishaupt, J.H., et al., *A novel optineurin truncating mutation and three glaucoma-associated missense variants in patients with familial amyotrophic lateral sclerosis in Germany.* Neurobiol Aging, 2013. **34**(5): p. 1516 e9-15.

365. Goldstein, O., et al., *OPTN 691_692insAG is a founder mutation causing recessive ALS and increased risk in heterozygotes.* Neurology, 2016. **86**(5): p. 446-53.

366. Del Bo, R., et al., *Novel optineurin mutations in patients with familial and sporadic amyotrophic lateral sclerosis.* J Neurol Neurosurg Psychiatry, 2011. **82**(11): p. 1239-43.

367. Iida, A., et al., *Optineurin mutations in Japanese amyotrophic lateral sclerosis.* J Neurol Neurosurg Psychiatry, 2012. **83**(2): p. 233-5.

368. Naruse, H., et al., *Mutational analysis of familial and sporadic amyotrophic lateral sclerosis with OPTN mutations in Japanese population.* Amyotroph Lateral Scler, 2012. **13**(6): p. 562-6.

369. Beeldman, E., et al., *A Dutch family with autosomal recessively inherited lower motor neuron predominant motor neuron disease due to optineurin mutations.* Amyotroph Lateral Scler Frontotemporal Degener, 2015. **16**(5-6): p. 410-1.

370. Li, C., et al., *Optineurin mutations in patients with sporadic amyotrophic lateral sclerosis in China.* Amyotroph Lateral Scler Frontotemporal Degener, 2015. **16**(7-8): p. 485-9.

371. Farhan, S.M.K., et al., *OPTN p.Met468Arg and ATXN2 intermediate length polyQ extension in families with C9orf72 mediated amyotrophic lateral sclerosis and frontotemporal dementia.* Am J Med Genet B Neuropsychiatr Genet, 2018. **177**(1): p. 75-85.

372. Keogh, M.J., et al., *Genetic compendium of 1511 human brains available through the UK Medical Research Council Brain Banks Network Resource.* Genome Research, 2017. **27**(1): p. 165-173.

373. Richards, S., et al., *Standards and guidelines for the interpretation of sequence variants: a joint consensus recommendation of the American College of Medical Genetics and Genomics and the Association for Molecular Pathology.* Genet Med, 2015. **17**(5): p. 405-24.

374. Penna, I., et al., *Selection of candidate housekeeping genes for normalization in human postmortem brain samples.* Int J Mol Sci, 2011. **12**(9): p. 5461-70.

375. Jara, J.H., et al., *Evidence for an early innate immune response in the motor cortex of ALS.* J Neuroinflammation, 2017. **14**(1): p. 129.

376. Turner, M.R., et al., *Evidence of widespread cerebral microglial activation in amyotrophic lateral sclerosis: an [11C](R)-PK11195 positron emission tomography study.* Neurobiol Dis, 2004. **15**(3): p. 601-9.

377. Sitte, H.H., et al., *Autoradiography with [3H]PK11195 of spinal tract degeneration in amyotrophic lateral sclerosis.* Acta Neuropathol, 2001. **101**(2): p. 75-8.

378. Boillee, S., et al., *Onset and progression in inherited ALS determined by motor neurons and microglia.* Science, 2006. **312**(5778): p. 1389-92.

379. Kitada, T., et al., *Mutations in the parkin gene cause autosomal recessive juvenile parkinsonism.* Nature, 1998. **392**(6676): p. 605-8.

380. Osawa, T., et al., *Optineurin in neurodegenerative diseases.* Neuropathology, 2011. **31**(6): p. 569-74.

381. Ito, H., et al., *Optineurin is co-localized with FUS in basophilic inclusions of ALS with FUS mutation and in basophilic inclusion body disease.* Acta Neuropathol, 2011. **121**(4): p. 555-7.

382. Korac, J., et al., *Ubiquitin-independent function of optineurin in autophagic clearance of protein aggregates.* J Cell Sci, 2013. **126**(Pt 2): p. 580-92.

383. Hattula, K. and J. Peranen, *FIP-2, a coiled-coil protein, links Huntingtin to Rab8 and modulates cellular morphogenesis.* Curr Biol, 2000. **10**(24): p. 1603-6.

384. Schwab, C., et al., *Optineurin in Huntington's disease intranuclear inclusions.* Neurosci Lett, 2012. **506**(1): p. 149-54.

385. Li, F., et al., *Structural insights into the interaction and disease mechanism of neurodegenerative disease-associated optineurin and TBK1 proteins.* Nat Commun, 2016. **7**: p. 12708.

386. Cirulli, E.T., et al., *Exome sequencing in amyotrophic lateral sclerosis identifies risk genes and pathways.* Science, 2015. **347**(6229): p. 1436-41.

387. Freischmidt, A., et al., *Haploinsufficiency of TBK1 causes familial ALS and fronto-temporal dementia.* Nat Neurosci, 2015. **18**(5): p. 631-6.

388. Bansal, M., et al., *Optineurin promotes autophagosome formation by recruiting the autophagy-related Atg12-5-16L1 complex to phagophores containing the Wipi2 protein.* J Biol Chem, 2018. **293**(1): p. 132-147.

389. Shen, W.C., et al., *Mutations in the ubiquitin-binding domain of OPTN/optineurin interfere with autophagy-mediated degradation of misfolded proteins by a dominant-negative mechanism.* Autophagy, 2015. **11**(4): p. 685-700.

390. Nakazawa, S., et al., *Linear ubiquitination is involved in the pathogenesis of optineurin-associated amyotrophic lateral sclerosis.* Nat Commun, 2016. **7**: p. 12547.

391. Cisse, S., et al., *Immunochemical identification of ubiquitin and heat-shock proteins in corpora amylacea from normal aged and Alzheimer's disease brains.* Acta Neuropathol, 1993. **85**(3): p. 233-40.

392. Selmaj, K., et al., *Corpora amylacea from multiple sclerosis brain tissue consists of aggregated neuronal cells.* Acta Biochim Pol, 2008. **55**(1): p. 43-9.

393. Pisa, D., et al., *Corpora Amylacea of Brain Tissue from Neurodegenerative Diseases Are Stained with Specific Antifungal Antibodies.* Front Neurosci, 2016. **10**: p. 86.

394. Buervenich, S., L. Olson, and D. Galter, *Nestin-like immunoreactivity of corpora amylacea in aged human brain.* Brain Res Mol Brain Res, 2001. **94**(1-2): p. 204-8.

395. Singhrao, S.K., et al., *New immunocytochemical evidence for a neuronal/oligodendroglial origin for corpora amylacea.* Neuropathol Appl Neurobiol, 1994. **20**(1): p. 66-73.

396. Stefanits, H., H. Budka, and G.G. Kovacs, *Asymmetry of neurodegenerative disease-related pathologies: a cautionary note.* Acta Neuropathol, 2012. **123**(3): p. 449-52.

397. King, A., et al., *Assessment of the degree of asymmetry of pathological features in neurodegenerative diseases. What is the significance for brain banks?* J Neural Transm (Vienna), 2015. **122**(10): p. 1499-508.

398. Sasaki, S. and M. Iwata, *Immunocytochemical and ultrastructural study of the motor cortex in patients with lower motor neuron disease.* Neurosci Lett, 2000. **281**(1): p. 45-8.

399. Yousef, A., et al., *Neuron loss and degeneration in the progression of TDP-43 in frontotemporal lobar degeneration.* Acta Neuropathol Commun, 2017. **5**(1): p. 68.

7. Supplementary material

Pathology quantitation algorithms

All code is written in the Apache groovy language.

pTDP-43/p62 positive pixel count

```
setImageType('BRIGHTFIELD_H_DAB');
setColorDeconvolutionStains('"Name" : "H-DAB default", "Stain 1" :
"Hematoxylin", "Values 1" : "0.65111 0.70119 0.29049 ", "Stain 2" :
"DAB", "Values 2" : "0.26917 0.56824 0.77759 ", "Background" : " 255
255 255 "');
runPlugin('qupath.imagej.detect.tissue.PositivePixelCounterIJ',
'"downsampleFactor": 3,  "gaussianSigmaMicrons": 2.0,
"thresholdStain1": 0.3,  "thresholdStain2": 0.2,
"addSummaryMeasurements": true');
```

CD68 cell count

```
setImageType('BRIGHTFIELD_H_DAB');
setColorDeconvolutionStains('"Name" : "H-DAB default", "Stain 1" :
"Hematoxylin", "Values 1" : "0.65111 0.70119 0.29049 ", "Stain 2" :
"DAB", "Values 2" : "0.26917 0.56824 0.77759 ", "Background" : " 255
255 255 "');
runPlugin('qupath.imagej.detect.nuclei.PositiveCellDetection',
'{"detectionImageBrightfield": "Optical density sum",
"requestedPixelSizeMicrons": 1.0,  "backgroundRadiusMicrons": 8.0,
"medianRadiusMicrons": 0.0,  "sigmaMicrons": 3.0,  "minAreaMicrons":
10.0,  "maxAreaMicrons": 400.0,  "threshold": 0.2,  "maxBackground":
2.0,  "watershedPostProcess": true,  "excludeDAB": false,
"cellExpansionMicrons": 5.0,  "includeNuclei": true,
"smoothBoundaries": true,  "makeMeasurements": true,
"thresholdCompartment": "Cell: DAB OD mean",  "thresholdPositive1":
0.15,  "thresholdPositive2": 0.4,  "thresholdPositive3": 0.6,
"singleThreshold": true');
```

Calbindin/Calretinin/Parvalbumin cell count

```
setImageType('BRIGHTFIELD_H_DAB');
setColorDeconvolutionStains('"Name" : "H-DAB default", "Stain 1" :
"Hematoxylin", "Values 1" : "0.65111 0.70119 0.29049 ", "Stain 2" :
"DAB", "Values 2" : "0.26917 0.56824 0.77759 ", "Background" : " 255
255 255 "}');
runPlugin('qupath.imagej.detect.nuclei.PositiveCellDetection',
'{"detectionImageBrightfield": "Optical density sum",
```

```
"requestedPixelSizeMicrons": 1.0,  "backgroundRadiusMicrons": 8.0,
"medianRadiusMicrons": 0.0,  "sigmaMicrons": 2.0,  "minAreaMicrons":
10.0,  "maxAreaMicrons": 400.0,  "threshold": 0.2,  "maxBackground":
2.0,  "watershedPostProcess": true,  "excludeDAB": false,
"cellExpansionMicrons": 5.0,  "includeNuclei": true,
"smoothBoundaries": true,  "makeMeasurements": true,
"thresholdCompartment": "Cell: DAB OD mean",  "thresholdPositive1":
0.2,  "thresholdPositive2": 0.4,  "thresholdPositive3": 0.6,
"singleThreshold": true');
```

OLIG2 cell count

```
setImageType('BRIGHTFIELD_H_DAB');
setColorDeconvolutionStains('"Name" : "H-DAB default", "Stain 1" :
"Hematoxylin", "Values 1" : "0.65111 0.70119 0.29049 ", "Stain 2" :
"DAB", "Values 2" : "0.26917 0.56824 0.77759 ", "Background" : " 255
255 255 "}');
runPlugin('qupath.imagej.detect.nuclei.PositiveCellDetection',
'{"detectionImageBrightfield": "Optical density sum",
"requestedPixelSizeMicrons": 0.5,  "backgroundRadiusMicrons": 8.0,
"medianRadiusMicrons": 0.0,  "sigmaMicrons": 1.5,  "minAreaMicrons":
10.0,  "maxAreaMicrons": 400.0,  "threshold": 0.5,  "maxBackground":
2.0,  "watershedPostProcess": true,  "excludeDAB": false,
"cellExpansionMicrons": 5.0,  "includeNuclei": true,
"smoothBoundaries": true,  "makeMeasurements": true,
"thresholdCompartment": "Nucleus: DAB OD mean",  "thresholdPositive1":
0.2,  "thresholdPositive2": 0.4,  "thresholdPositive3": 0.6,
"singleThreshold": true');
```

TPPP/p25 cell count

```
setImageType('BRIGHTFIELD_H_DAB');
setColorDeconvolutionStains('"Name" : "H-DAB default", "Stain 1" :
"Hematoxylin", "Values 1" : "0.65111 0.70119 0.29049 ", "Stain 2" :
"DAB", "Values 2" : "0.26917 0.56824 0.77759 ", "Background" : " 255
255 255 "}');
runPlugin('qupath.imagej.detect.nuclei.PositiveCellDetection',
'{"detectionImageBrightfield": "Optical density sum",
"requestedPixelSizeMicrons": 0.5,  "backgroundRadiusMicrons": 8.0,
"medianRadiusMicrons": 0.0,  "sigmaMicrons": 2.0,  "minAreaMicrons":
10.0,  "maxAreaMicrons": 400.0,  "threshold": 0.55,  "maxBackground":
2.0,  "watershedPostProcess": true,  "excludeDAB": false,
"cellExpansionMicrons": 5.0,  "includeNuclei": true,
"smoothBoundaries": true,  "makeMeasurements": true,
"thresholdCompartment": "Nucleus: DAB OD mean",  "thresholdPositive1":
0.2,  "thresholdPositive2": 0.4,  "thresholdPositive3": 0.6,
"singleThreshold": true');
```

RNAscope protocol – Ventana platform

Protocol # 161 : FUS - Amp 1HR (08/01/2018)

Procedure: mRNA Universal (v0.00.0210)

Discovery ULTRA Staining Module

Neuropathology Department, John Radcliffe Hospital Oxford, UK

Step No	Procedure Step
1	[mRNA Universal Procedure v2]
2	[All staining done using this procedure is for Research Use Only]
3	Enable Mixers
4	Warmup Slide to 37 Deg C
5	Apply 300ul of Reaction Buffer
6	Rinse Slide With Reaction Buffer
7	Adjust Slide Volume With Reaction Buffer
8	Apply Coverslip
9	Disable Slide Heater
10	Warmup Slide to 37 Deg C
11	Rinse Slide With EZ Prep
12	Adjust Slide Volume With EZ Prep
13	Apply Coverslip
14	[RECOMMENDED: Set to 97 C and 16min for FFPE cell pellets or 24min for normal FFPE tissue]
15	Rinse Slide With EZ Prep
16	Apply 300ul of EZ Prep
17	[Target Retrieval]
18	Apply Three Drops of mRNA Trgt Ret and Incubate for 4 Minutes
19	Incubate for 4 Minutes
20	Apply CC Medium Coverslip
21	Warmup Slide to [97 Deg C] from All Temperatures (Cycle 1)
22	Incubate for 8 Minutes
23	Apply 300ul of EZ Prep
24	Incubate for 8 Minutes
25	Apply 300ul of EZ Prep
26	Incubate for 8 Minutes
27	Disable Slide Heater
28	Apply Cell Conditioner #1
29	Apply CC Medium Coverslip No BB
30	Rinse Slide With Reaction Buffer
31	Adjust Slide Volume With Reaction Buffer
32	Apply Coverslip
33	Incubate for 4 Minutes
34	Rinse Slide With Reaction Buffer
35	Adjust Slide Volume With Reaction Buffer
36	Apply Coverslip
37	Rinse Slide With Reaction Buffer
38	Adjust Slide Volume With Reaction Buffer
39	Apply Coverslip
40	[Only select one mRNA option as multiple selections will yield negative results]
41	[Inhibitor for mRNA Red Detection will be applied]
42	Rinse Slide With Reaction Buffer
43	Adjust Slide Volume With Reaction Buffer
44	Apply Two Drops of ACD Inhib Red, Apply Coverslip, and Incubate for 4 Minutes
45	Warmup Slide to 37 Deg C, and Incubate for 12 Minutes

* one drop is one reagent dispense

Printed 05/31/2019 8:52:47 AM

Neuropathology Department, John Radcliffe Hospital Oxford, UK

Page 1 of 4

VSS v12.4 Build 15110.1

Protocol # 161 : FUS - Amp 1HR (08/01/2018)

Procedure: mRNA Universal (v0.00.0210)

Discovery ULTRA Staining Module

Neuropathology Department, John Radcliffe Hospital Oxford, UK

Step No	Procedure Step
46	Disable Slide Heater
47	[RECOMMENDED: Set to 37 C and 16min for normal FFPE samples]
48	Rinse Slide With Reaction Buffer
49	Adjust Slide Volume With Reaction Buffer
50	[Protease]
51	Apply Two Drops of mRNA Protease, Apply Coverslip, and Incubate for 0 Hr 4 Min
52	Warmup Slide to [37 Deg C], and Incubate for [0 Hr 16 Min] (Pretreatment #3 Temp RB)
53	Disable Slide Heater
54	Rinse Slide With Reaction Buffer
55	Adjust Slide Volume With Reaction Buffer
56	Apply Coverslip
57	Rinse Slide With SSC
58	Rinse Slide With SSC
59	Adjust Slide Volume With SSC
60	[Target Probe: RECOMMENDED: Set to 43 C for probe incubation]
61	Apply Two Drops of [PROBE 10] (Probe #1), Apply Coverslip, and Incubate for 4 Minutes
62	Warmup Slide to [43 Deg C], and Incubate for 2 Hours (Hybridization)
63	Disable Slide Heater
64	Incubate for 4 Minutes
65	Rinse Slide With SSC
66	Apply CC Coverslip
67	Rinse Slide With SSC
68	Rinse Slide With SSC
69	Incubate for 4 Minutes
70	Rinse Slide With SSC
71	Adjust Slide Volume With SSC
72	[Amp 1 AP]
73	[RECOMMENDED: Temp = 39 C for most samples]
74	Apply Two Drops of ACD RED AMP 1, Apply Coverslip, and Incubate for 4 Minutes
75	Incubate for 8 Minutes
76	Warmup Slide to [39 Deg C], and Incubate for 32 Minutes (Hybridization #2)
77	Disable Slide Heater
78	Rinse Slide With Reaction Buffer
79	Incubate for 4 Minutes
80	Rinse Slide With Reaction Buffer
81	Rinse Slide With Reaction Buffer
82	Apply Medium Cell Conditioner #1
83	Incubate for 4 Minutes
84	Apply Medium Cell Conditioner #1
85	Incubate for 8 Minutes
86	Rinse Slide With SSC
87	Adjust Slide Volume With SSC
88	[Amp 2 AP]
89	[RECOMMENDED: Temp = 39 C for most samples]
90	Apply Two Drops of ACD RED AMP 2, Apply Coverslip, and Incubate for 4 Minutes

Protocol # 161 : FUS - Amp 1HR (08/01/2018)

Procedure: mRNA Universal (v0.00.0210)

Discovery ULTRA Staining Module

Neuropathology Department, John Radcliffe Hospital Oxford, UK

Step No	Procedure Step
91	Incubate for 8 Minutes
92	Warmup Slide to [39 Deg C], and Incubate for 32 Minutes (Hybridization #4)
93	Disable Slide Heater
94	Rinse Slide With Reaction Buffer
95	Incubate for 4 Minutes
96	Rinse Slide With Reaction Buffer
97	Rinse Slide With Reaction Buffer
98	Apply Medium Cell Conditioner #1
99	Incubate for 4 Minutes
100	Apply Medium Cell Conditioner #1
101	Incubate for 4 Minutes
102	Apply Medium Cell Conditioner #1
103	Incubate for 8 Minutes
104	Rinse Slide With SSC
105	Rinse Slide With SSC
106	Adjust Slide Volume With SSC
107	Apply Two Drops of ACD RED AMP 3, Apply Coverslip, and Incubate for 4 Minutes
108	Warmup Slide to 37 Deg C, and Incubate for 0 Hr 12 Min
109	Disable Slide Heater
110	Rinse Slide With SSC
111	Rinse Slide With SSC
112	Adjust Slide Volume With SSC
113	Apply Two Drops of ACD RED AMP 4, Apply Coverslip, and Incubate for 4 Minutes
114	Warmup Slide to 37 Deg C, and Incubate for 32 Minutes
115	Disable Slide Heater
116	Rinse Slide With SSC
117	Rinse Slide With SSC
118	Incubate for 4 Minutes
119	Rinse Slide With Reaction Buffer
120	Rinse Slide With Reaction Buffer
121	Adjust Slide Volume With Reaction Buffer
122	Apply Two Drops of ACD RED AMP 5, and Incubate for 12 Minutes
123	Apply Coverslip
124	[Amp 5 AP incubation time: RECOMMENDED: 4 min]
125	Incubate for [1 Hour] (Hybridization #5)
126	Rinse Slide With Reaction Buffer
127	Rinse Slide With Reaction Buffer
128	Apply Coverslip
129	Incubate for 4 Minutes
130	Rinse Slide With Reaction Buffer
131	Adjust Slide Volume With Reaction Buffer
132	Apply Two Drops of ACD RED AMP 6, and Incubate for 4 Minutes
133	Apply Coverslip
134	Incubate for 32 Minutes
135	Rinse Slide With Reaction Buffer

Protocol # 161 : FUS - Amp 1HR (08/01/2018)

Procedure: mRNA Universal (v0.00.0210)

Discovery ULTRA Staining Module

Neuropathology Department, John Radcliffe Hospital Oxford, UK

Step No	Procedure Step
136	Rinse Slide With Reaction Buffer
137	Apply Coverslip
138	Incubate for 4 Minutes
139	Rinse Slide With Reaction Buffer
140	Adjust Slide Volume With Reaction Buffer
141	Apply Two Drops of ACD RED AMP 7, Apply Coverslip, and Incubate for 4 Minutes
142	Rinse Slide With Reaction Buffer
143	Adjust Slide Volume With Reaction Buffer
144	Apply Coverslip
145	Rinse Slide With Reaction Buffer
146	Adjust Slide Volume With Reaction Buffer
147	Apply Two Drops of ACD Activator, and Incubate for 8 Minutes
148	Apply One Drop of ACD Naphthol, and Incubate for 4 Minutes
149	Apply One Drop of ACD Fastred, and Incubate for 4 Minutes
150	Apply One Drop of ACD Fastred, and Incubate for 8 Minutes
151	Rinse Slide With Reaction Buffer
152	Adjust Slide Volume With Reaction Buffer
153	Apply Coverslip
154	Rinse Slide With Reaction Buffer
155	Adjust Slide Volume With Reaction Buffer
156	Apply One Drop of [HEMATOXYLIN II] (Counterstain), Apply Coverslip, and Incubate for [12 Minutes]
157	Rinse Slide With Reaction Buffer
158	Adjust Slide Volume With Reaction Buffer
159	Rinse Slide With Reaction Buffer
160	Adjust Slide Volume With Reaction Buffer
161	Apply One Drop of [BLUING REAGENT] (Post Counterstain), Apply Coverslip, and Incubate for [8 Minutes]
162	Rinse Slide With Reaction Buffer
163	Adjust Slide Volume With Reaction Buffer
164	Apply Coverslip